Superconducting Nanowire Devices for Optical Quantum Information Processing

School of Engineering
University of Glasgow

Luke James Baker

26 09 2017

Abstract

Near infrared photons are a promising choice for quantum information processing; their low transmission loss is necessary for applications such as long distance Quantum Key Distribution (QKD) in optical fibre and integrated quantum optics. An ideal proof-of-concept test of such applications would be to create, manipulate and detect single photons on a monolithic chip. Superconducting nanowire single photon detectors promise high system detection efficiencies, low dark count and low jitter under near-infrared photon illumination. Superconducting nanowire devices using NbTiN films show improved coupling efficiencies with the aid of oxidized silicon cavities. NbTiN devices were characterised in a fibre-coupled package, achieving high System Detection Efficiency (43%) and coherent key generation rates over 200km in a T12 QKD protocol simulation. Hairpin superconducting nanowires offer excellent integration with silicon waveguide optics and can achieve near unity absorption efficiencies. Hairpin devices fabricated from MoSi films were characterised using a custom pulse tube/^{3}He cryostat engineered for low vibration operation at 350mK and capable of near-infrared optical maps of superconducting nanowires. The devices exhibited high critical currents ($\sim$40μA), low jitter (51ps) and a dark count rate $<$10cps. Tests of perpendicular coupling efficiencies yield low system detection efficiencies due to high coupling losses. Using an alternative coupling method via grating couplers or cleave mounting, it is expected a much higher system detection efficiency can be achieved.

"A few weeks ago I was walking through the park and I came across something kind of weird- Something that I could not immediately explain. It was an arc in the grass of greener grass about 10 feet long as if someone had carefully spread fertaliser along a curving strip of the park. And once I saw it, I started to see more, dozens of them- One of them was even a full circle. When I find something, just hanging out in the park that I've never heard of and cannot explain... That's frustrating."

- Hank Green

Acknowledgements

I would like to thank everyone who supported me in any form of contribution towards the completion of this Thesis. Their knowledge is valuable, but their friendship is paramount.

Foremost, I must thank my supervisor Prof. Robert Hadfield for his approachability, enthusiasm and patience in developing my skills in research science. The help and guidance I have received from him has been invaluable.

I am grateful to Dr. Jian Li for his guidance in constructing the Rankinator. Without his expertise in radiofrequency signals, we would not have achieved a working cryostat in such a short time, if at all. I am also indebted to Robert Heath for his knowledge in optics, as well as programming skill, without which this project would have extended by several decades.

I'd also like to thank Dr. Robert Kirkwood not only for his skill in fabrication, but for the MoSi hairpin nanowire devices that achieved publication; Archan Banerjee for his work in optimised film growth, which allowed me to fabricate my own samples and Dr. Chandra Mouli Natarajan for his experience in optomechanics. I also thank Dr. Alessandro Casaburi for his early supervisory role.

Further gratitude goes to Dr. Shigehito Miki (NICT, Japan) and Dr. Val Zwiller (TU Delft, Japan) for supplying the SNSPD characterised in this Thesis; Dr. David Bosworth and Dr. Zoe Barber (University of Cambridge) for the optimised MoSi sputtering process and Dr. Andrew Shields (Toshiba European Research Laboratory, Cambridge) for his simulations of the characterised device under the T12 QKD protocol.

Special thanks goes to Steve McKernan for the quick turnaround in building and maintaining components of the Rankinator and Helen McLelland for her expertise and patient approach to resolving problems within the JWNC.

I'd also grateful for my little sister Amelia and my parents, Susan and Steven for their encouragement and financial support.

This work would not have been possible without funding for the Engineering and Physical Sciences Research Council (EPSRC).

Author’s Declaration

I declare that, except where explicit reference is made to the contribution of others, this thesis is the result of my own work and has not been submitted for any other degree at the University of Glasgow or any other institution. For the avoidance of ambiguity, a full breakdown of my personal contribution is stated in Table 2.1.

Chapter	**Personal Contribution**
1	Text.
2	Text; graphics and graph data.
3	Text; graphics and graph data; SEM, optical microscope and Attocube scanning images; MoSi fabrication recipe as adapted from Dr. Robert Kirkwood; OCT distance measurements; fibre ferrule spot alignment; Rankinator design adapted from Kelvinator design; cryostat installation of components and wiring; cryostat vibration damping; cryostat control and monitoring programs; sorption pump optimised operation procedure; Attocube control programming with the aid of Dr. Robert Heath; confocal microscope assembly and resolution tests; cryostat heat load calculations and measurements; assorted Python programming.
4	Text; graphics and graph data; OCT measurements and fibre spot positioning data; devices characterisation; analysis and discussion of results.
5	Text; graphics and graph data; SEM images; 4-Pin MoSi test structure design and fabrication; 4-Pin test structures characterisation and photoresponse maps; MoSi device characterisation and photoresponse maps with the aid of Dr. Jian Li; analysis and discussion of results.
6	Text.

Table 2.1: Author’s contributions to the work. All elements are works of the author, excepted where stated in the text.

Contents

List of Figures

List of Tables

Abbreviations & Symbols

Acronyms

AC Alternating Current.

AFM Atomic Force Microscope.

AGHS Active Gas-Gap Heat Switch.

APD Avalanche Photodiode.

ARC Anti-Reflection Coating.

BBR Blackbody Radiation.

BCS Bardeen, Cooper and Schrieffer.

CDT Centre for Doctoral Training.

CNOT Controlled-NOT.

DC Direct Current.

DCR Dark Count Rate.

DDE Device Detection Efficiency.

DSTL Defence Science and Technology Laboratory.

EBL Electron Beam Lithography.

ECL External Cavity Laser.

EELS Electron Energy Loss Spectroscopy.

EPSRC Engineering and Physical Sciences Research Council.

ERC European Research Council.

erf Error Function.

FEM Field Emission Microscopy.

FSO Free-Space Optics.

FWHM Full Width at Half Maximum.

GM Gifford-McMahon.

GRIN Graded Index.

HF Hydrofluoric Acid.

HRS High Resistivity Substrate.

HSQ Hydrogen Silsequioxane.

ICP Inductively Coupled Plasma.

JWNC James Watt Nanofabrication Centre.

KID Kinetic Inductance Detector.

LASER Light Amplification by Stimulated Emission of Radiation.

LEKID Lumped Element Kinetic Inductance Detector.

LHV Locally-Hidden Variable.

LOQC Linear Optical Quantum Computing.

LPF Low-Pass Filter.

MASER Microwave Amplification by Stimulated Emission of Radiation.

NA Numerical Aperture.

NICT National Institute of Information and Communications Technology.

NIR Near-Infrared.

NL Non-Locality.

NMR Nuclear Magnetic Resonance.

OCT Optical Coherence Tomography.

PEC Proximity Effect Correction.

PID Proportional-Integral-Derivative.

PMMA Poly-Methyl Methacrylate.

PMT Photon Multiplier Tube.

PNS Photon Number Splitting.

PPG Pulse Pattern Generator.

PT Pulse Tube.

QBER Quantum Bit Error Rate.

QC Quantum Computer.

QD Quantum Dot.

QIP Quantum Information Processing.

QKD Quantum Key Distribution.

QM Quantum Mechanics.

RF Radio Frequency.

RIE Reactive Ion Etching.

RMS Root Mean Square.

SDE System Detection Efficiency.

SEM Scanning Electron Microscope.

SLD Superluminescent Diode.

SMF Single-Mode Optical Fibre.

SNAP Superconducting Nanowire Avalanche Photodetector.

SNR Signal-to-Noise Ratio.

SNSPD Superconducting Nanowire Single Photon Detector.

SoI Si-on-Insulator.

SPAD Single-Photon Avalanche Photodiode.

SPD Single-Photon Detector.

SPDC Spontaneous Parametric Down-Conversion.

SQUID Superconducting Quantum Interference Device.

STJ Superconducting Tunnel Junction.

TCSPC Time-Correlated Single Photon Counting.

TES Transition Edge Sensor.

TIA Time Interval Analyser.

UHV Ultra-High Vacuum.

UV Ultra-Violet.

VAP Vortex-Antivortex Pair.

VASE Variable Angle Spectroscopy Ellipsometry.

VRU Vectorscan Resolution Unit.

WaSTe Wavelength Scanning Test.

Roman Symbols

A Cross-sectional area.

$\mathbf{B}$ Magnetic field vector.

$B(x)$ 1D magnetic field as a function of x.

d Film thickness.

E Energy.

$\mathbf{E}$ Electric field vector.

E_i Energy level of particle in state i.

E_k Kinetic energy.

e_m QBER from detection events of an m-photon signal state.

E_m QBER from an m-photon signal state.

f Frequency.

Δf Frequency bandwith.

f_P Laser pulse rate.

$g^{(2)}(\tau)$ Function of tine correlation interval between events.

G Gaussian distribution.

g Complex degree of temporal coherence.

G_t Temporal coherence function.

I Current.

I_C Critical current.

$I_{C,Dep}$ Critical deparing current.

I_{Noise} RMS Current noise level.

J Current density.

J_C Critical current density.

J_s Surface current density.

k Propagation vector.

k_C Thermal conductivity.

L Length.

L_k Kinetic inductance.

m Integer number of photons.

n Carrier density.

$\mathbb{N}$ Positive integer.

n_e Number density of quasi-particles.

n_i Number density i-type particles.

n_s Number density of superconducting electrons.

$\mathcal{P}$ Probability.

Q Heat transfer.

Q_m Gain of an m-photon signal state.

R_{det} Number of detection events.

R_L Load resistor.

R_n Resistance of nanowire in normal state.

T Temperature.

T_C Critical temperature.

t time.

t_R Dead time.

U Complex wavefunction of light.

w Width of nanowire.

Y_m Yield of an m-photon signal state.

Greek Symbols

α Arbitrary eigenvalue.

β Arbitrary eigenvalue.

$\Delta\ell$ Spatial resolution.

$\Delta(T)$ Energy gap of superconductor at temperature T(K).

Δt FWHM of variance in detector response time.

ς Ratio of penetration depth to coherent length.

κ Extinction coefficient.

λ_L Penetration depth.

λ Wavefunction.

Λ Pearl length.

N Refractive index.

$\eta_{Absorption}$ Absorption efficiency.

$\eta_{Coupling}$ Coupling efficiency.

η_{DDE} Intrinsic device detection efficiency.

$\eta_{Registering}$ Registering efficiency.

η System detection efficiency.

Φ Work function.

ϕ Diameter.

ψ Order parameter. The order of a superconducting system.

Ψ Wavefunction.

σ Standard deviation.

τ Specified time period.

θ Angle of latitude.

Θ Angle of longitude.

μ Average number of photons per laser pulse.

ξ_{GL} Coherence length.

$\chi^{(2)}$ Second-order interference effects.

Fundamental Constants

e Electron charge. $1.60217662 \times 10^{-19} C$.

ϵ_0 Permittivity of free space. $8.85418782 \times 10^{-12} m^{-3} kg^{-1} s^4 A^2$.

h Planck's constant. $6.62607004 \times 10^{-34} m^2 kg/s$.

k_b Boltzman constant. $1.38064852(79) \times 10^{-23} J/K$.

m_e Electron mass. $9.10938356 \times 10^{-31} kg$.

μ_0 Permeability of free space. $1.25663706 \times 10^{-6} mkgs^{-2} A^{-2}$.

Periodic Table of Used Elements

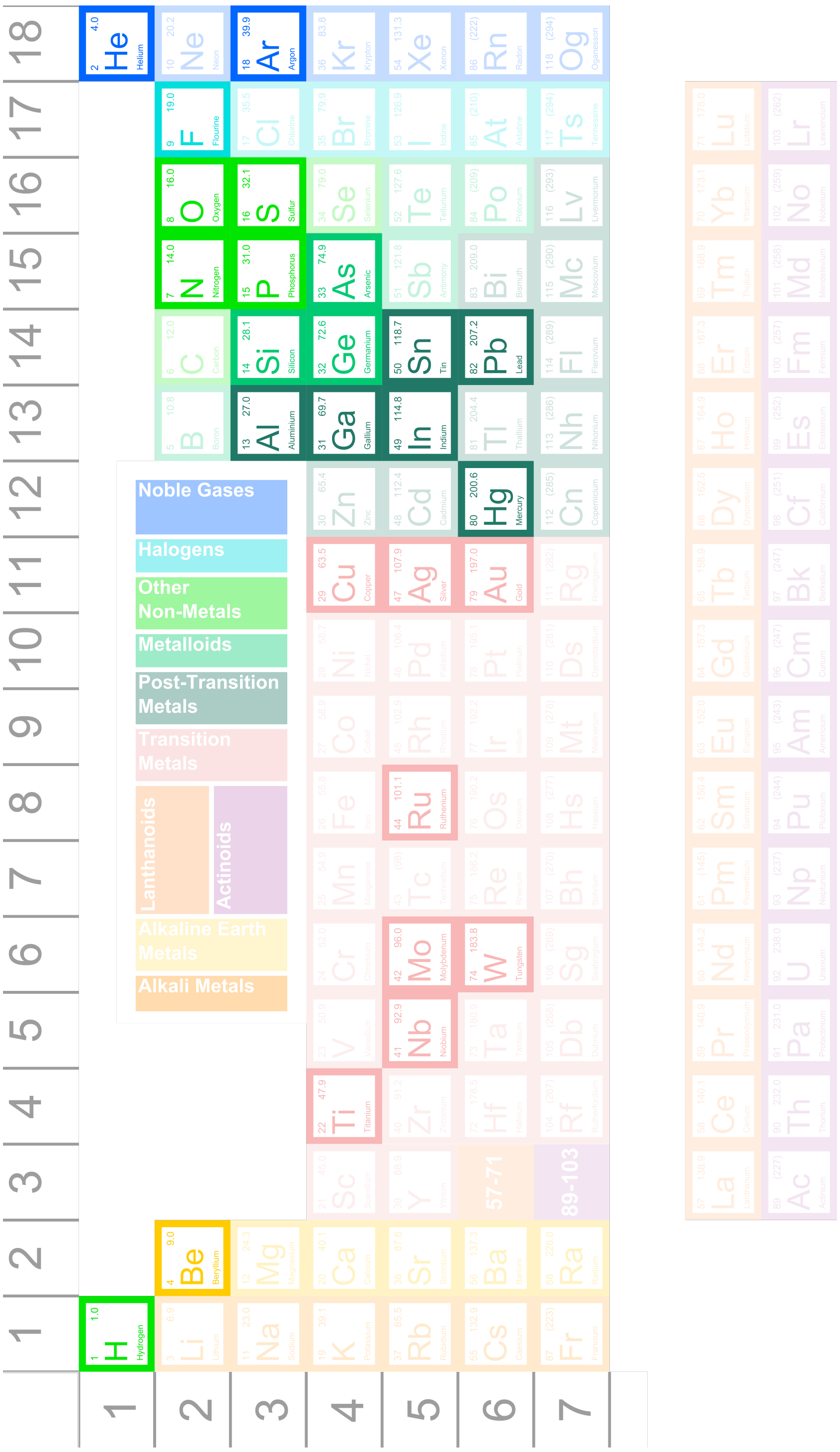

Chapter 1

Overview & Motivation

Quantum Information Processing (QIP) presents a new frontier in computing. By implementing the non-classical nature of quantum bits, known as qubits, algorithmic processes can be performed exponentially faster than their classical counterparts. In communications, the application of these quantum systems has led to the development of Quantum Key Distribution (QKD). QKD is a key generation process that is highly sensitive to external eavesdroppers and allows two users to generate keys that are practically impossible to crack. To conceptualise scalable optical QIP, single-chip processors would have to consist of three components: Sources to prepare qubits, gates to manipulate their state and sinks to perform measurements.

A promising medium for establishing real-world QIP is through quantum optics in which the basis of a qubit can be represented by several characteristics of light, including its polarisation. A 2001 paper by Knill, Laflamme and Milburn[1] proposed Linear Optical Quantum Computing (LOQC) in which algorithms were performed using single photons travelling through a waveguide track, interacting with phase-shifters and beam splitters, to then be measured by photo-detectors. Photonics benefits from low noise and high speed transmission. Photons also achieve some of the longest coherence times; this allows 1550nm silicon fibre-optics to be implemented in quantum communications and achieve long distance, low loss QKD. A picture of the physics of quantum optics is the focus of §2.2. Quantum Optics. The physics and application of QIP can be found in §2.4. Quantum Information Processing.

Photons can be described as single wave-packets with an energy proportional to their wavelength. It can be stated that their existence is a consequence of the conservation of energy after the transition of a charged particle between two energy states. There are many methods to instantiate single photon sources including; Spontaneous Parametric Down-Conversion (SPDC), an attenuated laser source or through the use of Quantum Dots (QDs), which offer deterministic photon output. In regards to gates, successful manipulation of single photon states have been achieved with beam splitters on single-mode waveguide circuits, but not yet with phase-shifters. The focus of this Thesis is on the final step: Detection.

Single photons are challenging to detect. They are extremely low energy states which can be easily drowned out by noise, blackbody radiation and unwanted scattering or absorption. It is both necessary and advantageous for single photon experiments to be performed at low temperatures (<5K) and in high vacuums (1×10^{-6}mBar). Superconducting Nanowire Single Photon Detectors (SNSPDs) are currently established devices with excellent performance characteristics, offering high System Detection Efficiency (SDE), low timing jitter and low dark count[2–5]. SNSPDs are meander nanowires made from superconducting materials whose properties allow for the detection of laser pulses two or three orders of magnitude weaker than common room temperature semiconductors. SNSPDs have been used in a wide variety of applied experiments, including applications in Quantum Key Distribution (QKD)[6–12], quantum computing[1, 13, 14], metrology[15], time-of-flight ranging[16] and medical applications in singlet oxygen luminescence detection[17]. The necessary background on superconductivity required to understand detector operation can be found in §2.1. Superconductivity. A more detailed picture of single photon detection can be found in §2.3. Single Photon Detection.

The main focus of this work was to construct and maintain a two-stage ^{3}He cryocooler capable of scanning reflection and photoresponse maps between 0.35-5K. For most known superconducting films that are used to create SNSPDs, their operating temperature and critical current are inversely proportional. A lower temperature is therefore capable of higher operational current biases and it will be seen how this leads to higher overall device efficiency (§2.3.3. Registering Efficiency). The cryostat is also useful for characterising films with transition temperatures lower than the base temperature of established pulse tubes 2K. The full details of the cryostat can be found in §3.3. Rankinator Design.

SNSPD devices characterised in this Thesis were constructed from two different superconducting films; MoSi and NbTiN. NbTiN has a low extinction coefficient, which reduces the absorption efficiency of the material. Thus, the device is placed in an optical cavity to increase its coupling efficiency and likelihood of absorption. By characterising these devices it is then possible to implement the devices in particular experiments. This is the main focus of §4. Cavity SNSPD Devices.

In order to establish full SNSPD fabrication procedures in Glasgow, work by Dr. Archan Banerjee was performed on optimising the sputtering process of varied superconducting films, including NbTiN and MoSi. The first part of §5. MoSi Devices details the fabrication and characterisation of simple MoSi test structures etched from these sputtered films. The aim of this work was to characterise the transport properties of the film and compare this with literature.

Meander SNSPDs present a difficulty in on-chip scalability as they are limited by the placement of a coupled fibre. Hairpin nanowires are an emerging design that allows for near unity efficiency detection of photons travelling through a waveguide. This would allow for scalable integrating of SPDs on a waveguide chip quantum computer. The second part of §5. MoSi Devices involved characterising a MoSi hairpin nanowire to test the device's efficiency and responsiveness. The main method of characterisation involved creating photoresponse maps of the device using the Rankinator setup.

Full details of device fabrication can be found in §3.1. Fabrication, device coupling methods are found in §3.2. Device Mounting Methods and characterisation methods found in §3.4. Low Temperature Measurements.

Chapter 2

Literature Review

This chapter reviews the relevant physics required to understand the nature and operation of Superconducting Nanowire Single Photon Detector (SNSPD); §2.1. Superconductivity and §2.2. Quantum Optics. It also reviews a range of Single-Photon Detectors (SPDs), their device architecture, operation and performance characteristics, with an in-depth focus on the SNSPD; §2.3. Single Photon Detection. Finally, it details SNSPD applications including quantum computing and Quantum Information Processing (QIP) §2.4. Quantum Information Processing; in particular, its application to the field of cryptography.

2.1 Superconductivity

Between 1908-11, Heike Kamerlingh Onnes[18] studied the resistance of metals at low temperature. He employed a newly developed glass walled cryostat, invented by the eponymous James Dewar just a few years earlier. The dewar could hold liquefied ^{4}He, which supported sample testing down to 4.2K. Kamerlingh Onnes used the cryostat to electrically test Hg below 4.15K, discovering the remarkable property that the material reached a resistance of zero below 2.4K. He dubbed this effect: superconductivity. This initiated a new field of research as superconducting processes occurred in a wide range of materials and had complex underlying physics. Moreover, if the effects could be harnessed, there was rich potential for practical applications. In 1933, Walther Meissner[19] and coworkers measured the magnetic field distribution expelled from superconducting samples of Sn and Pb. They found the material refused the penetration of any external magnetic field; in a sense, the material become invisible to any applied magnetic field. This second phenomenon presented the complete picture of superconductivity, which is

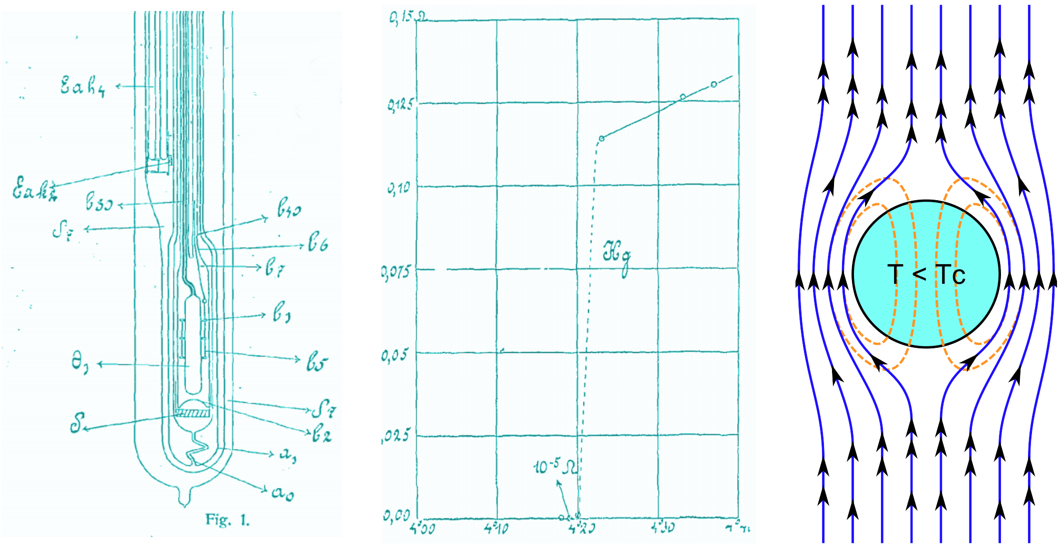

(a) (b) (c)

Figure 2.1: (a) Double walled glass dewar. (b) Kamerlingh Onnes' measurements of the resistance of Hg against temperature. Its resistance dropped to zero at 4.2K. (a) and (b) adapted from Kamerlingh Onnes' original paper[18]. (c) A representation of the expelled magnetic field around a superconductor due to the Meissner effect. The net affect of the field appears to warp around the superconductor.

defined as the temperature T_C at which a material shows the effect of diamagnetism and subsequently, perfect conduction.

The first theoretical explanations of superconductivity came in 1934 from Gorter and Casimir who posited the two-fluid model[20, 21]. They considered that conduction in a material formed two populations: The first was a density of quasiparticles n_e that acted like electrons and experienced scattering in the lattice, the second was a density of superconducting electrons n_s which experienced no scattering. Experimental measurements concluded that the density of normal and superconducting electrons starts to change below the transition temperature. Above T_C, the device would consist only of normal electrons and, as the temperature decreased below T_C, the density of superconducting electrons would increase rapidly, replacing the normal electrons (Figure 2.2).

2.1.1 The London Equations

In 1935, Fritz and Heinz London[21, 22] *et al* studied the nature of diamagnetism and proposed a theoretical explanation for the Meissner effect. They suggested that the external applied field created surface currents on the material that induced their own magnetic fields which opposed the flow of the applied field. They developed a series of equations to explain this effect. First, they described how the current in the superconductor was dependent on the superconducting electron density, which lead to the first London equa-

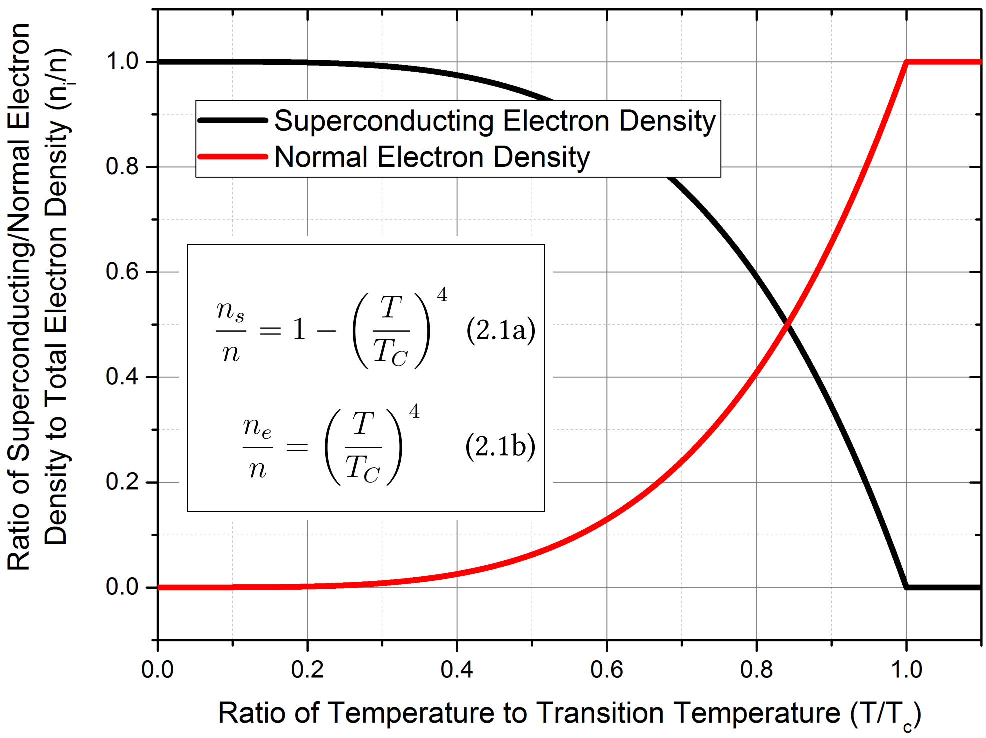

Figure 2.2: Relationship between superconducting electron density and normal electron density in the two-fluid model, where n represents the total carrier density and n_i represents the density of either superconducting or normal electrons.

tion (Equation 2.2a). By taking this equation and applying Faraday's law of induction (Equation 2.6c) they were able to show that an applied magnetic field would create a surface current density J_s that would negate the field, which was known as the second London equation (Equation 2.2b). To understand the change in magnetic field in relation to the superconductor, London and London applied this equation to Ampère's circuital law (Equation 2.6d) to achieve a second order differential equation whose solution produced an exponentially decaying magnetic field inside the conductor (Equation 2.2c) at a rate defined as the penetration depth (Equation 2.2d).

$$\frac{\partial J}{\partial t} = \frac{n_s e^2}{m_e}\mathbf{E} \tag{2.2a}$$

$$\nabla \times J_s = \frac{n_s e^2}{m_e}\mathbf{B} \tag{2.2b}$$

$$B(x) = B(0)e^{\frac{-x}{\lambda_L}} \tag{2.2c}$$

$$\lambda_L = \left(\frac{m_e}{\mu_0 n_s e^2}\right)^2 \tag{2.2d}$$

2.1.2 Ginzburg-Landau Theory

Ginzburg and Landau[21] produced their own theory in 1950. Their mathematics started from a different perspective, speculating that the makeup of a system was described by the order parameter, ψ. This parameter described the order of a system and was related to the superelectron density: $|\psi|^2 = n_s$. Using the Gibbs free energy equation and the order parameter, Ginzburg and Landau derived two simultaneous equations to that could describe superconductivity. Solutions to these equations produced two descriptive variables: The coherence length ξ_{GL}, which described the spatial length scale over which the order parameter varied, and the penetration depth λ_L, the same factor discovered by the London brothers in 1935 (Figure 2.3(a)). Ginzburg and Landau proposed that the ratio of these variables could be used to categorise two types of superconductors; Type I and Type II. A Type I superconductor (Equation 2.3b) featured an instantaneous transition in resistivity below T_C and perfect diamagnetism – no external field could penetrate the conductor. A Type II superconductor (Equation 2.3c) transitioned noticeably slower and allowed for the penetration of an external field, known as flux penetration.

Flux Penetration

Flux penetration occurs when a weak, external field penetrates a thin, Type-II superconductor. It can only occur if the nanowire width is much smaller than the Pearl length[23] ratio, $w \ll \Lambda$, where $\Lambda = 2\lambda_L^2/d$, and its thickness is thinner than the penetration depth, $d \ll \lambda_L$. This is shown in Figure 2.3(b) for the case of a superconducting strip with zero bias current. Flux penetration only occurs in quantised packets of $h/2e$ and, due to induction, causes a similarly quantised vortex supercurrent. It will be seen in

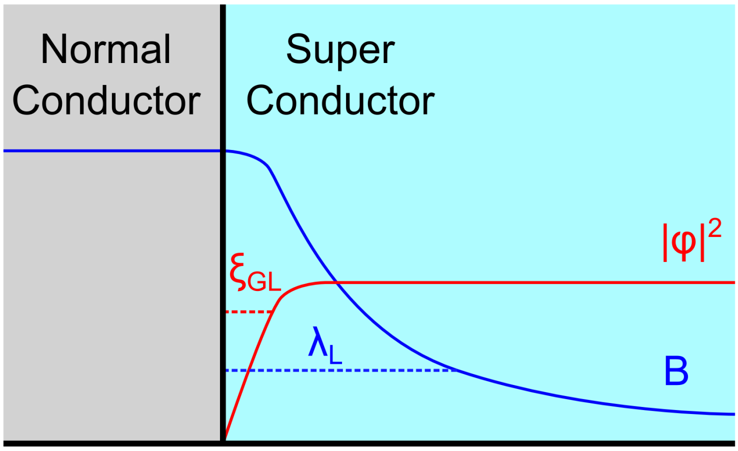

(a)

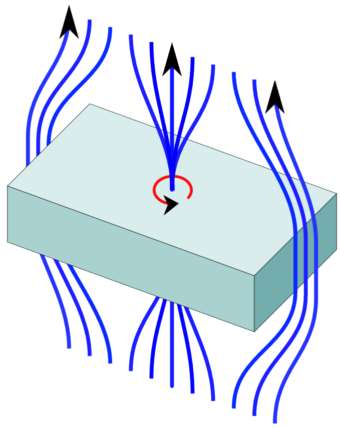

(b)

Figure 2.3: (a) Changes in the order parameter and the magnetic field strength between the boundaries of a normal conductor and superconductor. (b) The effect of flux penetration for a superconducting strip under no applied current.

§2.3.1. Intrinsic DCR in Superconducting Detectors how these and other vortices can cause intrinsic dark counts in a detector.

$$\varsigma = \frac{\lambda_L(T)}{\xi_{GL}(T)} \tag{2.3a}$$

$$\varsigma \ll \frac{1}{\sqrt{2}} \quad \text{Type I} \tag{2.3b}$$

$$\varsigma \gg \frac{1}{\sqrt{2}} \quad \text{Type II} \tag{2.3c}$$

2.1.3 BCS Theory

Ginzburg-Landau theory was useful in gauging the macroscopic effects of superconductivity, but the microscopic effects were not understood until 1957 after a publication by Bardeen, Cooper and Schrieffer who postulated BCS Theory[21, 24]. This theory yielded a set of relationships form which parameters of the material, such as specific heat and critical current density, could be calculated as a function of temperature and energy gap, $\Delta(T)$. The theory stated that, below a critical temperature, the fermionic electrons conducting through a material could combine to form bosonic quasiparticles coined Cooper pairs. When one electron in the pair lost energy through phonon interactions, its partner compensated, resulting in no absolute energy loss and leading to a material with no resistance. This effect can be interpreted in Figure 2.4; when an electron interacts with the material's lattice structure it changes momentum and produces a phonon. Hypothetically, this phonon directly collides with the other electron in the pair and changes its momentum to correct for the initial electron's loss.

Cooper pairs are electrons bound in a state at a lower energy than the summation of the minimum Fermi energy for each electron, which causes them to act as bosons. The binding energy required to break a Cooper pair into quasiparticles is defines as $2\Delta(T)$ and can be achieved through the interaction of an incident photon with an energy greater than or equal to the binding energy. The separated quasiparticles then return to acting as normal, fermionic electrons. Compared to common semiconductor materials, superconductors have energy gap values two or three orders of magnitude lower[25]. This key effect is fundamental to the operation of superconducting single-photon detectors.

BCS theory shows that the energy gap has a dependence on temperature, but does not directly solve for this dependence. Instead, it predicts the dependence for two specific conditions: In the first instance, when $T = 0$K, the energy gap reaches its peak value (Equation 2.4a) and, in the second instance, when $T \to T_C$, the energy gap decays to 0 (Equation 2.4b). Work by Mühlschlegel approximated the $\Delta(T)$ parameter, achieving analytical solutions for $\Delta(T)$ [26]. Later, Khasanoc *et al* developed an approximate equation to describe this relationship (Equation 2.4c)[27, 28]. In Figure 2.5 it can be seen how this equation closely fits the data collected by Mühlschlegel.

$$2\Delta(T = 0) = 3.53 k_b T_C \tag{2.4a}$$

$$2\Delta(T \to T_C) \approx 3.07 k_b T_C \sqrt{1 - \frac{T}{T_C}} \tag{2.4b}$$

$$\Delta(T) = \Delta(0) tanh \left[1.82 \left[1.018 \left(\frac{T_C}{T} - 1 \right) \right]^{0.51} \right] \tag{2.4c}$$

2.1.4 Limits of Superconductivity

Though it has only been implied thus far, a supercurrent is limited by several factors[29, 30]. Theoretically, the critical depairing current $I_{C,Dep}$ describes the maximum applied current to the device before it switches immediately to its normal state. This is caused by the depairing of Cooper pairs and can occur from an excess of applied energy - through an increase in temperature or an increase in current - or through spin flipping - through an increase in applied field[31]. Practically, the actual critical current of a physical device I_C will be limited by the effects of current crowding (§2.3.3. Geometry Dependence) in which the current density increases at the inner bends of a nanowire pattern. Increasing the ratio of $I_C/I_{C,Dep}$ decreases the energy gap of the Cooper pairs and allows for shorter wavelength photon absorption.

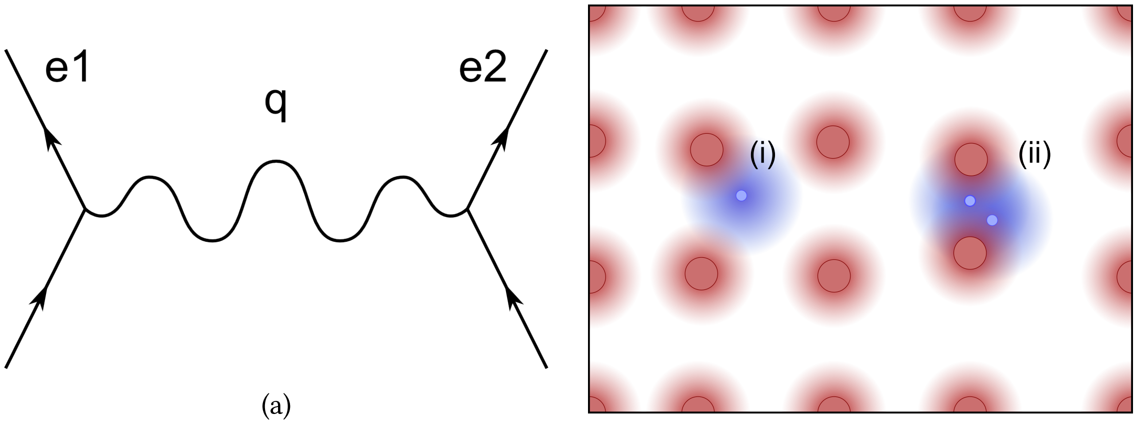

(a)

(b)

Figure 2.4: (a) Feynman diagram of a Cooper pair shows two electrons (e1, e2) bound by a phonon (q) interaction, noting their change in momentum before and after the interaction. (b) A single quasiparticle creates a region of attraction for phonons (i), which attracts other quasiparticles. The increased positive charge allows two quasiparticles to exist as a single Cooper pair (ii).

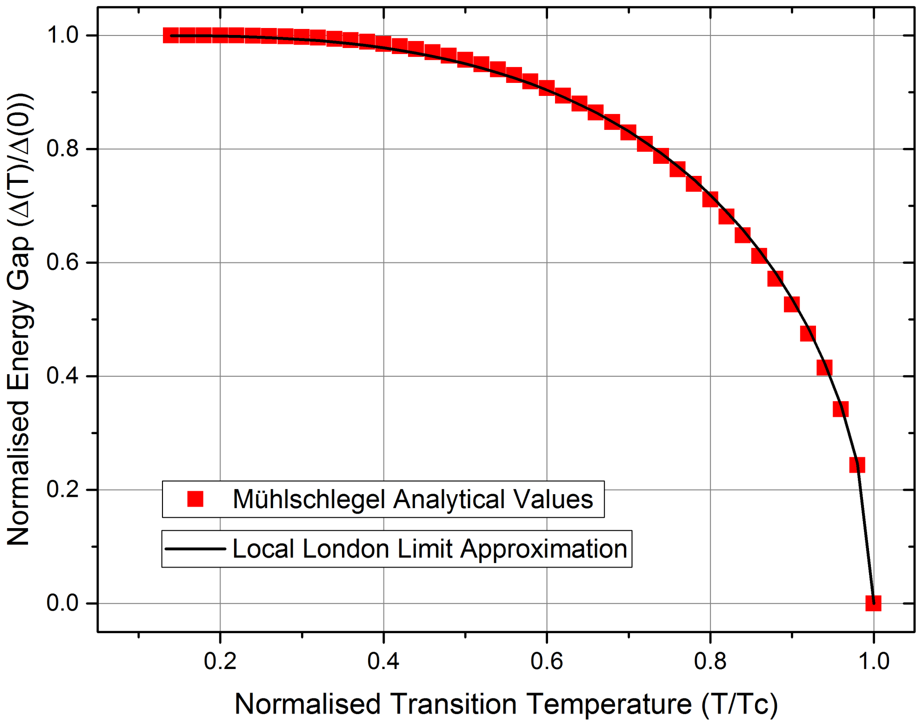

Figure 2.5: A graph showing the relationship between $\Delta(T)$ and temperature. This relationship has not been solved, but has been recorded analytically and approximated. The fitted curve has an R^2 value of 0.999.

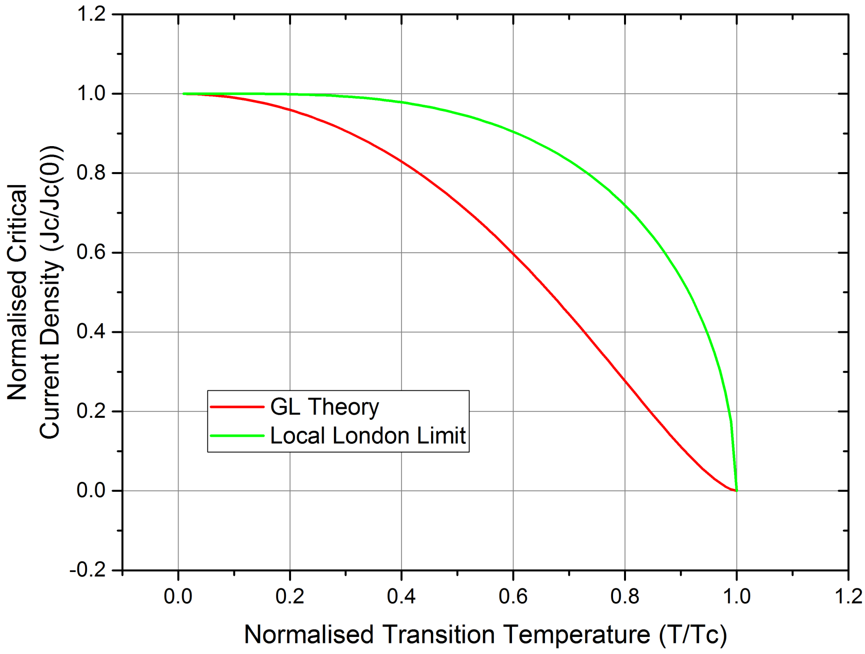

Figure 2.6: Relationship between temperature and current for Ginzburg-Landau and London models. In all models the critical current density decreases as the temperature reaches critical.

The switch from superconduction to normal conduction beyond the critical current occurs immediately, but returning to the superconducting state by reducing the bias current is a gradual change and this effect is known as hysteresis. In the normal state, phonon vibrations heat the material. When the bias is lowered below I_C, the phonon vibrations still occur, adding heat to the system. A much lower bias is therefore required in order to return the material to its superconductive state. This effect can be reduced by using a shunt resistor to remove the bias while the device to resets.

The supercurrent is also limited by the effect of an applied magnetic field in a similar fashion to an applied current. However, this is not the focus of study for the experiments performed in this thesis, so has not been discussed.

2.1.5 Temperature Dependence of Critical Current Density

From early models of superconductivity, it has been known that the relationship between critical current density and temperature is inversely parabolic. Using the Ginzburg-Landau simultaneous equations it is possible to obtain a relationship between critical current density and temperature for a scenario with no applied magnetic field (Equation 2.5a)[21]. In the case of Type II superconductors, such as MoSi, the curve is more severe (Equation 2.5b). This relationship is derived using the local London limit approximation ($\xi_{GL} \ll \lambda_L$) for a superfluid density in an anisotropic superconductor, under the Meissner effect and borrows the approximation of $\Delta(T)$ developed by Khasanoc *et al* discussed above (Equation 2.4c)[27, 28]. These relationships are compared in Figure 2.6.

$$J_C(T) = J_C(0)\left[1-\left(\frac{T}{T_C}\right)^2\right]\left[1-\left(\frac{T}{T_C}\right)^4\right]^{\frac{1}{2}} \tag{2.5a}$$

$$J_C(T) = \frac{\Delta(T)}{\Delta(0)} tanh\left(\frac{\Delta(T)}{2k_bT}\right) \tag{2.5b}$$

2.2 Quantum Optics

2.2.1 Brief History of Light

As late as the 19$^{\text{th}}$ century[32] scientists had opposing views about the composition of light; mainly whether it consisted of discrete particles or continuous waves. It was thought that the nature of light had finally been understood in 1873, when James Clerk Maxwell published a paper that unified the equations of electromagnetic theory. Gauss' law described the relationship between charge and electric field density (Equation 2.6a) and also suggested there could not exist magnetic monopoles (Equation 2.6b); Faraday's law of induction showed that a changing magnetic field induces a vortex current (Equation 2.6c) and Ampére's law showed how an electric field can conversely induced a vortex magnetic field (Equation 2.6d). As well as their description of electron conduction, these equations suggested, in the absence of an applied current, that the electric and magnetic field vectors form a wave equation with a fixed velocity, the speed of light. Maxwell suggested light was a wave of sinusoidally varying electric and magnetic fields that were each perpendicular vectors to themselves and the direction of propagation (Figure 2.7(a)). As well as having a vector direction, the E-field could have a rotation in the plane of propagation and relative phase in comparison to the orthogonal B-field component. This range of possible polarisations could be mapped to the surface of the Poincaré sphere[13] (Figure 2.7(b)). Maxwell's theory was adequate in explaining most optical observations, however, there were still experiments that could not be explained by these equations alone.

$$\nabla \cdot \mathbf{E} = \frac{\rho}{\epsilon_0} \tag{2.6a}$$

$$\nabla \cdot \mathbf{B} = 0 \tag{2.6b}$$

$$\nabla \times \mathbf{E} = -\frac{\partial \mathbf{B}}{\partial t} \quad (2.6c) \qquad \nabla \times \mathbf{B} = \mu_0 \epsilon_0 \frac{\partial \mathbf{E}}{\partial t} + \mu_0 J \quad (2.6d)$$

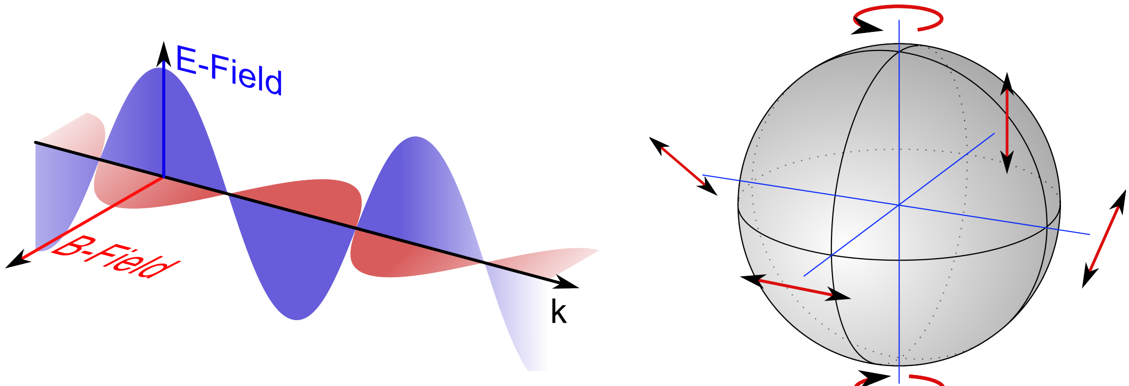

(a) (b)

Figure 2.7: (a) Propagation k of linearly polarised light based on Maxwell's equations. (b) Poincaré sphere for photon polarisations, each possible polarisation is a point on the surface of the sphere. North and south poles indicate circular polarisation, the equator shows linear polarisation and all other points on the surface represent elliptical polarisation

2.2.2 The Quantisation of Light

Kirchhoff coined the term 'Blackbody' in the 1860s as a material that absorbed and emitted perfectly at all frequencies of light[32, 33]. He also noted that the temperature of a blackbody dictated the intensity and central frequency of the emitted light (Figure 2.8(a)). In 1887, in a series of experiments, partially to understand and improve the efficiency of lightbulbs, Wien developed a cavity radiator to precisely measure the Blackbody Radiation (BBR) spectrum against temperature. BBR follows a steep peak at a central-frequency of emission intensity and its power density reduces exponentially at lower temperatures. From 300K to 3K the reduction is of the order of 10^9 and a further 10^5 when reduced to 0.3K. Lord Rayleigh attempted to theoretically describe this emission spectrum, but could only replicate an asymptote, suggesting all blackbodies emit an infinite amount of light as wavelength decreases. Around the same time, Max Planck, with a similar background in thermal physics, began working on this very problem, presenting his explanation in 1900. He assumed, without cause, that the energy spectrum had a limited resolution and forms discrete steps, or quanta (Equation 2.7). These steps were not only crucial in understanding the nature of light, but also founded the field of Quantum Mechanics (QM).

$$E = hf \quad \text{where} \quad h = 6.62607004 \times 10^{-34}\text{Js} \tag{2.7}$$

The photoelectric effect was first observed in 1887 by Hertz and revisited by Einstein in

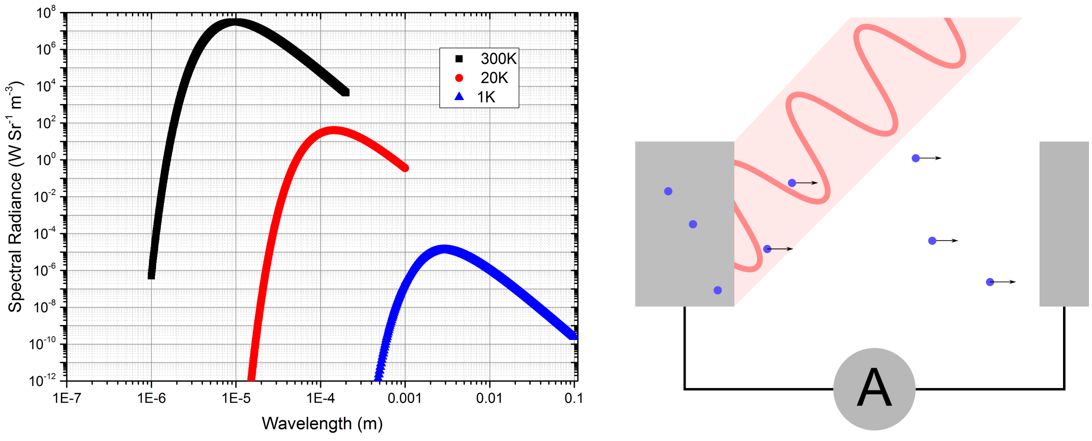

(a)

(b)

Figure 2.8: (a) BBR curves at 300K, 20K and 1K. As the blackbody curve lowers in temperature, its spectral radiance decreases dramatically and its peak also shifts towards longer wavelengths. (b) The photoelectric effect occurs when light at a wavelength below a threshold frequency causes electrons to be freed from the surface of a metal.

1905. The notable effects of the experiment show that, when light is shone on a photosensitive plate, the electrons that are released from its surface have a kinetic energy that is dependent only on the frequency of the incident light, not the intensity of the beam. Working with Planck's assumption, Einstein described the concept of a photon in which he considered that light itself was quantised and came in packets of energy dictated by Planck's relationship. He used this to explain the photoelectric effect; the energy of the photon, described by its frequency, is transferred to an electron in the metal, which requires a minimum energy to escape the material Φ with the remaining energy spent on movement E_k.

2.2.3 Photon-Atom Interactions

It can be thought that photons arise due to the conservation of energy. For an electron to transition between two quantum states, it either requires or must eject an energy delta. This change in energy occurs either by the production of a photon during an electron's transition to a lower energy state or the absorption of a photon during a transition to a higher energy state. Einstein postulated three theoretical equations to describe the rate at which light interacted with an atom or molecule. In simplified terms, these equations suggested light could either be emitted by an atom spontaneously, could be influenced into a coherent emission by another photon or could be absorbed by an atom as long as the energy transition of the electron orbital was equal to the photon energy as per

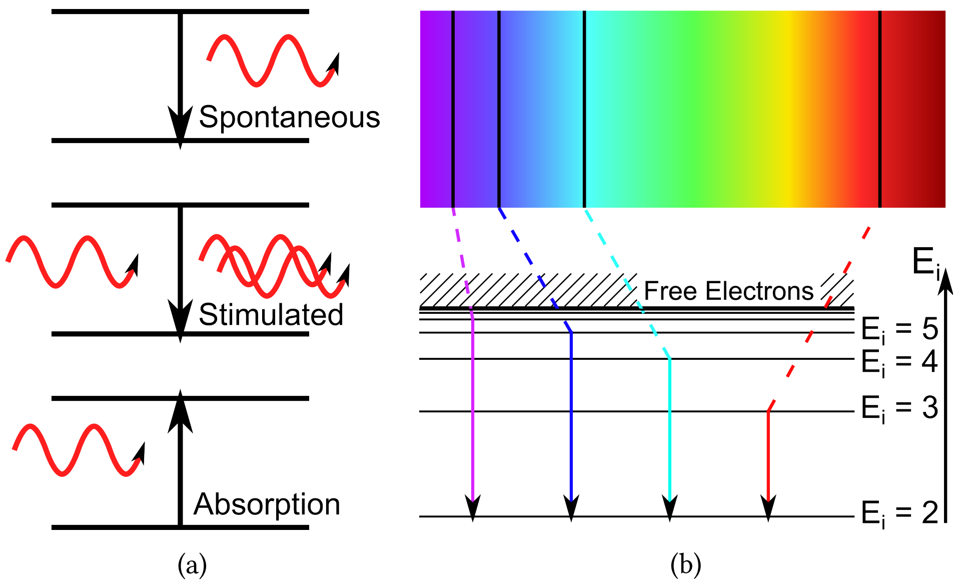

Figure 2.9: (a) Forms of photon interaction with electron population during state transitions. (b) Emission spectrum of the H atom, which emits photons within the visible spectrum.

(Equation 2.7) (Figure 2.9(a)). This effect can be visibly seen in the single electron orbitals of the H emission spectrum with no applied magnetic field under the Balmer series for transitions $E_i \rightarrow 2$ (Figure 2.9(b)). Higher energy photons are more likely to be absorbed by the atom as the energy state spacing becomes smaller at higher energy levels. If a photon arrives with any energy above a certain threshold, electrons will break free from the atom, as per the photoelectric effect.

2.2.4 Coherent Photons

The majority of light the fills the universe is incoherent and polychromatic, produced by multiple sources and reacting across many materials. In 1955, Charles Townes designed a device capable of producing coherent and monochromatic photons at microwave frequency. Microwave Amplification by Stimulated Emission of Radiation (MASER) operated by exciting a vacuum tube of ammonia gas to produce a coherent stream of 12.5mm wavelength light. This later lead to the development of Light Amplification by Stimulated Emission of Radiation (LASER), which would aid in advancing the field of quantum optics.

As photons can be considered single 'events' of light that don't interact with each other, being bosons, their probability statistics can be described by a Poisson distribution (Equation 2.8). In this case, the number of photon detection events over a short period m will have a variance Δm equal to the mean number of photon events within that same interval $\langle m \rangle$. An example of this would be light produced by a laser. Super-Poissonian light occurs when the photon number is large, such as in a blackbody radiator. In most optical experiments a classical or semi-classical theory of light will suffice, however, when the intensity of light becomes very low, in the case of sub-Poissonian light, new properties emerge that require the interpretation of quantum mechanics.

$$\mathcal{P} = \frac{\langle m \rangle^m}{m!} e^{-\langle m \rangle} \tag{2.8}$$

$\Delta m^2 > \langle m \rangle$	Super-Poissonian	Classical light beams
$\Delta m^2 = \langle m \rangle$	Poissonian	Laser light
$\Delta m^2 < \langle m \rangle$	Sub-Poissonian	Non-classical

In 1956 Hanbury-Brown and Twiss conducted an experiment in which highly attenuated photon light was partitioned through a beam splitter and then absorbed by two Single-Photon Detectors (SPDs). By measuring the correlation of photon detection between the two detectors $g^{(2)}(\tau)$, where τ represents the time delay between detection events, the researchers defined three categories of low intensity light. Evenly spaced anti-bunched light, randomly spaced coherent light and clumped groups of bunched light (Figure 2.10).

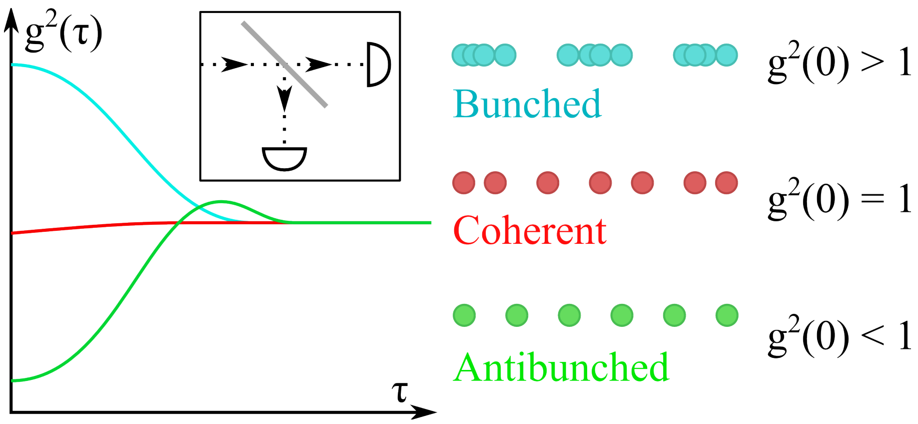

Figure 2.10: Photon detection against time. Anti-bunched light (Green) details evenly spaced photon packets. Bunched light (Cyan) involves groups of photon packets arriving together – Such as thermal radiation. Coherent and random light (Red) is a mixture of these – Such as laser light.

Generating Single Photons

Without the ability to generate single photons, it would not be possible to experimentally characterise single photon detectors. For Telecom wavelengths, ideal single photon generation is not yet viable, but there are several methods that approach it, which are presented here.

Spontaneous Parametric Down-Conversion (SPDC)[34, 35] involves the $\chi^{(2)}$ interaction of a non-linear crystal pumped with laser light to produce photons in pairs of different frequencies (Figure 2.11). Due to the conservation of momentum, the produced photons have combined momenta of the incident photon and have matching phases. The knowledge of one of the pair of photons can be used to give information about or 'herald' the arrival of the other. This process has a low occurrence, with an input flux around 10^{12} photons per one output pair[36], though this can be improved with the aid of an optical cavity[37]. SPDC also benefits from room temperature operation.

Quantum Dots (QDs)[38–40] are semiconductor heterostructures no larger than a few nanometres. By applying a small current or an input flux, electrons are excited to higher populations. Here they combine with holes to form pairs (excitons) that can radiatively decay emitting single photon. This process occurs in much the same way a photon is spontaneously emitted from an atom. The energy gap of the structure and, thus, the wavelength of the emitted photon, is dependent not only the material, but also the size of the QD. They are advantageous compared to other forms of single photon generation as they can be controllably placed, grown monolithically and generate photons deterministically. Numerous proof-of-principle experiments have also been carried out on QDs to show their compatibility with Si and GaAs integrated quantum photonics. An example QD is shown in Figure 2.11(b), which has been integrated into a micropillar cavity designed for a wavelength matching the expected emission. This improves the linewidth of its emission spectrum via the Purcell effect.

The simplest and most accessible approach is to strongly attenuate pulsed laser light. This does not create an ideal single photon source as photons are still produced from the laser following Poisson statistics; it is still possible, regardless of the attenuation, for bunching to occur. For 1550nm light, with a single photon energy of ~ 0.8eV, at a 1MHz pulse rate, a measured laser power - after attenuation - of -109dBm equates to 0.1 photons per pulse. This rate is chosen in most single-photon experiments as it ensures the incoming light is within the single photon regime and greatly reduces the likelihood of bunching.

2.2.5 Guided Wave Optics

Until recently, lab experiments involving light were performed using Free-Space Optics (FSO); mirrors and lenses on vibration damped optical tables. The method is ideal for interferometry experiments, where optical components need to be aligned extremely accurately. However, FSO suffers when used for long-distance communication as the sig-

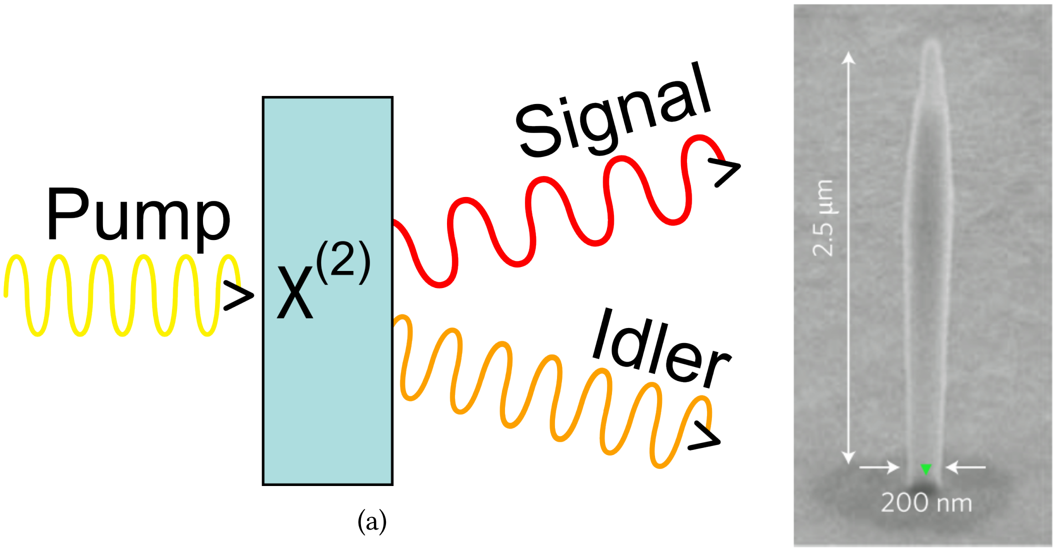

(a) (b)

Figure 2.11: (a) Input pump photon will, rarely, create two downconverted photons, where momentum is conserved. (b) An SEM image of a QD single photon source (Green triangle) within a 2.5µm tall cavity micropillar. Image adapted from source[41].

nals are affected by atmospheric turbulence or require long vacuum tubes. The concept of glass-guided fibre has existed since the 1920s, but still required decades of development before reaching its current state of high photon transmission with low loss. Silica glass optical fibre appeared around the 1970s. Its structure features a cylindrical core of dielectric material wrapped within a material with a lower refractive index (Figure 2.12(a)(i)). This almost entirely traps light via total internal reflection and has paved the way for cheap and efficient long distance communications across the globe. Silica glass optical fibre achieves its lowest attenuation between 1500-1570nm wavelength optics (Figure 2.12); current fibre capabilities show a signal loss of 2dB every 13km. Its low loss is favourable for the transmission of photonic qubits, which can achieve long coherence times (§2.4.2. Coherence Length).

Graded Index Fibre (GRIN) uses an index gradient around the core, rather than a direct boundary (Figure 2.12(a)(ii)). This creates gradual transitions through the fibre, rather than direct reflections and decreases modal dispersion. GRIN lens fibre can also be used on the end of regular fibre to focus the beam onto a spot. This lens is used in free-space optical coupling (See §3.3.6. Microscope Setup). A subset of guided waves includes an embedded strip design (Figure 2.12(a)(iii)). This design is used to produce silicon photonics on chip, in which light is confined within a layer of lower refractive index silicon oxide atop a Si substrate.

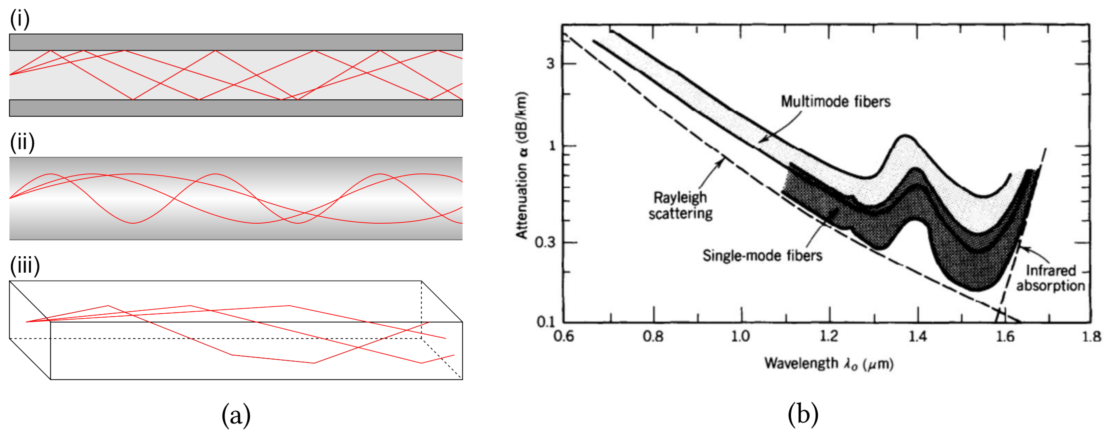

Figure 2.12: (a) Cross-section of variaties of multimode optical guides: (i) Optical fibre, (ii) Graded Index Fibre, (iii) Waveguide strip. (b) Ranges of attenuation coefficients for silica glass single-mode and multi-mode fibres. Image adapted from Saleih and Teich[33].

Single-Photon Evanescent Waves

A byproduct of total internal reflection is the creation of evanescent waves. When treating the boundary conditions of a waveguide under Maxwell's laws, for the case of a high illumination, it is found that the light beam does not perfectly reflect at the boundary. In fact a few of the photons escape, producing an exponentially decaying wave that runs parallel to, and outside of, the boundary itself Figure 2.13(a). These are the described as evanescent waves. In the single-photon case, when the photon contacts the boundary, it does not reflect perfectly, but passes through the interface. The outer medium, which has a higher refractive index, causes the propagation vector k of the photon to bend back into the medium of lower refractive index, as visualised in Figure 2.13(b). The portion of the photon that extends outside the medium is described as the evanescent wave[42]. This effect is exploited in the operation of hairpin waveguide devices.

2.3 Single Photon Detection

An ideal Single-Photon Detector (SPD) would absorb all incoming photons at a specified wavelength band that made contact with it, producing a signal above noise each and every time. It would also be able to; distinguish between different photons by incident time and position, have a Dark Count Rate (DCR) of zero and have a reset time significantly smaller than the time between each incident photon. Practically, SPDs are non-ideal and must be described by a set of performance metrics[43]. These can then be utilised to characterise and compare SPDs for particular applications.

The overall efficiency of the detector system is described by its System Detection Effi-

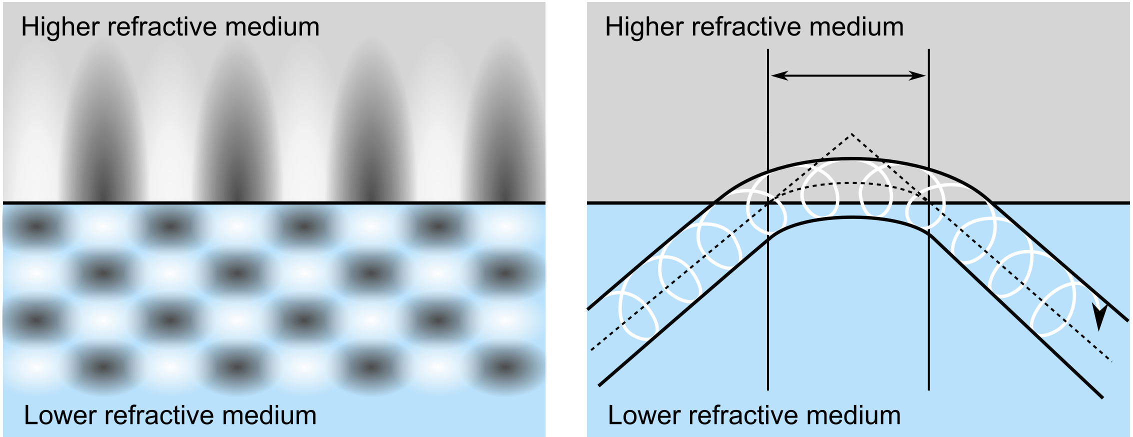

(a) (b)

Figure 2.13: (a) A light beam trapped within the walls of a waveguide by total internal reflection will not entirely conserve energy. It will lose some energy outside the barrier of the waveguide through evanescent waves. These waves exponentially fall away from the barrier and propagate parallel to the barrier. (b) In the single-photon case the higher refractive medium deflects the propagation vector of the photon back into the lower medium, including a slight shift in its position along the boundary that would not occur during a simple reflection.

ciency (SDE) (η_{SDE} or η) (Equation 2.9a), which consists of three components. Before input photons reach the detector, their loss due to photon scattering, reflection or absorption is described by the coupling efficiency $\eta_{Coupling}$. The absorption efficiency $\eta_{Absorption}$ describes the detector's ability to absorb photons based on its materials and geometry. The final parameter describes how likely an absorbed photon is to output a signal, known as the registering efficiency $\eta_{Registering}$. As the absorption and registering efficiency are only dependent on the device, these are sometimes referred to as the Intrinsic Device Detection Efficiency (DDE) (η_{DDE}) ((Equation 2.9b)).

$$\eta = \eta_{Coupling} \times \eta_{Absorption} \times \eta_{Registering} \tag{2.9a}$$

$$\eta_{DDE} = \eta_{Absorption} \times \eta_{Registering} \tag{2.9b}$$

2.3.1 SPD Parameters

Detection Efficiency

As discussed in the previous section (§2.2.4. Coherent Photons), photons from a laser are events that occur singly and, thus, can be modelled by a Poisson distribution where m describes the number of simultaneous photon counts. In order to calculate the efficiency of the device, we can model the detection probability also as a Poisson distribution. In an ideal SPD, the mean number of detection events per pulse $\langle m \rangle$ will be equal to the average number of photons per pulse from the laser μ. Of course, the real average will have a percentage reduction due to the SDE of the device η. Therefore, the mean number of detection events in the Poisson distribution becomes[25] $\langle m \rangle = \mu\eta$. This allows for the probability calculation of m number of simultaneous photon counts per pulse, $\mathcal{P}(m)$, shown in (Equation 2.10). The exponential component can also be simplified to 1 due to the dramatic attenuation of laser light $\mu \sim 0.1$ required to avoid photon bunching.

$$\mathcal{P}(m) = \frac{(\mu\eta)^m}{m!}e^{-\mu\eta} \approx \frac{(\mu\eta)^m}{m!} \tag{2.10}$$

The detected counts will be related to the probability of a detection event for each photon number across the average photon input rate per second, described by the laser pulse rate f_P. The expansion of this equation separates terms for each incident photon number (Equation 2.11a). For low intensity light, we only need consider the first order detection events as shown in (Equation 2.11b). This allows us to transfer the measurable elements of the detector into a value for its SDE.

$$R_{det} = \sum_{m=0}^{\infty} f_P \mathcal{P}(m) = f_P \frac{(\mu\eta)^m}{m!} = f_P \left(\mu\eta - \frac{(\mu\eta)^2}{2} + \frac{(\mu\eta)^3}{6} - ... \right) \tag{2.11a}$$

$$R_{det} = f_P \mu\eta \tag{2.11b}$$

Dead Time

After the absorption of a photon the detector may require a period of time to reset during which the detector is unable to detector any incoming photons. This is known as dead time t_R and can vary dramatically ranging from microseconds for Transition Edge Sensor (TES) to tens of picoseconds for other superconducting SPDs.

Jitter

The response time between a photon being absorbed by the detector and outputting a signal will vary between detection events. It is therefore useful to create a metric that describes how much the response time can vary. A histogram of response times can be recorded; its Full Width at Half Maximum (FWHM) describes the device's jitter Δt. This can be known to a high level of accuracy using a Time-Correlated Single Photon Counting (TCSPC) technique, discussed in §3.4.3. Timing Jitter.

Dark Count Rate

The Dark Count Rate (DCR) is a measurement of detector counts or device transitions that are not directly caused by the absorption of a single incident photon. The underlying mechanisms of DCR can be split into two sources: extrinsic and intrinsic DCR. Extrinsic effects are caused by external noise, such as BBR, and intrinsic effects are caused by internal effects of the detector, such as thermal noise. In superconducting, current biased devices, analysis of the DCR, as described by Engel[29] *et al*, shows two distinct effects to note: (A) DCR increases with increasing operation temperature and (B) DCR increases exponentially as the bias current approaches critical in a relationship of the form $log(DCR) \propto I$. Dark counts can also coincide with a detected photon, known as afterpulsing, which is discussed in more detail in §2.3.3. Afterpulsing.

Extrinsic DCR in Superconducting Detectors

Effect (A) is governed by extrinsic DCR. At low biases, a large source of DCR occurs from the detections of photons not from the intended laser source, but from BBR. As discussed in §2.2.2. The Quantisation of Light the spectral radiance of BBR is dependent on the temperature of the testing environment; a lower temperature environment will reduce the DCR caused by BBR. Noticeable BBR can also occur from room temperature radiation entering the cryostat via Single-Mode Optical Fibre (SMF). The spectral transmission of SMF changes with fibre bending radius; at the correct bending radius (12mm for 1550nm wavelength), with a few loops, SMF can be used as a high-pass filter to expel room temperature BBR[45].

Intrinsic DCR in Superconducting Detectors

It is possible to filter out extrinsic dark counts, but an SPD has a limited minimum DCR based on its internal effects. Effect (A) has an intrinsic element; increasing the temperature of the device increases the phonon vibration energy within the material, which causes more electrical noise. The majority of effect (B) is intrinsic and has various underlying mechanics consisting of: Fluctuations in the order parameter ψ (From GL theory §2.1.2. Ginzburg-Landau Theory), vortex excitations (caused by flux penetration §2.1.2. Flux Penetration) or quantum phase slips.

Phase slips are caused by a phase shift of 2π when a nanowire transitions due to thermal excitation between two meta-stable states. The change in phase registers as a Voltage pulse occurring in the device. At higher biases, the rate of phases slips increases exponentially[29], which matches the exponential increase in DCR of most SNSPDs. Though this effect arises from 1D nanowires, it can be applied to thicker nanowires with an equivalently small cross-sectional area, $wd \leq \xi_{GL}^2$.

Vortex excitations occur when a nanowire exceeds a width of $4.4\xi_{GL}$. Vortices are caused by a penetrating magnetic field which, due to induction, creates a loop of current on the

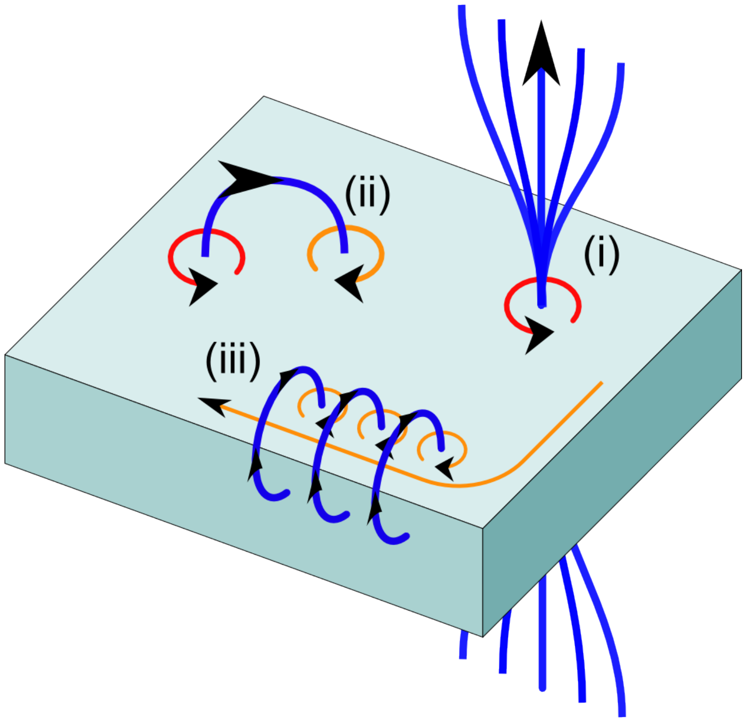

Figure 2.14: Phenomenological model showing possible occurrences of vortices in a Type-II superconductor under bias. (i) Flux pinning, (ii) VAP, (iii) Self-field vortices due to surface currents.

material's surface. Vortices can result from an external magnetic field perpendicular to the nanowire (Figure 2.14(i)), a self-field or edge vortex caused by surface currents in the material (under the Meissner effect) (Figure 2.14(iii)) or topological excitations, which can create linked pairs of vortices of opposite chirality, known as Vortex-Antivortex Pairs (VAPs) (Figure 2.14(ii)).

At lower biases, edge vortices created by surface currents can move across the nanowire strip via the Lorentz force and, occasionally, cause a dark count. A similar effect occurs for VAPs; the bias current creates a torque in the pair which causes them to align perpendicular to the current, lowering the binding energy. If the pair breaks from thermal agitation the vortices move to alternate edges and cause a count[46]. It is suggested, at least of devices at 4K, the dominate effect of DCR occurs from vortices overcoming the edge barrier.

Not all of the metrics in this section need be maximised; for metrology applications, such as a jitter measurement, it is more beneficial to use a high efficiency, room temperature detector such as an avalanche photodiode. However, for applications in quantum computing, each of these metrics are required to be maximised.

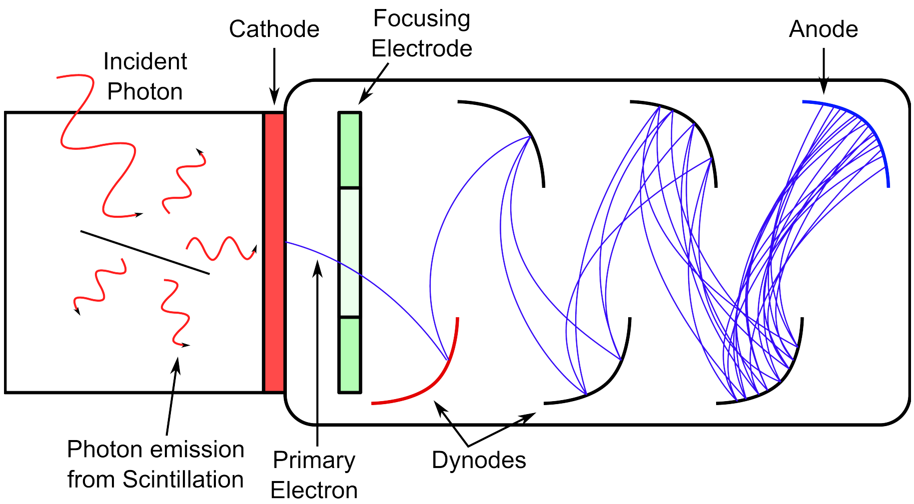

Figure 2.15: Diagram illustrating a photomultiplier tube. The photon, after travelling through the focusing electrode, hits the first dynode, releasing a number of electrons. These electrons are accelerated to the second dynode, upon which more electrons are released. This cascade effect continues until a macroscopic signal is achieved.

2.3.2 Types of Single Photon Detector

Photon Multiplier Tubes

The first SPD was the Photon Multiplier Tube (PMT), built in 1949[47]. The PMT is a vacuum tube with a light sensitive cathode for photon absorption and a series of dynode sheets (Figure 2.15). A single incident photon, with total energy high enough to exceed the work function, will liberate electrons from the cathode. The freed electrons are then accelerated to a dynode, which releases even more electrons. This process is repeated, causing a cascade effect until a macroscopic current is produced $\sim 10^6$ electrons. PMTs can achieve excellent DCR as low as 100Hz, but possess low SDEs at infra-red wavelengths[39].

Superconducting Transition Edge Sensors

Superconducting Transition Edge Sensors (TESs)[39, 48] are highly-sensitive calorimeters operated as microbolometers. The superconducting material experiences a measurable temperature change upon the absorption of a single optical photon with energy on the order of 1eV (For reference, a single 1550nm photon has an energy of 0.8eV). The device then resets through a thermal bath. This means the device has no dead time and allows it to resolve photon number. TESs have achieved some of the highest single photon SDEs at 95%[49] at an operation temperature of 100-200mK. However, due to the weak link of the thermal bath, TES devices suffer from large reset times around 1μs[49] compared to the ~100ps range of other SPDs. Due to its small output signal, TESs use Superconducting Quantum Interference Devices (SQUIDs) to increase the size of the output pulse (Discussed below in §2.3.2. Superconducting Tunnel Junctions).

Single Photon Avalanche Photodiodes

A Single-Photon Avalanche Photodiode (SPAD)[39, 50, 51] is a market standard SPD that consists of a P-N junction reversed biased above the breakdown voltage. An incident photon on the depletion region of the semiconductor creates electron-hole pairs which are accelerated across the device and produce enough kinetic energy to cause secondary pair creation (Figure 2.16). This cascade effect causes an avalanche in the SPAD, which is macroscopic and detectable. After detection, the bias is quenched in order to reset the device. For 1550nm single photon Telecom optics, the device requires an energy gap below ∼0.8eV. This is suitably offered by III-V compounds such as InGaAs. Unlike most other SPDs, SPADs operate at room temperature, not requiring expensive cold head setups, whilst still achieving low intrinsic DCR and high SDE; the highest SPAD efficiency to date is 46% for near-infrared photons[39]. However, they suffer from long dead times and a high likelihood of the effect of afterpulsing (see §2.3.3. Afterpulsing). Though these devices are unsuitable as SPDs in quantum computing applications, they can be used to accurately measure jitter in other devices. In a forward bias regime, for high input fluxes the measured output current is linearly proportional to the input optical power; SPADs in this mode are useful for reflection maps (§3.4.6. Mapping).

Superconducting Tunnel Junctions

Superconducting Tunnel Junctions (STJs)[21, 52] have the same architectures as Josephson junctions, but a slightly different operation. The Josephson effect was predicted by Brian Josephson in 1962[53]; In this setup, two superconducting materials are joined by a thin insulating barrier; both Cooper pairs and quasiparticles can tunnel through the barrier and create a Josephson current with a small applied bias. As the tunnelling effect is based upon phase matching between the barriers the I-V characteristics of STJs are step-like, rather than linear. These steps are multiples of the fundamental ratio $2e/h$. An incident photon, of a wavelength comparable to the energy gap, hitting the junction increases the quasiparticle density which modulates the Josphson current. This modulation is detectable from a SQUID read-out.

Two Josephson junctions in parallel create a Superconducting Quantum Interference Device (SQUID), which is highly sensitive to a change in magnetic flux. When a current is applied, it splits evenly across the Josephson junctions. If a small magnetic field is also applied through the centre ring, a screening current emerges that creates a continuous current loop around the device, which also causes a secondary magnetic field that repels the applied field, due to the effect of induction. This screen current changes the result of

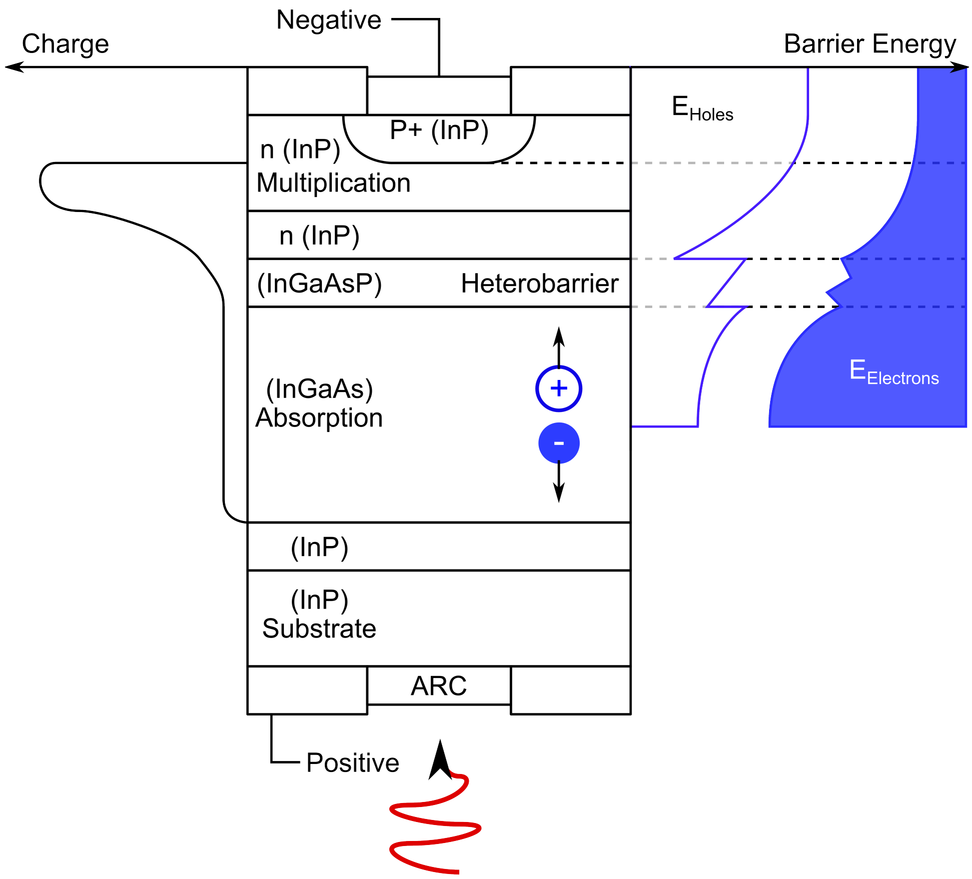

Figure 2.16: A photon arrives through the base of the substrate and is absorbed in the InGaAs region where it creates an electron-hole pair. The positively charged hole then has enough energy to overcome the heterostructure barrier and moves towards the negatively charged region. The hole is accelerated by the charged structure and enters the multiplication region with increased kinetic energy. This begins the avalanche process of creating more e-h pairs.

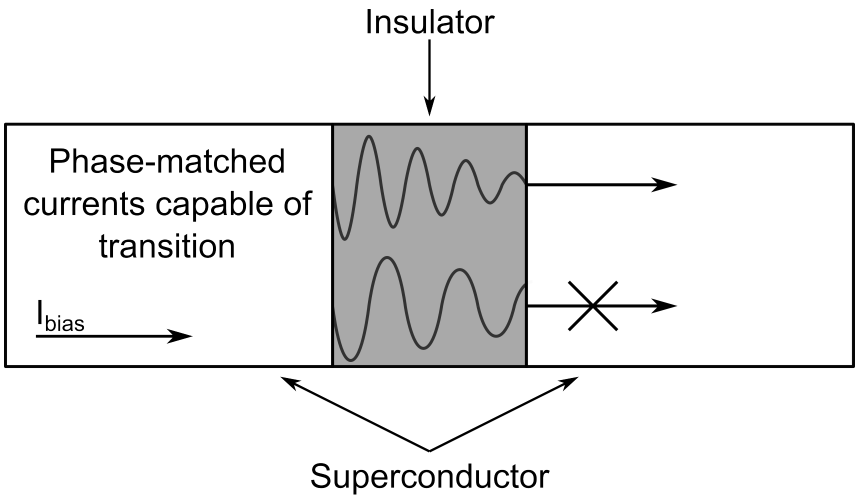

Figure 2.17: STJ diagram. Two superconducting components are separated by a thin insulating film.

the applied current through the device, which is detectable by a voltmeter.

Kinetic Inductance Detectors

Kinetic Inductance Detectors (KIDs) are resonating superconducting circuits, which were first proposed for infrared single photon detection by Mazin in 2004[54]. They are on the order of microns and detect light in the infrared. The resonant frequency of the circuit is dependent on the properties of the superconducting material, particularly its kinetic inductance. When a photon is incident on the detector, Cooper pairs are broken, altering the properties of the circuit, including its kinetic inductance. This, in turn, leads to a change in the circuit's resonant frequency, which is detectable through a capacitive-coupled transmission line.

Lumped Element Kinetic Inductance Detectors (LEKIDs) are similar in operation to KIDs, but they are coupled to the transmission line through a mutual inductance[55]. An LEKID can best be described as the circuit setup in Figure 2.18 with the inductor and capacitor alternately charging and discharging at a defined resonance frequency. When a signal travels down the transmission line, if the frequency of the signal is equal to the LEKID's resonant frequency, it will be reflected and this reflection can be detected. As with a KID, if a photon is incident on the device, Cooper pairs are broken, causing the material's properties to change and, therefore, its resonant frequency. This change in resonance can be related directly to the energy of the photon hitting the target.

Superconducting Nanowire Avalanche Photodetectors

Superconducting Nanowire Avalanche Photodetector (SNAP)[48] are a subset of SNSPDs consisting of ℕ rows of nanowires positioned and electrically connected in parallel (Figure 2.19). The groups of ℕ nanowires are connected together in series with a bank in-

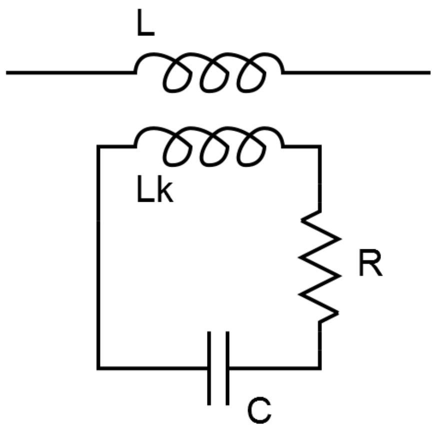

Figure 2.18: Circuit diagram of the LEKID. The transmission couples with the LEKID device and resonates at a frequency depenent on the properties of the LEKID. These properties alter when a photon is absorbed by the device.

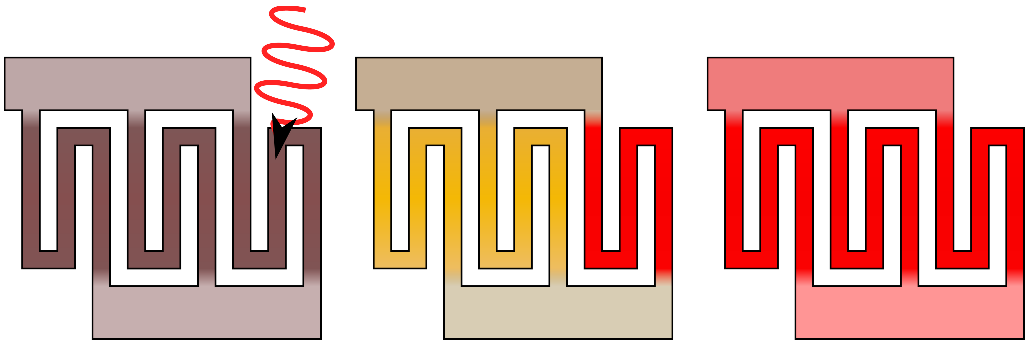

Figure 2.19: Diagram illustrating SNAP operation. The detector is made up of multiple detectors with a small active area biased near the critical current (brown). When a photon triggers one of the active areas (red), this diverts current through the parallel devices (yellow). The additional current causes these detectors to switch (red), which causes an output voltage pulse $\mathbb{N}$ times higher than a single meander.

ductance L_k. The nanowires are current biased such that $I/\mathbb{N}$ is near the critical current of the nanowires. If an incident photon is absorbed by one nanowire in a row of $\mathbb{N}$ nanowires, it will switch to its resistive state and divert its bias current to the other, still superconducting, nanowires. This extra bias will be enough to cause the other nanowires to switch. As a large bias is required to bias each nanowire to $I/\mathbb{N}$, when the device switches, the readout of the device will also be large at I. This leads to a larger SNR exactly $\mathbb{N}$ times higher than a normal SNSPD meander. Work by Heath[56] *et al* used a confocal microscope system - similar to that which will be described in §3.3.6. Microscope Setup - to model the detection characteristics of a SNAP with $\mathbb{N}$ parallel wires and within both single and multiphoton regimes.

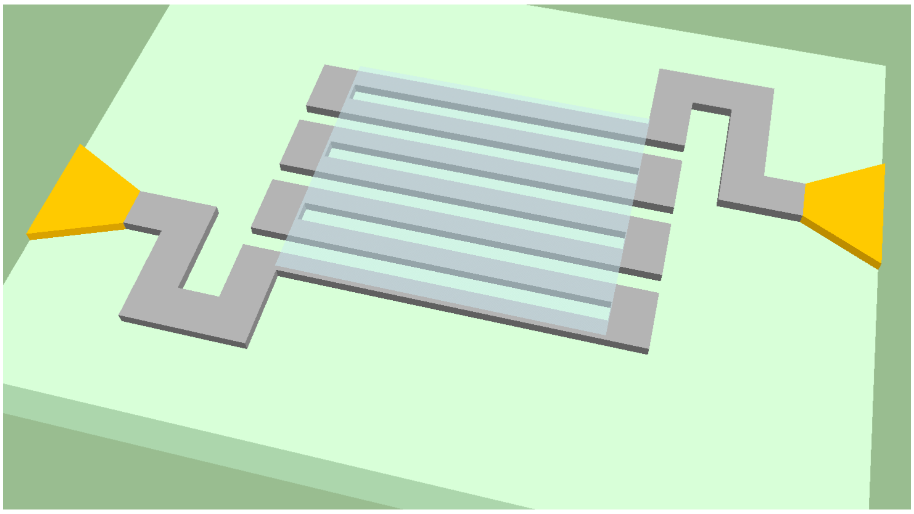

Figure 2.20: Model of a standard SNSPD on substrate (Not to scale). The meander in the centre is ten times thinner than the coplanar waveguides around it. The thickness of the film is of the order of a few nanometres and the substrate thickness is around several hundred microns. The active area is marked in cyan and usually $10 \times 10 \mu m^2$. Electrical connections to the device are made using wirebonds on the gold contact pads.

2.3.3 Superconducting Nanowire Single Photon Detectors

Superconducting Nanowire Single Photon Detectors (SNSPDs) are a thin superconducting material (5-20nm) patterned into a large area meander (Figure 2.20). When a high current is applied, below critical, the device becomes sensitive to single incident photons.The first experimental SNSPD was designed by Gol'tsman[25] *et al* at Moscow Pedagogical University in 2001. The experiment used a bow-tie constriction converging onto a NbN strip kept at 4.2K. By biasing the current through the device near its critical value, single incident photons would have enough energy to push the device into its resistive regime, which would be detectable on a read-out circuit.

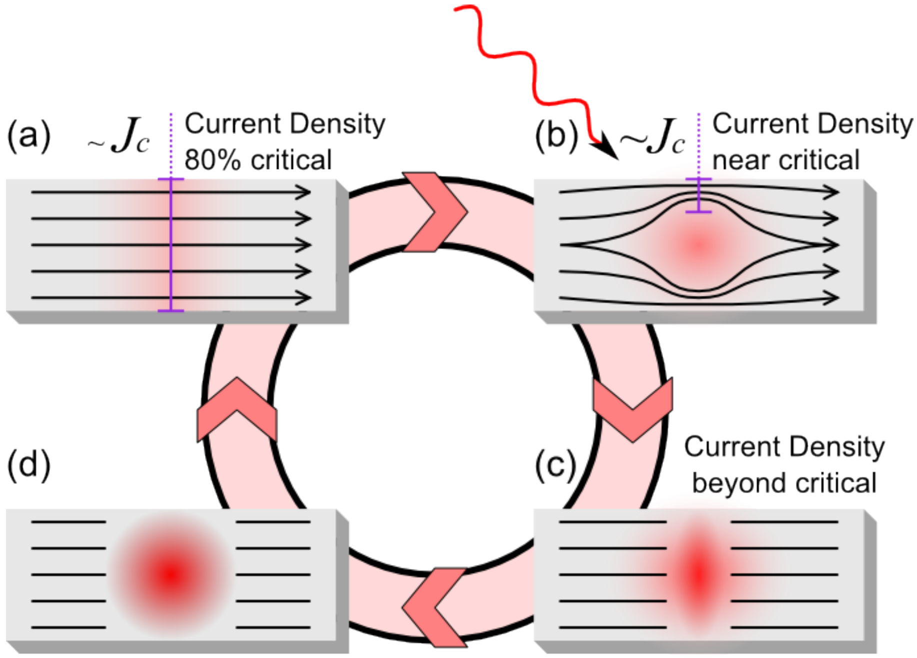

Figure 2.21: (a) the device is current-biased at superconducting temperatures, near its critical switching point. (b) An incident photon creates a hotspot region of quasiparticles. (c) The hotspot region expands quickly due to Joule heating. This causes the current to increase beyond its critical region, turning the device resistive. (d) The resistance of the device increases with Joule heating. The current is redirected through the load resistor, reducing the detector bias current to zero. The detector resets to its superconductive state and the bias current flows through it once more, as in (a).

The operation of an SNSPD[43] can be understood in Figure 2.21, and is explained using the hotspot model, introduced by Skocpol[58] *et al* and developed by Kadin[59] *et al.* Below the transition temperature, the nanowire is current-biased close to its critical current density; usually around $(90 - 99\%)I_C$ to achieve the highest response efficiencies. The supercurrent is made up of Coopers pairs with energy gap $\Delta(T)$. If a photon, with energy exceeding the superconducting energy gap hits the detector, the pair will transform from their superelectron state into quasiparticles. These quasiparticles act like normal electrons and create a hotspot region, which has an initial size on the order of nanometres, naively proportional to the energy of incident photon[60]. The hotspot increases in size due to the effect of Joule heating. When the resistance becomes too large, it is diverted through the load resistor, allowing the detector to cool and reset to its superconducting state. The effect of the hotspot, Joule heating and the sharp reset is detectable by the amplification of the reflections caused by the impendence mismatch between the device and the applied current. The device then resets on a timescale exponentially proportional to its inductance[57, 61], as described in Figure 2.22.

These devices are promising for the application of quantum computing; they can achieve high SDEs >80%, low dead times around 2-30ns, and a negligible DCR. Standard values of jitter sit around 60-120ps, but devices have been recorded with jitters as low as 16ps[57]. Jitter shows a further reduction from an increase in bias; it is expected this is due to the higher voltage pulse produced by a higher current, which increases the Signal-to-Noise Ratio (SNR) and the gradient of the rise-time of the pulse[44].

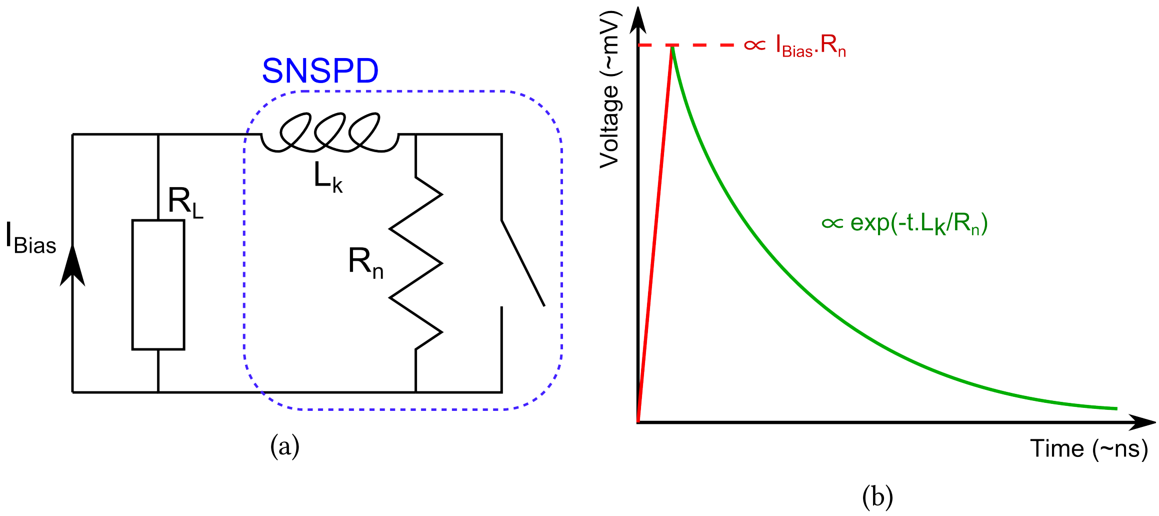

Figure 2.22: (a) Phenomenological model of an SNSPD[43] current-biased at I, with a load resistor R_L connected in parallel. L_k is the kinetic inductance of the nanowire and R_n is the normal resistance of the hotspot. The superconducting state is represented by a closed switch and a detection event is simulated by a quick action of opening and closing the switch. (b) Example pulse shape from phenomenological circuit model. When the switch is closed, there is a sharp rise dictated by to Ohm's law, then an exponential decay once opened as the SNSPD resets.

SNSPDs have been applied in a wide variety of experiments, including QKD[6–12], quantum computing[1, 13, 14], time-of-flight ranging[16] and mass spectrometry[62], metrology[15] and medical applications in singlet oxygen luminescence detection[17]. The focus is to improve their metrics through changes in design, materials or fabrication processes. The use of in-house closed-cycle cryocoolers, discussed in §3.3. Methods for Achieving Low Temperature, allows for systematic and reliable testing of SNSPDs in the range 5 to 0.35K. Devices with good performance characteristics can then be used in the applications as just described.

Registering Efficiency

As previously mentioned, the registering efficiency, or registering probability, is the likelihood a voltage pulse will trigger after the successful absorption of a photon. The intrinsic properties of the material will determine the registering efficiency as well as the necessary applied bias to operate the detector in the single photon regime. As the bias current increases towards critical, the density of Cooper pairs decreases. The dwindling pairs increase in velocity and energy, which increases the kinetic inductance of the device. This causes faster pulse reset times and leads to an increase in the registering efficiency of the device as well as an unwanted increase in the detector Dark Count Rate (DCR)[63]. The registering efficiency is not directly measured, but when characterising the device, a value of the registering efficiency can be calculated from the measurement of the SDE, simulations of the absorption efficiency and calculations of the coupling efficiency. If the coupling and absorption parameters are fixed, it is possible to calculate the maximum registering efficiency of the device by increasing the bias current until a plateau in the SDE is reached.

The Effect of Nanowire Constrictions

The main susceptibility of the registering efficiency is a nanowire's uniformity. Straight, clean edges result in an even distribution of current density across the device. A constriction in a nanowire[37] exists wherever there is a region with a narrowing cross-sectional area (Figure 2.23). This is usually caused by an error in fabrication due to unoptimised etch or vapour deposition processes. The centre of the constriction will be susceptible to a lower J_C and this will become the maximum J_C of the overall device. This lowers the maximum bias current of the device, which in turn lowers the sensitivity of the device at all locations along the nanowire, thus, reducing the registering probability.

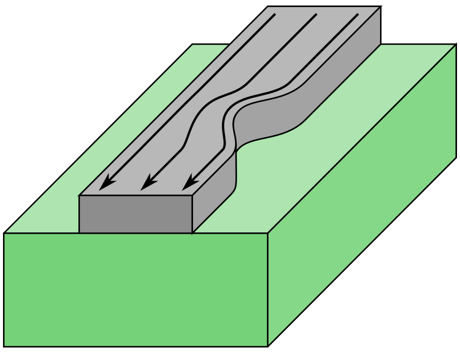

Figure 2.23: Variation in current density due to a constriction in the nanowire.

Materials

High performance SNSPDs have been achieved using superconductors such as WSi[5], MoSi[64], Nb[65], NbN[66], NbTiN[4] and MoGe[67]; information on the transition temperature of these materials is shown in Table 2.1.

It is apparent that the properties of superconducting materials offer a balance between operating temperature and efficiency. It is thought that the high carrier density and energy gap of NbTiN determines its high transition temperature and high critical current, but also its lower detection efficiency. The higher T_C allows a higher current bias before switching, which increases the SNR and lowers its timing jitter. It also allows the device to be tested in more common Gifford-McMahon cryostats, stable at 2-3K, which allows for more widespread applications of the devices (§3.3. Methods for Achieving Low Temperature). To mitigate the effects of the material's lower SDE, a wavelength optimised cavity layer is deposited on the film, increasing the device's coupling efficiency.

In comparison to NbTiN films, materials such as MoSi, MoGe and WSi have a much smaller carrier density. This leads to lower transition temperatures, but higher internal efficiencies. A lower carrier density gives the material a lower temperature dependent critical current density, but this in turn leads to a lower energy gap, which causes larger hotspots to from as a result of single photon absorption. These materials are fortunate in that, though their critical temperature is low, they are still operational in a Gifford-McMahon cryostat at 2-3K. Detection efficiencies can be improved by using a ^{3}He cryostat with a 3K inner shielding to reach temperatures below 0.4K, reducing BBR and increasing the device's critical current. In recent years, the accessibility of commercial 300mK cryostats has increased with the demand for low temperature testing.

The highest efficiency detectors to date were developed by Marsili[3] *et al* using amorphous WSi. The amorphous nature of its crystalline structure increases its compatibility with a wider range of substrates and improves uniformity in nanowire fabrication, making large scale fabrication more robust. The first amorphous MoSi detector was developed by Korneeva[64] *et al*, who considered working with materials that have low carrier densities as a method for achieving high efficiency detectors. Further to its high efficiencies, Verma[5] *et al*, demonstrated the material's low polarisation dependence. MoSi devices have also been applied to quantum communications experiments[68].

Material	**Nb**	**NbN**	**NbTiN**	**NbSi**	**WSi**	**MoSi**	**MoGe**	**MgB_2**
Bulk T_C(K)	9.26	16	16	...	5	7.5	7.36	39
Thin-Film T_C(K)	4.5	8.6	9.6	2	3.7	4.3	4.4	20
Film Thickness (nm)	5	3	4.5	10	4.5	4	7.5	10

Table 2.1: Table of superconducting films with bulk and thin-film transition temperatures. In the case of MgB_2, though the superconducting film has a high transition temperature, the material's properties of photon absorption is not applicable to 1550nm optics. Data from references [67, 69]

Properties of MoSi

The structure of MoSi film was studied by Archan Banerjee through the optimisation of the film's sputtering (§3.1.2. DC Magnetron Sputtering), of which more information can be found in his paper[70]. Measurements of Variable Angle Spectroscopy Ellipsometry (VASE) returned a complex refractive index of $N = 5.2502$ and $\kappa = 4.7736$ at 1550nm. The extinction coefficient κ is higher, which leads to its higher absorption efficiency as found in literature, particularly when compared to NbTiN films. Field Emission Microscopy (FEM) measurements were performed on the film, detailing an A15 structure (Figure 2.24) over short length scales, before the onset of amorphous behaviour. Its carrier density is $n \approx 3.24 \times 10^{22}\text{cm}^{-3}$, which is about a tenth of the value for higher T_C superconductors like NbN[71] ($n = 1.26 \times 10^{23}\text{cm}^3$) and agrees with the expected properties of high and low carrier density materials. Work by Caloz[72] *et al* has also shown saturation in count rate for MoSi devices at high bias currents, which coincides with a saturation in registering efficiency.

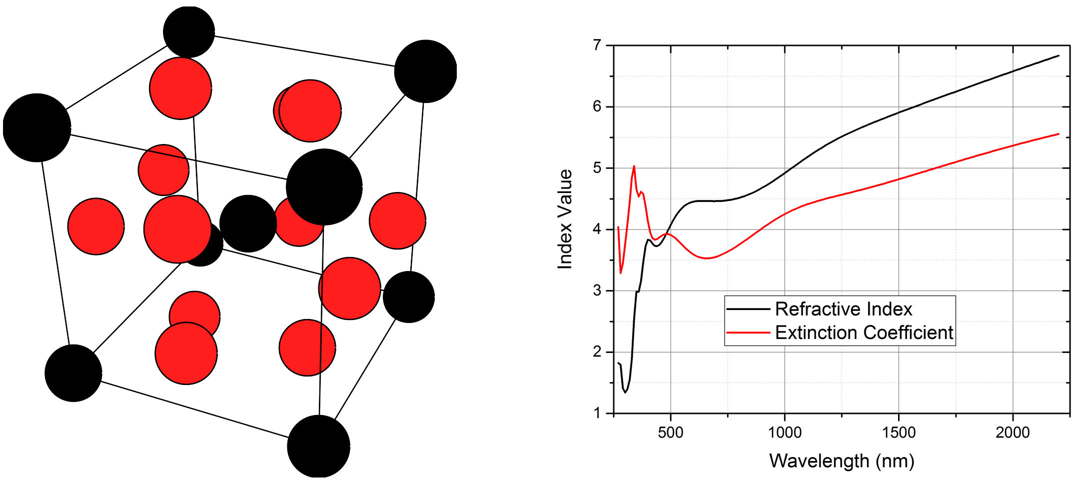

(a) (b)

Figure 2.24: (a) A15 structure of MoSi. (b) Absorption efficiency vs. wavelength of a simple optical stack of 10nm MoSi with a 5nm Si cap[70].

Coupling Efficiency

As explained previously, the coupling efficiency is an external parameter and details the efficiency of photons coming into contact with the device. There are several methods to couple light efficiently, the most common are shown as applied to parallel nanowires in Figure 2.27, consisting of perpendicular coupling, grating couplers or in-plane coupling.

Perpendicular Coupling

Perpendicular coupling involves shining light through a fixed fibre normal to the plane of the device. This is the standard procedure for characterising meander SNSPDs and

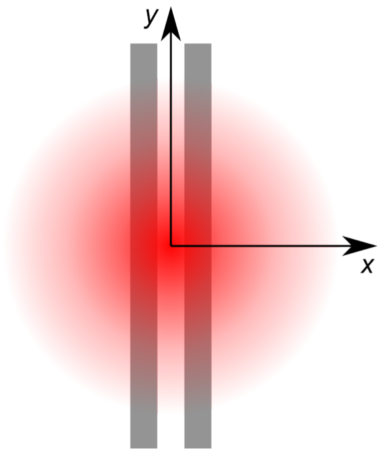

$$G(x) = \frac{1}{\sigma\sqrt{2\pi}} e^{-\frac{(x-\mu)^2}{2\sigma^2}} \tag{2.12a}$$

$$\sigma = \frac{FWHM}{2\sqrt{2ln(2)}} \quad \mu = 0 \tag{2.12b}$$

$$[G(x_b) - G(x_a)]\, G(y) = \frac{1}{\sigma^2 2\pi}\left[e^{-\frac{x_b^2}{2\sigma^2}} - e^{-\frac{x_a^2}{2\sigma^2}}\right] e^{-\frac{y^2}{2\sigma^2}} \tag{2.12c}$$

Figure 2.25: Gaussian functions over a single nanowire or nanowire hairpin.

can be achieved through fibre-alignment, which is detailed in §3.2.2. Fibre-Alignment Rig or by using a detached, movable microscope within the cryostat; this is the setup used in the Rankinator and described in §3.3.6. Microscope Setup.

An accurate estimation of the coupling efficiency for perpendicular light imagines photons in the laser spot as ballistic particles hitting a thin strip representing the nanowires, with intensity represented by a Gaussian beam. The laser will have a measured FWHM, which will correspond to a particular standard deviation. The Gaussian spot can be written as two perpendicular Gaussian functions; a y-component for the length of the nanowire and an x-component for the nanowire width. For simplicity, the spot is assumed to be in the centre of the nanowire structure – which simplifies $\mu = 0$ – with the nanowire having width at points a and b from the centre of the spot (where a is 0 for a single nanowire).

As the equation is symmetrical in both planes, only one quarter of the full nanowire needs to be calculated. For convenience the Gaussian function is normalised; by integrating the spot over the region of the nanowires in only the positive quadrant (and multiplying up by 4), the result will return the percentage of all ballistic photons hitting the nanowire from the Gaussian spot. The integrated Gaussian returns the error function (Equation 2.13d), similar to a sigmoid function. For single nanowires, as opposed to hairpins, in the x-axis, b becomes half the nanowire width and a reduces to zero.

Below is a list of common values used in this Thesis for a 50µm long nanowire, using the laser in the Kelvinator, FWHM = 8µm, the undamped Rankinator, FWHM = 4µm, and the damped Rankinator, FWHM = 2µm.

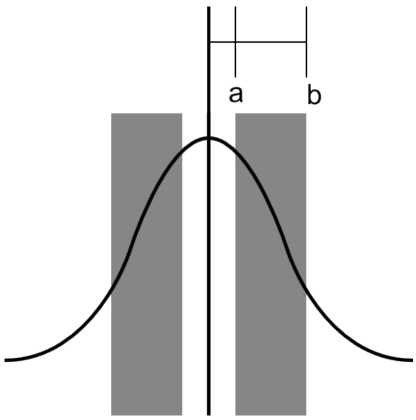

$$= 4\frac{1}{\sigma^2 2\pi}\iint_0^{x,y}\left[e^{-\frac{x_b^2}{2\sigma^2}} - e^{-\frac{x_a^2}{2\sigma^2}}\right]e^{-\frac{y^2}{2\sigma^2}} \tag{2.13a}$$

$$= 4\frac{1}{\sigma^2 2\pi}\frac{\pi\sigma^2}{2}\left[erf(\frac{x_b}{\sigma\sqrt{2}}) - erf(\frac{x_a}{\sigma\sqrt{2}})\right]erf(\frac{y}{\sigma\sqrt{2}}) \tag{2.13b}$$

$$= \left[erf(\frac{x_b}{\sigma\sqrt{2}}) - erf(\frac{x_a}{\sigma\sqrt{2}})\right]erf(\frac{y}{\sigma\sqrt{2}}) \tag{2.13c}$$

$$erf(x) = \frac{2}{\sqrt{\pi}}\int_0^x e^{-t}dt \tag{2.13d}$$

For a single nanowire:

$$erf(x) = \frac{x_b}{\sigma\sqrt{2}}\frac{y}{\sigma\sqrt{2}} \tag{2.13e}$$

Figure 2.26: Derivation of values for ballistic photons hitting a single or parallel nanowire strip. For a single nanowire case, *a* reduce to 0 and *b* reduces to half the width of the nanowire.

Coupling Efficiencies		**Hairpin Width/Gap**	**Nanowire Width (nm)**			
		140/90	**458**	**365**	**258**	**173**
FWHM (μm)	**8**	2.92	5.37	4.28	3.03	2.03
	4	6.77	10.72	8.56	6.05	4.06
	2	13.48	21.26	17.01	12.07	8.11

Table 2.2: Table of coupling efficiency values for different nanowire widths.

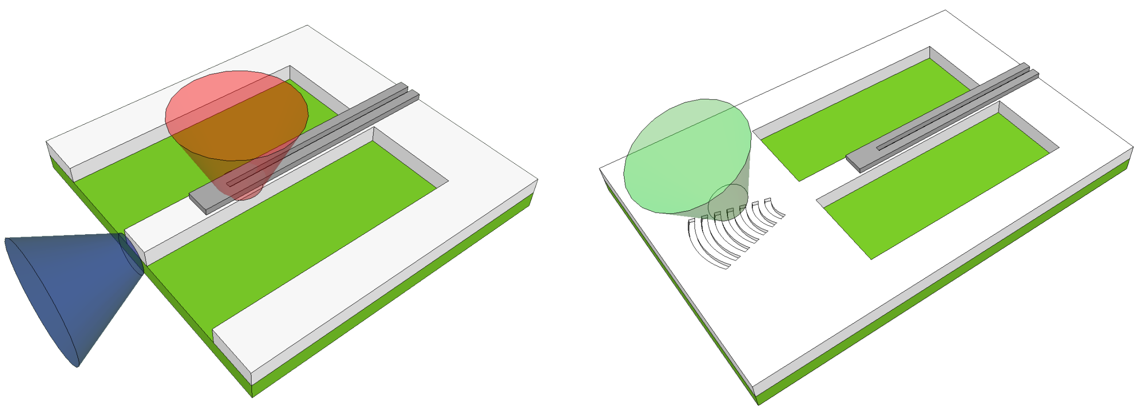

Figure 2.27: Three possible coupling methods for a nanowire. Perpendicular coupling (Red), suffers from low coupling efficiencies $\sim 11\%$ for hairpins and $\sim 55\%$ for meanders due to geometry of the device. In-plane coupling (Blue); this form of coupling could achieve some of the highest coupling efficiencies $>75\%$. Grating couplers (Green) could achieve coupling efficiencies above 30%.

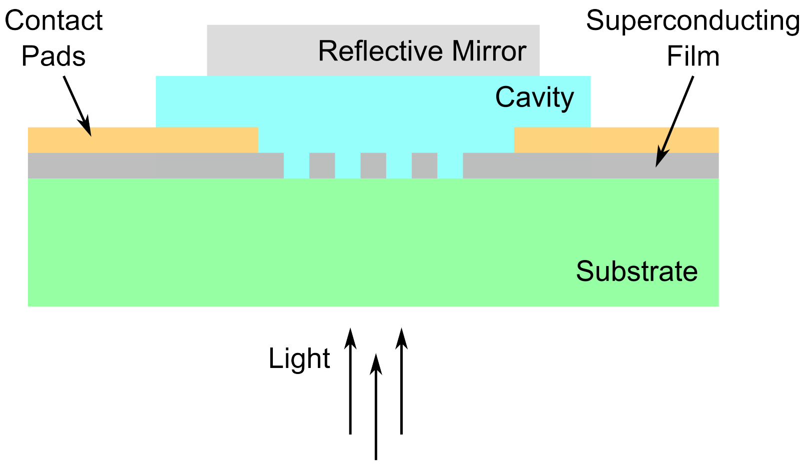

Figure 2.28: SNSPD with optical cavity structure The interference effects occur at the boundary between the substrate and the cavity.

Cavity Devices

To counter-act the large losses obtained in perpendicular coupling, optical cavities can be fabricated onto the device. The use of a cavity is to negate the effect of photon loss from reflections across a material boundary. This is achieved by creating reflections at the other end of the cavity such that photons returning to the boundary destructively interfere with photon's reflection from the boundary, leading to increased transmission[73]. This boundary in an SNSPD is normally located where the substrate contacts the superconducting film, increasing photon coupling into the film. Cavities are designed for specific input wavelengths such that the cavity thickness $d = \lambda/(4N\mathbb{N})$, where N is the refractive index of the cavity and $\mathbb{N}$ is in integer. Integer fractions of the specific input wavelength will also destructively reflect at the boundary. Additionally, reflecting photons are granted an extra pass through the nanowire, which increases coupling efficiencies even for wavelengths outside the affected cavity optimisation range.

Grating Couplers

Grating couplers[74] are radial structures with a periodicity dependent on λ/N. They resonate with angled incident light of a relatively large bandwidth and offer coupling efficiencies of $>30\%$. Using grating couplers is advantageous as they can be fabricated during the same step as the waveguide etch and are compatible with perpendicularly illuminated laser light. The disadvantage comes with the requirement of angled light, which requires further motors or modules to position the fibre at low temperatures.

In-Plane Coupling

For in-plane coupling the waveguide is lengthened and the entire chip is cleaved along it. The light is then illuminated directly into the waveguide and the device absorbs the evanescent waves of the travelling photons (§2.2.5. Single-Photon Evanescent Waves).

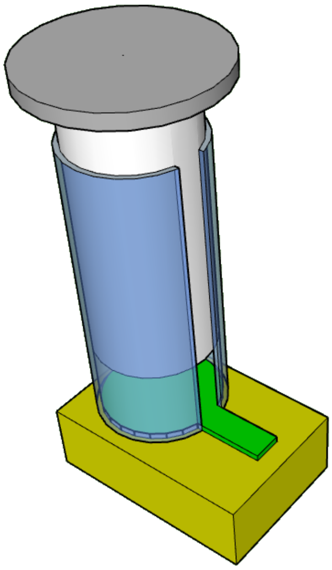

Figure 2.29: Keyhole alignment setup. The sleeve (transparent) holds in place the ferrule (white) and substrate with device (green). The sample mount (gold) is attached to the fridge.

In-plane coupling could achieve some of the highest coupling efficiencies $>75\%$.

Key-Hole Design

A promising method for alignment involves using a key-hole design developed by Miller[75] *et al* as shown in Figure 2.29. In this setup, the substrate is cleaved, via etching, into a keyhole shape, where the device is positioned at the centre of a circle. The device then slides into a cylindrical sleeve, along with the fibre ferrule, centring both of them. Compared to manual alignment, the keyhole design achieves consistently high coupling efficiencies >90% for most devices.

Absorption Efficiency

As described above, the absorption efficiency is an intrinsic property and reports the probability that a photon, in contact with the device, will be absorbed by it. There are several parameters that control the absorption probability, which are detailed below. Absorption efficiency will also depend on the properties of the film, as discussed in §2.3.3. Materials.

Geometry Dependence

When a current flows around a hairpin turn, the mass of electrons tends to concentrate at the inner boundary of the bend. This effect, known as current crowding, leads to a reduction in the critical current density of the nanowire at the bend and, thus, the detector's maximum critical current. To reduce the effect of crowding, there are sev-

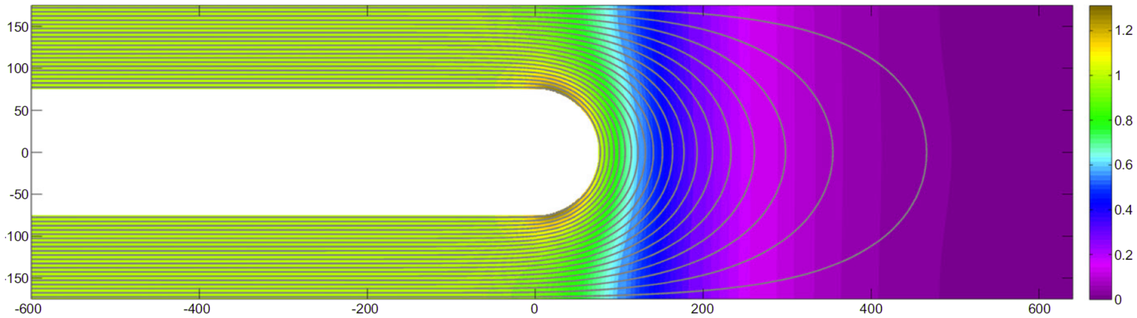

Figure 2.30: Current stream model representing current crowding at the bend in a superconducting nanowire structure within the limit $d \leq \xi_{GL} \ll w \ll \Lambda$. The planar distance is on the scale of nanometres and the colouring of the graph is normalised to the homogeneous current density far from the bend. The current density shows a clear increase at the inner corner of the bend. Image adapted from source [29].

eral alternative geometries. Berggren[76] *et al* proposed curving the inner walls of the nanowires, however the intricacies of this shape are difficult to replicate during fabrication. An alternate method is to extend the head of the nanowire bend, which alleviates the effect of crowding and is easier to fabricate.

Polarisation Dependence

In the case of perpendicular coupling, meander nanowires have a strong polarisation dependence. Photons polarised parallel to the nanowire meander (E-Field oscillations are parallel with long meander lines) have an increased coupling efficiency compared to a perpendicular polarisation. For this reason, it is important to use programmable or manually aligned polarisation controllers to find the maximum (and minimum) coupling efficiencies of the meander nanowire. Polarisation dependence can be reduced by using a material with a high extinction coefficient and has also been shown to reduce with the use of a perpendicular[77] or spiral (Figure 2.31) nanowire design. If an optical cavity is present, all polarisation orientations will see an increase in coupling efficiency at the optimised cavity wavelength, which may cause an increase in the polarisation disparity between parallel and perpendicular polarisations. The disparity will then increase as the wavelength deviates from the optimised cavity[5]. Polarisation disparity also decreases as the incident photon wavelength increases[78].

Fill Factor

The fill factor[79] of a meander describes the percentage of the active area which consists of superconductor (or photon sensitive material). It is the main reason why large, arcing curves cannot be used to alleviate current crowding (§2.3.3. Geometry Dependence). High fill factors occur for wider nanowires or smaller gap widths and vice versa for low fill factors. High fill factors can benefit from increased absorption efficiency and a

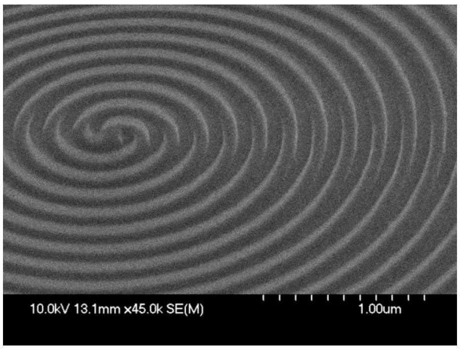

Figure 2.31: SEM of a spiral nanowire fabricated by the author.

reduction in the polarisation disparity of coupled photons. However, nanowire widths for single-photon responsiveness are roughly dictated by the size of the hotspot nucleation site[59] (§2.21. Hotspot model of SNSPD operation), so nanowire widths between 90-150nm are favoured.

Secondary Effects

Afterpulsing

A specific form of DCR occurs when the count from incident photon or a dark count, directly leads to any unintentional counts afterwards within a consistent time-window. This is known as Afterpulsing[80]. This effect is related to the applied bias against critical current of the device; the effect increases exponentially the closer the device is to critical, leading to long chains of afterpulses. These make a large contribution to the overall DCR.

After an incident photon is absorbed, the resulting voltage pulse causes a slight change in the circuit ground, which leads to a partial increase in the bias current through the SNSPD. As the bias is already close to critical, the change is enough to increase both the SDE and DCR. This effect derives from high frequency reflections at the amplifier chain. The effects of afterpulsing weaken with the use of higher frequency range amplifiers.

Latching

Latching[81] is the case where an SNSPD, or other low temperature SPD, gets caught in the transition between a resistive and superconducting state, such that an incident photon has no effect on the detector. In a standard device, during Joule heating and as the hotspot expands, the current is diverted from the device into the load resistor. The hotspot, normally, should expand for long enough such that $R_n \gg R_L$. This causes the current to channel through the load resistor, allowing the device to cool and reset to its superconductive state. The exponential effect of Joule heating does not occur instantly, there is a short time window where its effect is small. If the current reset occurs before the Joule heating enters a 'run-away' process, then the device will not completely cool

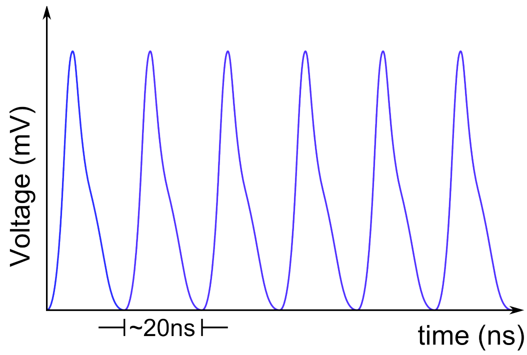

Figure 2.32: Illustration of the output voltage pulse produced by the effects of latching.

itself and only reset the process of Joule heating. The device then becomes stuck in a loop, constantly self-heating and cooling and never returns to its superconductive state until the applied current is lowered (Figure 2.32). This effect occurs at biases close to the critical current, but is also dependent on the device materials. Latching can be alleviated by lower operational currents – achieved by lower temperature testing – and by a choice of materials with a higher residual resistance ratio.

Waveguide Integrated SNSPDs

SNSPDs can suffer from large coupling losses in the case of perpendicularly coupled light as the absorption efficiency is dependent on the thickness of the superconducting film, which is usually 5-15nm. Even the highest efficiency materials with high optical absorption, such as WSi or MoSi, can see absorption losses[3]. Perpendicular coupling used to operate SNSPDs is also incompatible with a scalable chip design due to the limit of the size of the fibre ferrule.

A design for in-plane coupled detectors was first proposed by Hu[82] *et al* in 2009 and first realised by Pernice[83] *et al* 3 years later. The meander detector is replaced with a single hairpin that sits on top of a single-mode waveguide. As the signal photon travels through the waveguide and beneath (or above) the detector, its evanescent waves (§2.2.5. Single-Photon Evanescent Waves) become absorbed into the material, causing a detection event. The hairpin (Figure 2.33(a)) consists of two 120nm wires meeting at a headstock bend. Simulations were performed of this design by Kleanthis Erortokritou using Lumerical in which incident photons travelled through the waveguide. These simulations show the absorption efficiency of the device asymptotes to unity with the length of the hairpin (Figure 2.34).

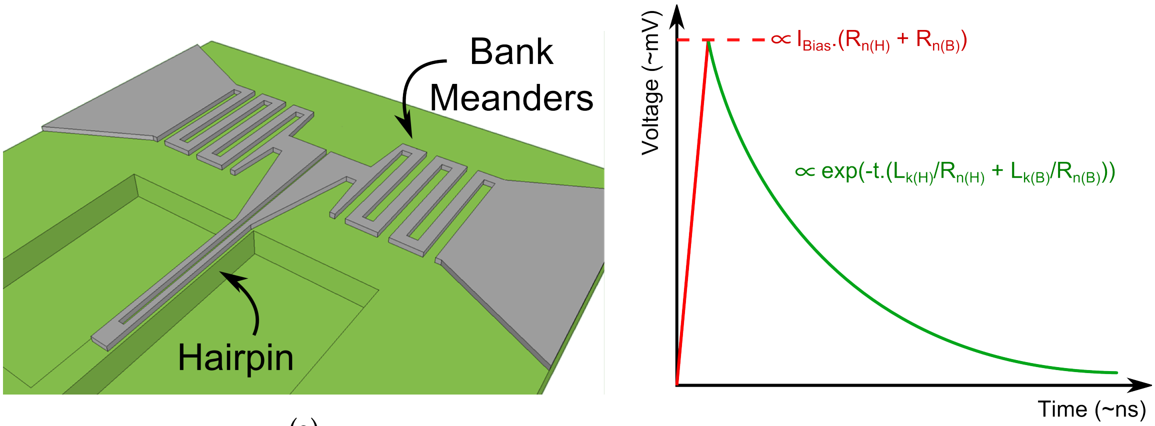

(a) (b)

Figure 2.33: (a) Standard hairpin nanowire design. The bank meander regions have a thicker nanowire size ∼200nm to avoid acting as a detecting region. (b) Example pulse shape of the hairpin. A sharp rise occurs upon the detection of the photon, which drops equally quickly because of the small length of the hairpin, which has an inductance $L_k(H)$ and resistance $R_n(H)$. The reset decay is extended by the bank meander regions, which have an inductance $L_k(B)$ and resistance $R_n(B)$.

After a detection event, the hairpin meander switches too quickly for the counter to detect its small voltage pulse, which is ∼25 times smaller than a meander SNSPD, equivalent to noise. Large bank meander regions are connected in series to the hairpin consisting of 220nm wide wires over an area around 10μm^2. These regions add a series inductance to the device, reducing its reset time and increasing the width of its pulse.

Though perpendicular coupling is not an efficient method for measuring the SDE of a hairpin nanowire, it can be useful in checking the nanowire's uniformity after fabrication. Coupling losses for hairpin nanowires under perpendicular illumination have been calculated in appendix §2.3.3. Perpendicular Coupling.

Waveguides are perfectly compatible with Si waveguide circuits, which makes waveguide detectors excellent candidates for Quantum Information Processing. Integrated waveguides have been fabricated using superconducting films such as NbTiN[84, 85] and substrates such as GaAs/AlGaAs[86] and SoI. Designs have also been proposed using flexible SiN membranes[87] that are manually placed on the waveguide. Waveguide have also been used to generate photon pairs through SPDC. Using an AlGaAs superlattice waveguide, Safarri[88] *et al* achieved high rates of simultaneous photon pairs to single photons.

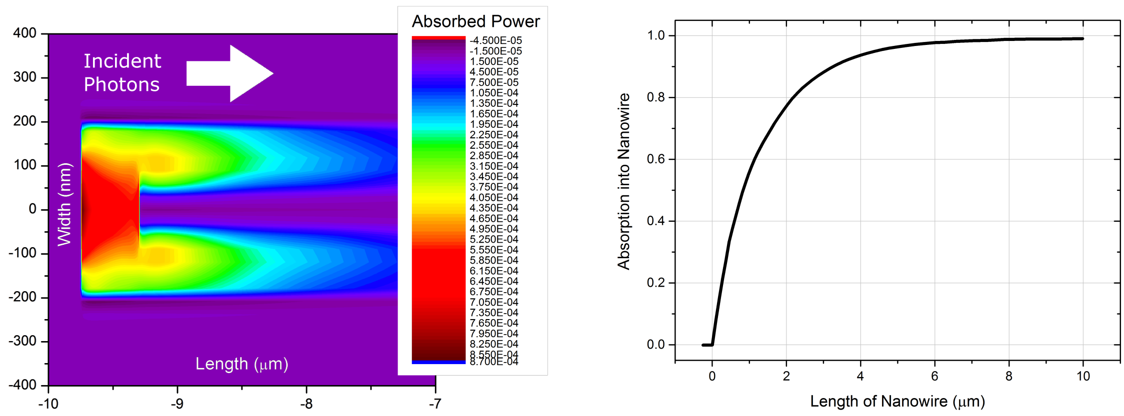

(a) (b)

Figure 2.34: (a) Absorption efficiency reaches unity with the length of the hairpin. A large portion of the incoming signal is absorbed in the headstock (bend) of the nanowire. (b) As the length of the hairpin increases, the absorption nears unity. Simulation by Kleanthis Erotokritou.

Jitter Asymmetry

Work by Schuck[89] *et al* studied a series of hairpin nanowires of different lengths. They noticed a slight asymmetry in the jitter curve (Figure 2.35(a)), rather than an expected Gaussian curve, which was not an effect of the measurement setup. They attributed the longer tail of the jitter to the shape of the pulse rise time of the detector, which can be seen in Figure 2.35(b). Though our physical understanding of SNSPD mechanics is incomplete, a possible explanation for this asymmetry is the combined effects of: fast cooling as the device restores itself to the superconducting state, the expanding hotspot via Joule heating and the bandwidth limit of the experimentation setup - the bandwidth limit has an effect on the kinetic inductance of the device, which effects the pulse decay time and, thus, the jitter.

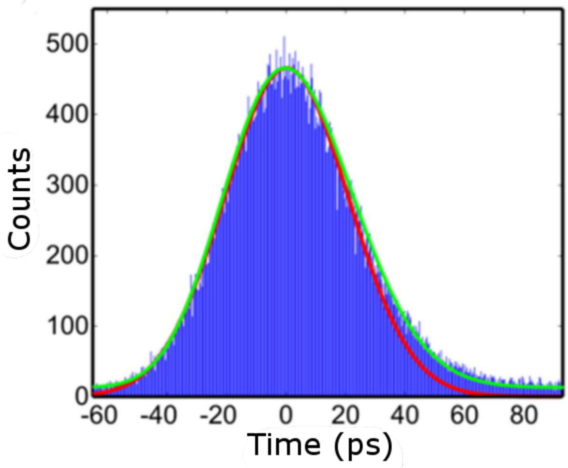

(a)

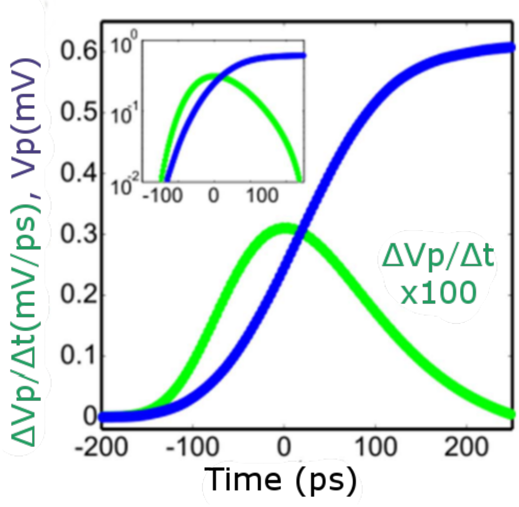

(b)

Figure 2.35: (a) Jitter histogram measurement showing results (green) and Gaussian fit (red). (b) Pulse rise time (blue) and derivative of rise time (green) showing asymmetry. Images adapted from reference[89]

2.4 Quantum Information Processing

2.4.1 Applied Quantum Mechanics

Planck's concept that photons could exist as discrete energy particles presented a contradiction with classical models of electromagnetism. A new form of physics had to be constructed to explain these new phenomena, which classical physical models could not. Both Heisenberg and Schrodinger developed mathematical principles for Quantum Mechanics (QM) around 1925, respectively creating a matrix and integral notation.

The basic principle is a wavefunction, which represents a system – such as a proton – and operators which alter or perform measurements on the system. The main feature of QM is the ability for a particle to exist in a linear superposition of multiple, orthogonal states, simultaneously. The number of states can be large, but, to use a simplified and relevant example, we can consider the application of QM in computing. In classical computers, a bit is stored and transferred as either 1 or 0. This can take the form of the current in a circuit, which can be on or off, or the macroscopic effects of magnetic domains in a hard disk, which have two opposing field directions. In contrast, a quantum bit, or qubit, exists as a linear superposition of both 1 and 0 simultaneously (Equation 2.14a). This can be represented by a point on any part of the surface of a sphere, known as a Bloch sphere (Figure 2.36).

$$|\Psi\rangle = cos\left(\frac{\theta}{2}\right)|0\rangle + e^{i\Theta}sin\left(\frac{\theta}{2}\right)|1\rangle \quad (2.14a)$$

$$|\Psi\rangle = \alpha|0\rangle + \beta|1\rangle \quad (2.14b)$$

$$\alpha^2 + \beta^2 = 1 \quad (2.14c)$$

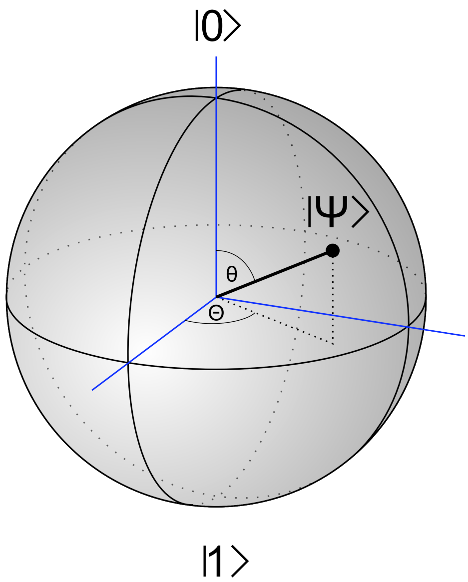

Figure 2.36: Bloch sphere describing possible orientations of a qubit along with its mathematical description.

A further principle of QM is that the act of measuring the wavefunction, collapses it into only one of its superimposed states with a probability related to its coefficient in the wavefunction (Equation 2.14b). In the case of a qubit, the act of measurement will return the classical 1 or 0 bit. It is important to note that, though the Bloch sphere has an infinite number of points on its surface and though this suggests an infinite amount of storage data within a single qubit, the wavefunction will always collapse into a single state after measurement. The benefit of QC here is not a difference of storage data size (The data size is the same as classical computing), but the reduction in processing time required to perform particular, applicable calculations using the wavefunction formalism (Discussed below, in §2.4.2. The Principles of QIP).

There is no understanding of what, in the existing world, is represented by a wavefunction or the act of measurement. Though the physics has applications and can calculate real values found in nature, the interpretation as to its representation is unknown.

2.4.2 The Principles of QIP

Since their invention, modern computers have experienced a rapid reduction in size as new technologies for micro and nanometre fabrication have developed. Though this trend has followed an exponential increase in computing power, there is a limit to its contraction. Eventually transistors will reach a size comparable to the de Broglie wavelength of the electron, at which point a mechanism as simple as a current will no longer be possible. This limit fast approaches along with the demand for greater processing power, higher communications fidelity and stronger transmission security. All of these conditions can be satisfied via the field of Quantum Information Processing (QIP).

QIP offers improved computation rate for numerous classical algorithms, such as Shor's algorithm[90], which finds the prime factors of an integer $\mathbb{N}$. In classical computing this would have taken an exponential amount of computing time, but in a quantum computer that processing time becomes sub-exponential. Grover's search algorithm[91] again, in a classical setting, has an operation number which is a function of the integer number of search terms $\mathbb{N}$, but in quantum computing reduces to a function of $\sqrt{\mathbb{N}}$. QIP also offers highly secure transmissions as the act of interfering with a qubit, by an outside eavesdropper, changes its state (A deeper discussion of this can be found in §2.4.4. Cryptography). Aside from computing speed and security, building these systems also develops our understanding and models of the physical medium in which the system is built.

Requirements of Universal QIP

In 1982, theorists Wootters, Zurek[1] and Diek[92] developed the no cloning theorem. The theorem proves that it is impossible for a qubit to be copied; the act of measuring a qubit, in an attempt to recreate it, destroys the qubit and produces classical states. This is not to say a particular state cannot be repeatedly created, rather, a state that currently exists cannot be duplicated from itself without first destroying it. Though this is a hindrance to storing information, it is advantageous in secure communication.

To replicate a state – and in doing so, destroy the original – a procedure known as teleportation can be performed. Using the original state and a prepared blank state, the original state can be measured and its information transferred to the blank state, creating the same version as the original.

Two qubits prepared from the same source or gate can obtain a feature termed entanglement[93]. In this case the wavefunction of both systems cannot be factorised into each of their individual components; the states become dependent on each other. In this form, which has no classical comparisons, the act of measurement of one qubit can be used to predict accurately the measurement result of the other entangled qubit, depending on how the source pair was prepared.

Two qubits entangled together appear to communicate information over long distances faster than the limit of light speed. This was the basis for the Einstein, Podolsky and Rosen paradox, as the laws of physics strongly suggest that no information can travel faster than the speed of light. There were two postulates to this paradox; either the entangled pair held Locally-Hidden Variables (LHVs) or they did not, known as Non-Locality (NL). John Bell postulated a simple statistical check[94] to see if the pair contained LHVs. He suggested that, if in measuring the two particles, opposite outcomes from each particle appeared more frequently than same outcomes, then the LHV postulate would not hold. Up to this date, in all experiments performed to check Bell's inequality, none have disproven it, suggesting NL holds.

Coherence Length

The superposition of states that represent a quantum mechanical particle do not exist in a perfect vacuum. Due to the interactions with other particles in the system, the QM state can decay, eventually settling onto a single state and becoming a classical particle as if it had been measured. This time (or length) can be described as a coherence period[33] and is based on the temporal coherence function G_t. That is, the average square intensity between the complex wavefunction of the medium U over a fixed time period τ. For a coherent state, as time progresses, the value of the ratio $|g(t)|$ (Equation 2.15) decreases, which means the initial wavefunction $U(t)$ and the wavefunction after the fixed time period $U(t+\tau)$ will differ more dramatically.

$$g(t) = \frac{G_t(\tau)}{G_t(0)} = \frac{\langle U^*(t)U(t+\tau)\rangle}{\langle U^*(t)U(t)\rangle} \tag{2.15}$$

2.4.3 Physical Utilisation of QIP

Beyond theoretical descriptions, physically creating systems that apply QIP have been shown possible through several media, including: Nuclear Magnetic Resonance (NMR), Ion Traps and Photonics. Though each of these processes shows continued improvement, it is likely the future of QIP and quantum computing will use a combination of mechanics.

In 2001, NMR was the first system to demonstrate Shor's algorithm[95]. IBM successfully factorised the integer 15 into 3 and 5 using the spin states of molecules to represent qubits and radiofrequency pulses as the circuitry to alter the molecular spins of the system[96]. Though progress continues to be made in this field, NMR still suffers from short coherence times.

Ions can be confined in free space using the EM-field; the complex nature of the electron state of a molecular ion allows them to behave as qubits. Quantum computation is achieved through the collective movement and communication of ions trapped within the confines of an EM-field. However, this medium also suffers from short state lifetimes.

Linear-Optical Quantum Computing

Currently, the leading optical approach is Linear Optical Quantum Computing (LOQC), which was first conceptualised in a 2001 article by Knill, Laflamme and Milburn[1]. They hypothesised qubits formed from photon polarisation with circuits formed from single photon sources; phase-shifters and beam splitters acting as universal gates and high-efficiency SPDs as sinks, with feedback from the SPDs able to re-interact with the system.

Single photon sources would require the known creation of a state within a single mode i from the vacuum state $|0\rangle_i \rightarrow |1\rangle_i$. An array of possible methods have been discussed in §2.2.4. Generating Single Photons. To recap, SPDC sources can generate pairs of single photons, but not deterministically, attenuated laser sources are also non-deterministic and not viable for a scalable chip structure. Quantum dots appear to be the most accessible feature, as they are scalable and allow for the deterministic production of single photons.

SPDs would read which mode a photon is in and the number of photons in each mode. For SPDs that cannot resolve photon number, this could be achieved using multiple SPDs and beam splitters. An array of possible SPDs have been discussed in §2.3.2. Types of Single Photon Detector.

Quantum Gates

Quantum gates need to be reversible and require the unitary operation of states via linear optics, which preserves the qubit coefficients in the system's space. Gates can be implemented through photonics with the use of beam splitters and phase-shifters. An example Controlled-NOT (CNOT) gate is shown in Figure 2.37. In this setup a Mach-Zehner interferometer is used to either flip or not flip the state of an input photon based on whether a π-phase shift has been applied to the phase-shifter. Theoretically, with the addition of two extra phase shifters, a quantum circuit component can be packaged to perform arbitrary, one-qubit unitary operations. An $\mathbb{N} \times \mathbb{N}$ array of these components would then be able to realise any unitary operator[97]. Practically, there is not yet any materials that can implement a determinable phase shift to travelling single photons.

There have been many successful attempts to apply QIS to photonics, including examples of quantum gates[93, 98–100], phase-shifters[97], teleportation[101] and entanglement[9, 97, 102–105], as well as a combination of beam splitters with waveguide integrated SPDs[106]. However, the most advantageous application of a photonic medium is in the field of quantum communications and cryptography.

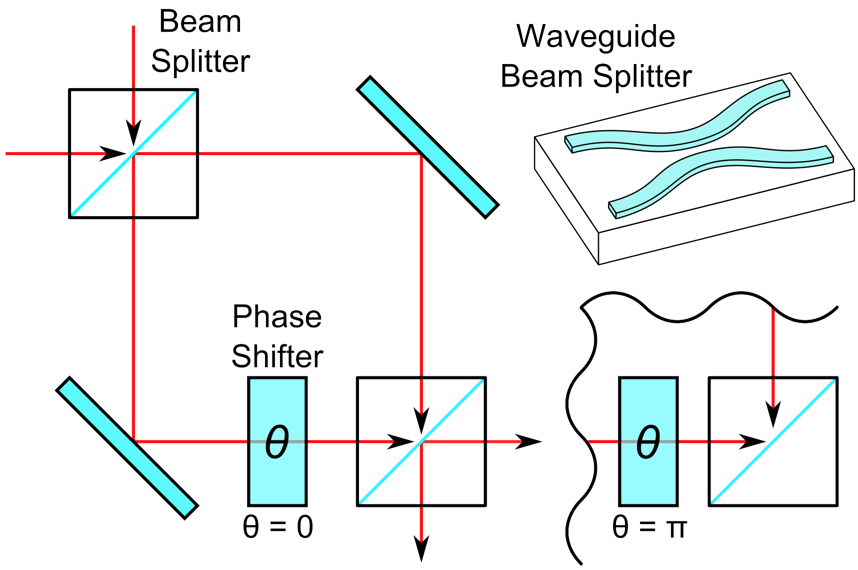

Figure 2.37: CNOT Gate implemented through a photonic medium. Two photons are combined at a 50-50 beam splitter, the output of which is then combined again at another beam splitter. At a phase-shift of 0, the output photons are the same as the input photons. At a phase shift of π, the output photon state is flipped compared to its input. Photonic beam splitters can be achieved using a partially reflective mirror or the interference between two waveguides in close proximity.

2.4.4 Cryptography

With the rise of computing and the internet came the requirements of encrypting large data sets; from bank details, to messages and passwords. The fundamental approach to encryption involves the use of a public key, given to the sender, to encrypt messages and a private key, owned by the receiver, to decrypt messages. In modern computer communications, the most widely used encryption algorithm is one based on the RSA algorithm (Figure 2.38) developed in 1978[107]. This method of encryption used two large prime numbers to compute the public and private key. This presented a simple way to encrypt and decrypt data if the keys were held, but mathematically rigorous to crack without them.

Quantum Key Distribution

Quantum Key Distribution (QKD) is the application of QM onto cryptography in order to create shared keys. The advantage of QKD over modern key sharing is that, due to the random nature of QM, it is almost impossible to crack the generated key. A modern RSA encryption is possible to crack given enough time or processing power. By comparison, a QM encryption is not possible to crack, other than by a negligible random chance. QKD has been successfully performed in many experiments [8, 9, 11, 12, 108]. Two particular methods of QKD are discussed below, the BB84 protocol (§2.4.4. The BB84 Protocol) and

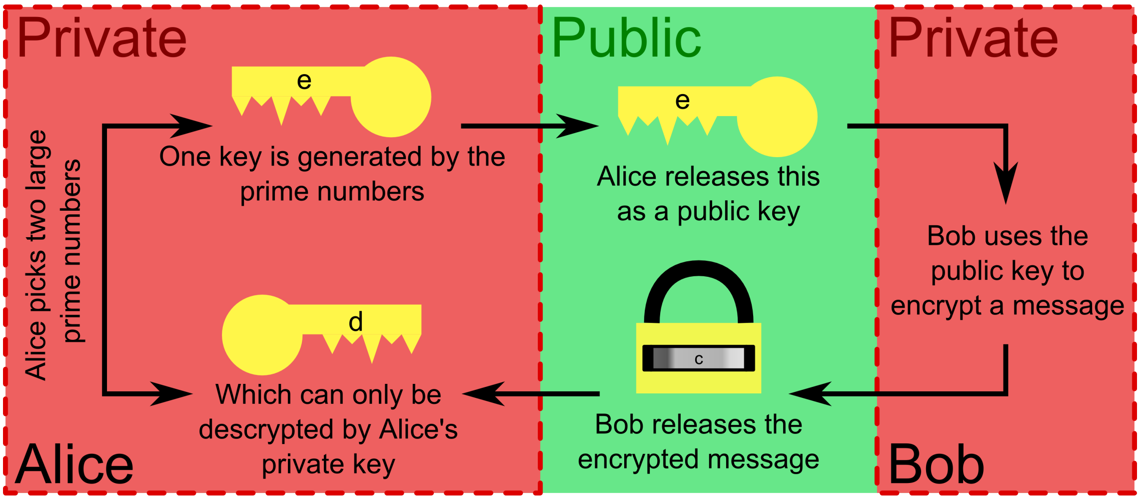

Figure 2.38: Under the RSA encryption method, Alice creates two keys that are long string prime numbers. One key is made public which can be used to encrypt a message from Bob. This message can then be decrypted by Alice's private key.

decoy state QKD (§2.4.4. Decoy State QKD).

Before discussing QKD protocols, it is important to understand two metrics: key rate and error rate. The key rate is a measure of the number of generated keys per second in a QKD protocol between two parties. The key rate is effectively a metric for the performance of the full system. The error rate measures the number of errors that can occur during signal transmission, which is to be expected as these QKD protocols are based on probabilistic outcomes. The ratio of error to key rate returns the Quantum Bit Error Rate (QBER). It will be seen how this metric can be used to detect an eavesdropper.

The BB84 Protocol

The BB84 protocol, invented in 1984[109] by Bennett and Brassard, describes the scenario of two parties, Alice and Bob, sharing messages between each other in order to produce a solitary key that only they know, which can be used to generate a basis for qubit encryption. This method can be utilised in any QM system, but a photonic description is the most practical example. The method is performed as follows:

First, Alice and Bob set up a scheme for encoding information in two different bases, with each basis further having its own pair of orthonormal polarisations. If a polarised photon passes through its correct basis, the correct binary value is returned. However, if the basis is wrong, the returned binary is random. This is detailed in Figure 2.39.

In the next step (Figure 2.40), Alice and Bob each create their own key, which is a dispensable and random sequence of bases. Alice writes a disposable message and passes it through her random basis, scrambling it. She then sends the coded transmission to

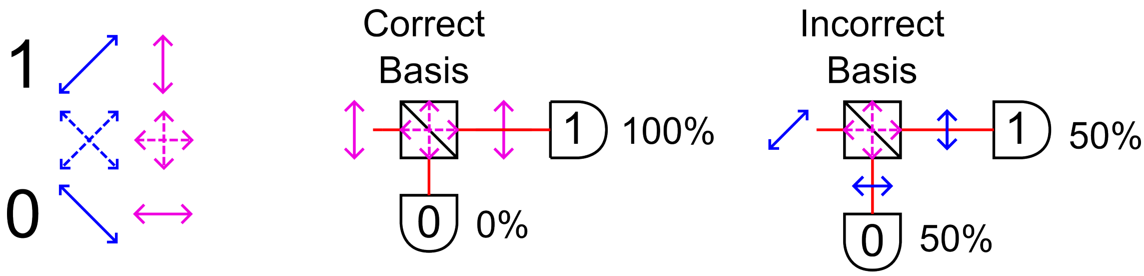

Figure 2.39: Left: Alice and Bob encode their information in two orthogonal bases, each with its own polarisation state for each binary output. Centre: the correct basis will return the correct binary output each time. Right: The incorrect basis will return a random binary output, but with equal probability as the two orthogonal bases in this case are polarised 45° from each other.

Bob and he decodes the message with his random basis selection. The two share their choice of bases via a public channel to determine for which bits the basis choices match (sifting). They then check a subset of their sifted bit stream to determine the quantum bit error rate (QBER). If no Eve is present, a secret key is created from the sifted bits, corresponding to a matching basis. Alice and Bob now have a key that only they know about and can use to encrypt and decrypt future communications.

However, suppose Eve is present. Due to the no cloning theorem, if Eve attempts to intercept Alice's disposable and encrypted message, she will destroy the data. As Eve cannot know, just like Bob, what Alice's random key is, Eve will then send a string of data to Bob with her interpretation of Alice's message. In the case where Eve does not exist, Bob will guess the correct basis for Alice's message half of the time and, in the incorrect basis, will get a correct output another half of the time. Therefore, Bob would expect a QBER of 25%. However, if Eve is listening, the combination of both Eve and Bob's incorrect basis will cause Bob to receive correct information at a slightly lower, but perceptively different percentage, corresponding to a QBER ∼44%. Thus it can be known if Eve is listening to or, rather, sabotaging Alice and Bob's conversation.

The BB84 protocol and variants have been successfully performed using SNSPDs at 1550nm[9, 11, 12, 108], including by Hadfield[7] *et al* in 2006, at a distance of 42.5Km, and Takesue[8] *et al* in 2007, at a distance of 200Km.

SNSPDs in QKD systems, along with other types of SPDs, are vulnerable to hacking attacks[110]. Eve can control when an SNSPD clicks by sending a long, high intensity signal to Bob's detector and shutting it off for a fraction of a microsecond. In this case, Bob's detectors will produce a pulse that appears the same as the pulses Bob receives from single photons. This allows Eve to record Alice's message without Bob knowing. Honjo[111] *et al* presented a solution to this problem by monitoring the rate of coin-

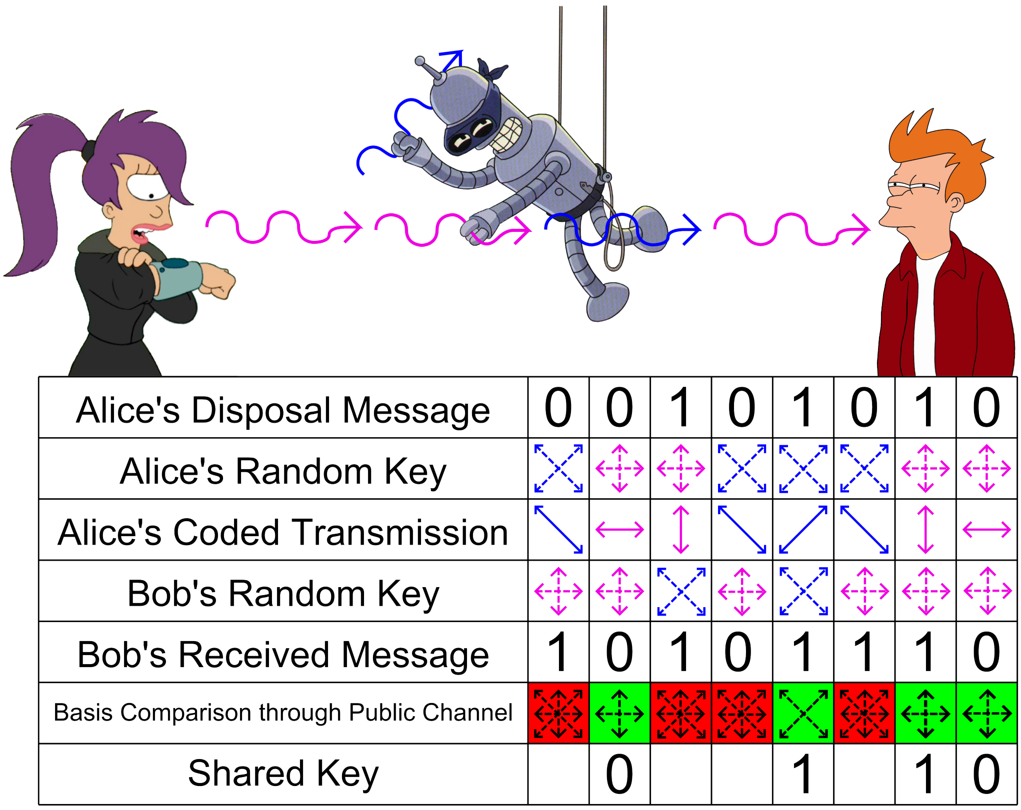

Figure 2.40: BB84 protocol. Alice is represented by the character on the left, Bob is on the right and Eve in the centre, attempting to intercept the data transfer.

cidence detections at Bob's detector. They identified that in a normal, single photon transmission, the coincidence rate would be low, but if Eve was to perform a blinding attack, the coincidence rate would rise sharply and become noticeable.

Decoy State QKD

Practical QKD systems use an attenuated laser source as a single photon emitter. Due to the statistical nature of light, it is possible for two photons to arrive together, even at very low attenuation rates. Eve can take advantage of this by suppressing single photons, but splitting multiphoton signals, sending Alice's message to Bob, but also allowing an exact copy to be collected by herself. This is known as a Photon Number Splitting (PNS) attack. Decoy state QKD is a resolution to this complication.

First postulated by Hwang[112] and later developed by Lo[113] *et al*, decoy state QKD (Figure 2.41) involves Alice sending a series of façade states at differing photon number intensities along with the single photon signal state. Each state will have a specific yield: $Q_m = Y_m e^{-\mu}(\mu^m/m!)$, dependent on the number of transmitted photons m. The state will also have a QBER $E_m = e_m$. After transmission, Alice sends the intensity levels of each state m through a public channel. Bob can use this information to calculate a weighted average of $Q_m E_m$ and compared it with the measured result from his detection.

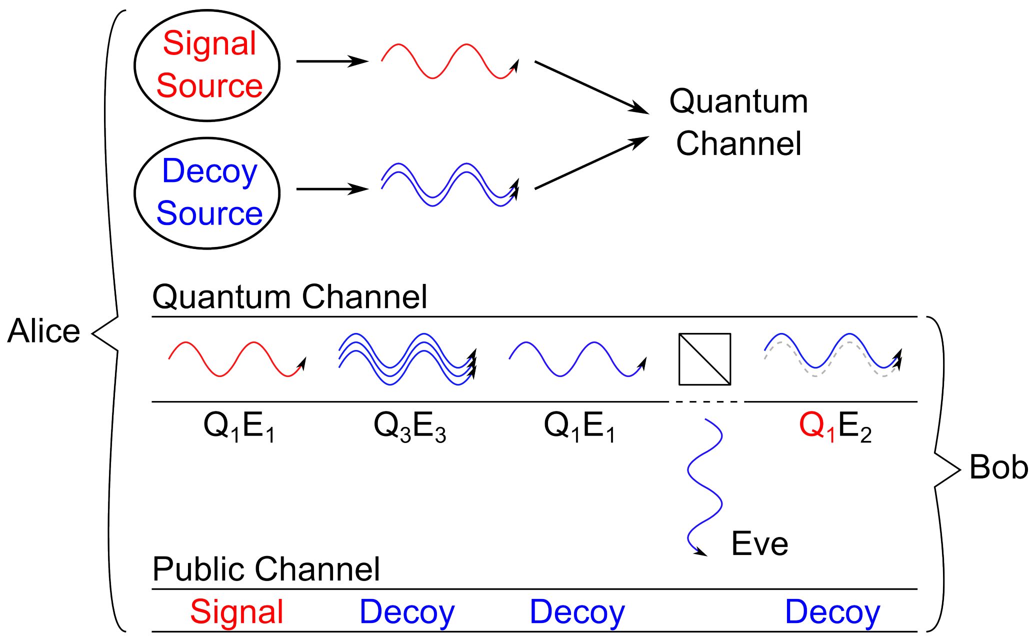

Figure 2.41: Alice sends Bob a series of decoy states at different intensities, only a small portion of which are part of the signal. She also sends the photon intensity through a public channel. If Eve performs a PNS attack, Bob will recognise the change in weighted QBER when comparing his measured results with the information Alice sent through the public channel.

If Eve has performed a PNS attack on a state, she will decrease the intensity of that incoming state: $Q_{<m}E_m$. When Bob performs the comparison of the weighted errors, it will not match the expected values, revealing Eve's attack. This method has been demonstrated successfully by Lo[113] *et al.*

T12 Protocol

An advanced version of the decoy State QKD, known as the T12 protocol, was first introduced and demonstrated by Lucamarini[114] *et al.* This method avoids the ideal scenarios under which previous theoretical QKD experiments are based on and gathers a series of separate protocols together to achieve high efficiency QKD in a non-ideal experimental setting. T12 combines an efficient variation of the BB84 protocol - to increase the system key rate - with the decoy State technique QKD by Hwang and Lo at a GHz clock rate. However, the full description of the protocol is beyond the scope of this Thesis.

Current Progress in QKD

The UK Quantum Technology Hub for Quantum Communications Technologies (QComm) has received £24 million for a five year funded project (2014-19) focused on setting up a UK wide QKD network. For photonic quantum computers to be a viable computing method, they will need to be scalable. This is achievable if the computer components can be placed on a monolithic chip. Work on single photon sources, gates and detectors has shown that this is possible using waveguide optics. Current development focuses on continued improvement of component parameters as well as a focus on integration through Si waveguide circuits.

Chapter 3

Experimental Methods

This chapter focuses on the practical aspects of creating and characterising an SNSPD. §3.1. Fabrication gives an in-depth detail of the processes and challenges during fabrication. §3.2. Device Mounting Methods discusses coupling methods for light, including in-plane waveguide coupling and perpendicular fibre coupling. The Quantum Sensors group uses several cryostat, which together have a minimum temperature of 2-3K. In order to improve values of SDE and characterise certain materials with transition temperatures below 1K, a new cryostat would have to be built. The central goal of this Thesis was to build and maintain a cryostat - dubbed the Rankinator - capable of scanning photoresponse maps at a resting temperature of 300mK. Its design and operation are discussed in §3.3. Rankinator Design. The final section §3.4. Low Temperature Measurements is used as a reference for circuit setups used to characterise the devices in this Thesis.

3.1 Fabrication

3.1.1 Facilities of the JWNC

The James Watt Nanofabrication Centre (JWNC) at Glasgow University is a 1400m^2, £70M clean room maintained by 23 technicians. It is supported in funding from the EPSRC (Including 2 CDTs), DSTL, 2 quantum technology hubs, 5 ERC fellowships and 230 further companies. Of the machines used during this research, the JWNC features:

- A Vistec VB6 E-Beam capable of Electron Beam Lithography (EBL) with a resolution of 1.25nm. Additionally, vacuum chambers, spinners and hotplates to prepare the chip for EBL. The VB6 is also soon to be replaced with newer model.

- An MA6 mask aligner for photolithography.

- Two vapour deposition tools (Plassys MEB 550S E-Beam evaporator) which include crucibles of Ti and Au.

- An Ultra-High-Vacuum (UHV) sputtering machine (Plassys VI, MP 600S), discussed in more detail below (§3.1.2. DC Magnetron Sputtering).

- A Reactive Ion Etching (RIE) station (Oxford Instruments RIE80+) which has an interferometer to monitor etch depth.

- A Scanning Electron Microscope (SEM) (Model 4700), capable of nanometer resolution images both using primary and secondary electron scattering. The images also present an accurate reading of scale based on the working distance of its detectors.

- An Atomic Force Microscope (AFM) (Bruker Icon), capable of height profiles at nanometer resolution.

- Additional and standard equipment, such as optical microscopes, dicing machines and other height profilers (Veeco Dektak 6M).

3.1.2 DC Magnetron Sputtering

The Plassys MEB 550S E-Beam evaporator is an UHV ($< 5 \times 10^{-9}$ Torr) sputtering machine with a load lock for rapid sample exchange Figure 3.1. The system has five sputter guns of Mo, Ge, Si, Nb and Ti in a confocal configuration. There is a heater capable of reaching 700°C for heating substrates during deposition and a liquid nitrogen trap allowing substrates to be cooled close to 77K prior to deposition.

DC magnetron sputtering is achieved by applying a fixed, high frequency E-field to create an ion plasma. A supplied, closed M-field is also applied to trap the electrons and lowers the ionisation gas pressure. The chamber is mixed with an Ar gas (30 sccm) and the sample is rotated (60rpm) as the target shutter is opened and the particles hit the sample (100mm working distance at 5° from vertical). Film thickness is calibrated through repeat measurements of thickness after recording different deposition rates and times. To optimise the film grown on the sample, it is electrically tested over a variety of RF power values, each over a range of different discharge currents. More detail of the opti-

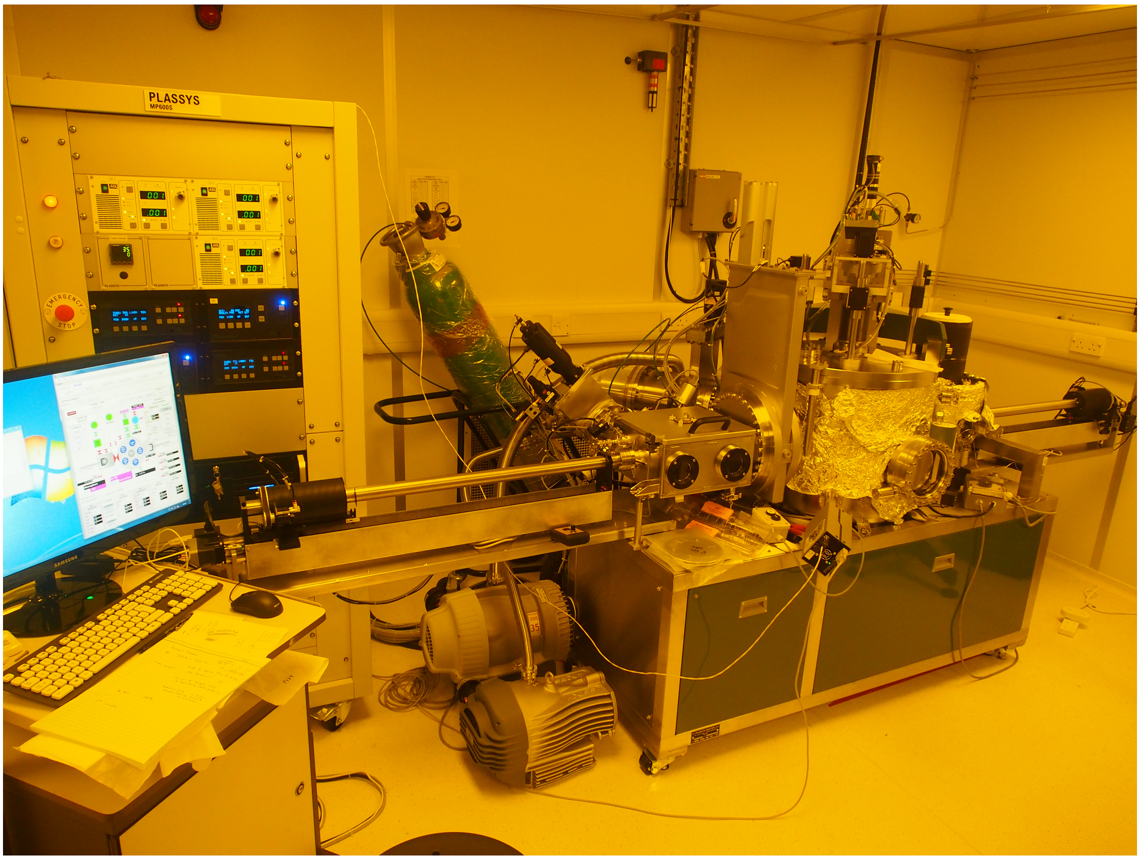

Figure 3.1: Plassys VI UHV sputtering deposition system in the Glasgow University JWNC.

misation process for sputtered films can be found in the work performed by Banerjee[70] *et al.*

3.1.3 Lithography

In the late 1700s, Alois Senefelder created a process in which a wax pattern was used as a mask to acid etch a plate of polished limestone. Modern lithography is not far removed from this process; nanolithography uses a mask pattern to cover a material, which can then be etched away or built upon by evaporation to create patterns on the scale of 10nm to 1μm. Nanolithography has two main approaches: Photolithography and EBL (Figure 3.2).

Photolithography involves coating the device in a light sensitive film and exposing it to light through a negative mask of the pattern. Developing the exposed regions leaves behind the intended pattern for further processing. EBL is a serial process and involves accelerating electrons through a potential onto a substrate coated with resist. The electrons change the solubility of the resist allowing the negative or positive pattern to then later be developed. EBL is a slower and more expensive process, but achieves higher resolution patterns <5nm compared to the UV light used in photolithography, which patterns with a resolution >10nm. For this reason it is the favourable method of choice for patterning nanowire SNSPDs.

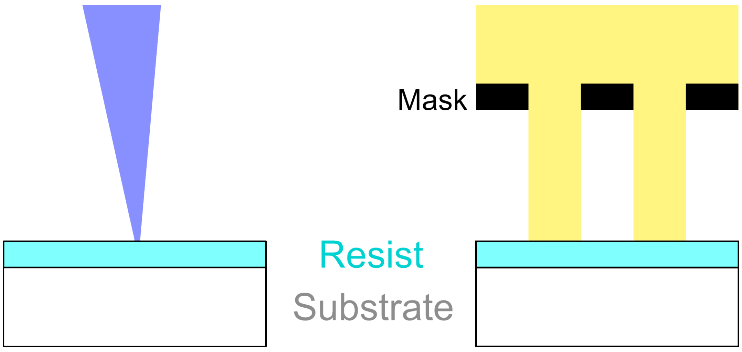

Figure 3.2: Comparison of E-Beam and photolithography. Photolithography uses light shone through a mask to pattern the resist, whereas E-Beam lithography is a serial process using accelerated electrons. The mask used in photolithography is patterned by E-Beam, but can be reused many times.

Resists

A positive resist is subject to bond breaking when exposed to the E-Beam, which dissolves during the development stage. A negative resists creates bonds and the non-exposed resist dissolves during the development stage. Positive resists remove the patterned area directly drawn by the user after development, whereas negative resists will keep the patterned area and remove everything else.

Two common resists are Poly-Methyl Methacrylate (PMMA) and ZEP520[115]. PMMA can achieve up to 10nm resolution patterns, but suffers from high sensitivity to etching gases of C_2F_4 and SF_6. ZEP, compared to PMMA, has higher sensitivity (Better pattern resolution), stability (Longer shelf-life) and durability during the etching process. However, ZEP suffers from larger edge roughness and has a higher sensitivity during the development process in which a slight change in temperature or development time can produce unwanted results. Due to its higher resolution, ZEP was the chosen resist for pattern nanowires in this Thesis.

3.1.4 EBL Process

The Vistec VB6 is an E-Beam lithography tool capable of patterning at a resolution of 1.25nm. It operates by accelerating electrons through a 100kV potential onto a substrate coated with resist. The electrons project a Gaussian spot on the sample, interact with the resist and change its solubility. The use of Au alignment markers allows accurate positioning of multiple E-beam steps to within an error <1.25nm. Its design allows the user to specify an E-Beam current, or dose, and pattern spot size, the most effective parameters of which are obtained from multiple dose tests. To understand this, it is first necessary to detail the design and operation of the VB6, as in Figure 3.3.

The electron gun hits the substrate with a maximum main-field size of 1310.7µm with its deflection coils capable of 2^{20} individual exposure points. This produces the minimum resolution factor of 1.25nm. The features of any E-Beam pattern must have these base units to avoid aliasing. The E-Beam scan splits the design into large main-fields and smaller sub-fields. Having such a large main-field leads to skewing of the pattern near its edges and stitching errors on the border between main-fields. The skewing effect can be reduced by centring a small pattern within a large main-field, far from its edges. The stitching errors are mostly avoided through software checks by the E-Beam before processing.

The Gaussian spot size of the beam is adjustable to create patterns at different resolutions. This is set in tandem with the dose of the beam and the system's Vectorscan Resolution Unit (VRU). The VRU parameter controls the stepping distance between E-Beam exposures in intervals of the minimum resolution Figure 3.4. Small features use a small spot size, with a lower dose value and a reduced VRU, whereas large features use a slightly higher dose, larger spot size and an increased VRU. A VRU set too large would leave parts of the sample unevenly exposed. A VRU set too small would lead to bunching exposure points, overdosing the sample and increasing the E-Beam operation time. However, the effect of the VRU is also tied to the size of the dose and bunching is a useful tool when the dose is low.

Dose Tests

The dose is a measure of charge per unit area of the E-Beam on the resist; it is the literal size of the beam current hitting the substrate. Beam dwell time is the length of time at each 'pixel' in the pattern (Equation 3.1). A maximum writing frequency for the VB6 is 50MHz, which equates to 20ns dwell time. From this, a rough range of doses can be chosen, but in practice an ideal dose value can only be found through dose testing, in which an array of samples with different doses are patterned in the E-Beam then scrutinised under the SEM Figure 3.5. Successful devices were fabricated using a 4nm spot size at a VRU of 4 for small features and a 45nm spot size with a VRU of 43 for large features.

$$Beam\ Dwell\ Time(s) = \frac{Dose(\mu C\ cm^{-1}) \times Spot\ Size(cm)}{Beam\ Current(A)} \tag{3.1}$$

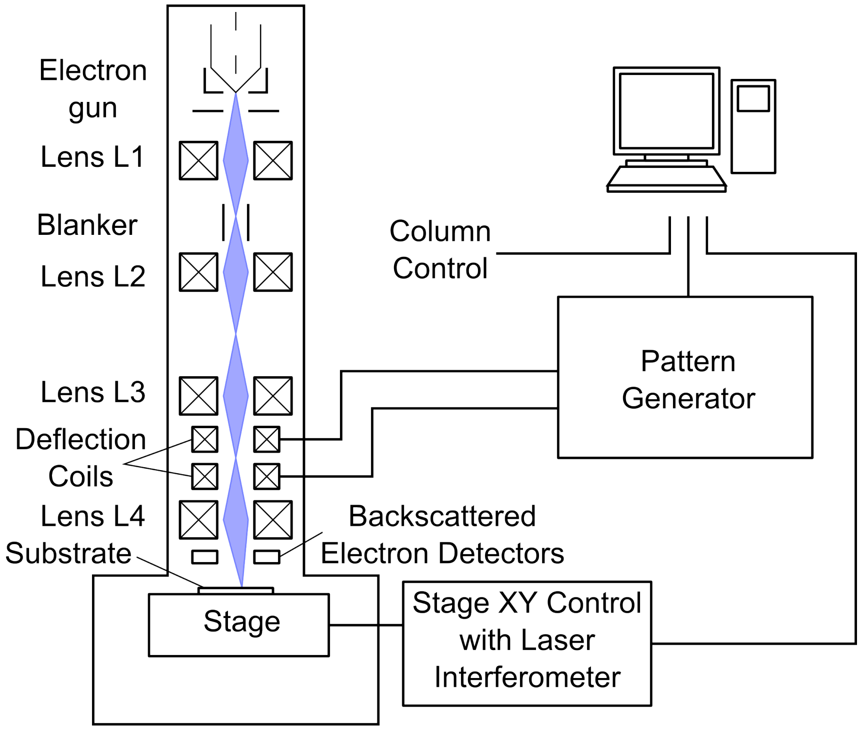

Figure 3.3: VB6 design. At the top, an electron gun creates a source of electrons, which are then accelerated to 100kV at a velocity of 0.57c, with relative wavelengths around 4pm. Each of the lenses in the tube use an adjustable magnetic field to deflect and focus the beam down the column. L1 focuses the beam onto the blanker, the blanker acts as a switch to halt the beam from hitting the sample. L2 and L3 are demagnifying lenses to control the beam size. The deflector coils scan the beam in the x and y direction, creating the pattern dictated by the user. L4 is a further focusing lens. The backscatter detectors at the base of the beam are used to detect Au markers from the chip when aligning for subsequent E-Beam steps.

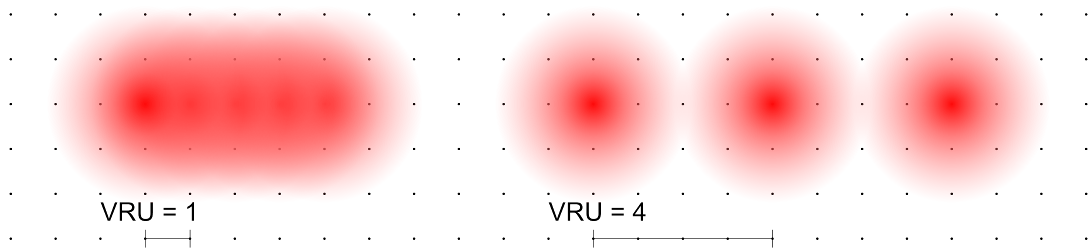

Figure 3.4: VRU for a spot size of 4nm. A small VRU (VRU = 1) leads to parts of the chip being exposed by a higher dose. A large VRU (VRU = 4) leads to areas that are unevenly exposed.

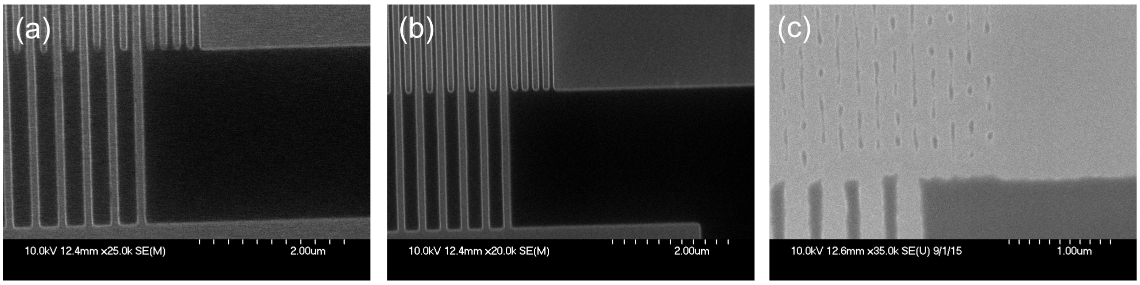

Figure 3.5: Examples of patterns under different doses. (a) The dose is too small; the ends of the nanowire have not fully developed, leading to smaller wire widths (100nm instead of 110nm). (b) In the range of a good dose. (c) The dose is too large, causing the negative of the pattern to spread across the bar regions intended for the nanowires.

Supplementary Nanowires

As can be seen in Figure 3.5(b), the fabrication pattern for the nanowire meander has extra lines in parallel to the working device. These will be etched into the final meander, but will not act as part of the final working detector. Their existence is to aid in fabrication as the edge of the device, the large rectangle to the side of the parallel nanowires, will produce a large dose during the fabrication process. This will cause the outermost nanowires to have a varying width compared to the inner nanowires. Adding unused parallel wires to the device edge reduces the effect of this extraneous dose.

The Proximity Effect

When exposing the pattern to the E-Beam, the edges of a shape will experience a smaller dose compared to the centre of the shape due to the number of exposed points surrounding it. Proximity Effect Correction (PEC) is a mathematical modification to the dose which increases the dose at the edge of all features to avoid this unwanted effect.

Development

The development process for ZEP is very temperature and time sensitive. In order to achieve the same results each time the process must be performed within a strict time and temperature window. In the recipe for the MoSi test structures (§3.1.7. Fabrication Process for MoSi Structures), the sample is placed in Oxylene at 23.3°C and agitated in the solution for 60s. A variation in the temperature by a degree, or variation in the time by a few seconds, can lead to an unwanted change in the size of the pattern mask.

3.1.5 Reactive Ion Etching

The nanowires are defined by Reactive Ion Etching (RIE) in which the film is placed in a vacuum chamber and bombarded with an ion plasma. This process combines both chemical and physical etching, which leads to high etch rates. The chemical aspect involves placing the sample within a chamber of ionised plasma. The plasma reacts with the film to form bonds that strip atoms from its surface. The physical aspect involves accelerating the plasma towards the film, which causes the ions to break atoms away from its surface. The etch performed is also anisotropic; that is to say the plasma's etch rate is higher when interacting with a horizontal lattice plane than a diagonal or vertical plane. This anisotropy can be optimised to achieve almost flat recesses in the film.

Etching performed in this Thesis involved a 10nm MoSi film in a CF_4 plasma (§3.1.7. Fabrication Process for MoSi Structures). The basic process of this etch[116] involves the reaction of F radicals to separate the Mo and Si atoms (Equation 3.3). The timing of the etch is estimated at 2m15s, but this process is monitored by an interferometer, which dictates the exact time. A sample etch interferometry graph is shown in Figure 3.6.

$$CF_4 \rightarrow CF_3 + F \tag{3.2}$$

$$MoSi_2 + 14F \rightarrow MoF_6 + 2SiF_4 \tag{3.3}$$

Film Redeposition

At the edges of the nanowire, bright parallel and non-uniform lines can be seen. This is an effect that occurs during the nanowire etch step, known colloquially as the 'Evil Crown'. As this is a negative process, material around the nanowire is removed, but so it the resist that defines the nanowire, albeit at a lower rate. The etched MoSi can redeposit onto the top and sides of the nanowire due to the sides of the resist being etched away and the anisotropic nature of the etch. The re-stacked material is minimal, but can have some effect on the transport properties of the nanowire. This processed is described in Figure 3.7(a) with an example SEM image shown in (b).

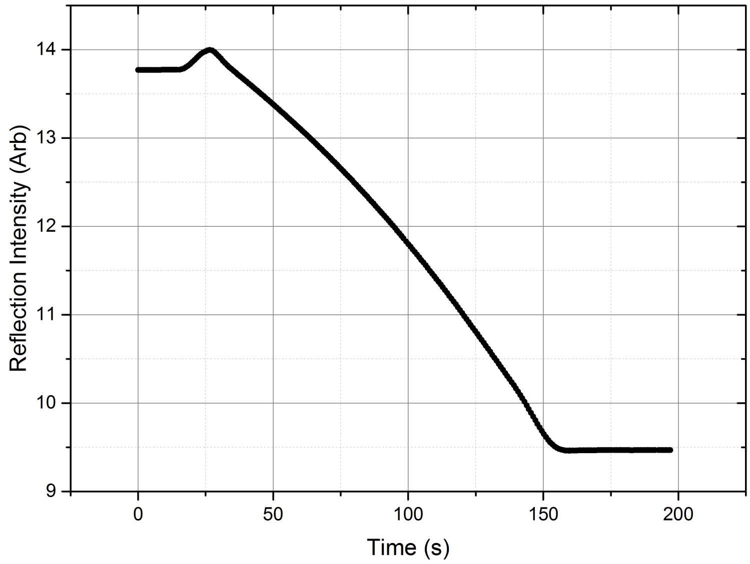

Figure 3.6: Example of Interferometry graph for MoSi film during a CF_4 etch. The initial jump in reflection intensity is an artefact of light reflection from the 5nm Si cap. The slope details the etch rate of the MoSi film. The graph levels off upon reaching the Si substrate.

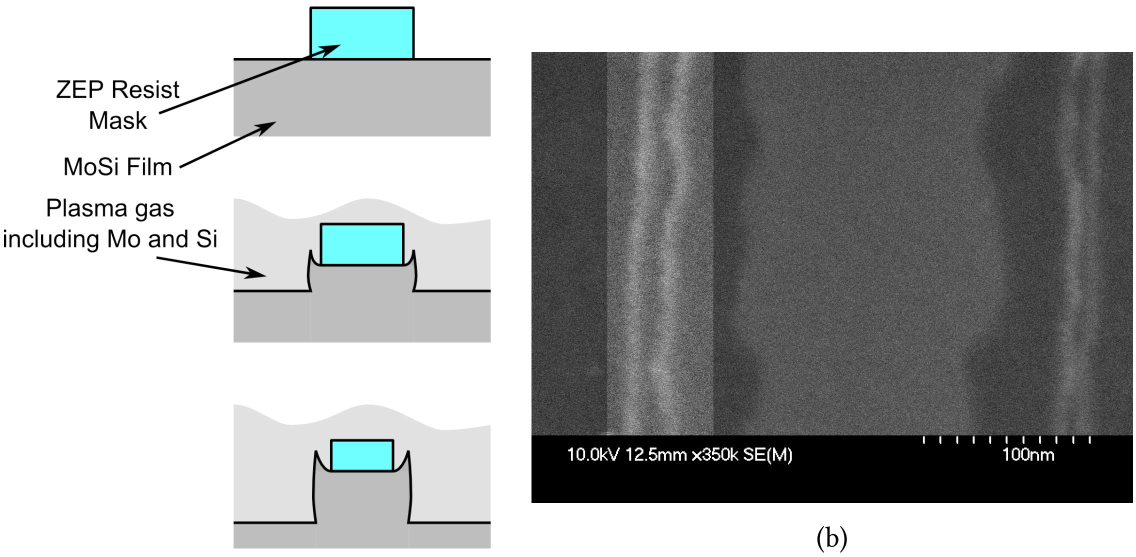

(a)

(b)

Figure 3.7: (a) A general depiction of the redeposition effect on a MoSi nanowire. (b) SEM image of a nanowire after etching with the effect of redeposition highlighted.

3.1.6 Fabrication Process for NbTiN Cavity Devices

The fabrication procedure for the NbTiN devices characterised in this Thesis is detailed in Figure 3.8 for supplied Delft University devices and Figure 3.9 for supplied NICT devices.

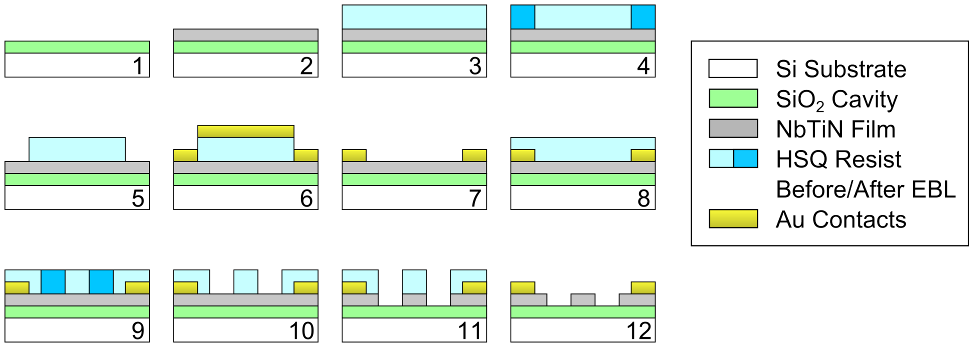

Figure 3.8: SNSPD fabrication procedure for devices similar to Delft NbTiN cavity devices[117]. 1. A Si substrate (white) is thermally oxidised to create a 225nm SiO_2 layer (green). 2. The 6nm superconducting film is deposited by reactive magnetron sputtering using a single $Nb_{0.7}Ti_{0.3}$ alloy target (Ggrey) in a N_2/Ar environment at room temperature. The first E-Beam step concerns depositing the Au contact pads. 3. Hydrogen Silsequioxane (HSQ) is spun onto the sample, reaching a thickness of a few 100nm and then baked. 4. EBL is performed to define the pattern of the Au contacts and Au markers in the resist (bBlue). 5. The chip is developed, stripping away the exposed resist. 6. 20nm Nb and 60nm Au (gold) is layered on the chip by vapour deposition. The Nb layer alleviates the lattice mismatch between Au and the Si substrate. 7. The resist is removed by soaking in Hydrofluoric Acid (HF). 8-10. The second E-Beam run is used to pattern the nanowire design for the etch process and involves the same processes as that in steps 3-5. This is a pattern negative, in which unwanted material in the film is removed, leaving behind the specified nanowires. 11. RIE removes the film unshielded by the resist using a plasma of SF_6 and O_2. 12. The undeveloped mask is removed with HF.

3.1.7 Fabrication Process for MoSi Structures

Figure 3.10 details the full fabrication process used to develop the amorphous MoSi devices characterised in §5. MoSi Devices. The 4-pin test structures were sputtered in an optimised process by Archan Banerjee in the JWNC and then fabricated by the author.

The 4-pin test structures were sputtered using an optimised recipe developed by Archan Banerjee [70]. The chip was co-sputtered onto a 298µm High Resistivity Substrate (HRS) using confocal Mo (99.99% purity; International Advanced Materials) and Si target (99.999% purity; Kurt J. Lesker Company Ltd) in a load-locked UHV chamber (base pressure $< 5 \times 10^{-9}$ Torr) in an Ar plasma. This produced a 10nm thick film of $Mo_{80}Si_{20}$, as confirmed by Electron Energy Loss Spectroscopy (EELS) measurements. A 5nm Si capping layer is also sputtered on top to protect the film from oxidation degradation; this does not affect the superconducting properties of the film and coincidently, slightly increases the optical absorption efficiency of the device for perpendicularly coupled light.

The hairpin devices were sputtered and optimised by Dr. David Bosworth and Zoe Barber

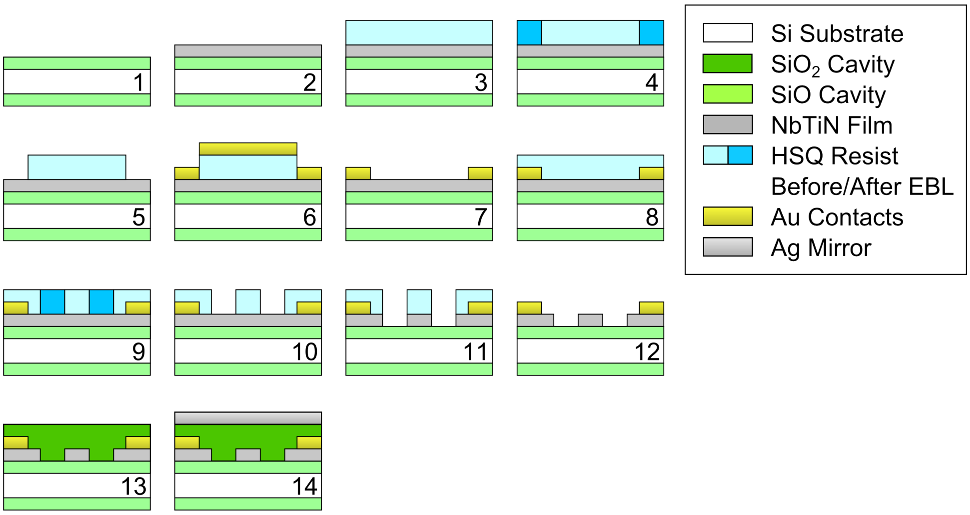

Figure 3.9: SNSPD fabrication procedure for devices similar to NICT NbTiN cavity devices[4]. 1. A Si substrate (white) is thermally oxidised on both sides to create a 270nm SiO_2 layer (green). The extra backside layer acts as an Anti-Reflection Coating (ARC) for the incident back coupled light. 2. The 5nm superconducting film is deposited by DC magnetron sputtering. 3. HSQ is spun onto the sample and the chip is baked, as above. 4. EBL is performed to define the pattern of the Au contacts and Au markers in the resist (blue). 5. The pattern is developed. 6. 20nm Nb and 60nm Au (gold) is layered on the chip by vapour deposition. 7. The resist is removed using HF. 8-10. The second E-Beam run is used to pattern the nanowire design for the etch process. 11. RIE removes the film unshielded by the resist using a plasma of CF_4[89]. 12. The undeveloped mask is removed with HF. 13. A 250nm SiO_2 spacer is deposited[118] on top the film (dark green), which acts as the second cavity. 14. A 100nm thick Ag mirror is sputtered on top of the cavity.

at Cambridge University[119]. 10nm $Mo_{83}Si_{17}$ were deposited using a single alloy target by DC magnetron sputtering onto a Si-on-Insulator (SoI) substrate along with a 5nm Si capping layer. The substrate consisted of a small band of 220nm Si (designated for the waveguide), a 2µm band of SiO_2 and a 600µm Si base. The device was then fabricated by Dr. Robert Kirkwood at the JWNC.

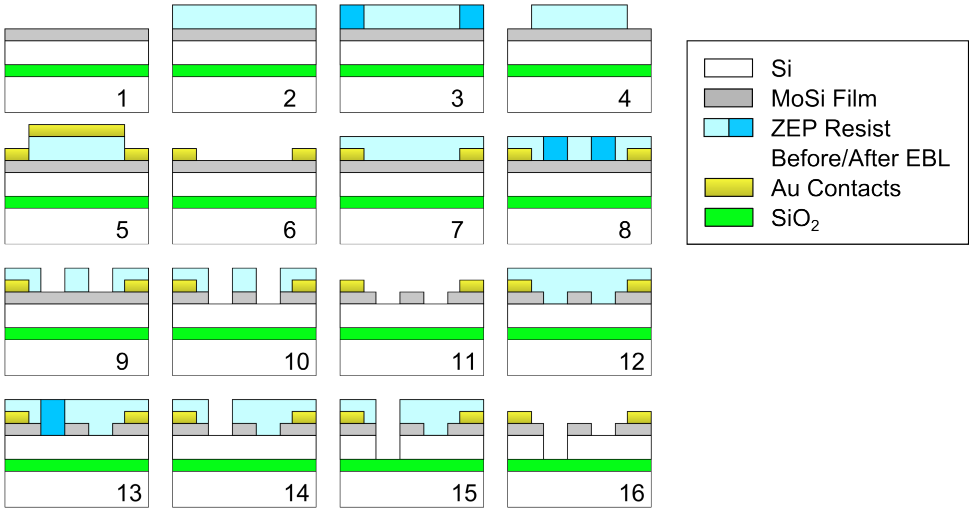

Figure 3.10: Lithography process for MoSi devices. 1. A Si substrate (white) is cleaned using Ar plasma and then MoSi (grey) is deposited through sputtering. The optimisation of the sputtering rate for a 10nm MoSi film was devised by Archan Banerjee. 2. The first E-Beam step concerns setting the Au contact pads. ZEP resist (50% Anisole) (cyan) is spun at 4000rpm for 60 seconds, reaching a thickness of 110nm. The chip is baked for 4 minutes at 180°C. The back of the substrate is cleaned with an acetone swab to ensure a flat base. The chip is submitted for E-Beam processing. 3. EBL is performed to define the pattern of the Au contacts and Au markers in the resist (blue). 4. The chip is agitated in Oxylene at 23.3°C for 60 seconds, stripping away the exposed resist. This stage is highly time and temperature dependent, a few seconds or degrees either side can lead to unwanted feature sizes. 5. 15nm Ti and 75nm Au (gold) is layered on the chip by vapour deposition. The Ti layer alleviates the lattice mismatch between Au and the Si substrate. 6. The resist is removed by soaking in solvent (1165-Stripper) overnight. The sample receives ultrasonic treatment to remove unwanted Au. This can take anywhere between 2-6 minutes, as directly observed. 7-9. The second E-Beam run is used to create the pattern for the nanowire etch process. The E-Beam run is performed in the same manner as steps 2-4, but the pattern is a design negative. 10. RIE removes the thin film unshielded by the resist using a CF_4 gas. The timing of the etch is estimated at 2m15s, but is altered based on the response of an in-situ interferometer. 11. The remaining resist is, again, soaked in solvent overnight and then given ultrasonic treatment. The process just described is used to develop the MoSi 4-pin test structures. Regarding the MoSi hairpin nanowires, an additional set of steps are needed to define the waveguide. These continue as follows: 12-14. A third E-Beam run is used to create the pattern for the waveguide etch process. 15. The waveguide is etched using an Inductively Coupled Plasma (ICP) RIE with $SiCl_4$ at a width of 500nm with a depth of 220nm - corresponding to single-mode 1550nm light. 16. The remaining resist is stripped and the chip is diced, leaving a device which is ready for testing. Two other test waveguides were also patterned 10µm either side of the hairpin as part of an optimisation process for later development of optical splitters.

3.1.8 Fabrication Errors

During optimisation of the fabrication process, many errors have to identified and mitigated. The following errors refer to Figure 3.11. (a) The dose used for the first EBL step was too low causing the smaller Au markers to lift from the sample. (b) For the etch pattern, two different size of E-Beam were required. A 45nm spot was used for the largest features on the chip, such as the wider sections of the coplanar waveguides. However, this beam is too small to pattern the smaller region of the coplanar waveguides, and can produce a reduced dose causing the features to obscure. A smaller beam of 4nm is required for these sections. (c) Slight stitching error caused by two contiguous main-fields that have been misaligned. This causes a lower dose in the gap between the main-fields and can have a significant effect if present at small sample features. To avoid this, main-fields are centred on the smallest or most vital components being processed. (d) The original fabrication procedure noted large amounts of resist residue after stripping. This was reduced through a longer strip time and longer ultrasonic treatment. (e) The sample development time was too large, causing an apparent glow around Au features. (f) Areas of the resist on the nanowire have not been completely removed during the final stages of processing. This should not have any significant effect on the electrical properties of the nanowires.

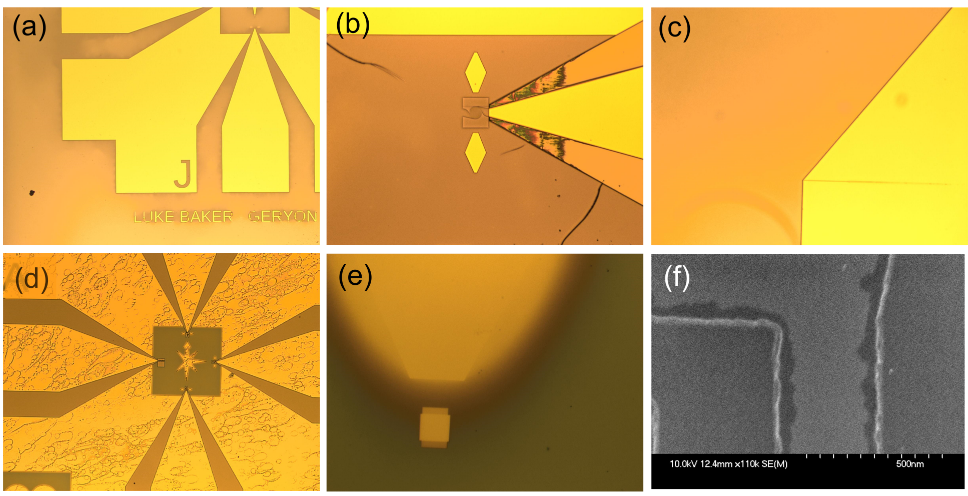

Figure 3.11: Notable errors during fabrication.

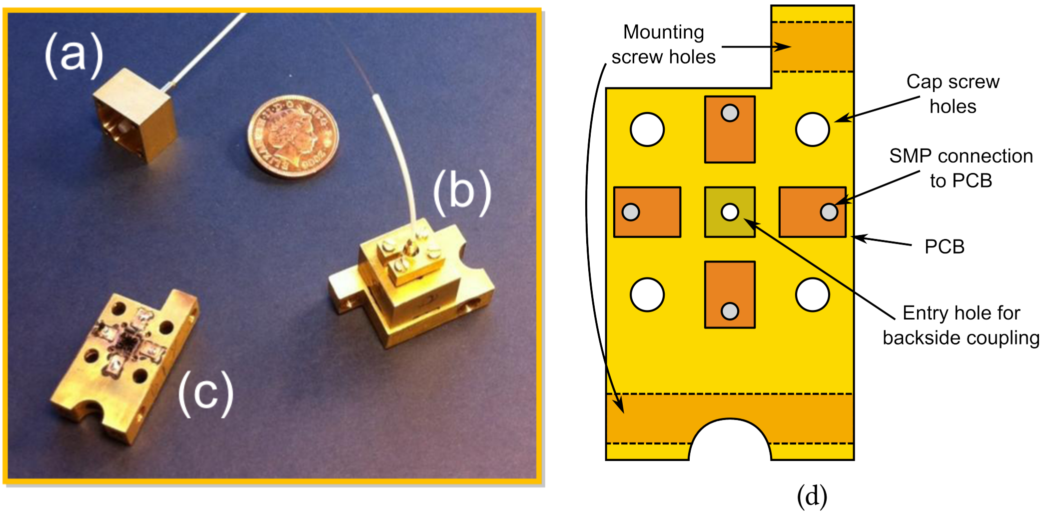

Figure 3.12: Standard device mounts. (a) Fibre coupled cap. (b) Shielded mount with coupled fibre. (c) Unshielded mount with chip in centre. Image courtesy of Dr. Alessandro Casaburi. (d) Labelled sample mount. The chip is attached to the centre of the mount and wire bonds are joined from the chip to the PCB board. Backside coupling can be achieved through the hole in the centre of the mount.

3.2 Device Mounting Methods

3.2.1 Electrical Coupling

Sample Mounts

Standard samples mounts can be seen in Figure 3.12 (d). These are Au coated copper blocks with SMP connections on the base. The pins of the SMP connections are soldered to small PCBs on the top of the chip, which are suitable for wirebonding. The chip is attached to the mount either through Be_2Cu clamps screwed into the PCB or a thermal adhesive that functions at cryogenic temperatures, such as nitrocellulose lacquer or silver paste. These are mountable to each of the fridges and can be attached to the microscope housing in the Rankinator and Kelvinator. Crucibles for these mounts (a) can also be attached to fibre couple the devices at room temperature (b). Two new sample mounts have recently been designed by Dr. Jian Li for the Rankinator to allow for in-plane and perpendicular coupling of hairpin waveguides Figure 3.13. The process for cleaving the chip during fabrication is still being optimised.

Wirebonding

An electrical connection to the sample is achieved using an ultrasonic wedge bonder (Kulicke & Soffa Model 4123). The gold contacts of the sample are wire-bonded to the RF board and grounded through the sample mount (Figure 3.14). The bonder uses a wedged tip, threaded with Al wire ($\phi \sim 100\mu m$). The tip is brought into contact with the

(a) (b)

Figure 3.13: Sample mounts for (a) horizontal and (b) vertical coupling. An SMP connection is made in the back of the holder, where its pin is soldered to the top of the PCB. Electrical connections are achieved by wirebonding from the PCB directly onto the chip.

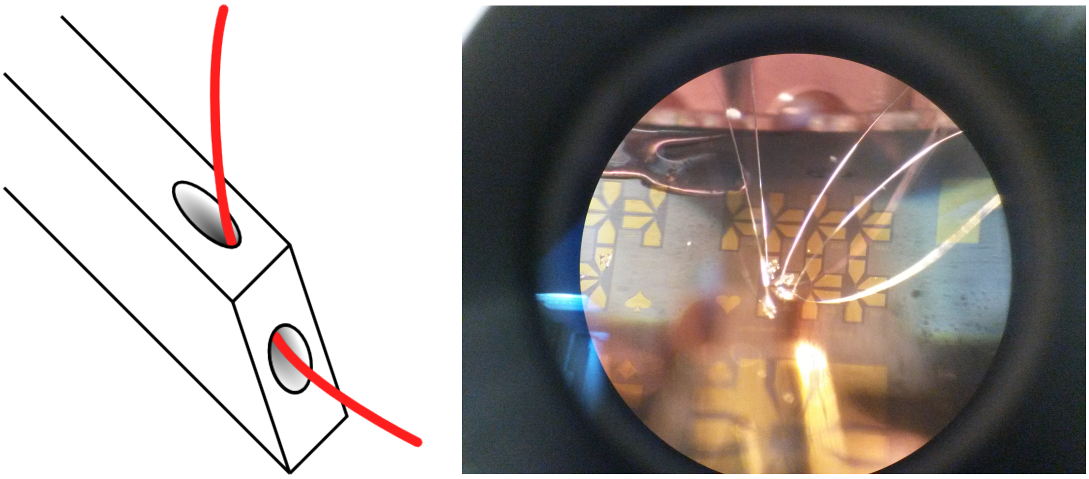

(a) (b)

Figure 3.14: (a) Wirebonder tip with aluminium wire (Red). When the tip is compressed it receives ultrasonic vibrations that weld the wire to the contact material. (b) An example chip with several bonds.

sample and vibrated at ultrasonic frequencies, welding the Al wire to the surface. This process is performed twice for each end of the loop and then repeated for subsequent bonds. The wired connections produce arcs (or loops) over the chip which, for most experiments, have no restriction. For device microscope characterisation in both the Rankinator and Kelvinator, the arc height cannot be higher than 2mm or the wire will contact the microscope fibre tube, creating an unwanted ground and greatly decreasing the SNR of the signal through the wire.

3.2.2 Fibre Coupling Methods

Working in the single photon regime requires high coupling efficiencies and low heat loads. This presents a difficulty in aligning an optical fibre onto a device, either at room temperature, that retains its position, or in situ, that induces minimal heat load. One method involves in situ motors for external control of fibre movement. Accurate though they are, these motors create large heat loads, which smaller cryostats cannot handle. To achieve high coupling efficiency in smaller cryostats the chip and fibre should be aligned manually at room temperature. The alignment must also hold across a wide temperature range and over several cooldowns. Room temperature, fibre coupling methods are discussed below. Low temperature motors are discussed in §3.3.5. Attocube Piezo-Electric Positioners.

Fibre-Alignment Rig

This research used a fibre alignment setup designed by Michael Haertig Figure 3.15, a masters student at Heriot-Watt in 2008. It involves manually positioning a fibre ferrule over the device region (Corning SMF 28, ϕ = 9µm) and can be used for both front and backside coupled detectors. The ferrule is tipped with a GRIN Lens that focuses the output 1550nm light to spot with a FWHM 8-10µm at a distance of 20µm. This is split into two steps, Z-axis positioning and planar positioning.

Z-Axis Positioning

First, the fibre is aligned in the Z-axis. This is achieved using Optical Coherence Tomography (OCT), shown in Figure 3.16. This process is a form of interferometry; a beam of white light with a low coherence is split, one path leads to the sample and one to a reference mirror. The two light beams reflect and interfere. The measured beam strength is related to the relative distance of the sample to the reference mirror. In the referenced setup there is a slight variation in that the reflector is actually the end of the fibre ferrule, which acts as a weak mirror. An example of the interference pattern can be seen in Figure 3.17. Analysing the frequency spectrum of the response returns a value of the separation distance. Shims, which are thin 10-200µm washers, are used to alter the distance of the fibre until it is positioned within the range of 25-50µm. During cooldown, the sample mount will partially shrink, moving the fibre and chip closer together. Due to this, the fibre, at room temperature, must be more then 25µm from the chip, to ensure it does not contact or crack it. This should achieve a direct coupling efficiency above 80% for a Gaussian beam at 40µm distance[51].

Planar Position

To achieve planar positioning, the loose cap is held on a moveable platform underneath the fixed sample mount (as in Figure 3.16(b)). The crucible holds the fibre ferrule and can be moved independently of the sample. In the camera setup in Figure 3.15, an infrared camera records the position of the sample with the position of the spot from the fibre

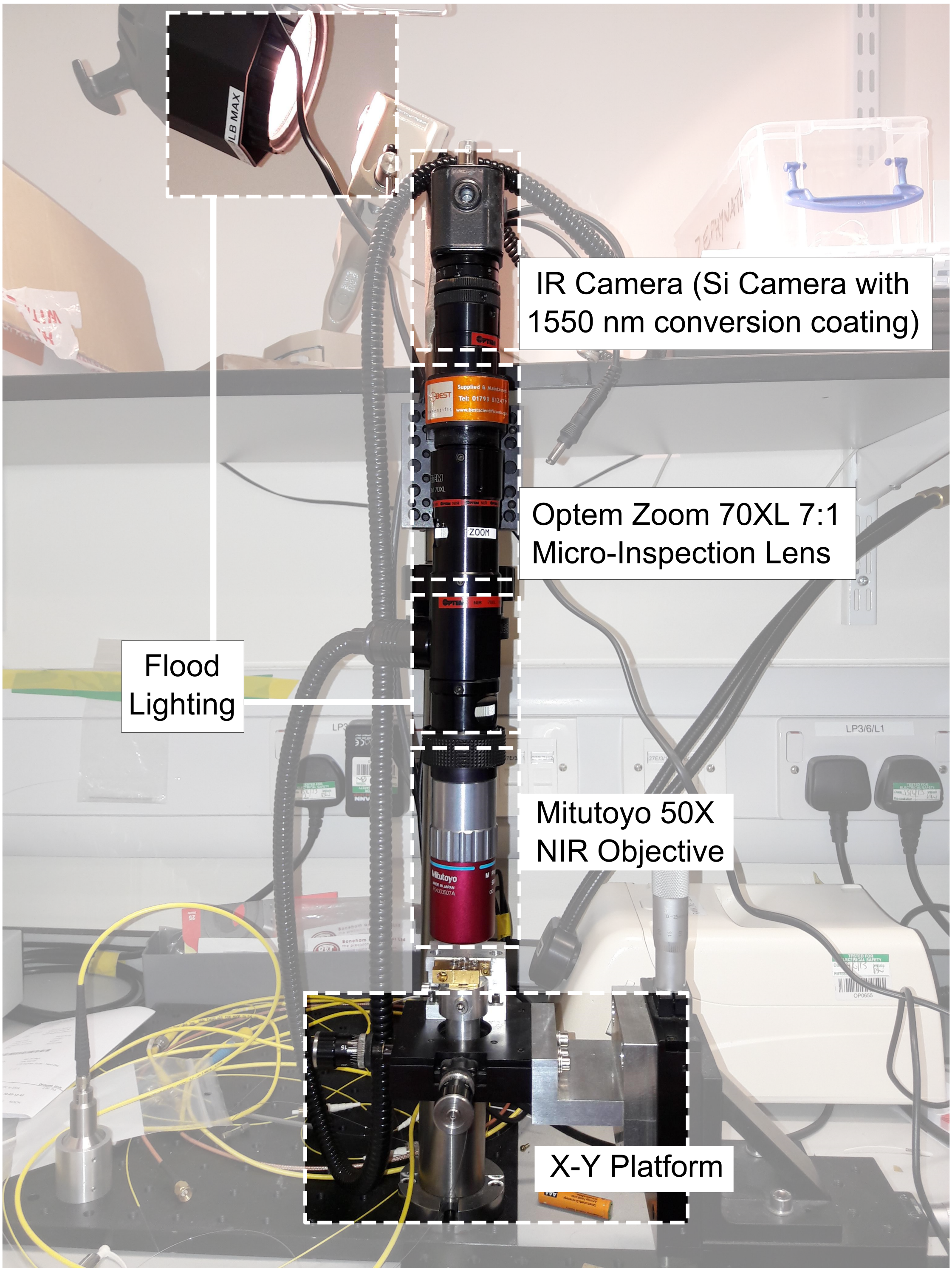

Figure 3.15: Fibre alignment camera setup. The sample sits at the base of the microscope. The fibre sits in a crucible pointing up into the sample on the moveable X-Y platform. White light is flooded onto the chip and is partially reflected by the sample into the Si CCD camera. The camera has a fluorescent coating that converts the incoming 1550 nm light to a shorter wavelength. The X-Y stage allows for fine, manual, planar positioning of the fibre to the sample. Multiple attempts are needed to align the fibre as the act of screwing the crucible into place causes the fibre to move.

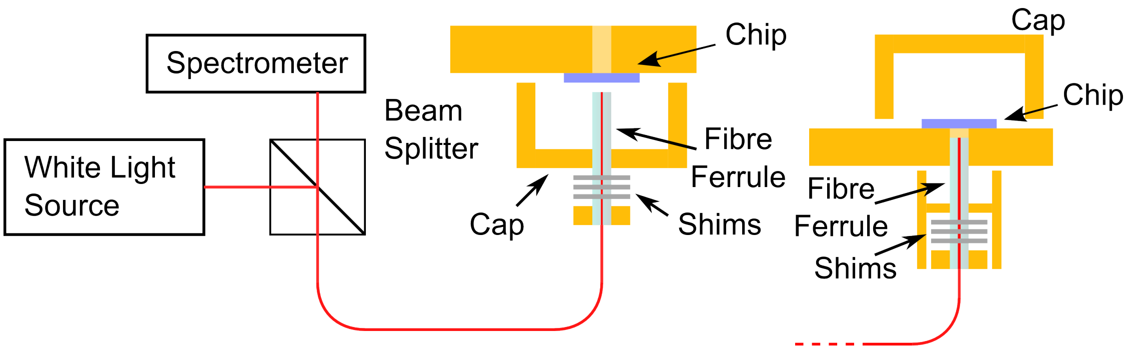

(a) (b)

Figure 3.16: Diagram of OCT measurement of sample distance. A white light source outputs a spectrum of light. The light is split, but only the portion travelling to the sample is used. Part of the light reflects off of the end of the fibre ferrule and part reflects off the chip. The two reflected beams recombine in the fibre with a phase difference dependent on the wavelength of the light. If the phase difference is zero, the corresponding wavelength is proportional to the separation distance. These images show how the fibre is positioned for both (a) front side and (b) backside coupling. The vertical dimensions have been stretched for clarity.

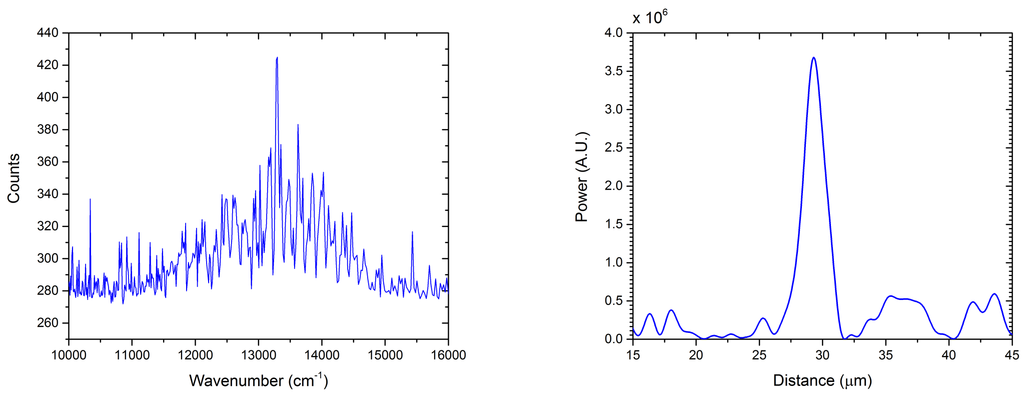

Figure 3.17: (a) Results of an OCT measurement as wavenumbers. (b) A Fourier transform of the data, after interpolation, returns the relative distance between the ferrule and the chip. This ferrule is approximately 30µm from the sample.

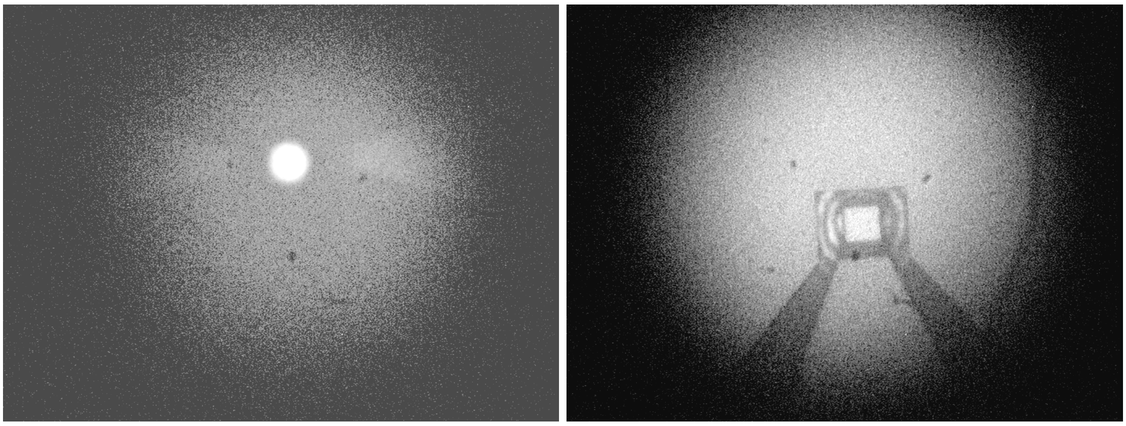

(a) (b)

Figure 3.18: Example of spot image from fibre ferrule. (a) A Delft device. The nanowires are not visible under NIR light; two markers point to where the centre of the laser spot should be positioned. (b) An NICT device. By blocking the centre laser spot, the laser's Airy discs become visible. Here, the left portion of the circles are brighter than the right, indicating the fibre is not completely aligned onto the device. A small misalignment like this can reduce the device efficiency by around 30%. Contrast has been increased for clarity.

ferrule. The ferrule is repositioned until the laser shines beneath the device. Once the fibre is in place, the crucible is screwed onto the sample mount. This method can take several hours as the act of tightening the screws causes the fibre to shift position slightly. Examples of the infrared images from the camera are shown in Figure 3.18. To aid in positioning the laser, gold markers can be used to home in on the device or, in some cases, a backing square is used to block the laser's centre spot. By blocking this spot, the laser's Airy disc becomes visible and are then used to align the spot.

3.3 Rankinator Design

Case for a Low Temperature Environment

It is possible that room temperature, or high temperature superconductors will become the future components for Quantum Computers (QCs). However, assuming superconducting technology continues to be the main focus of QCs, experiments will need to be performed at temperatures <10K. Fortunately, there are additional benefits to this. SNSPD efficiency is highly dependent on temperature and lower operation temperatures leads to higher SDE, which is due to several factors. First, the power density of BBR diminishes with lower temperatures. From 5K to 0.4K, BBR shrinks by five orders of magnitude and this lowers the extrinsic DCR of the device. Second, a lower temperature reduces the internal DCR of the device due to the lower energy of intrinsic phonon vibrations. And third, the critical current density of a device is inversely proportional to temperature; the lower the operational temperature the higher the device can be biased and thus the higher its SDE.

Methods for Achieving Low Temperature

Low temperature environments can be achieved using wet or dry cryostats. Wet systems use liquid coolants; commonly liquid N (to reach 77K) or liquid He (To reach 4.2K). A wet setup uses an enclosed chamber surrounded by the coolant which reaches equilibrium after 1-2 hours. These systems can run indefinitely and, due to a lack of mechanical parts, can achieve extremely low noise levels. However, they require constant refilling of liquid N/He, which can be expensive.

Closed cycle coolers reverse the locations of the chamber and the coolant. Here the coolant is enclosed within a loop or vertical container. Liquid ^{3}He can achieve temperatures below 400mK, with the aid of liquid ^{4}He. A dilution fridge is a closed cycle cooler that uses a mixture of ^{4}He and ^{3}He. Below 800mK, part of the ^{3}He becomes separated from the ^{4}He/^{3}He mixture. The separated ^{3}He is then syphoned into its own partition with the sample attached to the outside. This setup achieves temperatures of 1-100mK

Common dry setups make use of a Gifford-McMahon (GM) or Pulse Tube (PT) cryostat that can reach partially oscillating temperatures of 2.5-5.0K. These systems remove heat by oscillating compressed He gas. The exchanged heat is then transferred through a cooling water system or air cooled. GM coolers use a mechanical displacer which produces, at the 2nd stage, vibrations on the order of 20µm parallel to the tube and $\sim$5µm perpendicularly. By comparison, a remote motor PT uses an external rotary displacer (more detail in §3.3.3. Pulse Tube Operation below), which causes slightly lower vibrations of 4-7µm and $\sim$2µm parallel and perpendicularly, respectively[120]. Both cryostats have an advantage in requiring minimal manual monitoring and can maintain stable temperatures at high heat load for longer time periods at far cheaper running costs.

Adiabatic refrigeration[121] uses the magnetic properties of certain paramagnetic materials to reduce their internal temperatures. By applying a magnetic field, the paramagnetic aligns with it, expelling the heat needed for the alignment to occur. After the expulsion of heat, the field is switched off, returning the paramagnet to a disordered state, which lowers its temperature. This technique can achieve temperatures of 1-100mK. However, this does require a paramagnetic material and, even with such a material, the applied magnetic field would cause heightened dark counts due to flux pinning and reduce the maximum J_C of the device. This makes adiabatic refrigeration an unviable method for SNSPD characterisation.

3.3.1 Rankinator Overview

The Rankinator, shown in Figure 3.19, is a combination two-stage PT, holding a 50K and 3K stage and two-stage ^{4}He/^{3}He sorption pump. The cryostat can achieve low noise testing with the aid of four shields; a room temperature outer shield, a 50K shield, a 3K shield and a Mu-metal magnetic shield, which blocks out external, low frequency magnetic fields, reducing the effects of flux pinning described in §2.1.2. Flux Penetration. The cryostat is capable of 0.35K device characterisation and mapping using a 1550nm confocal microscope attached to nanometre resolution Attocube stepper and scanner motors.

To achieve base temperature device characterisation, the cryostat uses 4 coaxial cables connected from the outer shielding to the 4K stage and Be_2Cu wiring (which has a low specific heat capacity) from the 4K to 0.35K stage. O-free Cu is used when navigating the coax cables at 0.35K due to its higher conduction properties than regular Cu coaxes. An RF line can be be fitted for measurements of single-TM multiplexing detectors. A hermetically sealed fibre feedthrough allows 16 optical fibres into the fridge consisting of 8 single-mode fibres for 1550nm optics (1260-1650nm, SMF-28-100) and 8 multimode fibres for $\sim$900nm optics (400-2400nm, FG-050-LGA).

3.3.2 Vacuum & Cryovacuum

Achieving cryogenic temperatures <77K in large cryostats requires vacuum technology[122] due to the condensation of molecules in the atmosphere on the apparatus. The cryostat is first vacuum pumped to a high vacuum (1×10^{-5} mBar or 7.5×10^{-6} Torr). At such a high vacuum the chamber enters molecular gas flow in which gas molecules no longer collide with each other. The cryostat normally takes 1.5 hours to vacuum pump, but is dependent on how long the fridge has been unused as room temperature. When sitting idle, the metal components of the fridge absorb O_2 and N_2, which will desorb during pumping, known as outgassing.

When operating the PT, once it reaches 100K, it begins to act as a cryopump in which the remaining molecules will condense onto the system over time. This both reduces the internal pressure and maintains a base vacuum pressure. This is required to counteract the natural leak rate of He into the fridge. The Rankinator setup uses a roughing pump (Adixen ACP15 Roots) to achieve molecular flow, where it then automatically switches to a turbo pump (Adixen ATP80).

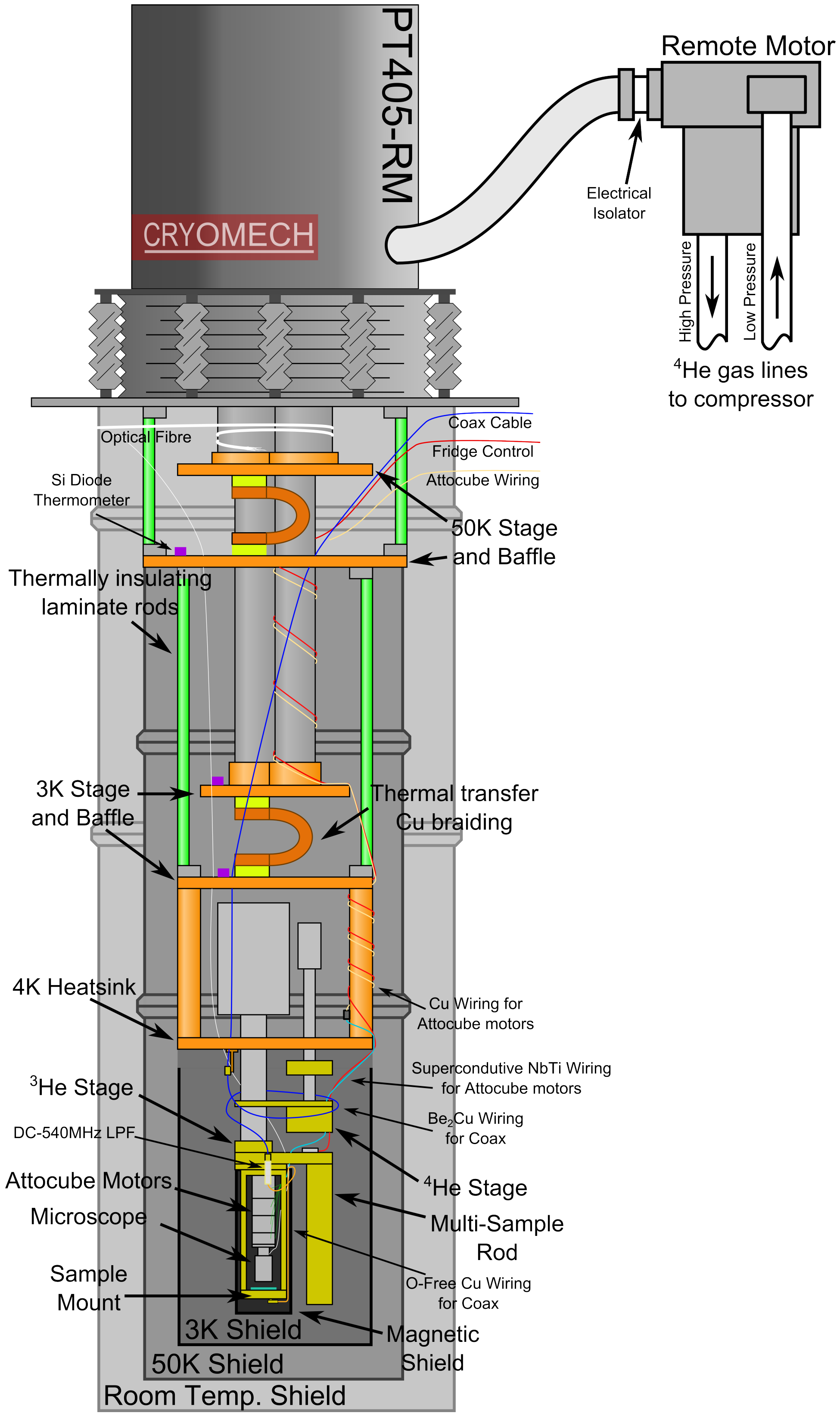

Figure 3.19: Overview of the Rankinator cross-section. The PT has two stages at 50K and 3K. Each stage is thermally connected to a baffle using Cu braids, whilst also being mechanically damped using the thermally insulating laminate rods. The ^{3}He sorption pump is attached to the 3K baffle. Silver tape is used to cover the holes at the top of the 3K shield when closing up.

3.3.3 Pulse Tube Operation

The Rankinator is cooled by a pulse tube cooler (Cryomech PT405-RM), which provides 500mW cooling power at 4K with low vibration due to the remote motor and bellows. A PT consists of ^{4}He gas in a closed tube that oscillates in pressure. At the sample stage, the gas pressure is low; heat is removed from the stage by transferring it to the He gas. At the compressor, the gas pressure is high and heat is removed from the gas through a network of cooling pipes, allowing regions of low pressure to stay cold. This creates vibrations at the stage of roughly 4-7μm parallel to the pulse tube and ∼2μm perpendicularly[120]. The basic process of PT operation[123, 124] is described in Figure 3.20. There are a few variations to this setup for the operation of the PT405-RM, which are described in detail in Figure 3.21 [125, 126].

The excess heat from the PT is exchanged through a Cryomech compressor (CP2870), which itself is cooled by a local cooling water loop. The local loop is further cooled by the building's maintenance loop, which itself is cooled by an outdoor air-cooled compressor. The Cryostat compressor monitors He, water and oil flow. These temperatures oscillate by ±1% over an hour, as shown in Figure 3.22.

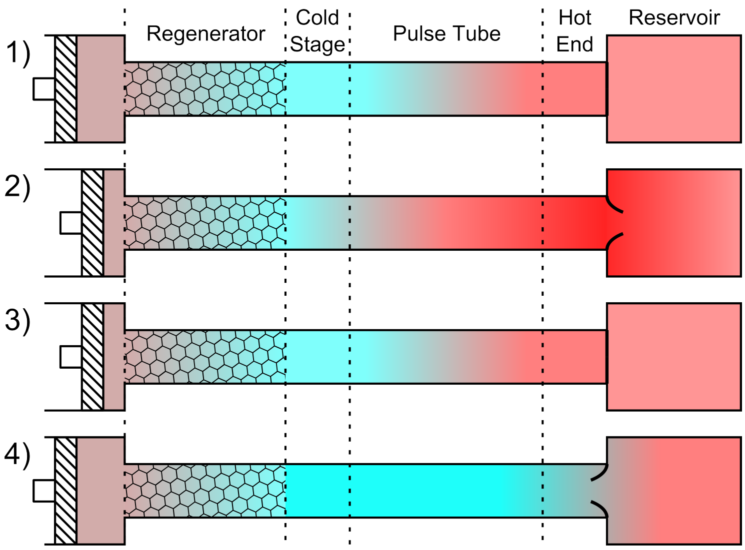

Figure 3.20: The PT can be imagined as a horizontal tube of gas connected to a piston which oscillates the pressure of the system. The regenerator cools the gas as it flows down the tube, absorbing the heat. 1) The system is as rest and pressure equalised. 2) The piston compresses the gas. The gas pressure increases to a state higher than the reservoir. Gas from the hot end of the pulse tube moves through the orifice into the reservoir. 3) A short time later, the pressure becomes equalised and the orifice closes. 4) The piston moves back, expanding the gas. The flow of gas moves from the reservoir through the hot end. Low pressure gas in the pulse tube moves towards the cold end. The cold, low pressure gas moves through the cold stage, picking up heat from the objects attached to the stage. 1) The pressure equalises and the cycle is repeated.

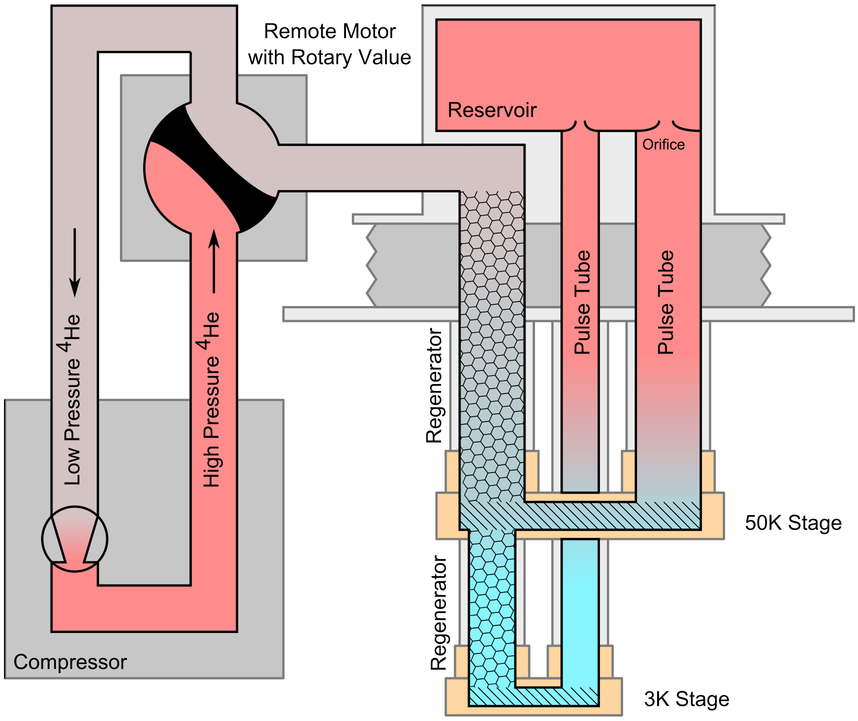

Figure 3.21: A schematic of the PT (PT405-RM) used in the Rankinator. There are two pulse tubes joined to a single reservoir. The gas oscillation is performed by a rotary valve inside the remote motor, which sends and extracts low and high pressure ^{4}He gas respectively. The compressor package[125] uses an oil-based lubricant to compress the pure low-pressure He that returns from the cold head. The heat of compression is removed via a heat exchanger and the oil from the compression process is removed in a series of oil separators and filters, which are themselves water cooled. The compressed He is then fed to the cold head.

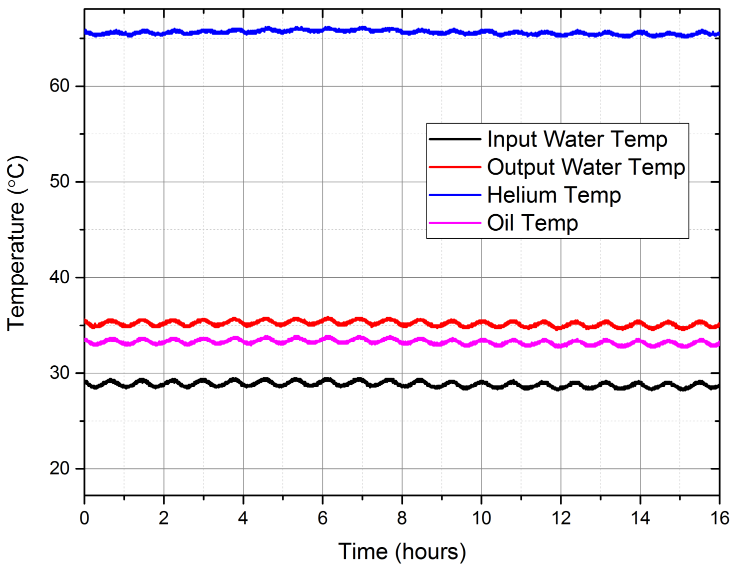

Figure 3.22: Compressor component temperatures over time during PT usage. The temperatures oscillate over a period of ~47mins.

3.3.4 Sorption Pump Operation

A diagram of the sorption setup can be seen in Figure 3.23 including the rough placements of the pump heaters and heat switches. The (^{3}He/^{4}He) sorption pumps[127, 128] are two, similar, closed cycle coolers that consist of an absorptive, activated carbon (charcoal) connect via a long tube to a still for collecting the liquid (^{3}He/^{4}He). The charcoal has a large surface area of varyingly sized holes. Around 5/6K and below, the charcoal absorbs the enclosed ^{3}He/^{4}He gas. Around 16/19K and above the gas is expelled into the tubes. The temperature of the charcoal is controlled by pump heaters; these are two 300Ω/400Ωresistors acting as a heater for the ^{3}He/^{4}He charcoal in each cooler. The pump heaters are normally biased to a temperature of 40-45K to ensure a majority of the He gas is desorbed.

The two sorption pumps are thermally isolated from the rest of the fridge to ensure it stays cold as long as possible. The pump heaters require quick heat dissipation after desorbing the required amount of (^{3}He/^{4}He) gas. On its own, due to its isolation, this would take a several hours; instead the heat load is dissipated by the aid of Active Gas-Gap Heat Switch (AGHS) attached to each sorption pump. The heat switches are small sorption pumps with their own charcoal, ^{3}He gas and 10kΩ pump heaters. When on, the AGHS dispels He and allows the flow of heat between the isolated sorption pump and the rest of the fridge. When off, the He is reabsorbed creating a vacuum and barring any thermal transfer (Figure 3.23 inset). The sorption pump has an unloaded cycle time of ten hours, but in its current setup the additional heat load from the Attocube wires and coax cables reduces this to just under 4 hours.

The detailed operation of the sorption pumps is described in Figure 3.24, which shows the temperature of each element over time. At a glance, this process involves using liquid ^{4}He to liquefy ^{3}He. The charcoal has a double purpose in both releasing the liquid He contents and absorbing any remaining He gas to reduce the vapour pressure on the liquid, lowering its temperature further. The sorption pump has an unloaded cycle time of 10 hours, but in its current setup the additional heat load from the Attocube wires and coax cables reduces this to just under 4 hours.

3.3.5 Attocube Piezo-Electric Positioners

The Attocube motors are a set of high voltage piezoelectric micron to nanometre range positioners. They make use of an impulse drive that moves the motor through both static friction and rapid displacement. The motors are used to precisely position an attached

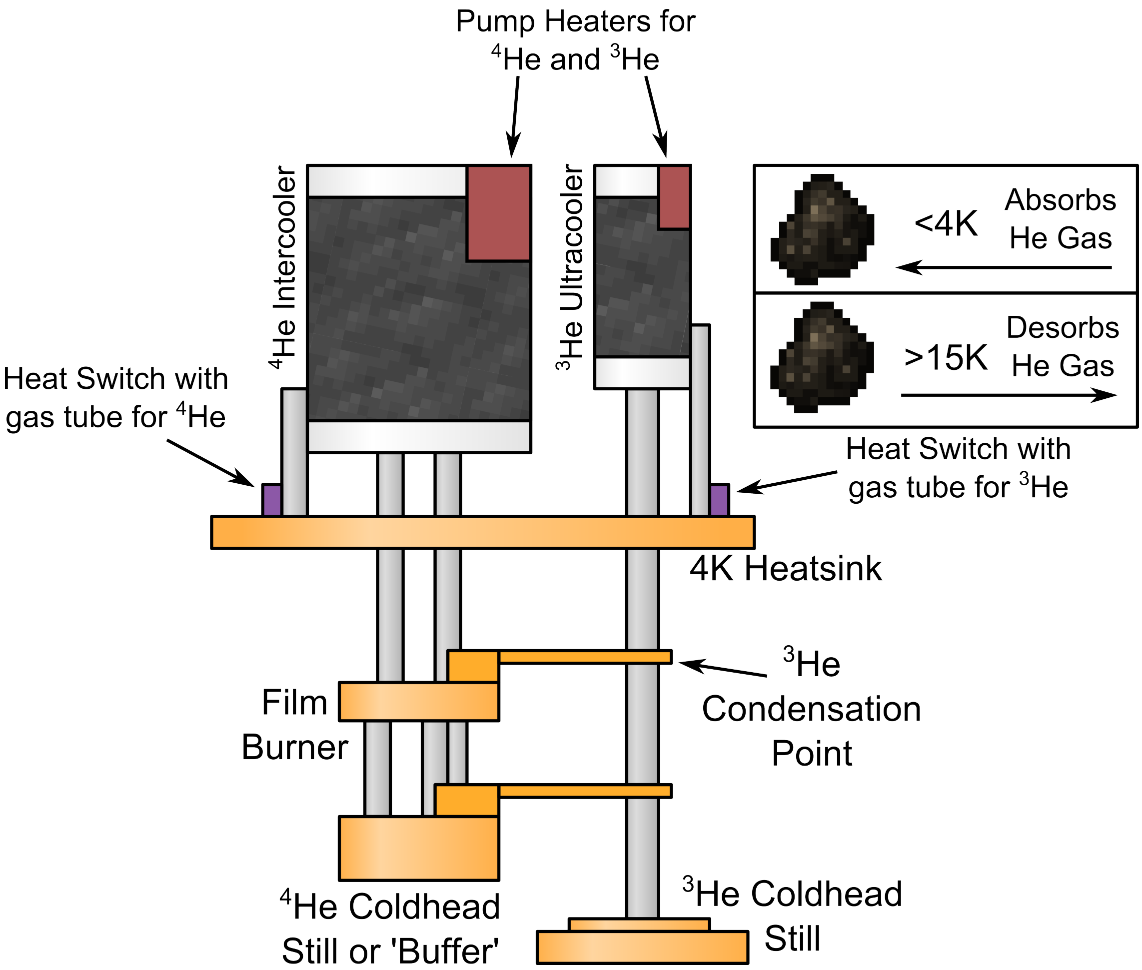

Figure 3.23: The coolers are placed vertically (with a freedom of 10°). The activated carbon (charcoal) absorbs the He gas <4K and desorbs the gas >15K. The sorption pump has two sample heads; a ^{4}He coldhead 'Buffer' and a ^{3}He coldhead still. The pump heaters heat the sorption pumps to 40-45K to allow the gas to desorb into the pipe. The heat switches, when turned on, dissipate the heat onto the 4K heatsink.

microscope over high light-sensitive regions of the device and create large reflection maps, to view device features, or response maps, to measure its sensitivity to an influx of light. The Attocube stack in the Rankinator consists of a Z-axis stepper motor (ANPz101-A4-278), two X-axis stepper motors perpendicular to each other (ANPx101-AA-528) and an XY-scanner motor for finer planar positioning (ANSxy100-90-499). The planar motion of the scanner and steppers are orientated in the same direction to make stepper and scanner map comparison simpler.

Stepper Motors and Z-Axis Positioning

The Stepper motors use static friction to pull the stepper platform along a straight path. As shown in Figure 3.26, the piezo expands relatively slowly and static friction acts to drive the clamped table along with it. The piezo can then contract quickly, sliding beneath the table, but leaving the table in place. This process is repeated to discretely step

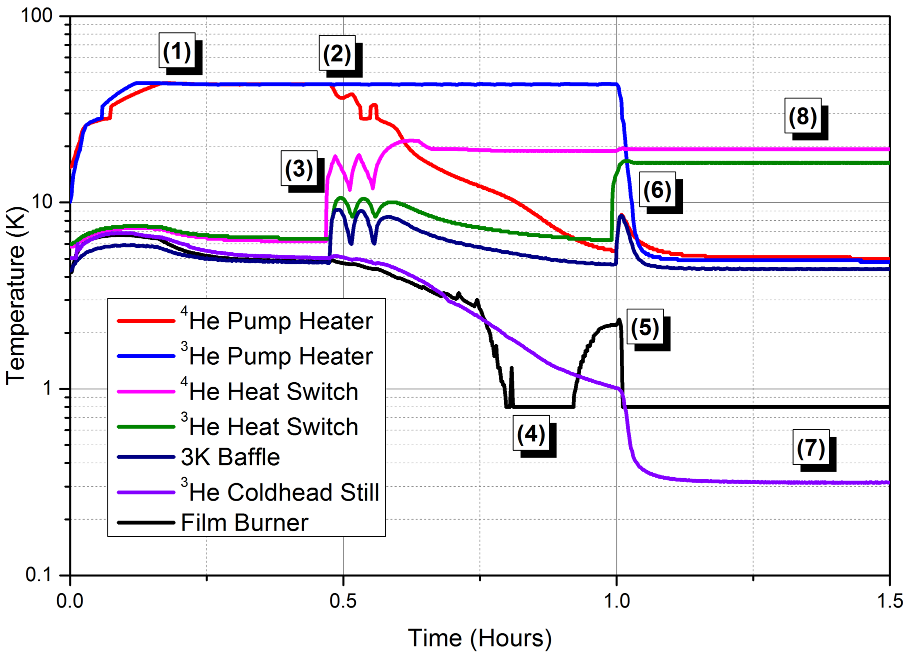

Figure 3.24: During the initial cooldown from room temperature, as the sorption pump dips below 40K, both pump heaters are current biased at a temperature of 40-45K, which causes the charcoal to desorb its stored(^{3}He/^{4}He). This speeds up the cooldown process of the isolated sorption pumps. Once at base temperature, the sorption pump can begin operation. Normally, the pump heaters are left on to keep the isolated sorption pumps ∼5K. If they are not left on continuously, the sorption pumps will rise to 12K. In the rare case the pump heaters have not been on continuously, as in this graph, the first step **(1)** is to current bias them around 40-45K. This desorbs the ^{4}He/^{3}H3 gas from the charcoal. The ^{4}He gas begins condensing inside the pipe, causing the liquid to drip down into the ^{4}He coldhead still or 'buffer' stage. After about 0.5-1.5 hours **(2)** the ^{4}He pump heater is turned off and the ^{4}He heat switch is turned on dissipating the heat from the buffer stage. **(3)** This step requires a jagged on and off routine as the process of turning on the ^{4}He heat switch has the unwanted effect of heating up other elements of the fridge. This unwanted heating is counteracted by the very liquefying of the ^{4}He. As the pump heater cools below 6K, the charcoal begins absorbing the remaining ^{4}He gas. The increased vacuum in the tube reduces the vapour pressure on the liquid ^{4}He causing its temperature to decrease to ∼0.9K. Once the fridge is stable, the buffer and film burner will cool to below 0.8K **(4)** (The actual temperature is lower, but the film burner thermometer is not accurate below 0.8K). The film burner thermally contacts the ^{3}He pipe, condensing the ^{3}He gas inside. In doing so, the liquid ^{4}He in the buffer stage begins evaporating. The technique here is to use as much ^{4}He to liquefy the ^{3}He as possible. Once the film burner begins warming (or the ^{3}He reaches below 1K) **(5)** the ^{3}He pump heater is turned off and the ^{3}He heat switch is turned on **(6)** allowing the heat to dissipate. As the pump heater cools to ∼5K, the charcoal begins absorbing the remaining ^{3}He gas, reducing the vapour pressure on the ^{3}He liquid and allowing the still to reach 0.4K or lower **(7)**. The sorption pumps have now reached base temperature, which will last from 3-10 hours depending on heat load. During this time, both heat switches are kept on **(8)** in order to dissipate any heat from the sorption pumps away from the stills.

(a)

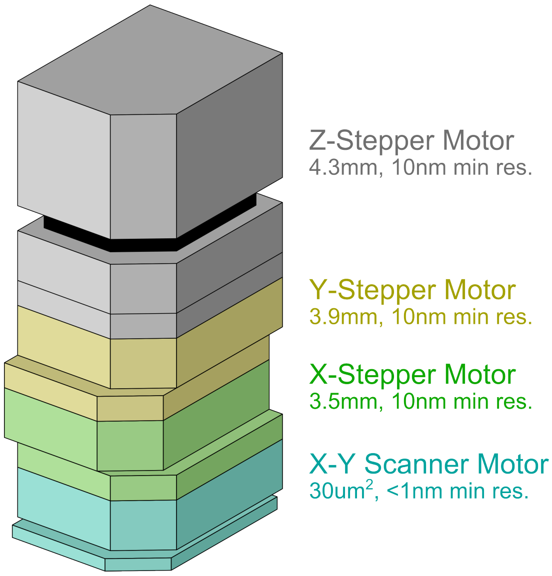

(b)

Figure 3.25: The Attocube stack (a) and as labelled (b). The stack from top to base consists of the three piezoelectric stepper motors for Z, Y and X movement, then a set of piezoelectric scanning motors that move in both the X and Y direction. The full movement range of the steppers is partially smaller than the expected range of 5mm. This could be due to bunched wiring around the stack or the weight of the microscope attached to it.

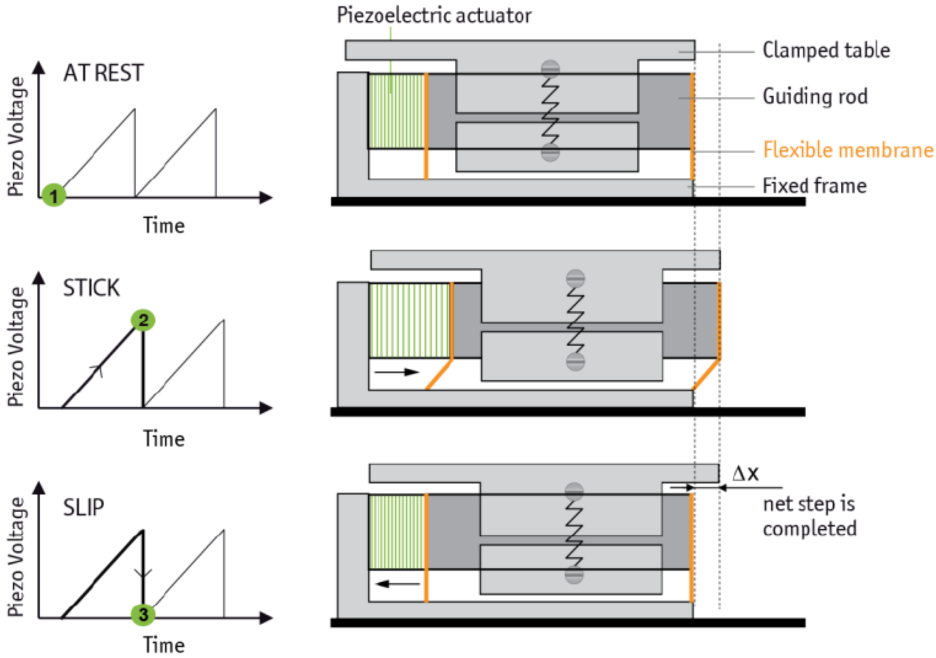

Figure 3.26: The stepper begins at rest. A relatively slow rising Voltage is applied to the piezo, moving the clamped table due to static friction. The piezo voltage is cut-off, relaxing the piezo, which slips under the clamped table, but keeps the table in its new position.

the clamped table along one axis. The stepper manual claims they can achieve a minimum step size of 0.8μm at cryogenic temperatures. In practise this is slightly larger at 2μm, possibly due to the weight of the setup. Mostly, this is not an issue as the scanners are capable of the necessary high resolution maps of the device and the large resolution maps from the steppers are adequate in locating the device on the chip.

The stepper motors produce a huge heat load that can reduce the cycle time of the fridge by up to 90%. This heat load occurs from two factors; the alternating voltage applied to the piezos and the resistive readout of the stepper's position. When below 0.4K, the steppers are only used in short bursts to coarsely position the microscope before starting a scanning map.

Scanner Motors and Planar Positioning

The Scanner motors move by applying DC voltages to their piezos, expanding the element. The piezo's are directly attached to the table, which moves as they do. The scan range is heavily dependent on temperature. To calibrate for this effect a reflection map was performed on a high contrast chequerboard sample made of $5\times5\mu m^2$ Au squares (using the microscope setup discussed below, §3.3.6. Microscope Setup) at 5K and 0.33K. The results of the maps are shown in Figure 3.27. There is an asymmetry in perpendicu-

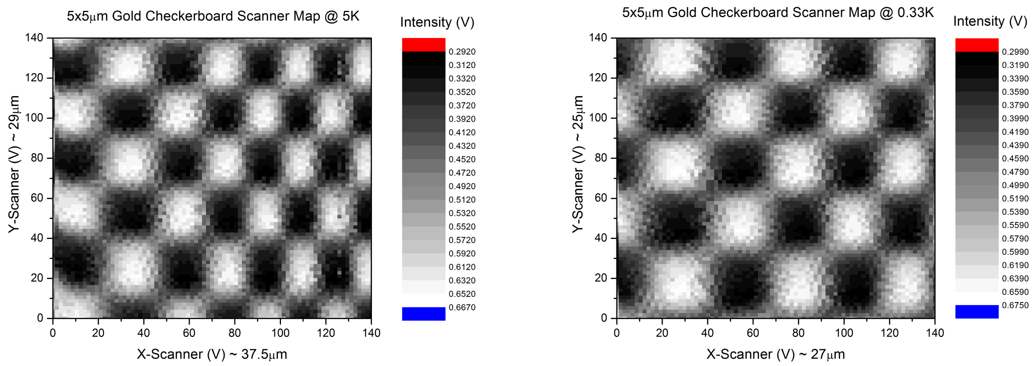

(a) (b)

Figure 3.27: Scanner map of a high contrast chequerboard sample. At 5K, the X/Y-axis moves a distance of 37.5/29µm. At 0.33K, the X/Y-axis moves a distance of 27/25µm.

lar movement ranges of the two scanner directions; the Y-axis has a smaller movement range. This could be caused by a faulty piezo or a slightly higher resistance in the Y-axis wiring which causes the applied voltage from the room temperature Attocube controller to be reduced at the piezo. Nearing the limits of the scanner's movement (∼40µm), the applied voltage and movement distances are no longer linearly related. This is an expected feature of the scanners and is caused by the piezo material reaching the limit of its extension. It is most noticeable in the X-axis movement as the Y-axis was unable to reach its maximum movement distance. The scanner is also sensitive to step size, an applied voltage step larger than 10V will push the scanner outside its linear movement regime. For this reason its control program is limited to a 10V step range. The scanning maps do produce heat load that does reduce the cycle time of the sorption fridge, but only by ∼5% under continuous usage.

3.3.6 Microscope Setup

Attached to the Attocubes motors is a fibre and microscope lens tube setup enabling a 1550nm laser to be focused onto the chip (As seen in Figure 3.28). The lens tube consists of a collimating (354280-C) and a focusing (354330-C) lens. The ferrule is positioned by hand; this is done by projecting infrared light through the ferrule and collimated lens to achieve the longest projection distance from the housing before attaching the focusing lens. The lens tube is capable of focusing a spot with a FWHM of 1.19µm as described by the Sparrow criterion below (Equation 3.4).

Spot Resolution

For a standard optical instrument affected by diffraction and aberration, the Rayleigh criterion[129, 130] can be used to calculate the minimum resolution of the instrument.

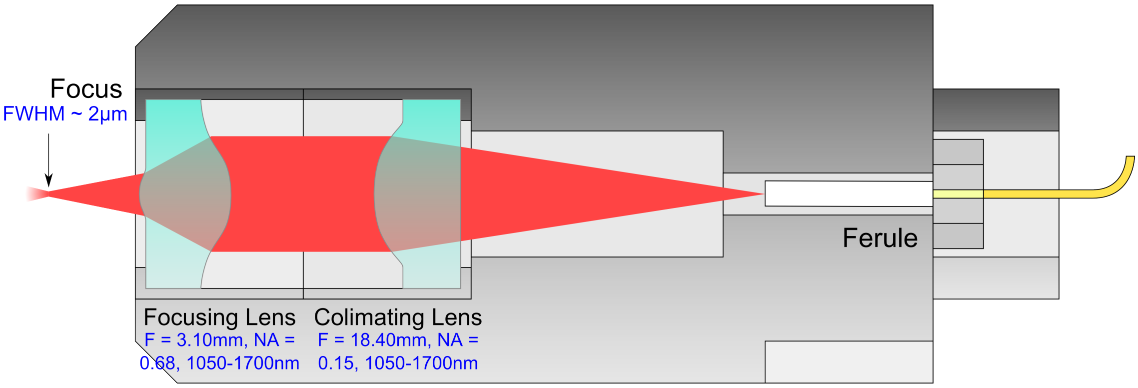

Figure 3.28: Microscope lens tube setup. The fibre is positioned to achieve an infinite focal lenfth in the collimating lens. If the beam is collimated correctly, the focusing lens can be affixed without concern for its position in the microscope.

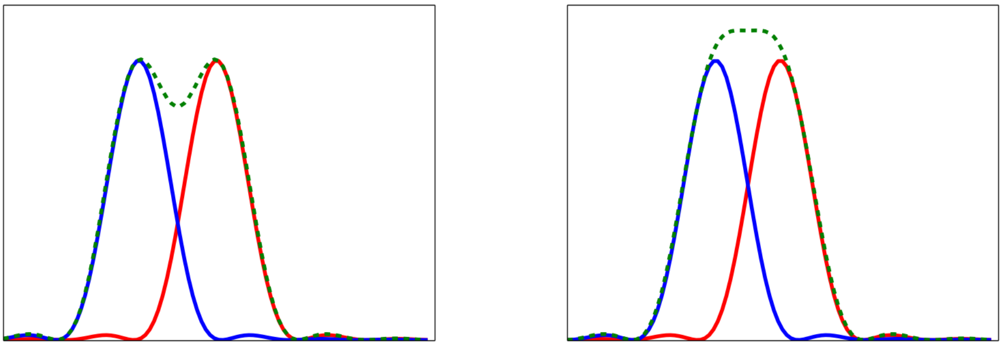

(a) (b)

Figure 3.29: (a) Rayleigh criterion for spatial separation of optical instrument. (b) Sparrow criterion. Using the focusing lens with NA = 0.68, the minimum resolvable FWHM for 1550nm light is 1.19μm.

This resolution is the minimum distance between two point light sources such that these two spots are still resolvable. In the case of a nanowire chip, this refers to two points on either side of a material boundary $\Delta\ell$. The Rayleigh criterion posits that this occurs when the peak of one spot lines up with the first minimum of the next spot (Equation 3.4)(Left). The Sparrow Criterion[131] argues that the two spots are still resolvable if the combination of their functions creates a flat peak, rather than a saddle in the case of Rayleigh (Equation 3.4)(Right). This criterion achieves a slightly smaller minimum spatial resolution and is applicable if the optical instrument is only affected by diffraction. These equations are visualised as two point light sources in Figure 3.29.

$$\Delta\ell = \frac{0.61 \times \lambda}{NA} \quad \& \quad FWHM = \frac{0.52 \times \lambda}{NA} \tag{3.4}$$

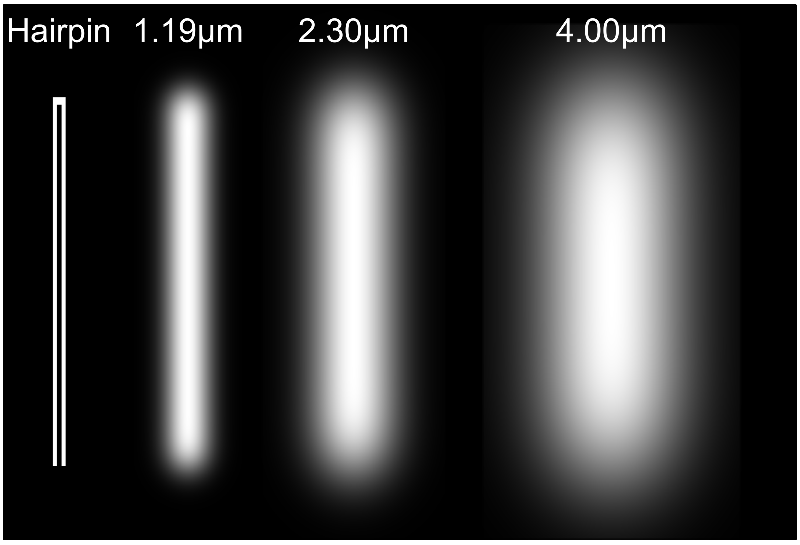

Figure 3.30: Examples of convolution of the microscope spot with a hairpin nanowire. The hairpin sample is a nanowire, 110nm thick with a 120nm gap. Each proceeding image shows a convolved Gaussian spot over the nanowire at: the minimum spot possible for the microscope, 1.19μm, the minimum spot recorded in the Rankinator with vibration damping, 2.30μm, and the same spot in the Rankinator without vibration damping, 4.00μm.

Gaussian Convolution

The nanowires intending to be imaged are 110nm wide, which are not resolvable under the microscope. A simulation of the convolution of a Gaussian laser spot over the nanowires can be performed as a litmus test for the expected image. In the example in Figure 3.30, three different Gaussian spots have been convolved over the same hairpin nanowire, which can be compared to the counts maps or reflections maps taken over the device.

Vibration Damping

In practise, even after vibration damping the system, the best FWHM achievable will not reach the Sparrow criterion. The PT in the cryostat produces large mechanical vibrations, which negatively impact the results of our reflection and counts maps (see §3.3.3. Pulse Tube Operation). Though the PT has vibration damping braids connecting to the external stage, low level vibrations still are an issue in the lower stages. The laser spot size is measured at 4.3μm for the standard setup. A better spot size of 2.3μm is achieved by adding additional damping support underneath the outer shielding to reduced internal vibrations (Figure 3.31).

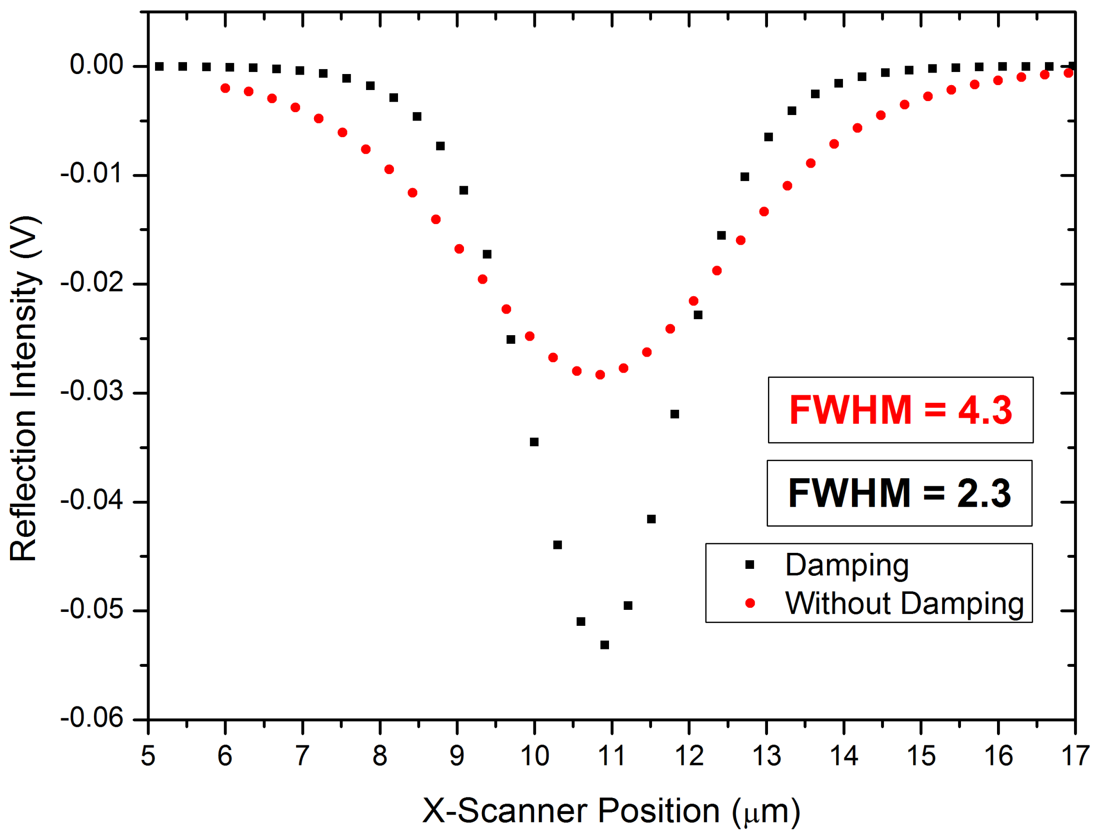

Figure 3.31: Change in microscope spot size with and without damping. This data was taken by scanning the laser over a transition between Au and Si, producing an estimation of the laser's spot size. Though these values are only approximate, the improvement in resolution is clear.

3.3.7 Wiring

A universal problem in low temperature cryostat experiments stems from a standard physical law: electrical conduction parallels heat conduction. The Rankinator presents a challenge in needing to reach 0.35K whilst also having fidelity in its control of input coaxes, temperature monitors and Attocube motors.

The PT is monitored by three (DT-670) Si diodes housed by a Cu bobbin. Two diodes are sensitive at 1-5K and one has its highest sensitivity around 40-80K. Each diode measures temperature using a 4-pin setup, the power of the PT at this stage is enough to cover the small load of the Si diodes. The sorption fridge is controlled and monitored by 11 devices, totalling 24 wires. Six of these are simple Si diodes that record the temperature of each component in the system; two RuO_2 diodes are used on the $^3He/^4He$ heads for their accuracy at low temperature. There are two resistive pump heaters that act on the $^3He/^4He$ sorption pumps to allow the release or absorption of $^3He/^4He$ gas. Two more are heat switches which are used to allow and bar the transfer of heat between the sorption pumps and the 4K heatsink (See §3.3.4. Sorption Pump Operation for sorption pump description and Table 3.1 for a list of sorption pump connections). For the 9 two-wire measurements, constantan loom was used ($\phi = 2.3\mu\text{m},\ 54\Omega/\text{m}$ at 4K) favouring a lower heat load over accuracy. For the $^4He/^3He$ Head temperatures Cu loom was used ($\phi = 2.3\mu\text{m},\ 3.5\Omega/\text{m}$ at 4K) favouring accuracy over heat load.

The full loom was connected to the baseplate of the sorption pump then thermally anchored to each higher stage before reaching the hermetic seal. Through the hermetic seal, the wiring is them split through a breakout box (Figure 3.32). All the Si diodes and buffer head are monitored through a Lakeshore 224 temperature monitor which is capable of self-converting the resistance values into temperatures. The ^3He head RuO_2 diode is monitored through a SIM921 resistance bridge; the diode came with a data conversion chart for converting resistance into temperature, which was implemented into the Python readout. To power the pump heaters and heat switches, two programmable Keithley 2200 series current supplies have been used.

The Attocube stepper and scanner motors consist of 5 modules. The scanner modules require two wires for each movement axis, whereas the stepper motors have an extra three per axis for position readout. Both motors produce manageable heat loads above 5K and most maps are taken at this temperature. Below 0.4K, the scanner motors produce little heat load even during operation; at this temperature the main source of heat load comes from the stepper motors. Large currents are supplied to the steppers dur-

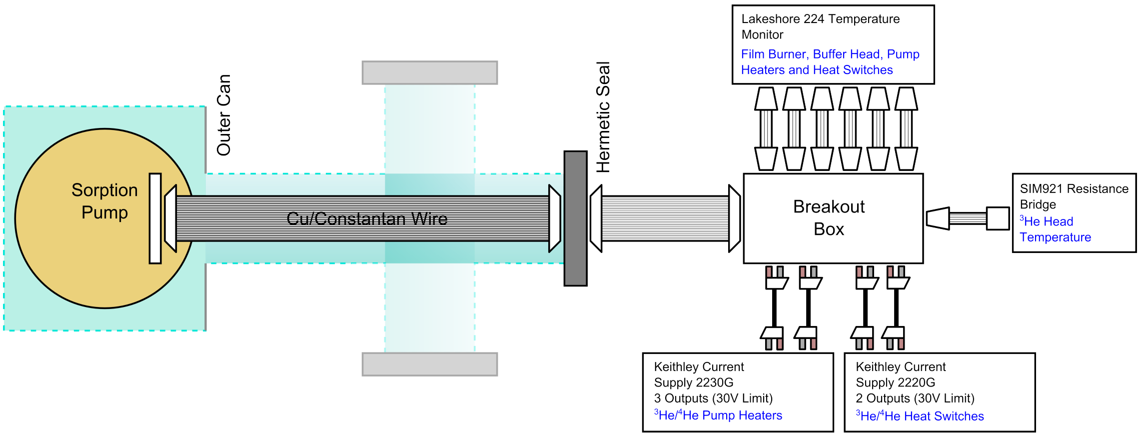

Figure 3.32: Sorption pump micro-pin wiring diagram. The hermetic seal is not placed on the outer can, but inside a T-piece outside the can. This creates the extra room needed for more wiring seals.

ing both movement and readout, but their heat load can be reduced by using a quicker mapping program with a deliberately smaller accuracy. (See §C. Additional Programs). The connection of the wiring from the motor to the control box outside the cryostat also produces a large heat load. To reduce this, silver-plated Be_2Cu wires (Coax Co. SC-086/50-SB-B) were used between the critical ^{3}He head and 3K Stages (Figure 3.33); these benefit from extremely low heat conductivity (0.5μW/mK at 4K), but are expensive and fragile - with a minimum bending curvature of 3.2mm.

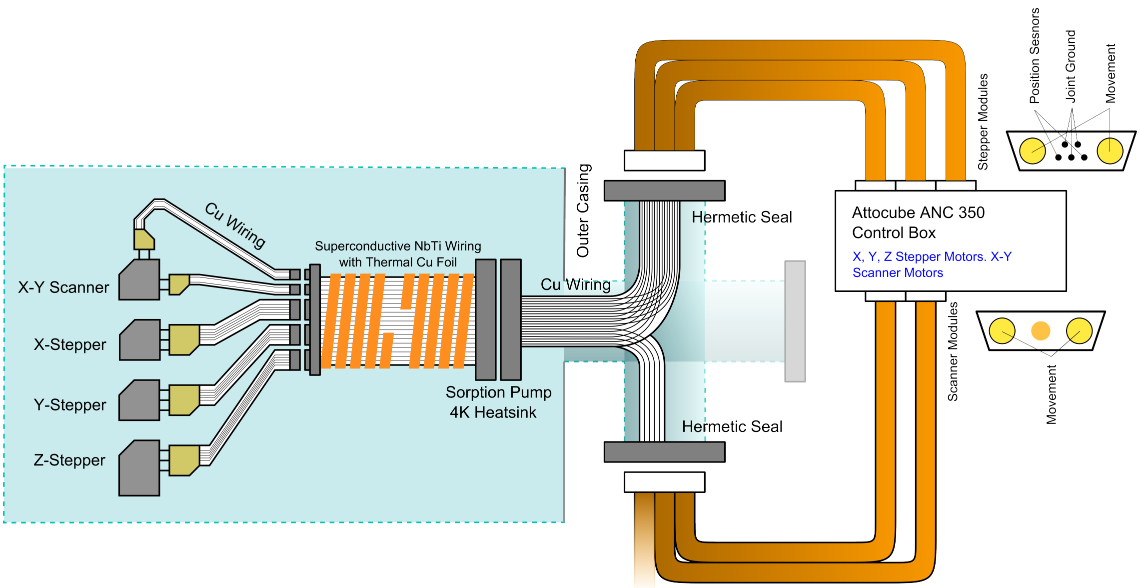

Figure 3.33: Attocube wiring in Rankinator. From the motor connections inside ^{3}He stage magnetic shielding, normal copper wiring is used. From ^{3}He to the sorption pump's 4K heatsink, a supconductive NbTi-loom is used. This is wrapped in Cu foil, which is in thermal contact with either the ^{3}He head or the 4K heatsink to ensure the NbTi is superconducting along the full loom. From then on, the remaining wiring is a Cu based loom.

The Rankinator can hold up to 4 devices for characterisation below 0.4K. The connections are made using Be_2Cu coaxes between the 4K heatsink and the ^3He head of the two-stage closed-cycle cooler, with the remaining distance to the device covered by Cu coax. This reduces the heat load to the ^3He stage, but also allows the Be_2Cu wiring to be removed when not in use. An additional RF line can be fitted for measurements of single-TM multiplexing detectors (Figure 3.34).

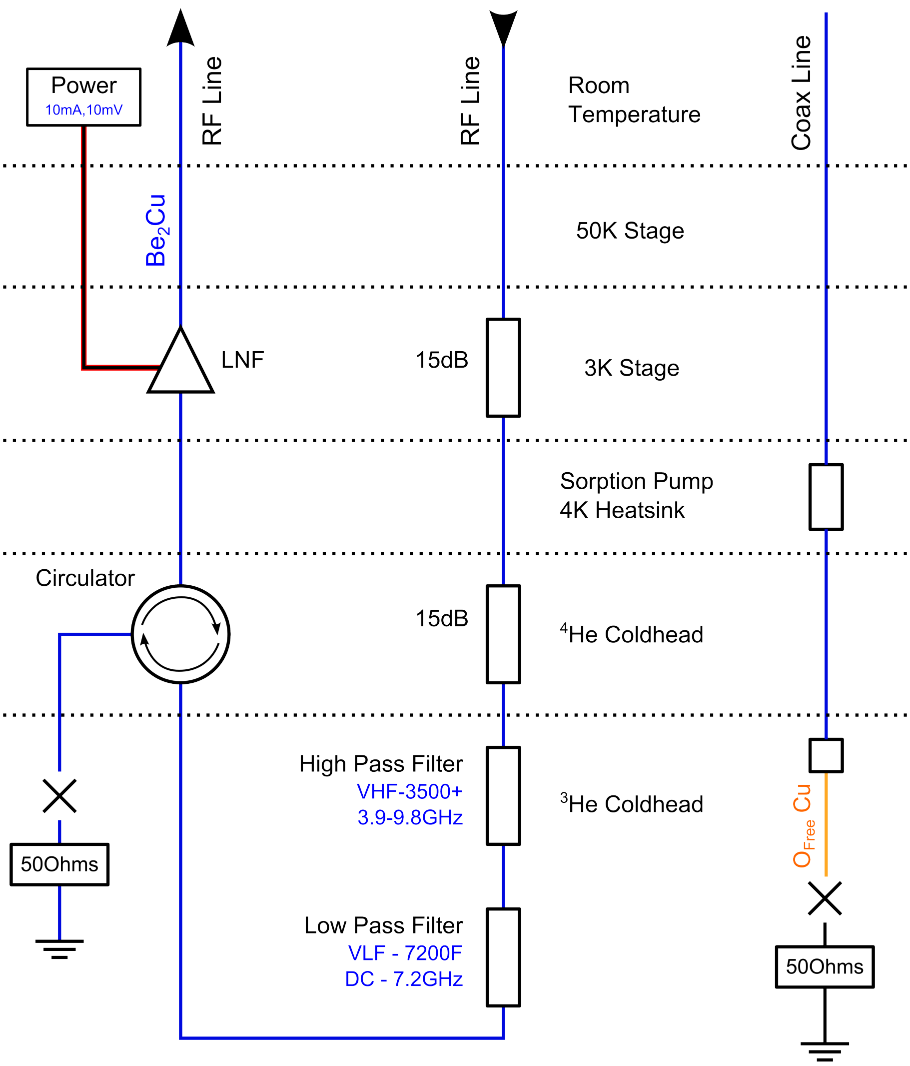

Figure 3.34: The RF-Line, which exclusively uses Be_2Cu wire (blue), is attenuated heavily before it reaches two filters which block out unwanted noise. The circulator acts to further reduce the noise when measuring the reflected pulses from the sample (marked with an X). Saturation of the components occurs above the maximum input power of 50dBm. The 4 coax lines use silver-plated Be_2Cu wire for its low thermal conductivity and O-free Cu (orange) within the ^3He head stage. O-free Cu has had its O impurities removed, allowing for much higher electrical conduction than simple Cu wiring.

Diode Type	**Monitor**	**Impedence/ Junction Voltage**	**Voltage/ Current**
Si Diode	Film Burner	0.5-1.8V	10μA DC
Si Diode	^{4}He Pump Temperature	0.5-1.8V	10μA DC
Si Diode	^{3}He Pump Temperature	0.5-1.8V	10μA DC
Si Diode	^{4}He Switch Temperature	0.5-1.8V	10μA DC
Si Diode	^{3}He Switch Temperature	0.5-1.8V	10μA DC
Resistive Heater	^{4}He Pump Heater	400Ω	35V
Resistive Heater	^{3}He Pump Heater	300Ω	20V
Resistive Heater	^{4}He Heat Switch	10kΩ	4V
Resistive Heater	^{3}He Heat Switch	10kΩ	4V
Ruthenium Oxide	^{4}He Coldhead Still/Buffer Head	1kΩ-3kΩ	1μA max.
Ruthenium Oxide	^{3}He Coldhead Still	1kΩ-7kΩ	100nA max.

Table 3.1: List of sorption pump connections.

Noise Analysis

The majority of the noise in the cryostat will occur from thermal agitation of room temperature components and is constant across the majority of the frequency spectrum. The Root Mean Square (RMS) of the current can be estimated using the Johnson-Nyquist relationship (Equation 3.5), where Δf describes the bandwidth of the signal frequency. At room temperature, using the RF-Bay LNA-580 amplifiers (Δf = 580MHz), the load resistor (100kΩ) contributes a noise level of ~10nA.

$$I_{Noise} = \sqrt{\frac{4k_bT\Delta f}{R_L}} \tag{3.5}$$

3.3.8 Heat Load

The ^{3}He head can reach ~0.35K for up to 10 hours during each cycle, but this is heavily dependent on the heat load applied to the head. Applying more heat load to the ^{3}He head increases the minimum ^{3}He head temperature reached which is inversely proportional to the cycle time of the sorption pump. From the wiring materials noted above, it is relatively straight forward to estimate the total heat load on the system at the 3K and 0.35K stage using the heat transfer equation (Equation 3.6). Table 3.2 and Table 3.3 lists these results respectively, along with information about the used materials. For reference, measurements of ^{3}He head temperature vs head load are detailed in Figure 3.35.

From these rough estimations it is clear the heatload at the 3K stage, ~3mW, is much lower than the maximum heat load of the cryostat >500mW. The heat load at the ^{3}He head is ~137µW, which is much larger compared to the heat load tests performed by Chase Cryogenics. This does not prevent the $_3$He head from operating, but it does heavily reduce its cycle time from a possible 10 hours to 3.5 hours. The complication arises from the wiring of the sorption pump controls and Attocube motors.

$$Q = k_C A \left(\frac{T_2 - T_1}{L}\right) \tag{3.6}$$

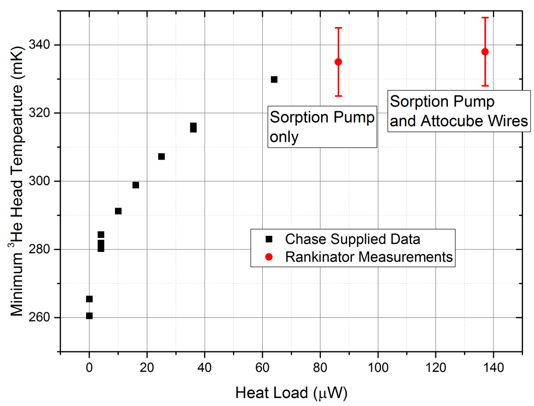

(a)

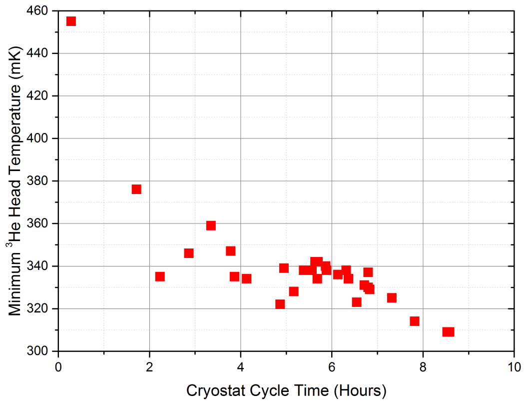

(b)

Figure 3.35: Graph (a) shows the minimum ^{3}He head temperature against applied heat load. Included is data supplied by the manufacturer Chase (black) as well as measured results of the minimum temperature from the Rankinator during cooldowns with and without the attocube wiring (red). With the current setup, the fridge reaches temperatures of 355mK, suggesting a heat load near ∼200μW. Due to the fidelity needed to control the Attocube motors, the wiring needs to have a low resistance, which also creates a high thermal conductivity and, thus, additional heat load on the system. Graph (b) shows the minimum heat load against minimum ^{3}He head temperature. There is a clear inverse relationship between the lowest temperature reached and the cycle time.

Material	**Temp Change (K)**	**Use**	**Wires**	**Cross Section (mm^2)**	**Thermal Conductivity (W/m*K)**	**Head Load (mW)**
Cu	50-5	Sorption Pump	6	2.93×10^{-2}	400	1.58
Constantan	50-5	Sorption Pump	18	4.29×10^{-2}	21.2	0.368
Be_2Cu	50-5	Coax Lines	4	5.42×10^{-1}	1.72×10^{-6}	8.39×10^{-8}
Cu-Loom	50-5	Attocube Motors	19	6.63×10^{-3}	400	1.13
Be_2Cu	50-5	RF-Line	2	5.42×10^{-1}	1.72×10^{-6}	8.39×10^{-8}

Table 3.2: Heat load connections from room temperature to the 3K stage. When every connection is being used, this produces a rough heat load of 3.08mW.

Material	Temp Change (K)	Use	Wires	Cross Section (mm^2)	Thermal Conductivity (W/m*K)	Head Load (mW)
Cu	5-4	Sorption Pump	6	2.93×10^{-2}	400	70.3
Constantan	5-4	Sorption Pump	18	4.29×10^{-2}	21.2	16.4
Be_2Cu	4-0.35	Coax Lines	4	5.42×10^{-1}	1.72×10^{-6}	1.36×10^{-5}
Cu-Loom	4-0.35	Attocube Motors	19	6.63×10^{-3}	400	50.4
NbTi	5-4	Attocube Motors	19	7.85×10^{-3}	0	0
Be_2Cu	5-4	RF-Line	2	5.42×10^{-1}	1.72×10^{-6}	8.67×10^{-6}

Table 3.3: Heat load connections from the 3K stage to 0.35K. When every connection is being used, this produces a rough heat load of 137.1μW. The NbTi wires are superconducting below 5K, so do not thermally conduct and supply no heat load.

3.3.9 External Components

Figure 3.36 gives a description of each component needed to measure and control the Rankinator. Figure 3.37 shows a pulley system needed to lift the outer radiation shield of the cryostat. Two counterweights allow for effortless movement of the shield when closing up the fridge.

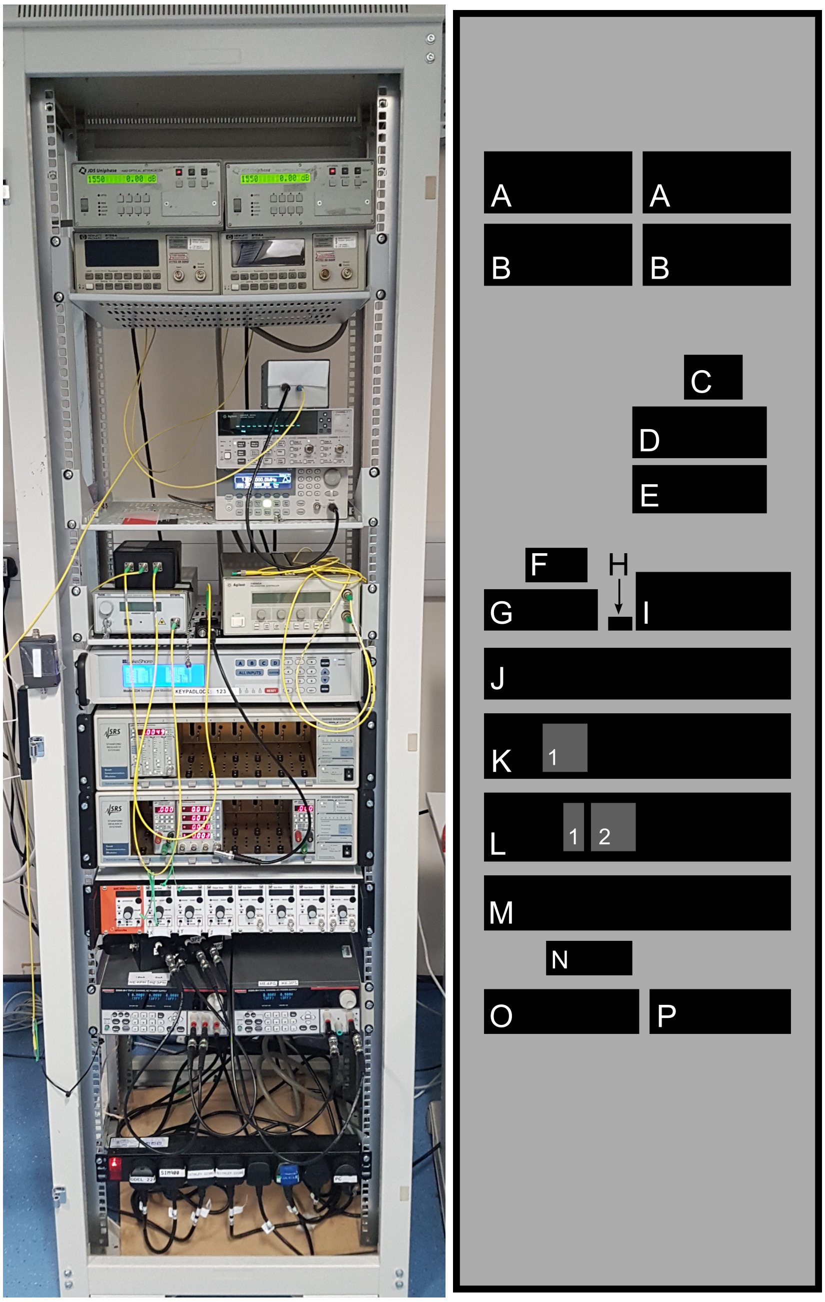

Figure 3.36: Control electronics rack for the Rankinator cryostat. A) Two optical attenuators (JDUniphase HA9). B) A further two optical attenuators (Hewlett Packard 8156). C) 1550nm butterfly laser diode (Thorlabs, SLD; 2.5mW FWHM linewidth = 90nm (SLD1550S-A2)). D) Universal counter (Agilent 53132A). E) Pulse pattern generator (Keysight 33220A). F) Optical circulator (FC/PC:6015-3-APC). G) ThorLabs fibre-coupled benchtop SLD (2.5mW, FWHM linewidth = 90nm, S5FC1550P-A2). H) InGaAs SPAD (DET10C/M). I) Programmable polarisation controller (Agilent 11896A). J) Lakeshore temperature monitor (Model 224). K) Sim900 mainframe with components: K1 – Resistance bridge (SIM921). L) SIM900 mainframe with components: L1 – Isolated voltage sources (SIM928) and L2 – voltmeter (SIM970). M) Attocube motor control box (ANC350). N) Breakout box for ^{3}He-stage temperature monitoring and control. O) Keithley 3-channel power supply (2230G-30-1). P) Keithley 2-channel power supply (2220G-60-2). The optical path is directed by single mode optical fibres (SMF-28) (yellow cables).

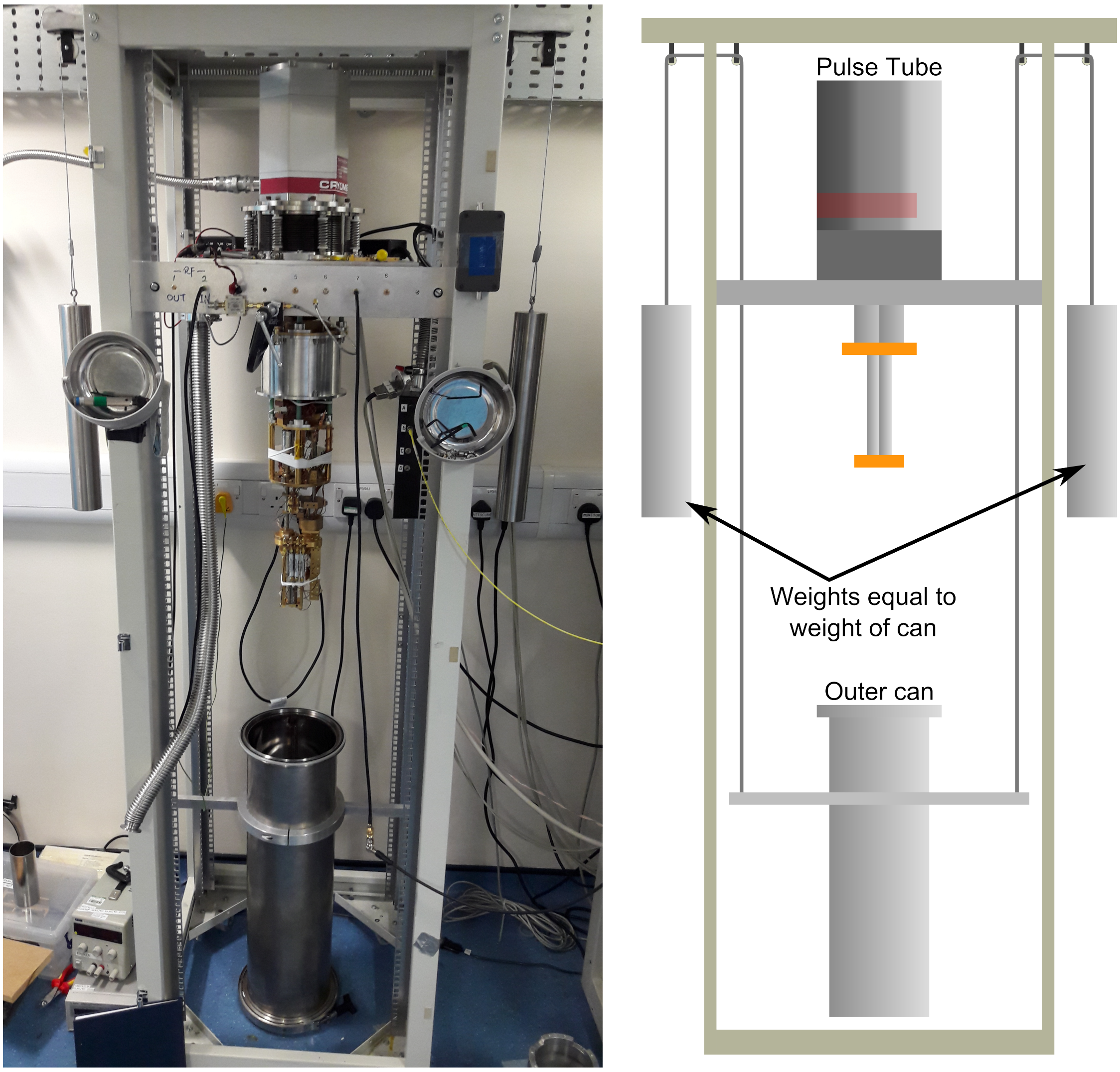

Figure 3.37: Pulley system for the outer shielding of the Rankinator. The weights counterbalance the weight of the outer can for easy closing and opening.

3.4 Low Temperature Measurements

Low temperature characterisation of an SNSPD gives critical information on the performance of the device and on the fidelity of its design and fabrication process. These metrics are used in comparison to steer detector design towards an optimum operation. The following section details each of these measurements used to characterise the devices in §4. Cavity SNSPD Devices and §5. MoSi Devices.

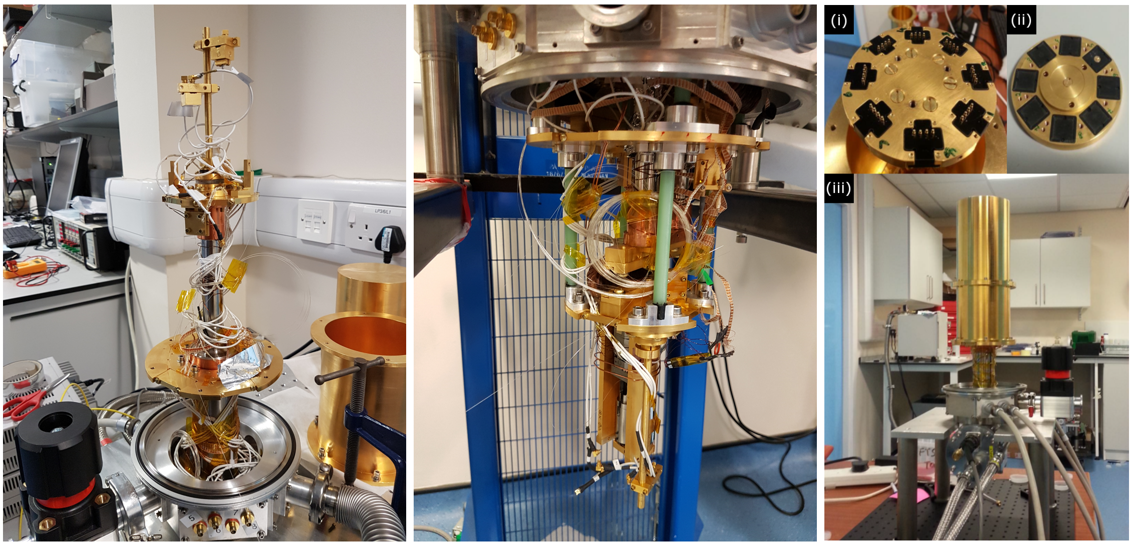

(a) (b) (c)

Figure 3.38: (a) The Zephynator, a two-stage GM cryostat. (b) The Kelvinator, two-stage PT cryostat. The microscope housing sits at the base of the 3K stage. (c): (iii) Thin film testing station. (i) The films are pressed onto pogo-pin connections with a (ii) capping lid.

3.4.1 Additional Cryostats

The Quantum Sensors group at Glasgow University currently has access to several cryostats of different functions and base temperatures (Figure 3.38). The Zephynator is a two-stage GM cryostat capable of reaching 2.5-2.0K base temperature. This cryostat is capable of electrical testing and pre-fibre coupled sample testing. The Kelvinator is a two-stage cryostat (PT403) with an isolated motor, much like the Rankinator. It can reach a base temperature between 4.0-3.0K depending on heat load and can perform nano-optical measurements with the aid of a 1550nm microscope setup attached to 5-axis Attocube motors – the same setup as that of the Rankinator (§3.3. Rankinator Design). The thin film testing station is a GM cooler as with the Zephynator, but only focuses on bulk and thin film electrical testing using a custom built sample holder capable of testing 8 samples simultaneously. The sample holder uses 4 pogo-pins on each sample to perform 4-pin characterisation measurements without the need for wirebonding.

3.4.2 Current-Temperature Characteristics

If the sample superconducts, its I-V characteristics can be used to extract the critical current I_C. From the setup in Figure 3.39, the device resistance is monitored and a current sweep is applied between two limits along both polarities. The device will switch between its superconducting and normal states, altering its resistance, which is mea-

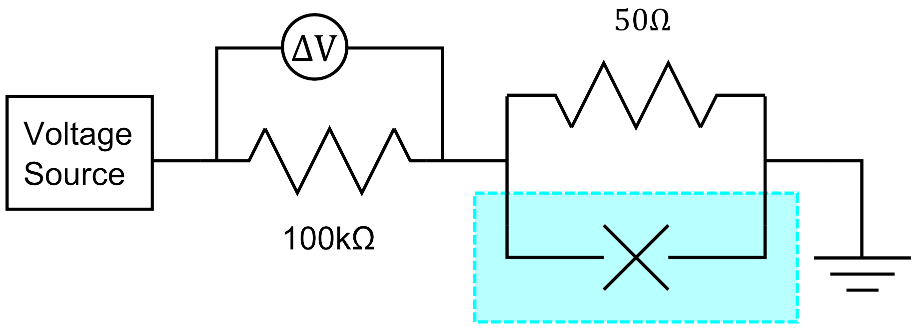

Figure 3.39: A current is passed through the superconducting device (X) by creating a potential across a load resistor (100kΩ). The resistance of the device can be known from the potential divider circuit setup. When the device becomes resistive, current redirects through the shunt, allowing the device to reset. Due to the effects of hysteresis, the highest critical value is produced only from a rising positive current or decreasing negative current.

sured and can also display the effects of hysteresis (as discussed in §2.1.4. Limits of Superconductivity). The 50Ω shunt is used to divert the current from the device while in its resistive stage; this allows the device to recover into its superconductive state and avoid the effect of latching (§2.3.3. Latching). With no shunt, the device requires the critical current to reach a value much lower than I_C before it resets completely, which appears as a large hysteresis in the I-V data.

The relationship between critical current and temperature, as discussed in §2.1.5. Temperature Dependence of Critical Current Density is relatively parabolic. The equation for the parabolic curve can be used to extract the energy gap of the nanowire material. In order to fit this relationship, the critical current of the device needs to be recorded at small variations in temperature. Though most GM or PT cryostats offer a relatively stable base temperature, their transition between different temperatures is fast. To record I-V characteristics (and thus the critical current) of devices in quick succession, a low integration time voltmeter is used. The Keithley 238 model provides exemplary performance, measuring voltage at a minimum time integration of about 416µs, or 2400 data points per second.

3.4.3 Timing Jitter

This measurement setup is used to measure jitter, Δt, the variation in the detector's time delay (§2.3.1. Jitter). In the setup below (Figure 3.40), a pair of photons are created that follow separate paths, hitting the detector (X) and an APD. This method is a form of

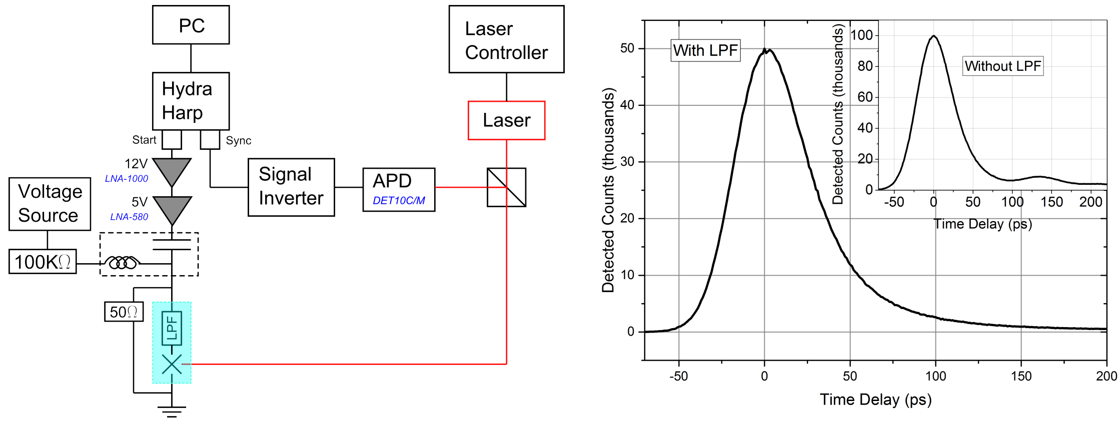

(a) (b)

Figure 3.40: (a) Circuit diagram for jitter measurement. A 1550nm laser is split; one wing is detected by an APD (InGaAs diode DET10C/M) and the other travels into the cryostat and hits the sample (X). Both pulse responses are compared in a Time Interval Analyser (TIA) (HydraHarp). (b) The experiment is repeated around 10,000 times, returning a histogram of response data. The FWHM describes the jitter and, in this case, is around 140ps. The LPF also removes reflections that occur in the amplifier chain.

TCSPC in which an APD is used to start a stopwatch which times how long it takes for a count to occur from the device being characterised. Several thousand measurements are taken to ensure the result is statistically significant. A histogram of these results is produced and the FWHM of the time variation of the delay gives a value for the jitter. A standard value for jitter is of the order of 120ps, but has been shown to dip as low as 16ps.

The use of a LPF at the device stage removes the effect of afterpulsing (§2.3.3. Afterpulsing) caused by reflections at larger frequencies between the signal amplifiers[80]. Without the LPF, the effect of afterpulsing can become large and create a secondary peak in the jitter histogram (Figure 3.40(b) inset).

3.4.4 System Detection Efficiency

The SDE is measured by using the setup in Figure 3.41. A calibrated photon flux is shone onto the active region of the device and the count rate is registered. The optical attenuation is swept from the multi-photon to the single photon regime and the current bias is also swept from negligible up until the critical current is reached. The photon flux and detector count rate are recorded through each sweep. The SDE can be measured inside the region about which there is a linear relationship between the log scale of both photon flux and photon count. By extracting this linear region, its efficiency can then be calculated using (Equation 3.7a) for single photon detection or (Equation 3.7b)

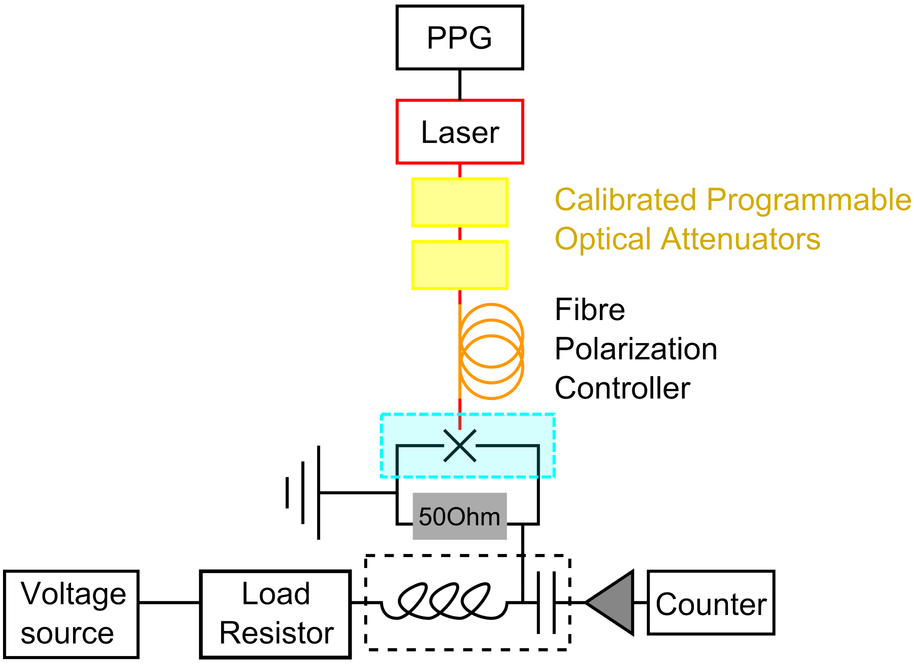

Figure 3.41: Circuit diagram for SDE measurement. A programmable PPG (Agilent 33220A) supplies a pulsed power input to the laser (Thorlabs, fibre-coupled benchtop SLD; 2.5mW, FWHM linewidth = 90nm). The attenuation of the laser is swept (Hewlett Packard 8156A) and its polarisation is controlled (Agilent 11896A). When the detector becomes resistive from a count, reflections from the impedance mismatch of the circuit create an AC signal pulse, which is amplified (LNF500, LNF1000) and counted (Agilent 53131A).

when in the multi-photon regime. The highest attenuation (lowest photon flux) is used to measure the device's DCR, which is subtracted from the total counts of the detector when calculating SDE. For the below equations, R_{det} is the count rate (for an ideal detector), f_P is the frequency of the Pulse Pattern Generator (PPG), μ is the rate of photons per pulse and η is the SDE of the device.

$$R_{det} = f_P \mu \eta \tag{3.7a}$$

$$R_{det} = f_P \left(1 - e^{\mu\eta}\right) \tag{3.7b}$$

As discussed in §2.2.4. Generating Single Photons there are no existing devices that can produce an ideal stream of anti-bunched, single photons. However, single-photon states can be generated that are mostly anti-bunched by heavily attenuating a laser source. This is not ideal as the attenuation does, occasionally, create two or more bunched photons. This effect can be mitigated by operating in a regime where the mean photon number per pulse on the detector is well below 1. A single 1550nm photon has an energy of ~ 0.8eV. For a 1MHz pulsed 1550nm laser, a measured power of -109dBm equates to just under 0.1 photons/pulse.

3.4.5 WaSTe Measurement

A Wavelength Scanning Test (WaSTe) (Figure 3.42) measures the count rate of a detector while altering the flux wavelength, attenuation and polarisation for a fixed detector bias. This returns the SDE of the device over a range of wavelengths and polarisations. The WaSTe measurement repeatedly scans the polarisation controller tracing out fixed points on the Poincaré sphere. It does not find the maximum or minimum polarisation alignment, but gives a rough estimate for high and low polarisation alignment. The registering efficiency of the device will be dependent on the input energy of the photon. Higher energy photons (lower wavelength) are likely to increase the probability of the detector outputting a signal. This suggests the SDE of the device will increase with a decrease in wavelength.

Three different lasers are used to perform the measurement at different wavelengths, Two Yenista External Cavity Lasers (ECLs), from 1340-1440nm and 1560-1680nm, and one Agilent laser from 1440-1590nm. The switch between different boxes occurs at 1440nm and 1560nm. As the lasers will not produce exactly the same power output, a power calibration measurement is recorded at each wavelength before the WaSTe measurement is performed. This is then used to correct the influx power after the WaSTe measurement is taken.

3.4.6 Mapping

With the addition of the fibre microscope setup attached to the 3D positional Attocube motors, the cryostat gains the capability of creating reflection and counts maps across the device. The Z-axis stepper motor is used to focus the spot from the lens tube and the X-axis stepper, Y-axis stepper and XY-axis scanners allow for coarse and fine maps over the device in blocks of $\sim$2mm^2 and $\sim$30µm^2, respectively. The resolution of the images are limited by the spot size of the microscope, which can achieve a FWHM, of 2.3µm when the setup is vibration damped (§3.3.6. Vibration Damping). To create a reflection map (Figure 3.44(a)) a broad bandwidth 1550nm laser is directed through a circulator into the microscope housing. The reflections from the surface of the chip are directed back through the circulator and recorded by an InGaAs diode. Different heights and materials reflect the laser light with different intensities, building up an image of the region being mapped. Examples of these are given in Figure 3.43.

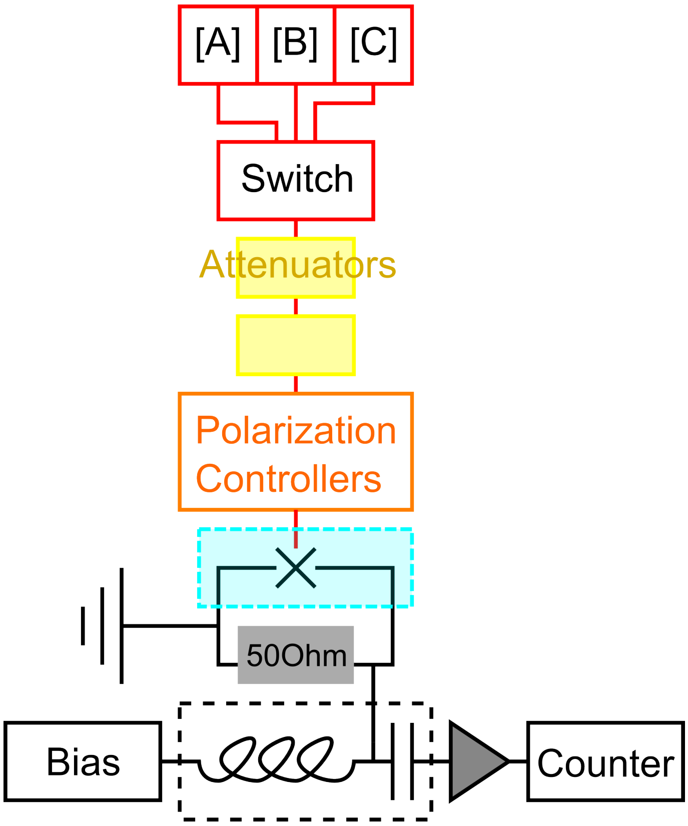

Figure 3.42: Circuit diagram for Wavelength Scanning Test measurement. Three lasers are used to fire over three different wavelength ranges from 1340nm to 1640nm (Two Yenista ECLs, [A] from 1340-1440nm, [B] from 1560-1680nm and one Agilent laser, [C] from 1440-1590nm). The attenuators work up to a wavelength of 1650nm, which sets the upper limit of the measurement. The polarization controller is operated electronically, scanning over a large range of polarisation angles to find both the highest and lowest intensity of incoming light. The entire process runs via a Python script written by Dr. Robert M. Heath.

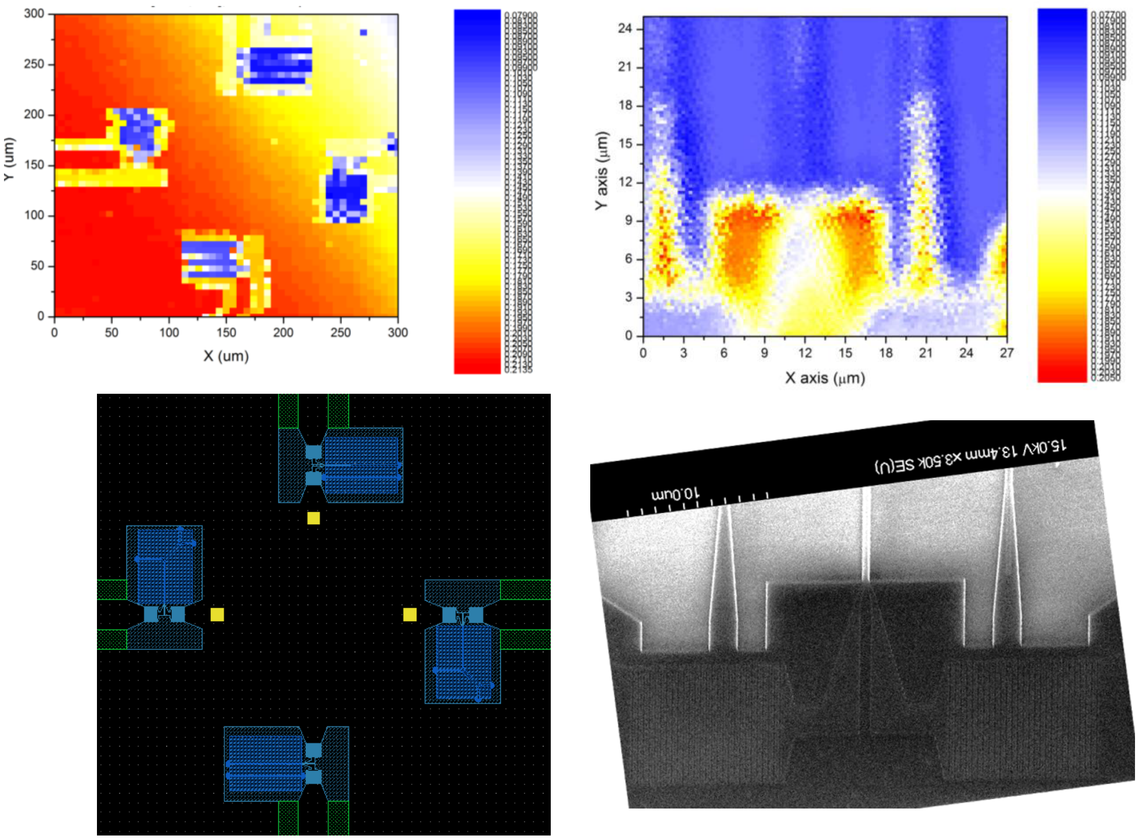

Figure 3.43: The top images are reflection maps taking with the Attocube motors and microscope in-situ, the lower images are a GDS design and SEM of the detectors that have been scanned. Left: Coarse map of a set of waveguide detectors using the X and Y stepper modules over ∼2mm. Right: Fine map taken with the XY-scanner module over ∼30µm region. SEM image taken by Robert Kirkwood.

A photoresponse map uses a similar setup (Figure 3.44(b)). Here, a flux of 0.1 photons per pulse is shone onto the device, in much the same way as an efficiency measurement. Unlike a reflection map, the SLD is replaced with a pulsed laser at 1MHz (20ns pulse length with a 5ns rise time). Using a pulsed laser gives the detector time to reset between detection events. The response of the device is then recorded at each pixel of the map for a fixed bias, polarisation and intensity. This map is taken over the same area as an equivalent reflection map, giving a description of the device's active area.

Photoresponse maps will vary with temperature, current bias point and photon flux. Data from a photoresponse map details if the device is single-photon sensitive, uniform and also shows what position of the active area is the most responsive for finding the highest efficiency measurements to, ideally, couple fibre.

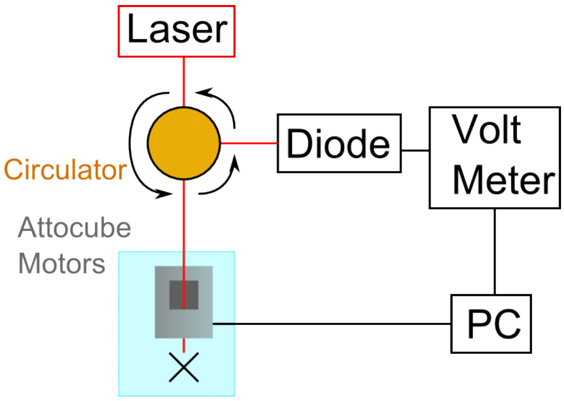

(a)

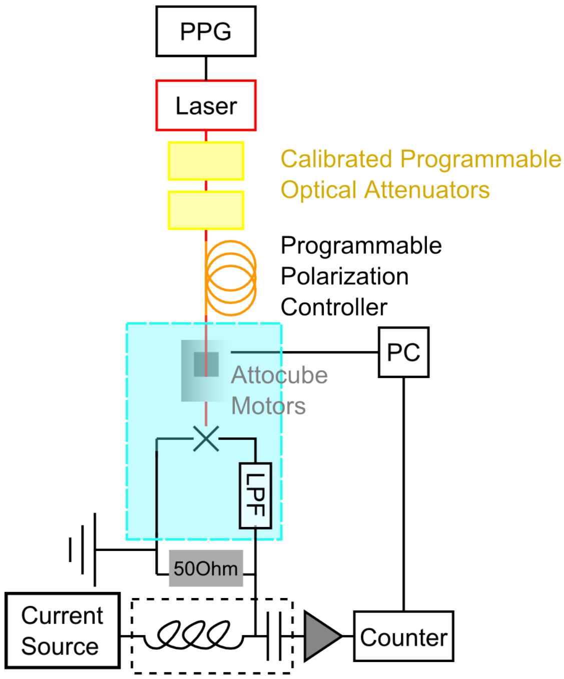

(b)

Figure 3.44: (a) Circuit diagram for creating a reflection map. The laser (Benchtop (S5FC1550P-A2, 2.5nW, FWHM Linewidth = 90nm) passes through a circulator and enters the microscope housing (Described in §3.3.6. Microscope Setup), which focuses the light onto the sample. The light is reflected back through the microscope and through the circulator into an InGaAs SPAD (DET10C/M). The intensity of the diode is measured by a voltmeter. As the Attocube motors move to each discrete pixel of the chip, the intensity of the reflections are measured, building up a reflection map. (b) Circuit diagram for creating a counts map. This setup is very similar to the efficiency setup in Figure 3.41, albeit a few changes. The bias and polarisation is fixed as decided by a previous efficiency measurement. The laser is then set by the PPG and attenuated to 0.1 photons per pulse. As with a reflection map, at each pixel of the Attocube's movement, a measurement of counts is taken, producing the photoresponse map.

Chapter 4

Cavity SNSPD Devices

This chapter focuses on two batches of NbTiN cavity SNSPD meanders and their applications in QKD experiments as detailed in §4.1. Overview & Motivation. §4.2. Device Structure and Mounting details the structure and fabrication process of each device. The devices were then characterised with results shown in §4.3. Cavity Device Results. The results returned from the device with the highest efficiency was used to simulate the T12 QKD protocol, achieving a positive key rate at distances spanning the width of the UK.

4.1 Overview & Motivation

The UK quantum technologies hub is a £270 million investment aiming to establish single chip quantum computers as well as secure quantum communications across several cities in the south of the UK. The prospect of a QKD security network is viable through the application of sub-Poissionian photon sources and fast SPDs with high SDEs and low timing jitter. SNSPDs offer high performance metrics and have been applied to a variety of QKD[6–12] and quantum computing[1, 13, 14] experiments. The focus is to improve their metrics through changes in design, materials or fabrication processes. Devices with good performance characteristics can then be used in the applications as just described.

It is apparent that the properties of superconducting materials offer a balance between operating temperature and efficiency. It is thought that, the higher carrier density and energy gap of NbTiN films determines its high transition temperature. This allows the device to be applied in more common GM cryostats, stable at 2-3K. However, these films suffer from low absorption efficiencies, likely due to their carrier density. These lower efficiencies can be mitigated by including a wavelength optimised cavity layer, which increases coupling of light into the device. The use of a cavity is to negate the effect of photon loss from reflections between a material boundary. They increase transmission of light from the substrate into the superconducting film, as well as grant an extra pass of the light through the nanowire.

The work in this chapter aims to characterise perpendicularly coupled NbTiN cavity SNSPDs and record their performance metrics. Two batches of devices were tested from Technical University Deflt in The Netherlands and NICT in Japan. The devices were tested in a GM at 2-3K as well as the Rankinator down to 0.35K. The results of the highest performing device were then applied to simulations of the T12 QKD protocol over an increasing distance (As detailed in §2.4.4. Decoy State QKD). It was found that the device could perform the T12 protocol with a low DCR over a distance of 200Km, which is roughly the distance between Bristol and London. This suggests the device and the T12 protocol could be implemented in a real world scenario.

4.2 Device Structure and Mounting

4.2.1 Structure

The Kavli Institute for Nanoscience at Technical University Delft[2] supplied NbTiN films placed on an oxidised Si substrate forming a simple cavity via the Si/SiO_x interface reflection for front side coupled fibre testing. The SNSPDs consisted of nanowires with both 100nm widths and gaps and were designed to cover an active area of $10\times10\mu m^2$. These devices were optimised for 1310nm wavelengths, for applications in the metrology of quantum-dot technology[132] (at 1310nm) and medical applications in the detection of luminescent singlet oxygen in photodynamic therapy[17] (at 1270nm). Detectors of this design had previously demonstrated 23.2% SDE at 1310nm[2].

The National Institute of Information and Communications Technology (NICT)[4] supplied NbTiN films on an Si substrate housed in a double cavity for backside coupled fibre testing. The meander nanowires were 100nm wide with 60nm gaps and covered an active area of $15\times15\mu m^2$. Devices of this design have previously achieved high SDE values at ~70% and achieved jitter values as low as 68%. These devices were optimised for 1550nm wavelengths and have many applications in QKD (such as those discussion in §2.4.4. Quantum Key Distribution). A full description of the fabrication procedure for both devices can be found in §3.1.6. Fabrication Process for NbTiN Cavity Devices.

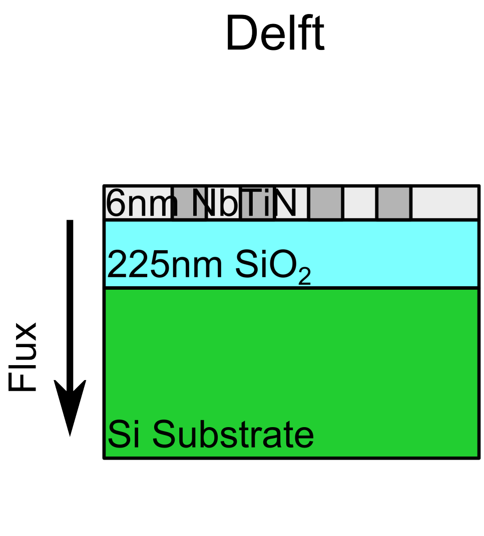

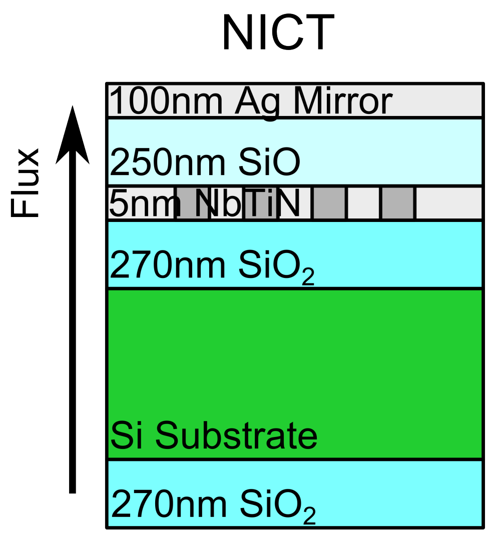

Figure 4.1: (a) Deflt device material stack. (b) NICT device material stack. The direction of the incident photon flux is indicated.

Cavity Structure

The Delft devices have cavity designs optimised for front side coupled 1310nm wavelength detection. The light enters the front of the chip and the cavity acts to reduce reflections at the boundary between the NbTiN and SiO_2, as discussed in §2.3.3. Cavity Devices. Optical stack simulations performed by Tanner[2] *et al* (Figure 4.2) return over 50% absorption efficiencies in the wavelength range of 1050-1650nm.

The NICT devices are backside coupled and implement three cavities, two of which act as Anti-Reflection Coatings (ARCs). The 250nm thick SiO layer acts as the main cavity that uses a Ag mirror. This reduces reflections from photons entering the NbTiN layer. The 270nm SiO_2 acts as the ARC, increasing the absorption of photons into the film from the substrate where a simple cavity structure alone would not achieve as high absorption efficiencies[4, 118]. Optical stack simulations performed by Miki[2] *et al* (Figure 4.2) achieve absorption efficiencies over 80% from 1400-1800nm.

4.2.2 Mounting

Both the Delft and NICT devices were wire bonded (§3.2.1. Wirebonding) onto sample mounts and electrically tested to ensure a working current. The devices were then optically coupled using the fibre-alignment rig discussed in §3.2.2. Fibre-Alignment Rig. This form of packaging achieves consistent, high coupling efficiencies and allows for easy transfer and installation of samples in any other cryostat with fibre coupled input. The Delft devices were coupled using standard single mode fibre (Corning SMF28, ϕ =

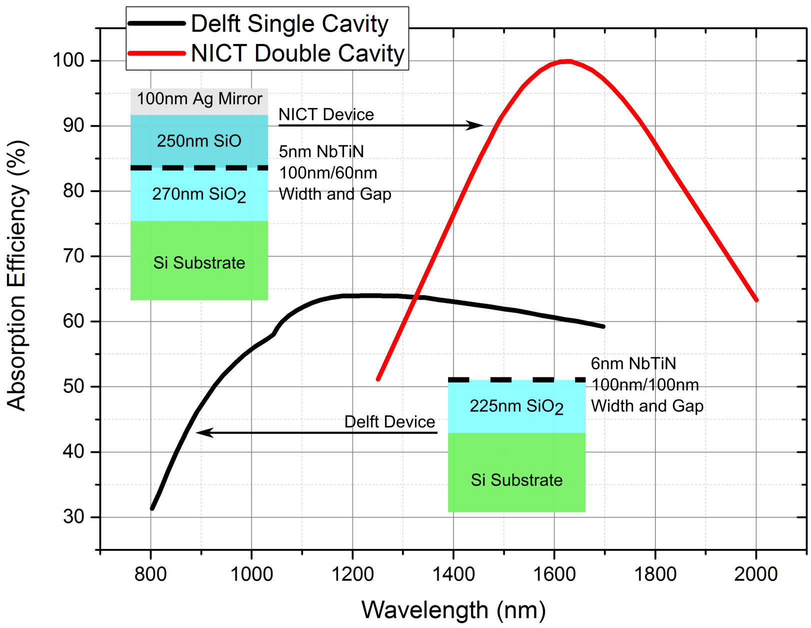

Figure 4.2: Simulated absorption spectrum of the optical stack of the Delft[2] and NICT[4] detectors. The Delft detector was simulated using front coupled light and the NICT detector using backcoupling light. The simulations do not account for the geometry of the nanowires.

9µm) at a distance above 25µm. The spot alignment can be seen in Figure 4.3. Au markers were used to direct the spot onto the centre of the chip as the device is not visible in the fibre-alignment rig. Device C10 shows excellent alignment, whereas B17 is off centre, which lowers its highest possible coupling efficiency.

The NICT devices were backside coupled using a Graded Index (GRIN) lens fibre. GRIN lens fibre uses a gradient refractive index to focus the output laser spot from the fibre onto a point. The OCT results of each sample can be seen in Figure 4.4. In positioning the laser spot, though the meander absorbs 1550nm focused laser light, the surrounding etched region is invisible to the laser. This creates a visible Airy disc around the device, which would usually be too dim to see in comparison to the central laser spot. The discs allow for precise manual positioning of the laser spot onto the centre of meander active area. This can be seen in Figure 4.5. It is important to note that uneven illumination of the Airy discs can lead to possible coupling losses of ∼30%.

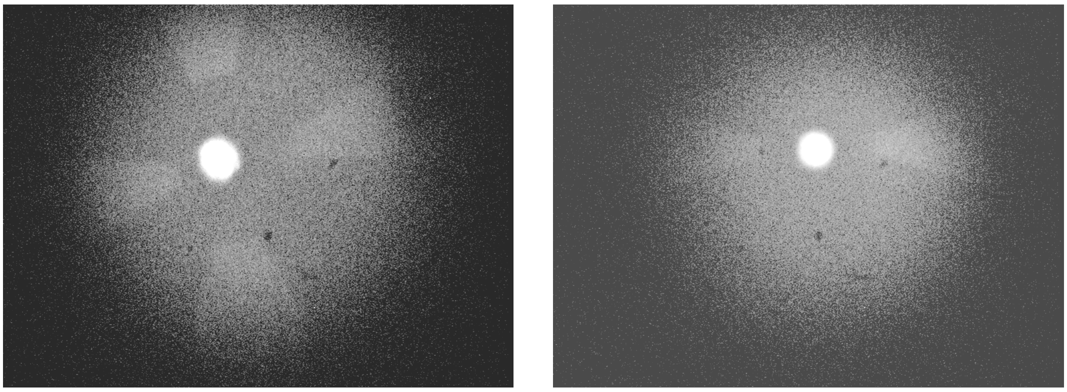

(a) (b)

Figure 4.3: Infra-red shifted optical image of the 1550nm laser front-side coupled for detectors (a) B17 and (b) C10. The substrate is transparent to the incident light, so Au cross markers are used to help position the spot of the fibre over the device. (a) uses four markers, whereas (b) uses 2. Contrast has been increased for clarity.

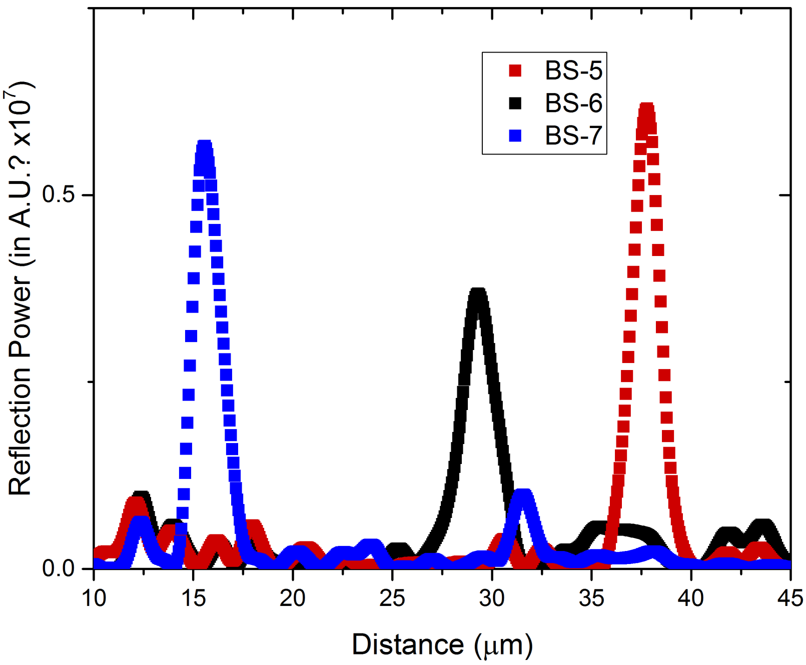

Figure 4.4: OCT measurements for NICT devices. The fibre distances were 37.7μm, 29.3μm and 15.6μm for devices BS-5, 6 and 7 respectively.

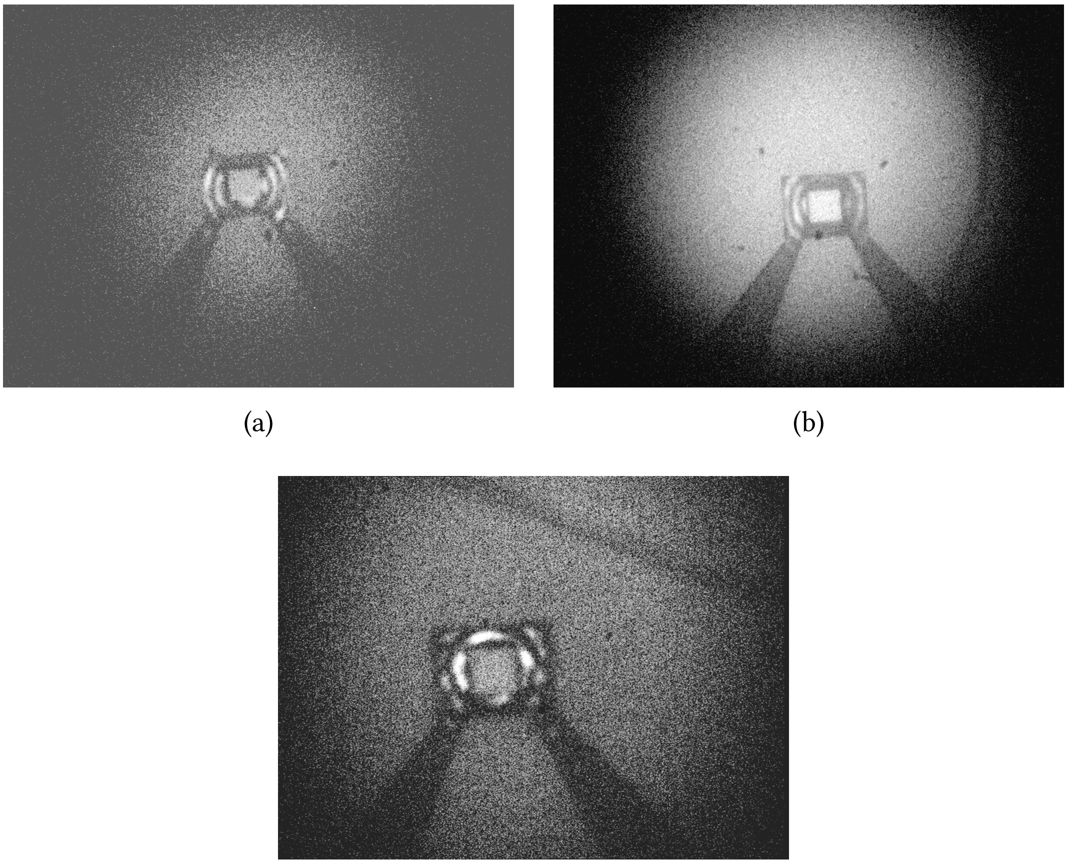

(a) (b)

(c)

Figure 4.5: Infra-red shifted optical image of the 1550nm laser backside coupled through the detector. The SNSPD is the grey square in the centre, which absorbs the majority of the laser light. The surrounding structure is invisible to 1550nm light, allowing a clear view of the airy discs. (a) and (c) show the alignment of device BS-5 and BS-7 respectively; the Airy rings are evenly lit suggesting excellent laser spot alignment onto the device. (b) shows the alignment of device BS-6; the left region is brighter, suggesting the measured efficiency of the device will be partially lower than expected. Contrast has been increased for clarity.

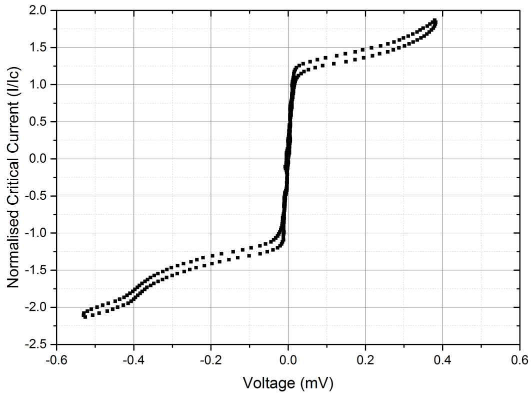

Figure 4.6: I-V characteristics of device C10 using a 50Ω shunt at 2.2K. The device achieved a critical current of 7.5μA

4.3 Cavity Device Results

4.3.1 Frontside Coupled Delft Devices

Current-Voltage Characteristics

A measurement of the I-V characteristics of the Delft devices was performed in the Zephynator at 2.2K, as shown in Figure 4.6. The best performing Delft device, C10, had a critical current of 7.5μA.

SDE Measurements

An SDE measurement was performed on all Delft devices in the Zephynator at 2.2K using a polarisation controller, which was manually aligned to record the highest and lowest measurements of SDE (Figure 4.7). C10 achieved an SDE of ∼16% at 1kHz DCR. This is much higher than the result recorded by Tanner[2] *et al*, using a similar device under 1550nm light illumination at 2.8K, who achieved 7.8% at 2.8K.

Between 1.0-1.2kHz DCR, the device achieved an SDE of 16.1% for aligned polarisation and 9.1% for low polarisation alignment, giving a high dependence on polarisation at ∼57%. It is also possible the polarisation is aligned only to a local maximum/minimum, rather than its highest/lowest possible value, as the polarisation alignment in the Zephynator setup is a manual process. At higher bias currents, there is an expected saturation in the SDE. This occurs due to the device reaching its peak registering efficiency, as discussed in §2.3.3. Registering Efficiency.

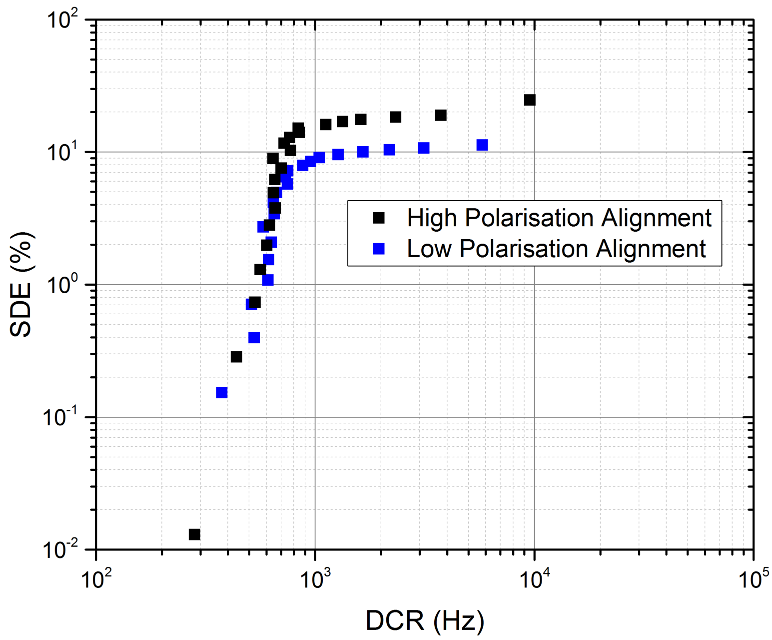

Figure 4.7: SDE measurement for Delft device C10, showing its dependence on polarisation alignment.

WaSTe Measurements

A WaSTe measurement was performed in the Kelvinator at 3.5K using an input wavelength range of 1330nm to 1650nm over 32 separate wavelengths, shown in Figure 4.8(a). The polarisation dependence between high and low polarisation alignment is also graphed in (b). There is an increase in SDE as the wavelength nears the cavity optimised 1310nm, which matches simulations performed by Tanner[2] *et al.* Though the size of the SDE variation from the change in polarisation *decreases* with increasing wavelength (Smaller black vertical lines), the value of polarisation dependence - the relationship between min and max SDE - actually *increases*, as shown in (b). When the wavelength is optimised for the cavity, all polarisation orientations will see an increase in absorbtion effiency and, thus, SDE. As the wavelength moves away from the optimised cavity length, the polarisation dependence increases, as discussed in §2.3.3. Polarisation Dependence.

4.3.2 Backside Coupled NICT Devices

Current-Voltage Characteristics

The NICT devices were characterised in the Zephynator at 2.2K and the Rankinator at 0.38K (Figure 4.9). The NICT device BS-6 had a critical current of 9.0μA and ∼14.5μA respectively. As expected, at lower temperatures the device exhibits a larger critical

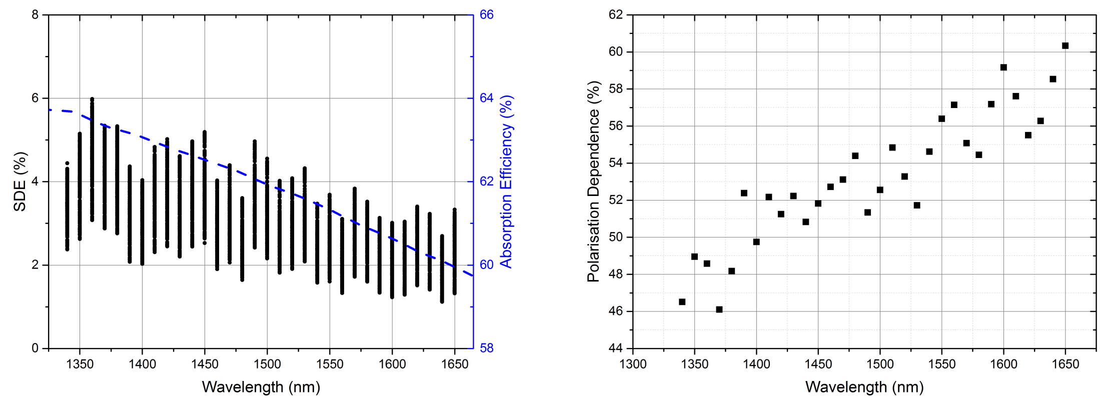

(a) (b)

Figure 4.8: (a) WaSTe measurement for device C10 including absorption efficiency curve. (b) Polarisation dependence against wavelength.

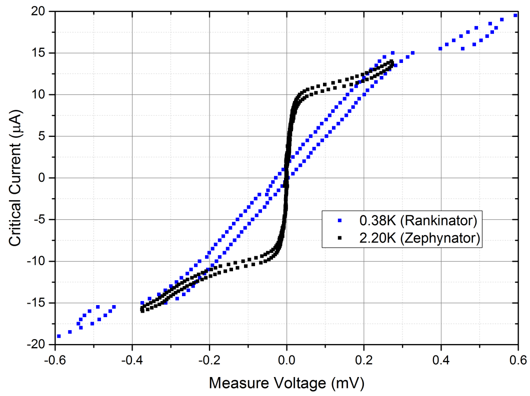

Figure 4.9: I-V characteristics of device BS-6 measured at 2.2K in the Zephynator and 0.38K in the Rankinator.

current. There is a series resistance in the Rankinator setup of $\sim 20\Omega$, which is noticeable compared to the Zephynator, which has a negligible series resistance. This is possibly due to the Be_2Cu wiring in the Rankinator, which has a slightly higher resistance than standard Cu wiring.

Pulse Shape & Timing Jitter

The jitter and pulse shape of the devices were recorded in the Rankinator at an applied bias of 14µA ($0.97I/I_C$) at 0.35K (Figure 4.10). Device BS-6 had a jitter of 140ps, with a pulse width of approximately 2ns. Other NICT devices have achieved much lower jitters at 68ps. The pulse is large with a high SNR due to the low operating temperature. The decay of the pulse shape consists of two regions of in-series inductors. The main nanowire meander has a decay rate around ~1.13ns, indicating a kinetic inductance of 56.6nH.

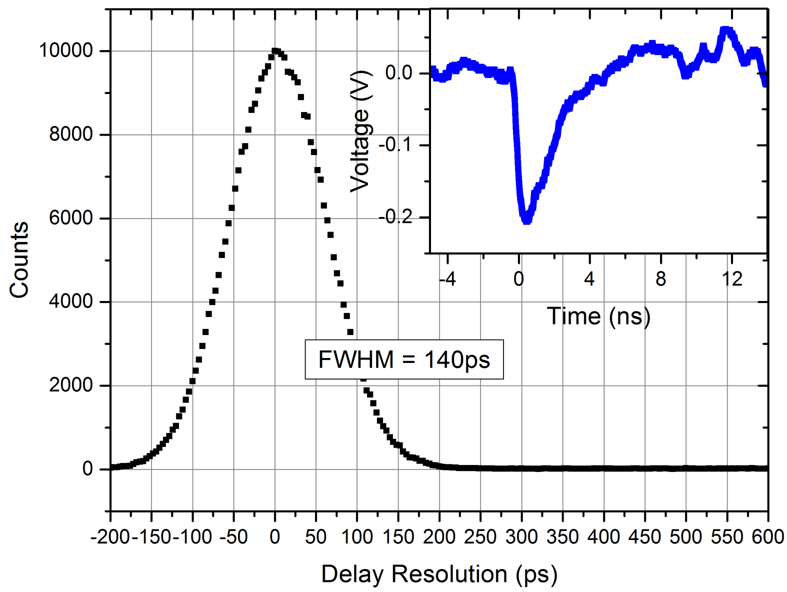

Figure 4.10: Jitter of NICT device BS-6 at 0.35K under an applied bias of 14μA ($0.97I/I_C$) with pulse shape inset.

SDE Measurement

A series of SDE measurements on the NICT devices were performed at 3.5K in the Kelvinator and at 0.35K in the Rankinator. BS-6 was tested in both fridges at different temperatures. At 1kHz DCR, it achieved an SDE of 48% and 31% at 0.35K and 3.50K respectively (Figure 4.11 (a)). The device was also tested in the Zephynator at 2.2K under high and low polarisation regimes, achieving an SDE of 43% at 1kHz DCR (Figure 4.11 (b)). The best devices fabricated by Miki[4] *et al* have achieved efficiencies ∼70%. The low comparison may have been due to poor alignment when using the fibre-alignment rig.

Device BS-6 has significant temperature dependence, which is explained by the significantly lower DCR in the Rankinator at 0.38K, compared to the Kelvinator at 3.5K. This is due to a difference in the radiation shielding of the fridges, where the Kelvinator uses a 50K shield the Rankinator uses a 3K shield, which significantly lowers the BBR in the chamber. The lower temperature of the device also allows for a higher bias current, leading to increased registering efficiency. The device also has a high polarisation dependence of 35% due to its higher fill factor from its smaller nanowire gaps (60nm).

WaSTe Measurement

A WaSTe scan was performed between a wavelength range of 1330nm to 1660nm every 5nm for each NICT device (Figure 4.12). In both Device BS-6 and BS-5 there is a trend of increasing SDE as the wavelength nears the optimised wavelength of the cavity. This is

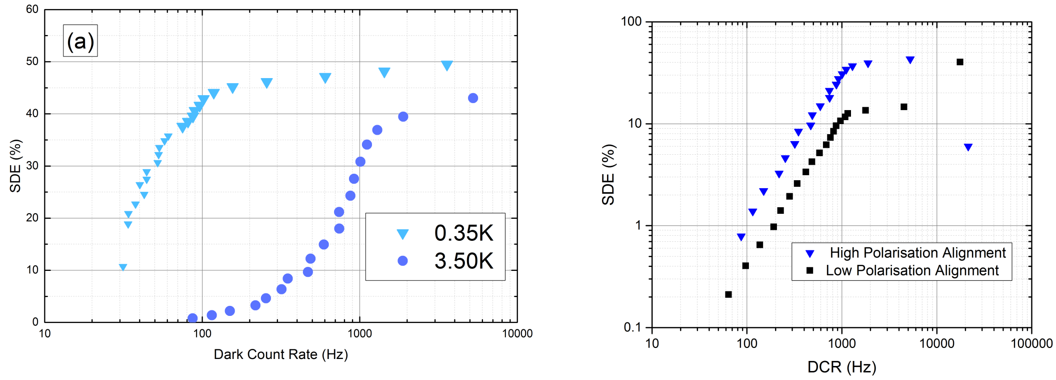

(a) (b)

Figure 4.11: (a) SDE Measurement for NICT device BS-6, comparing temperature dependence at 0.35K and 3.5K. (b) SDE measurements at high and low polarisation alignment.

expected from the simulations performed in §4.2. Optical stack absorption simulation for NICT and Delft NbTiN detectors, the results of which have been included on the graphs. Both devices show a large polarisation dependence ∼67%, which is larger than the 50% dependence found in the Delft, single cavity devices. This could be due to the extra cavity in the NICT device, which should increase the device's maximum SDE for all incident photon orientations, but have a more significant effect on photons with the correct orientation. For device BS-6 there is a significant jump at 1520nm wavelength. This jump could occur due to a poor power calibration measurement (§3.4.5. WaSTe Measurement); it is likely the calibration measurement was recorded while the laser was still warming, causing an unreliable power reading.

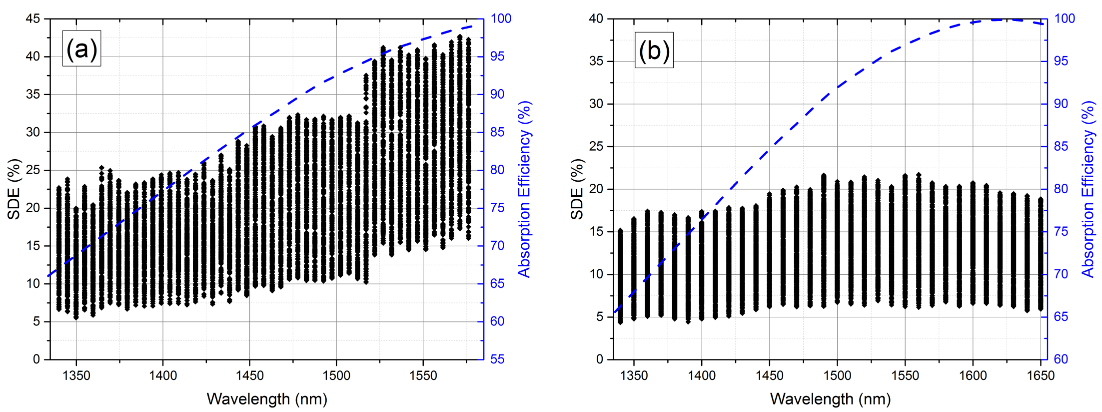

Figure 4.12: WaSTe measurement scans for devices (a) BS-6 and (b) BS-5. These show high correlation with the absorption curve simulation based on these devices. BS-6 shows a much higher SDE compared to BS-5.

Projected Performance in a QKD Link

A simulation of the T12 protocol was performed using the results of DCR with SDE collected from device BS-6 characterised at 0.35K (Figure 4.13). The process of decoy state QKD and the T12 protocol are discussed in more detail in §2.4.4. Decoy State QKD. The simulation was performed using an increasing communication distance, which was represented by a signal decay rate caused by the loss at 1550nm light through Si optical fibre.

Over 230km the SNR is too small and the key rate drops dramatically. This is due to the DCR dominating over the signal strength with a corresponding increase in QBER above the secure threshold. At 220-230km the protocol is still capable of generating a positive key rate. These results suggest this device could be used to establish the T12 QKD protocol between cities across the south of the UK (∼150-250km).

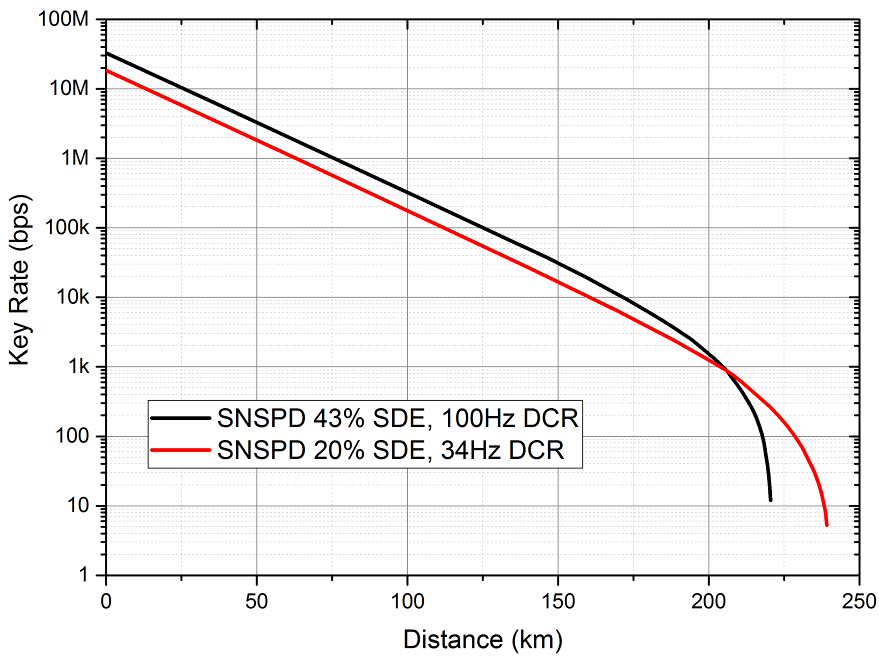

Figure 4.13: Simulation of secret key creation rate over increasing distance using the results collect from NICT device BS-6 in the Rankinator at 380mK. Courtesy of Dr. Andrew Shields, Toshiba European Research Laboratory, Cambridge.

4.4 Conclusion

Two groups of NbTiN cavity SNSPDs were fibre-coupled and characterised between 0.35-3K. Two were single cavity Delft devices (B17 and C10) and three were double cavity NICT devices (BS-5, BS-6 and BS-7). The devices all achieved high critical currents

$\sim$10μm at 2.2K, which is expected for NbTiN. For the single cavity devices, the Delft detectors achieved lower values of total SDE $\sim$15% and the double cavity NICT detectors achieved higher SDEs $>$20%. Cavity resonators continue to present a viable method for both reducing polarisation dependence and increasing the SDE of meander SNSPDs. Peak SDE was achieved by BS-6 at 43% under a DCR of 1kHz at 0.35K, which may be an effect of poor alignment as previous NICT devices have achieved higher SDEs $\sim$70%.

Both sets of devices showed strong polarisation dependence, which is expected for a meander structure, particular in NbTiN, which has a low extinction coefficient. The polarisation dependence in the NICT devices was $\sim$67%, slightly higher than the Delft devices at $\sim$50%.

The fibre-coupling of packages worked as intended allowing for easy transfer of devices between cryostats. Device BS-6 showed a slight misalignment of the fibre in the crucible, suggesting a higher SDE could be achieved if realigned. The results of device BS-6 were used to perform a simulation of the T12 QKD protocol over an increasing distance. With its low DCR and high SDE, the simulations showed this device could achieve a positive key generation rate at 1kbps over a distance of 200km. This device could be used in T12 QKD protocols spanning cities across the south of the UK, between 150-250km.

Chapter 5

MoSi Devices

This chapter focuses on two batches of amorphous MoSi devices; a series of 4-pin test structures, studied to extract the transport properties of MoSi films and hairpin nanowire devices for applications in integrated optics. This is detailed in §5.1. Overview & Motivation. §5.2. Device, Design & Fabrication describes the structure of the devices. The 4-pin test structures were characterised in the Kelvinator, to measure their transport properties, and in the Rankinator, to map their responsiveness. The hairpin structure was characterised in the Rankinator to analyse its uniformity. These results are discussed in §5.3. Results.

5.1 Overview & Motivation

Linear optical quantum computing can be applied through the use of quantum dots as photon sources, beam splitters and phase shifters as gates and SNSPDs as detectors. In order to realise monolithic chip quantum computing, these components will need to be scalable. This requires SPDs that can be integrated with optical waveguides and achieve high performance metrics including SDEs above 90%. Improving performance metrics requires varying all steps of device fabrication and characterisation. Part of the focus of the work at Glasgow was to begin sputtering films for device fabrication using Plassys VI. The optimisation of these processes was studied by Dr. Archan Banerjee[70].

It is thought that high SDE devices can be achieved with low carrier density materials such as WSi[5] and MoSi[64]. These films offer higher absorption efficiencies, but require lower operating temperatures, which leads to a lower bias currents. Though these devices can operate at base temperatures of 2-3K, their SDE is much lower then when operating below 1K. The high absorption efficiency of these materials can be integrated with Si waveguides to realise hairpin nanowire devices. (As has been discussed in §2.3.3. Waveguide Integrated SNSPDs) MoSi hairpin nanowires achieve almost unity absorption efficiencies for incident light coupled through the waveguide.

The work in this chapter aimed to characterise the films sputtered using the optimisation recipe developed by Dr. Archan Banerjee. This involved fabricating several nanowires of increasing thickness and measuring the current-voltage characteristics of the devices over a range of temperatures. From this it was possible to extract a value of the energy gap, allowing a comparison of the transport properties of the film to literature. This work also involved characterising a MoSi hairpin nanowire device, sputtered using a recipe developed by Dr. Zoe Barber and Dr. David Bosworth at Cambridge University. The device was fabricated at Glasgow by Dr. Robert Kirkwood and then characterised with the aid of Dr. Jian Li in the Rankinator. By scanning perpendicularly across the responsive region of the hairpin it was possible to prove the device's uniformity and thus establish its viability as a component in a Si optics monolithic quantum computer.

5.2 Device, Design & Fabrication

5.2.1 4-Pin Test Structures Design

In order to characterise the transport properties of the sputtered MoSi, 4-pin test structures or 'Bridge' structures needed to be fabricated. These test structures consisted of 50μm long nanowire at widths of 100, 200, 300, 400, 500nm, 1 and 2μm and were connected to 4 contact pads, to achieve 4-pin measurements (Figure 5.1).

5.2.2 4-Pin Test Structures Fabrication

Nanowire Errors

Bright Spots

Images of the nanowire structures were taken using the SEM after etching and some of these are shown in Figure 5.2. There was an unexpected defect in the nanowires (that can be seen most clearly in the 200nm image); the nanowire appears to have a bright central channel with darker edges. As the SEM images are created by back-scattered electrons, the brightness relates to the properties of the material. As this colouration is one continuous band, it is likely this is left over resist that was not successfully removed after

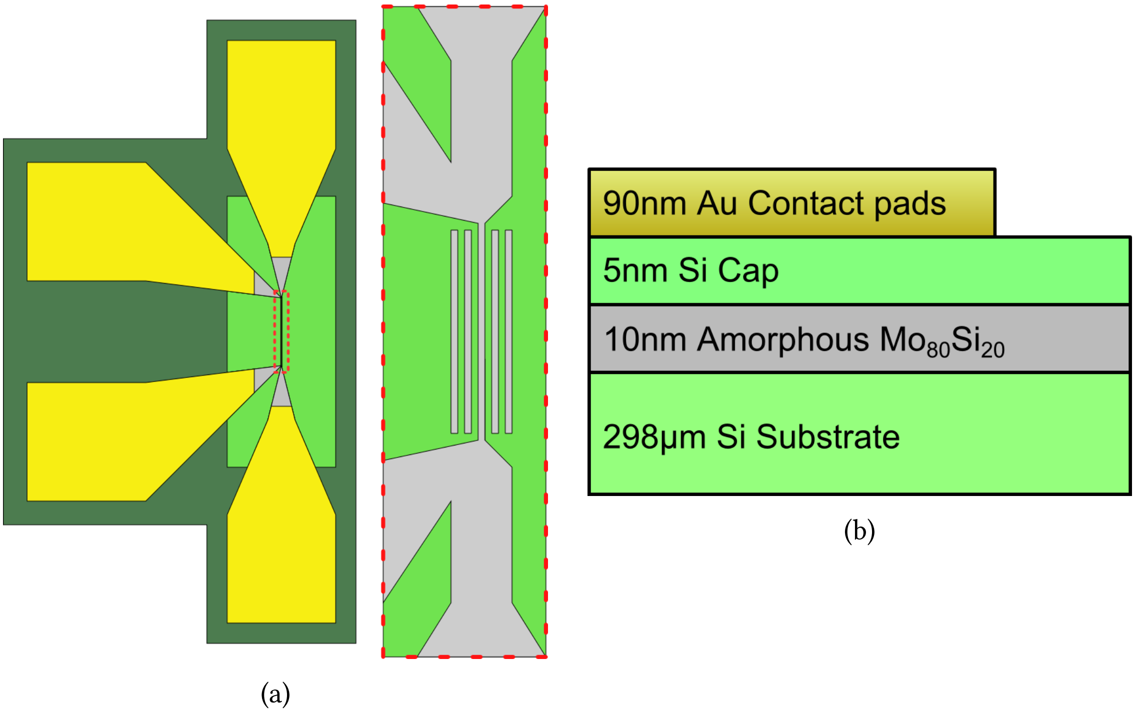

Figure 5.1: (a) 4-pin nanowire test structures design and material stack (Not to scale). The green regions are E-Beam patterns for etching, with the lighter green region using a smaller beam size. (b) Device materials stack, 90nm Au contact pads with a 5nm Si cap on 10nm $Mo_{80}Si_{20}$, with a substrate of 298µm Si.

being soaked in 1166-Stripper. This is likely to have little to no effect on the properties of the nanowire.

Film Redeposition and Non-Uniform Edges

There are non-uniform and bright parallel lines at the edges of the nanowires. This is caused by the effect of material redeposition, as was discussed in §3.1.5. Film Redeposition. The etched material has latched back onto the tops and sides of the nanowire. The redeposited material can have some effect on the transport properties of the nanowire. Besides this effect, the edges of the nanowires are clearly non-uniform. This indicates the nanowire will experience constriction effects, as discussed in §2.3.3. The Effect of Nanowire Constrictions. This will partially reduce the maximum value of the J_C, the maximum bias of the devices and also the registering efficiency.

Variation in Nanowire Size

The widths of the nanowires after fabrication were determined by analysing the SEM images of the nanowires using the image processing software *ImageJ*. They were measured from the absolute edge of each nanowire, including the effects of film redeposition. The results of the measurements returned a significant decrease in the intended nanowire widths, which are detailed in Table 5.1. A pattern-negative was used to design the nanowires and it is likely this pattern was developed larger than intended, shrinking

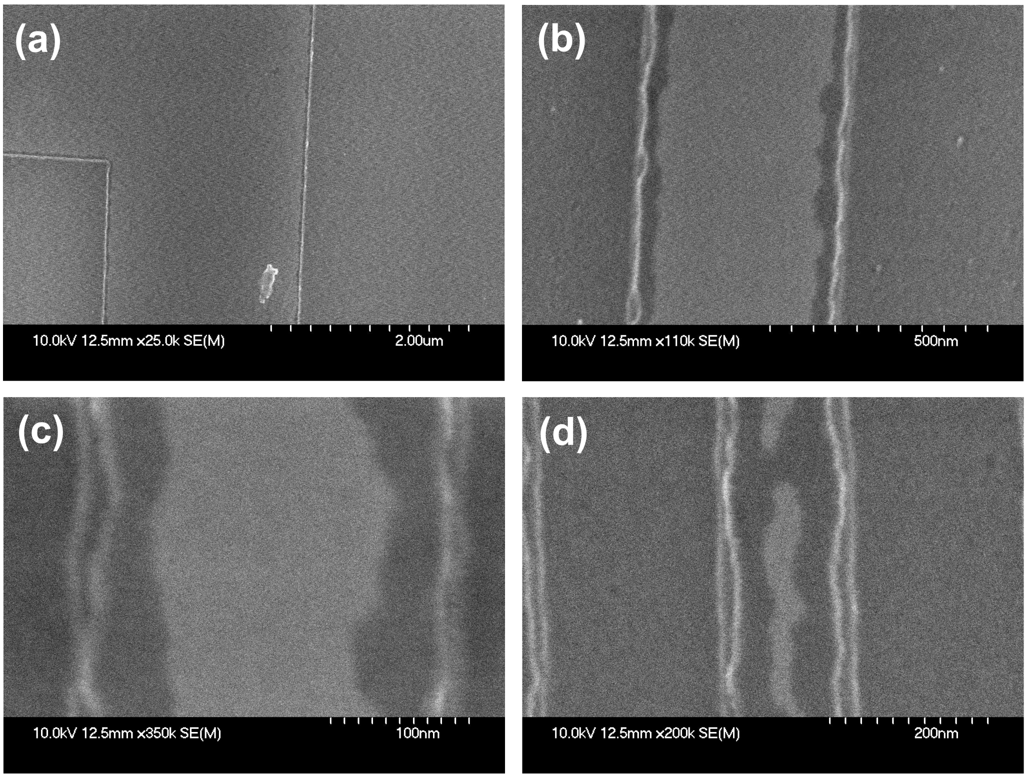

Figure 5.2: SEM images of nanowires after etching process for nanowire widths (a) 2µm, (b) 458nm, (c) 258nm and (d) 173nm.

the nanowire sizes. This could have been caused by too high a dose, but it is more likely the ZEP used during the spin process had become denser due to the evaporation of the anisole solvent over time. This caused the smallest nanowire (S27383_500) to become disconnected. The second smallest wire (S7383_250) also did not return reliable readings for resistance. Despite these imperfections, the other nanowires still achieved a working current, albeit at reduced widths.

In order to retrieve material properties from the devices, the test structures were characterised in the Kelvinator cryostat (See §3.4.1. Additional Cryostats) between transition temperature ranges of 3.5K and 7.0K. The temperature was manually altered by switching off the pulse tube and warming the cryostat above the critical temperature of the devices, around 6.2K. The pulse tube was then switched back on until the cryostat reached base temperature again at 3.5K. The warming and cooling of the cryostat occurs quickly; a transition from 3.5K to 6.5K takes ∼2m 35s, while the reverse cooling transition is non-linear, with the cryostat rapidly descending to 4K in under a minute before taking an extended time to reach 3.5K. A similar effect occurs in the Zephynator. By contrast, the Rankinator, though it can achieve much lower temperatures, either takes too long to transition ∼30m between 7 and 4K or transitions equally quickly, ∼1m between 2K and 0.35K (See Figure 5.3).

Device	Design Sizes (nm)	Measured Wire Widths (nm)
25	2000	2003
50	1000	957
100	500	459
125	400	364
167	300	258
250	200	173

Table 5.1: List of design wire widths and measured widths. The reduction in size is due to fabrication error.

Short Integration Time Measurements

The Keithley 238 source and measurement unit has a fast integration time at 416µs, which allows for over 2000 measurement points per second and is more than adequate for the rapid change in temperature in the cryostat. The Keithley box uses separate units to measure voltage and, though the units are individually fast, the Keithley requires about a second to switch between each unit. This limits the rate of data acquisition; measuring a full range I-V curve takes around 15s. During warmup, a 15s time interval corresponds to a 0.5K discrepancy and during cooldown returns a discrepancy of 2K for measurements above 4K. Each measurement sweep took into account the discrepancy in temperature as an error.

5.2.3 Hairpin Structures

Hairpin waveguide devices achieve single-photon detection through a waveguide circuit. A method such as this offers almost unity absorption efficiencies and can be integrated with Si waveguide gates for applications in QIP. As mentioned in §2.3.3. Waveguide Integrated SNSPDs, the short nanowire length of the hairpins corresponds to a low inductance in the device, which also leads to a fast reset time. A short reset time would normally be ideal for a higher count rate, but is too fast in this case. The 200nm wide bank meander regions act to slow the reset time by increasing the device's inductance, whilst not being responsive to incident single photons, such that only the hairpins respond to the incident light. The design of the hairpin is shown in Figure 5.4 and the full

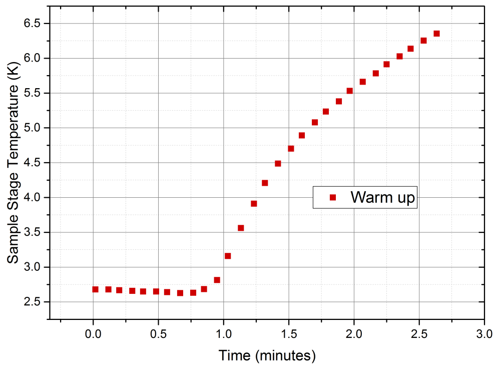

(a)

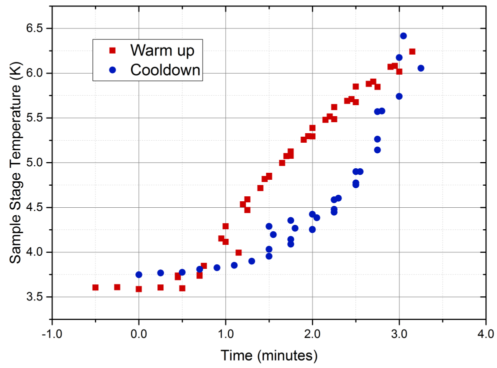

(b)

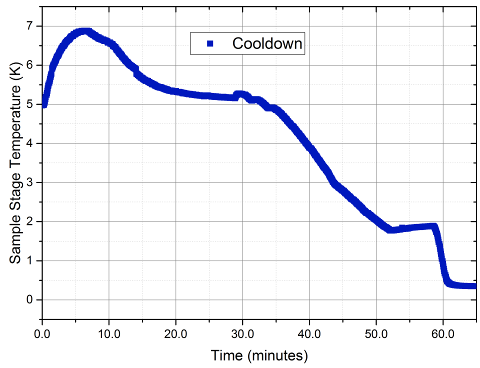

(c)

Figure 5.3: Speed of cryostat temperature changes for (a) Zephynator, (b) Kelvinator and (c) Rankinator.

fabrication procedure is detailed in §3.1.7. Fabrication Process for MoSi Structures. The hairpins were 140nm wide nanowires, with a 90nm gap, confirmed by AFM measurements in Figure 5.5.

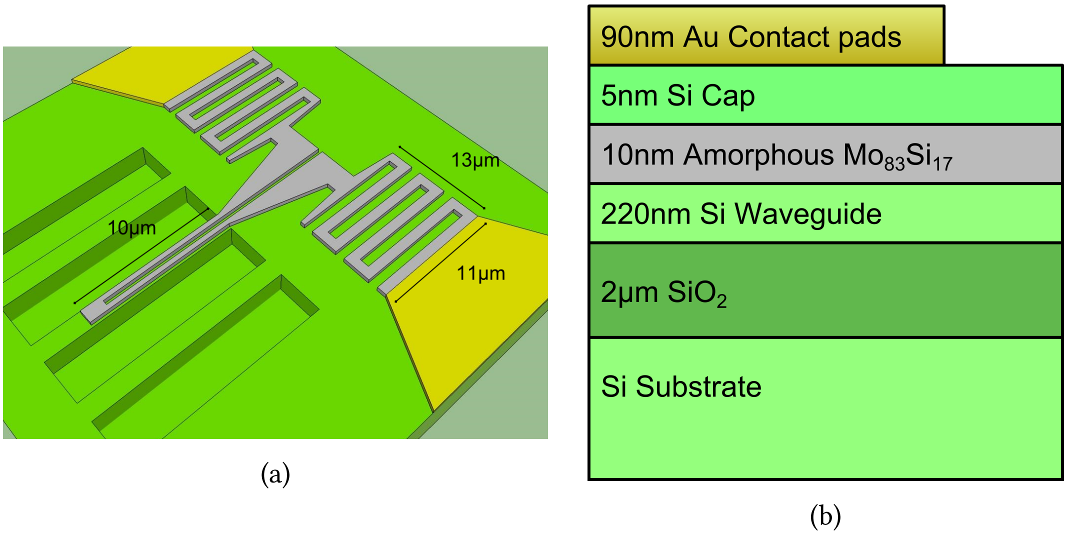

Figure 5.4: (a) Hairpin nanowire design (Not to scale). The 10μm long hairpins are 120nm wide wires with a 140nm gap. It sits on a 500nm wide and 220nm tall waveguide. The bank meander regions are 200nm wide with 90nm gaps, which act to increase the reset time whilst being unresponsive to single photon light. (b) The device has a 5nm Si cap, 90nm Au contacts and sits on an Si-on-Insulator (SoI) substrate. The 600μm Si substrate has a 2μm SiO_2 layer on top before a 220nm Si layer.

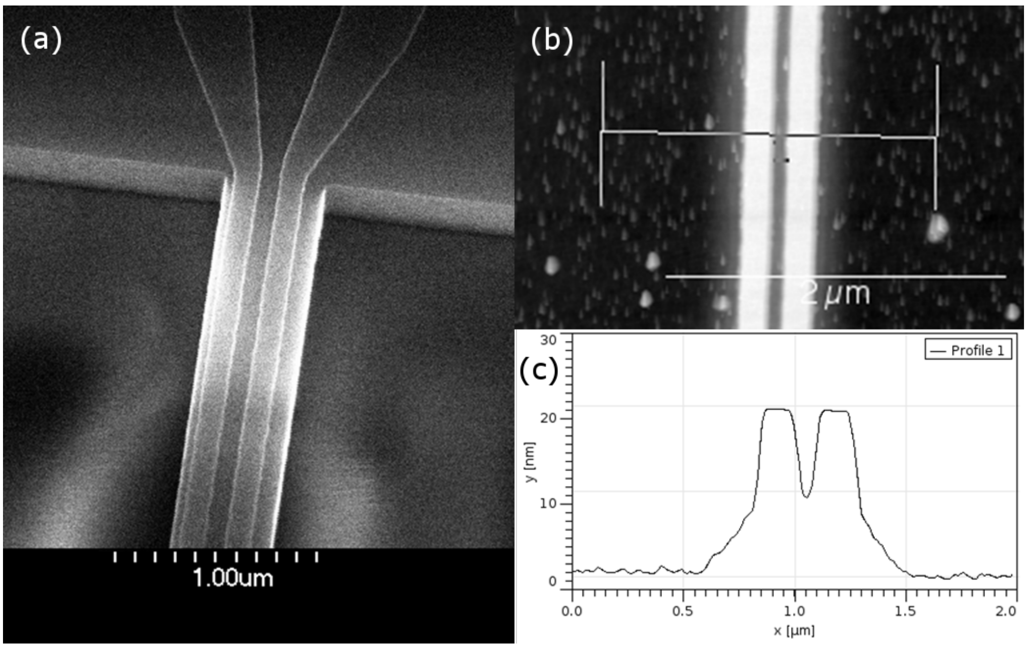

Figure 5.5: (a) SEM image of MoSi hairpin on 220nm Si waveguide. (b) SEM measurement of hairpin width. (c) AFM measurement of hairpin thickness and width. The nanowires are (140 ± 2)nm wide with a (90 ± 2)nm gap. The gap forms a triangular join due to the triangular tip of the AFM cantilever. Images taken by Dr. Robert Kirkwood.

Perpendicular Optical Stack Simulation for MoSi Hairpin

As discussed in §2.3.3. Waveguide Integrated SNSPDs, hairpin devices, particularly MoSi hairpins, have almost unity absorption efficiency for in-plane coupled 1550nm light. As this device is designed for in-plane coupling and does not possess a purposeful optical cavity, it does not show high absorptive features at a defined wavelength. The spectral response of an infinite thin plane of $Mo_{83}Si_{17}$ was simulated for perpendicularly coupling light on a 1D optical stack mimicking the layers of the integrated waveguide of the hairpin device, using an infinite air gap and infinite Si substrate, as shown in Figure 5.6. It has a relativity low absorptance at 1550nm of 46.01%. There is an unwanted optical cavity in this stack, created by the 220nm Si segmeant, which is of an appropriate size to interfere destructively with incident 1460nm light and to a lesser extent with 1550nm light.

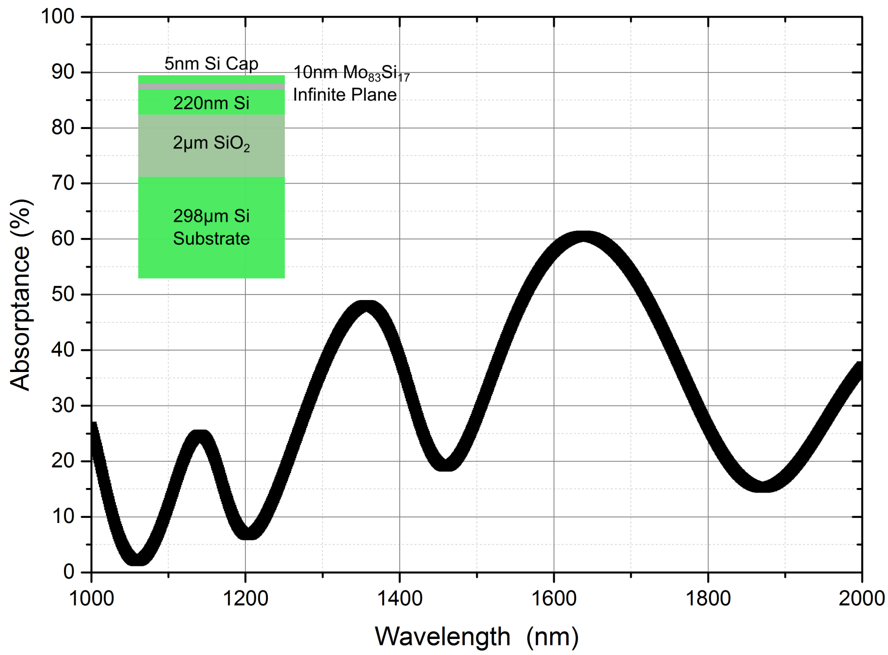

Figure 5.6: Optical stack absorption efficiency simulation for MoSi Devices. The absorption efficiency is low at 46.01% for 1550nm light. Simulation performed by Dr. Robert Heath.

5.3 Results

5.3.1 4-Pin Test Structures

Resistance per Square

The test structures (S27383_Spades) were measured using a 4-pin probe setup at room temperature. Using the measurements of nanowires widths collected in Table 5.1, an estimate of the resistance per square of each device could be collected, as shown in Table 5.2. The nanowires returned a range of values between (259 ± 74)mΩ/sq. Research by Korneeva[64] *et al* on MoSi films with similar stoichiometry achieved resistances of 430mΩ/sq for 4nm films. The relationship between this value and film thickness is linear and translating this result from a 4nm to 10nm film returns a value of 172mΩ/sq. Though the full range of nanowires does not match this value, for wider nanowires it does approach it; 184mΩ/sq and 188mΩ/sq for the 2003nm and 957nm wide wires respectively. As the width decreases, the square resistance diverges more dramatically. This could be explained by the inhomogeneity during nanowire fabrication. As discussed in §5.2.2. Film Redeposition and Non-Uniform Edges the edges of the nanowires have been damaged due to the severe etch, causing some redeposition at the edges. The strength of this effect is proportional to the nanowire width and would have the strongest effect on the thinnest nanowire.

Device	**Measured Wire Widths (nm)**	**Resistance per Square (mΩ/sq)**
25	2003	184
50	957	188
100	459	201
125	364	247
167	258	325
250	173	950 - 578

Table 5.2: List of nanowires and corresponding resistance/square for S27383_Spades 4-pin test structures. The resistance measurements returned for device S7383_250 fluctuated between two extreme values and was considered unreliable. Device S27383_500 failed to conduct.

Current-Voltage Characteristics

The test structures were cooled and warmed between 3.5K and 7.0K, while rapid I-V characteristics were recorded using a 50Ωshunt and this was repeated for all working test structures. The I-V characteristics against temperature of two wires (957nm and 173nm) are depicted in Figure 5.7. As expected, critical current is proportional to nanowire width and inversely proportional to device temperature. The thicker nanowire shows a larger jump in voltage when switching because of the larger applied bias range.

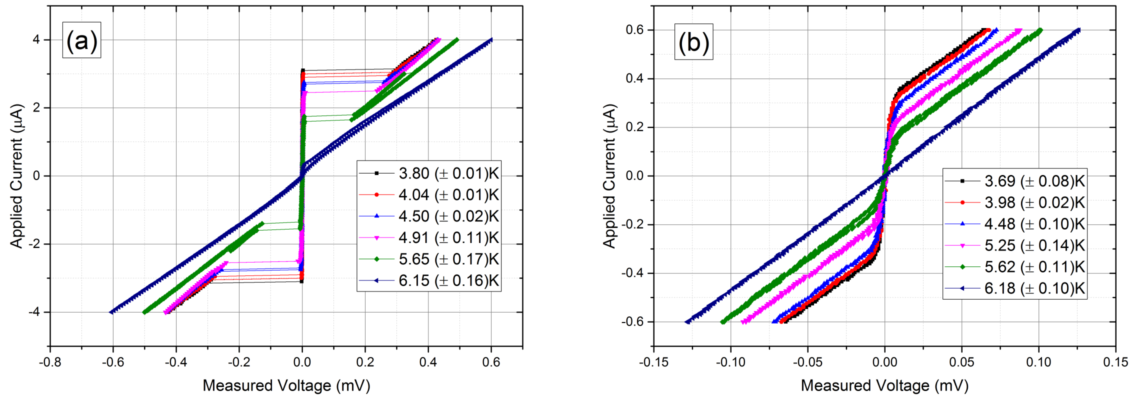

Figure 5.7: I-V characteristics of 10nm MoSi 4-pin test structures against temperature for device (a) Spades_50 (957nm) and (b) Spades_250 (173nm).

Critical Current Density versus Temperature and Wire Width

By using previous measurements of nanowire width and film thickness, values of the critical current density were calculated, as depicted in Figure 5.9(a). In Figure 5.9(a) the critical current density J_C shows a similar relationship with temperature for each nanowire width, but there is a trend for J_C to decrease with decreasing width, which is unexpected. A similar observation appears in the curvature of the $J_C(T)$, which becomes more pronounced with shorter width. As discussed in §5.2.2. Film Redeposition and Non-Uniform Edges, this could be a fabrication error related to the rough edges of the nanowires, which would have a more prominent effect on thinner nanowires. All structures achieved a critical current density within the range (0.280 ± 0.077)MAcm^{-2} at 3.8K for a 10nm film. In literature, this value for $Mo_{80}Si_{20}$ films has been measured by Lita[133] *et al*, who reported (0.7 - 1.4)MAcm^{-2} for 6.3nm films at 250mK and Korneeva[64] *et al*, who reported (1.6 - 2.5)MAcm^{-2} for 4nm films at 1.7K. Our experimental value is much lower than that of literature, but this could be due to our film being thicker (10nm) and $J_C(T)$ does appear to decrease with increasing film thickness. As this is a density measurement, it does imply that the critical current should be the same for all films with similar stoichiometry. However, thinner films are more susceptible to flux pinning, as discussed in §2.1.2. Flux Penetration, which may explain this trend.

Energy Gap

Each curve was fit to (Equation 2.5b) using a Levenberg-Marquardt fit to find the parameters of T_C and energy gap $\Delta(0)$ such that the squared sum of data points to the fit function was minimized, as shown in Figure 5.8. From this, $\Delta(0)$ was extracted for each nanowire Figure 5.10(a). Lower values of energy gap were returned during the fit for a data fit that returned a low R^2 value. As the worse fits occurred in the thinner nanowires, this suggests fabrication errors have significantly altered the transport properties of the nanowires. Accounting for all nanowires, an average of the measured results returns $2\Delta(0) = (1.8156 \pm 0.0484)$meV. Korneeva[64] *et al* have measured the energy gap for bulk film MoSi, finding a value of $2\Delta(0) = 2.28$meV, which is a significant distance from the values measured in these experiments. It is likely this is related to the inhomogeneity at the edge of the nannowire caused by the redeposition of material during the etch. This effect would cause constrictions in the nanowire (§2.3.3. The Effect of Nanowire Constrictions), which would reduce the wires maximum critical current density. It is also important to keep note that there is a slight difference between these film thicknesses; the Korneeva films, from the Moscow group, were 4nm thick compared to our 10nm thick films.

Temperature Change Speed

One of the large hurdles in this measurement was the speed of the temperature change, which happens quickly, producing large errors in temperature measurements for the lower temperatures whilst warming up, and the higher temperatures whilst cooling down. This can be seen in the large errors of Figure 5.10(b). A more accurate approach would have been to use a Proportional-Integral-Derivative (PID) controller attached to heat switches in the system to set an array of static temperature states for measurement.

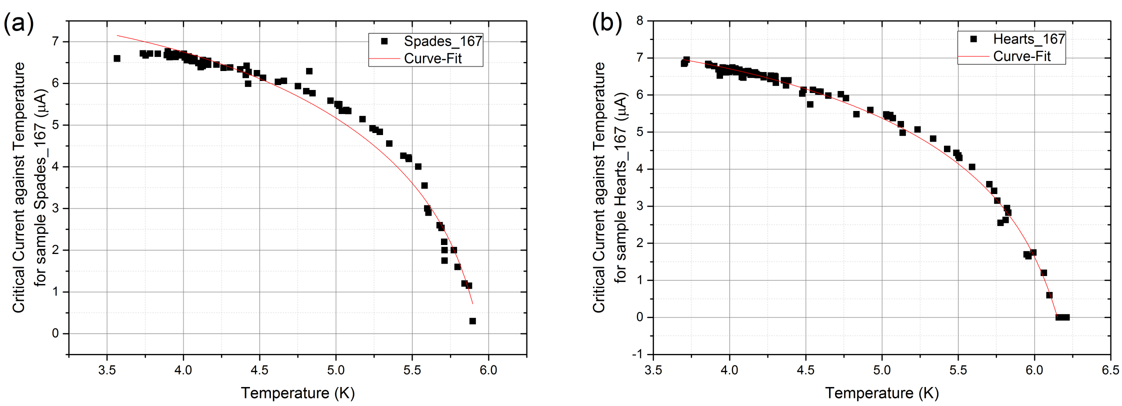

Figure 5.8: Graphs of the Levenberg-Marquardt fit of critical current data against temperature for devices (a) Spades_167 and (b) Hearts_167.

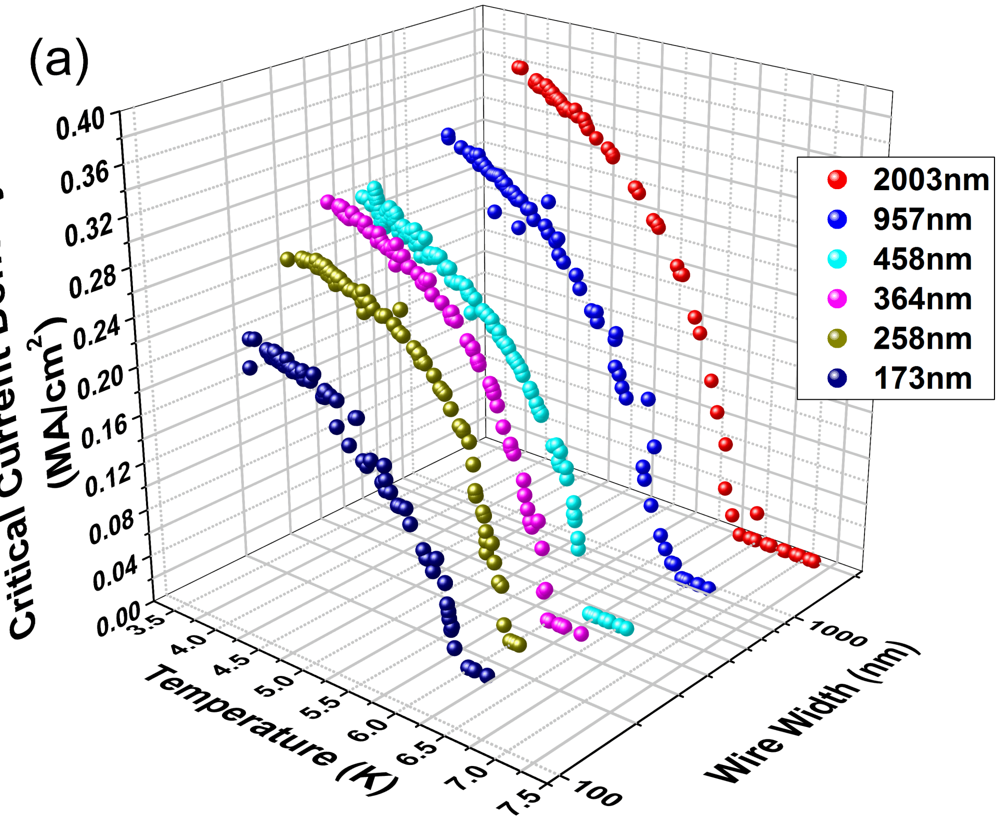

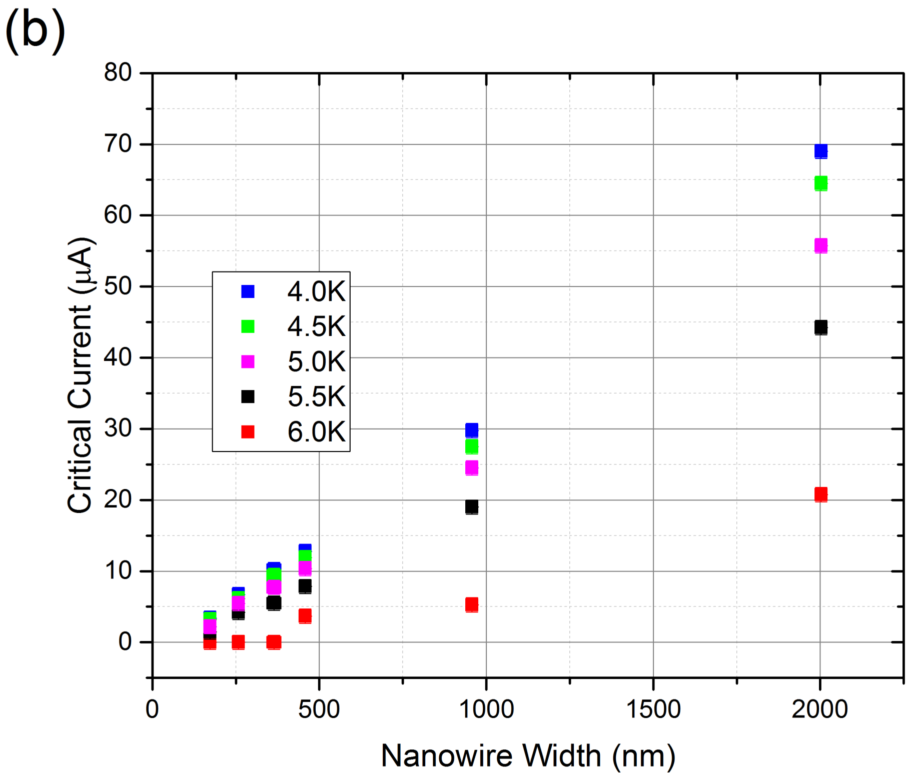

Figure 5.9: (a) Transport properties of different thickness of MoSi nanowire. (b) Cross-section of data at specific temperatures.

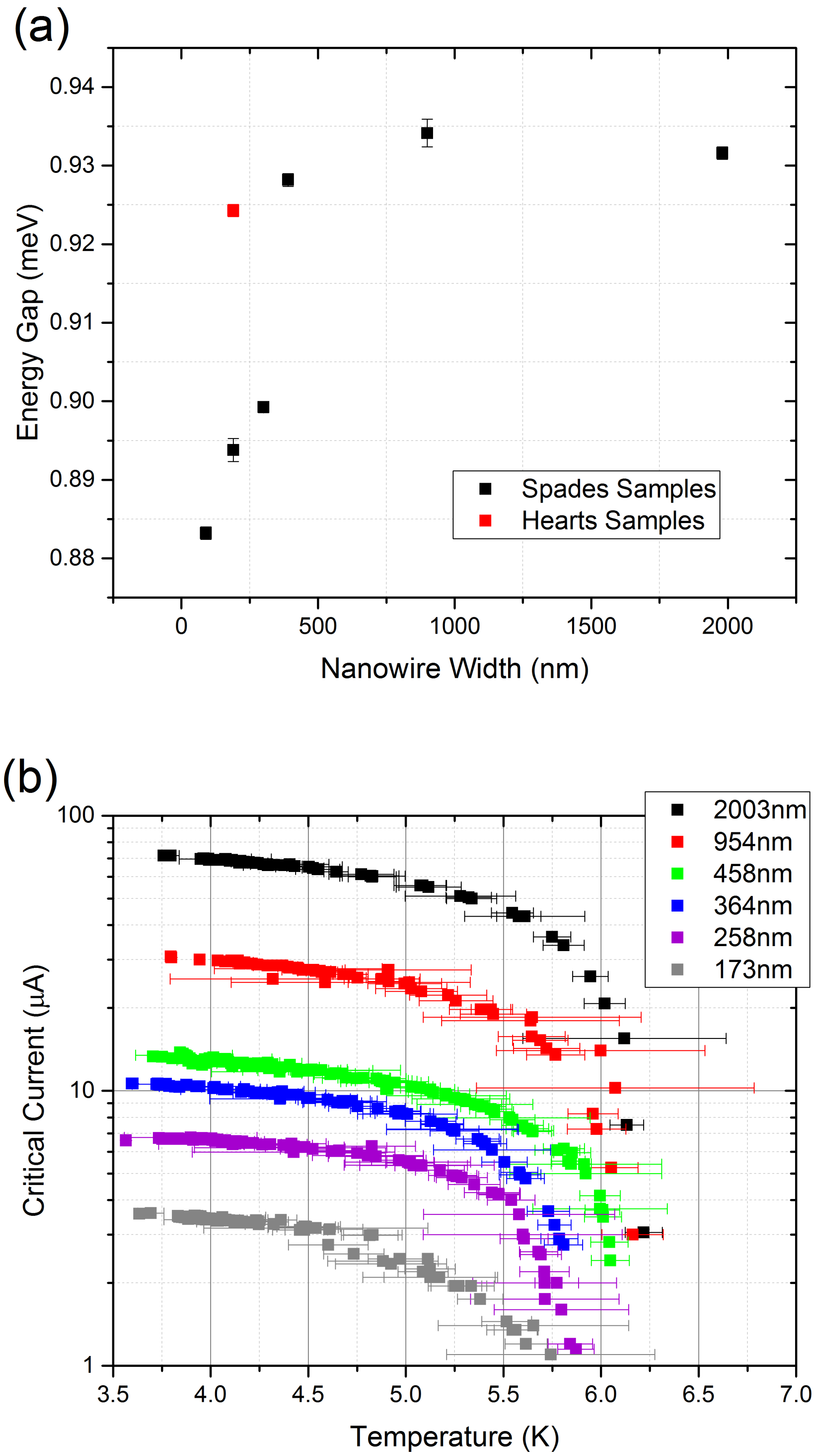

Figure 5.10: (a) Fitted values of $\Delta(0)$ using (Equation 2.4a) at 0K against nanowire width. (b) Critical current versus temperature for different nanowire widths.

Photoresponse Maps

Photon response maps were taken across a few of the nanowires in the Rankinator and Kelvinator at 5K, 2.5K and 400mK. The values of corrected flux have been included with each map; these values were calculated based on the size of the Gaussain spot and device width and can be found in §2.3.3. Perpendicular Coupling. All of the nanowires mapped featured constrictions (§2.3.3. The Effect of Nanowire Constrictions). Particularly, the constrictions appeared at the very ends of the nanowire length. This could be explained by a higher dose during fabrication at those specific points due to the disconnected parallel wires (See §3.1.4. Supplementary Nanowires). These additional wires were used to decrease the dose of the central nanowire, but they are partially shorter in length as to avoid contact with the guides leading off to the contact pads. Only one of the nanowires achieved a low efficiency single photon sensitivity (S27383_Spades_250 (173nm)), though this is to be expected as the width of the other working nanowire was far above the 110nm needed to achieve it.

As can be seen in Figure 5.12(f), there is a response across the entirety of the nanowire, but only for high input fluxes, well within the realm of the multi-photon regime. At the highest count rate, at a nanowire constriction, the value of SDE for each device has also been estimated.

Change in Photoresponse with Increased Flux

A photoresponse map was taken in the Kelvinator over device S27383_Hearts_125 at gradually increasing increments of input flux Figure 5.12. For low flux, the constriction is the prominent feature of the map above DCR. As the flux increases, entering the multiphoton regime, the rest of the nanowire becomes more responsive and the count rate across the nanowire equalises to that of the constriction.

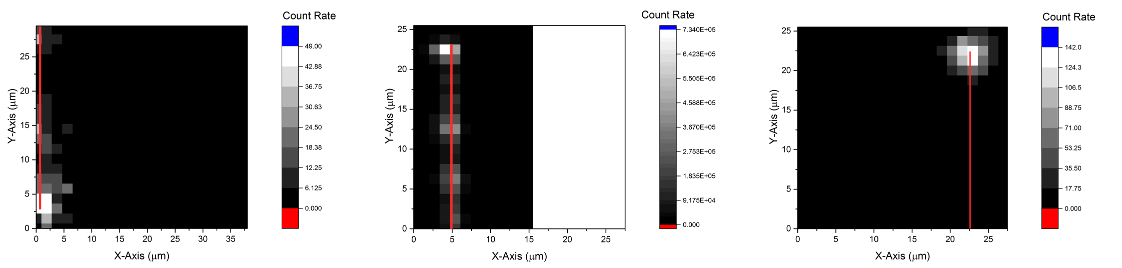

(a) (b) (c)

Figure 5.11: Photoresponse maps of MoSi test structures, sample S27383, recorded in the Rankinator. The nanowire's position is roughly marked by a red line. (a) Device Spades_125, thickness at 5.27K, 31.2µA bias and 620kp/p input laser flux. (b) Device Hearts_100 at 0.35K, 137µA bias and 620p/p. (c) Device Spades_250 at 0.35K, 22.5µA bias and 0.1p/p.

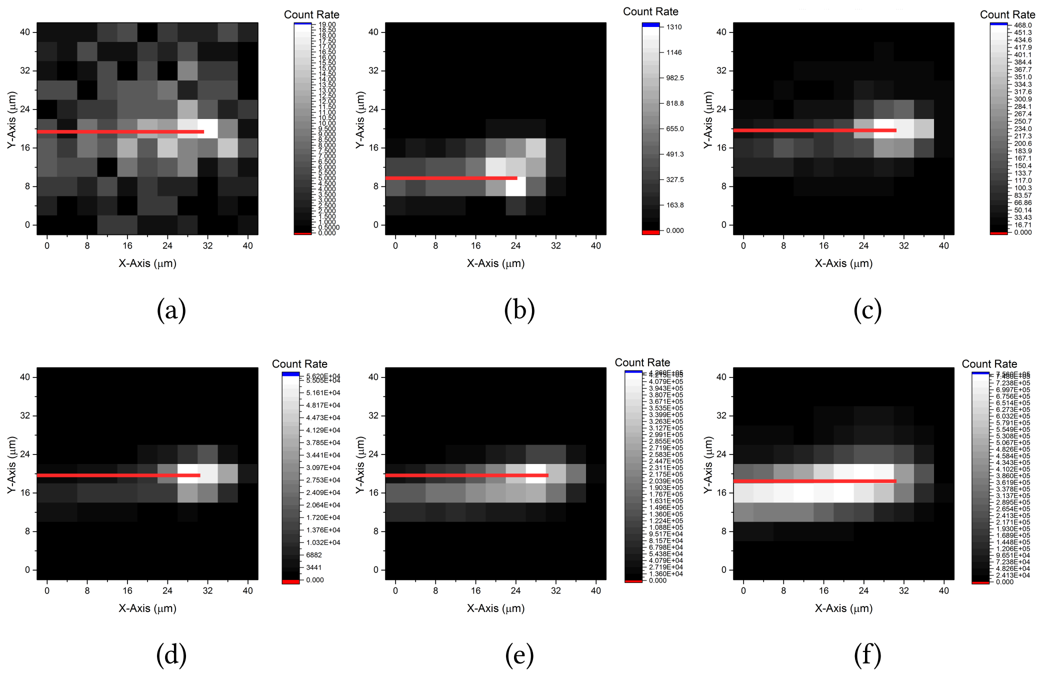

Figure 5.12: Photoresponse maps recorded in the Kelvinator at 3.5K of device S27383_Hearts_125, with a nanowire thickness of 364nm. The flux was increased gradually. The nanowire's position is roughly marked by a red line. (a) 4.43K, corrected flux: 6913p/p, SDE $\sim 0.27\%$. (b) 4.88K, corrected flux: 11kp/p, SDE $\sim 1.2\times10^{-5}\%$. (c) 4.43K, corrected flux: 17kp/p, SDE $\sim 2.7\times10^{-6}\%$. (d) 4.44K, corrected flux: 46kp/p, SDE $\sim 1.2\times10^{-4}\%$. (e) 4.44K, corrected flux: 69kp/p, SDE $\sim 6.2\times10^{-4}\%$. (f) 4.44K, corrected flux: 109kp/p, SDE $\sim 6.9\times10^{-4}\%$.

Bias Versus Count Rate Over a Range of Incident Photon Flux

For two of the most responsive nanowires, the microscope was positioned at the highest response region and the devices' response was measured for a range biases and photon flux. These devices were Spades_250, a 173nm nanowire and Hearts_125, a 364nm nanowire. For the thinner wire the count rate was measured over a bias of 10-200μA in steps of 0.5μA across a photon flux of 196kp/p to 62p/p (-46 to -81dBm) (Figure 5.13(a)). There are notable saturation regions in this data, the first of which is the focus of Figure 5.13(b). This effect confirms the constriction found in Figure 5.11(c). The initial saturation effect occurs at the constriction only and, as the bias is increased, other sections of the nanowire become responsive, causing secondary saturations. This saturation in count rate has been observed in other MoSi devices, as described in §2.3.3. Properties of MoSi.

In the case of the thicker wire, the count rate was measured over a bias 12-15μm in steps of 0.05μm across a photon flux of 780 to 0.08p/p (-70 to -110 dBm). There are spikes in the count rate which reach 2×10^{7}cps and occur at high biases and high flux. These spikes are an effect caused by the device latching and the universal counter reaching its maximum count rate. As the bias increases, the device SDE also increases. Even after correcting the incoming flux, the SDE is still very low. This is due to the wider width of the nanowire (173nm), which may favour multi-photon over single-photon sensitivity.

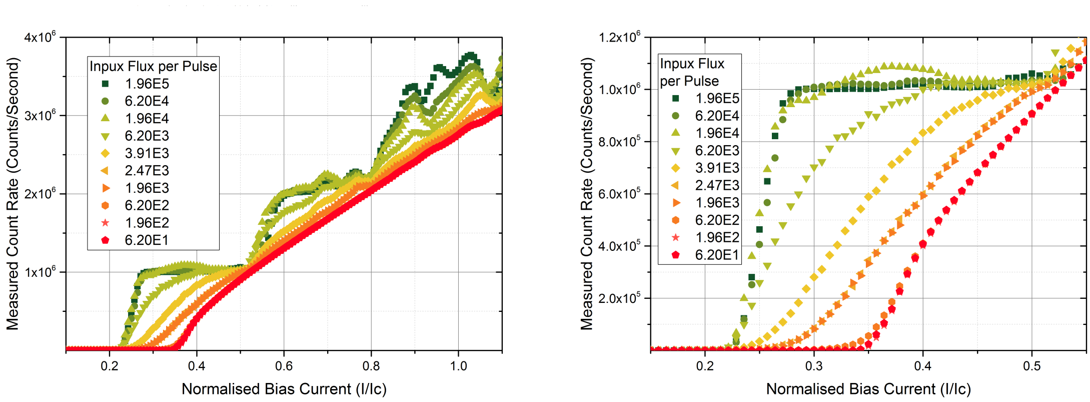

(a) (b)

Figure 5.13: (a) Count rate against normalised bias and input flux for sample S27383_Spades_250, which had a width of 173nm. (b) Zoom in on 0.2 – 0.5% of normalised bias in (a). There are three plateau features in (a). It is expected the first plateau occurs due to only the constriction responding to the incident photons. As the flux increases, secondary constrictions begin responding to the photon flux, increasing the count rate.

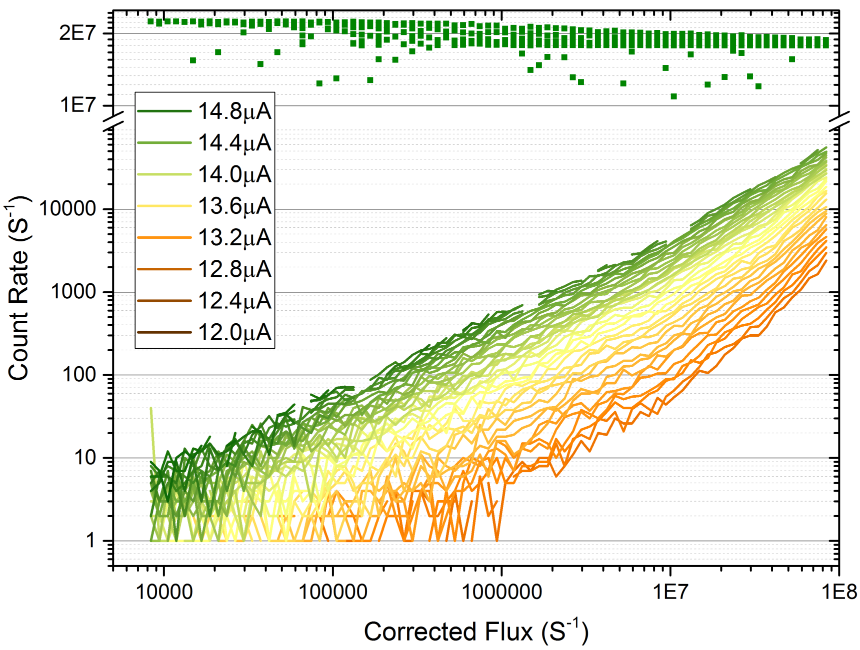

Figure 5.14: Count rate versus corrected flux for 458nm nanowire photoresponse. The legend has been shrunk for clarity. Correct flux is ∼10% of input flux to account for the Gaussian beam hitting the thin nanowire (See §2.3.3. Perpendicular Coupling). SDE $\sim 1 \times 10^{-4}$%. Saturation spikes around 2×10^{7}cps have been separated from the main plot.

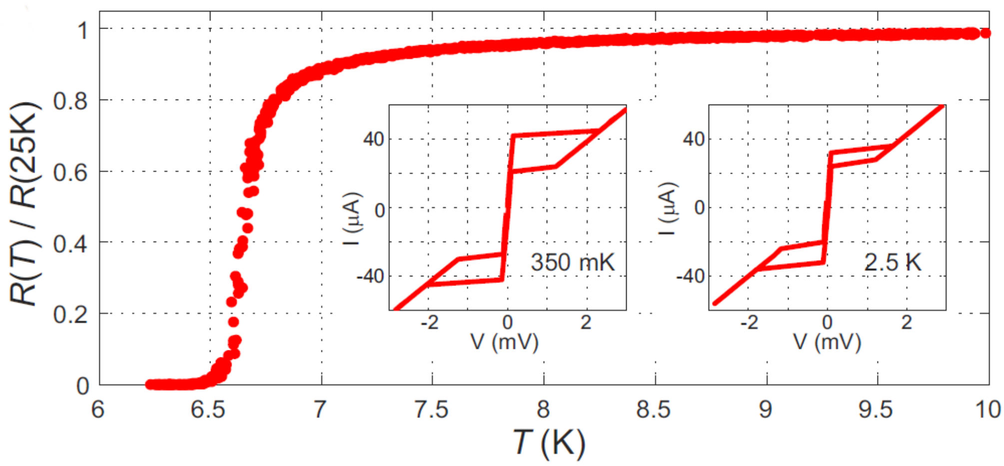

Figure 5.15: Temperature dependence of MoSi device. Device achieved a critical current of 41µA and 32µA at 350mK and 2.5K respectively, with a T_C of 6.7K.

5.3.2 Nano-Optical Testing of Hairpin Waveguide

Device Stoichiometry

The intention of the 4-pin measurements above was to use the collected data of the MoSi film to test and improve upon the sputtering recipe and also compare the results with other MoSi devices. The MoSi device characterised in this section was sputtered in Cambridge under different optimisation parameters. As confirmed by Electron Energy Loss Spectroscopy (EELS) measurements, the hairpin had a slightly altered stoichiometry to the 4-pin test structures; The Cambridge films (Hairpin devices) were $Mo_{83}Si_{17}$ and the Glasgow films (4-pin test structures) were $Mo_{80}Si_{20}$. It is not known how severe the effect of this change is on the transport properties of the devices, but it is likely any noticeable differences between the transport properties of the films arise from variations in the fabrication procedure.

Transport Characteristics

The hairpin device S22258_Delta_West was characterised in the Rankinator with the help of Dr. Jian Li. The device achieved a critical current of 41µA and 32µA at 350mK and 2.5K respectively with a critical temperature of 6.7K (Figure 5.15). The resistance of the device in its non-superconducting state was lower than the 50Ω shunt; in order to avoid the effect of latching an 18Ω shunt was used instead. Results from Verma *et al* also show high values for transition temperature (7.2K), and thus critical current, in bulk MoSi. The hairpin nanowire also achieved a high critical current even at 2.5K (∼20µA). This suggests the device could perform well at the base temperature for most PT setups (2-5K).

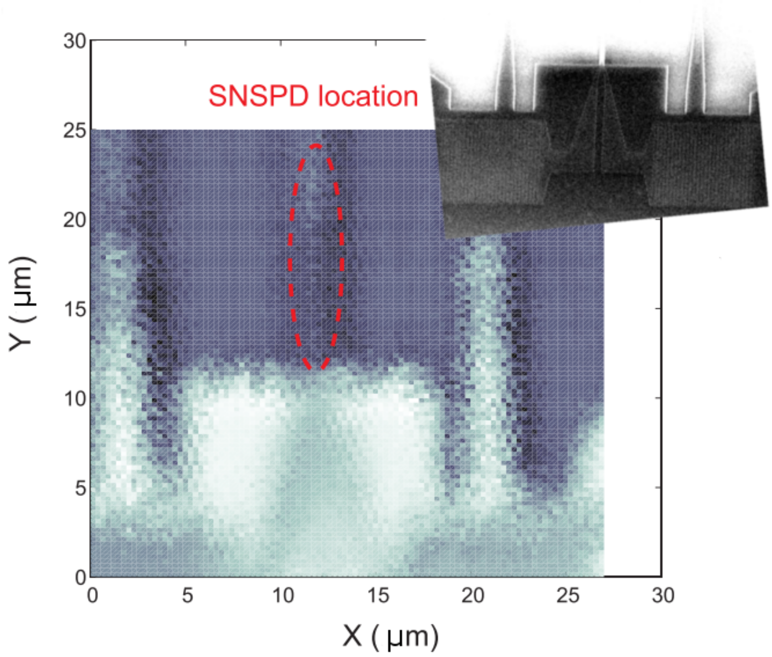

Figure 5.16: Scanning map over the detector. The hairpin is highlighted in red. Though it is not entirely visible, its position is apparent based on the surrounding structures.

Reflection Map

A reflection map across the device was taken. The map, pictured in Figure 5.16, shows the device and hairpin region as referenced by the inset SEM image, as well as a portion of the bank meander regions. As discussed above, this device had tapered waveguides on either side of the hairpin in preparation for future experiments involving waveguide beam splitters.

Counts Maps

A photoresponse map was taken at a bias current of 37μA at 350mK (Figure 5.17). The laser was pulsed at 1MHz, with a power of 12.6fW (-109dBm), which translates to 0.1 photons per pulse, and a FWHM of 2.3μm. As discussed in §3.3.6. Gaussian Convolution, this is due to the convolution of the Gaussian spot over the small nanowires. Using a convolution calculation of a 2.3μm Gaussian spot over the hairpins, the FWHM that should be expected is 2.5μm along the X-Axis and 10μm along the Y-Axis, shown in Figure 5.17(b) insert. The counts map has an asymmetric, Gaussian shape with a FWHM of 2.2μm in the X-direction and 9.7μm in the Y-direction. This suggests the hairpin is responsive across the entirety of the 10μm wires, indicating clean and uniform edges in the structure after fabrication. It is possible that this device would have absorption efficiency close to unity for in-plane, waveguide coupled light.

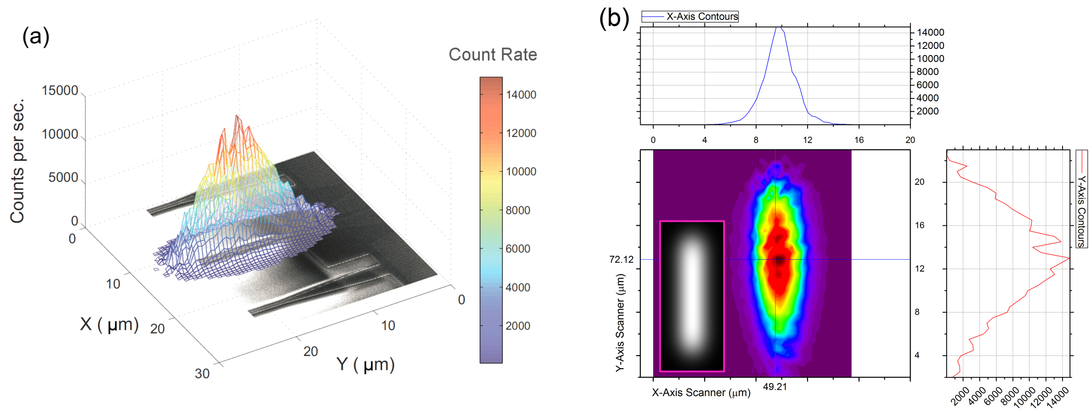

Figure 5.17: (a) Counts Map over the hairpin. The largest count rate exists over the hairpin region with all other regions equal to the DCR of 10Hz. (b) Measurements of FWHM of the response region, which has almost equal dimensions to a convolution calculation of a Gaussian spot over the hairpin nanowires, suggesting the device is uniformly responsive.

Pulse Shape

The pulse shape of the device is shown in Figure 5.18. It has a large SNR and pulse height due to its low temperature, which allows the device to operate at a large bias current. Its rise time is <1ns, but its reset time is longer than most meander SNSPDs ∼5ns. This limits the count rate of the detector to 0.20GHz, compared with 0.33GHz for other MoSi meander devices[5]. As discussed in §2.3.3. Waveguide Integrated SNSPDs this is due to the bank meander regions, which are regions of nanowires with a width ∼220nm. These add a series inductance to the device which increases the reset time and reduces the effect of latching.

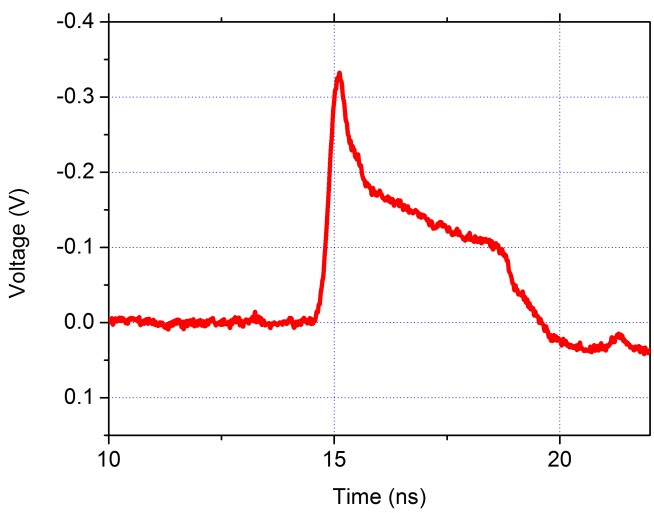

Figure 5.18: Pulse shape of the detector. It has a short rise time, characteristic of an SNSPD, but with a long shelf before resetting due to the bank meander regions.

Jitter

A detector response histogram was taken at the highest response region of the device, returning a jitter value of 57ps (Figure 5.19(a) insert) and 51ps (Figure 5.19 (a)) with the addition of a LPF in the experimental setup. This is faster than other MoSi meander devices, which have achieved >70ps[5]. This is expected due to the small inductance of the short hairpin nanowire.

A Gaussian fit is used to calculate the value of jitter from the histogram plot, but the points of data show a clear asymmetry when compared with the Gaussian. As discussed in §2.3.3. Jitter Asymmetry it was considered that this was an effect of the pulse rise time of the device. A derivative of the pulse rise time was taken (Figure 5.19 (b)), but the shape is not asymmetric, dispelling this reasoning. An alternate explanation is the effect of afterpulsing. A majority of the afterpulses are caused by high frequency reflections at the amplifier chain. Adding a LPF removes a majority of these reflections, but not all of them. Afterpulsing can also occur due to the background DCR as the DDE partially increases after a count.

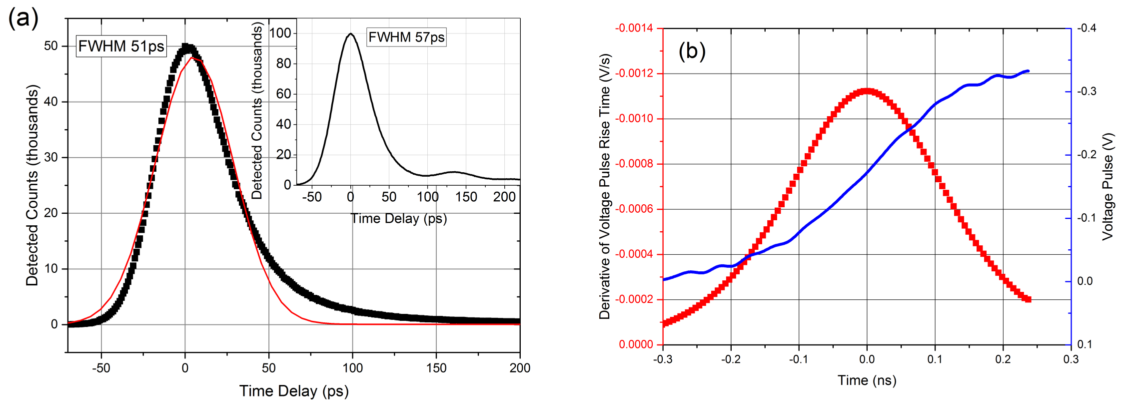

Figure 5.19: (a) Jitter histogram of MoSi detector. The Insert shows the same jitter measurement without the use of a LPF. (b) The rise time (blue) from the pulse shape was fit to a sigmoid approximation then its derivative was taken (red) to check its symmetry.

SDE at High Response Point

Whilst positioned at the highest response position, an SDE measurement was taken from 36-38.6μA with an attenuation range of -143dBm to -31dBm, which equates to a photon flux per second of 6.2×10^{12} to 39 (Figure 5.20). The input laser had a Gaussian spot with a FWHM of 2.3μm. A plateau in the efficiency occurs between a bias of 0.927-0.937I_C (38-38.45μA) at a value of $(5.4 \pm 0.1)\%$. Just below 0.939I_C (38.5μA), the SDE drops to 0.4 of a %. SDE drops here because the counter is saturating while the data processing software is still attempting to fit the sigmoid curve. The actual value, beyond the saturation point, is likely far lower and this is also true for Figure 5.21(b) and Figure 5.22(b).

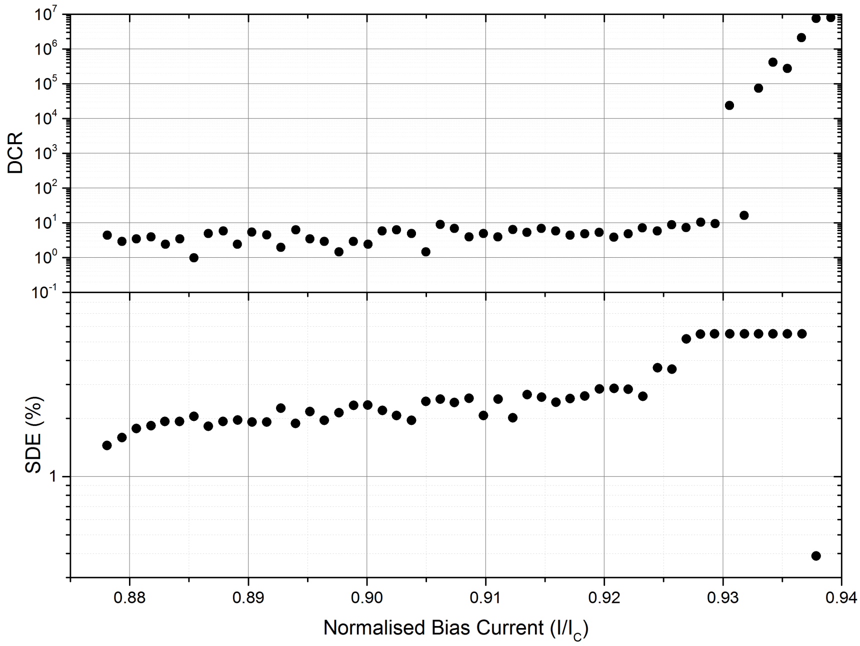

Figure 5.20: Results of DCR and SDE measurements against change in bias current for device S22258_Delta_West at 0.351K. The device had a critical current of 41μA at this temperature.

Possible Values of DDE from Experimental Results

Due to the small size of the hairpin when compared with the Gaussian laser spot, the perpendicular coupling efficiency is reduced to $(11.5 \pm 0.15)\%$ (See §2.3.3. Perpendicular Coupling). In the simulation of a MoSi optical stack, the material was found to have an absorption efficiency of $(46.01 \pm 0.01)\%$ (§5.2.3. Perpendicular Optical Stack Simulation for MoSi Hairpin). Using the measured value of SDE at $Mo_{83}Si_{17}$.3%, the values for perpendicular absorption, coupling efficiency and (Equation 2.9a), the registering efficiency of the device is calculated to be $(102.1 \pm 3.4)\%$. Though it is clear there are physical effects not being accounted for in the simulations - cavity thickness and film thickness may be different, nanowire widths may be different - it can be presumed that the registering efficiency is reaching unity and suggests MoSi is an excellent material for SNSPDs. If this device were to be coupled in-plane through a waveguide, as discussed in §2.3.3. Waveguide Integrated SNSPDs, its absorption efficiency could be as high as 99.5%. Using this data and assuming unity registering efficiency, the DDE of the device could also sit at 99.5%. This is more than double the experimental values of 38.5% DDE for perpendicular coupling. In-plane coupling of the waveguide could achieve 30% efficiency through grating couplers, or 90% through spliced, in-plane coupling – as discussed in §2.3.3. Coupling Efficiency - suggesting a device SDE of $\sim 90\%$.

SDE Plateau

In Figure 5.20, Figure 5.21(b) and Figure 5.22(b), all three SDE graphs show a plateau in the SDE at high bias and this effect occurs before the saturation of the DCR. This is a common observation and is tied to the bias current of the device[43, 83]. It is expect this is caused by a saturation in the registering efficiency[64]. That is to say, the device registers a count for all photons that are successfully absorbed. These results confirm the internal registering efficiency is near unity. The practical SDE is lower due to geometric coupling losses as discussed above.

Further SDE Measurements

Further measurements were performed over a longer range of biases, between 25-40μA at a higher resolution of 0.05μA through a flux range of 10^{-4} to 10^{6} photons per pulse. There is a visible multi-photon region in Figure 5.21(a) at 25.0μA. The results of the SDE in Figure 5.21(b) are from the perspective of only single photon counts. Fitting the multi-photon SDE equation (Equation 3.7b) onto the multi-photon region returns an SDE of ∼0.13%. This has been marked on the graph by a red triangle. The multi-photon regime can also be seen at high flux for a 29.0μm bias.

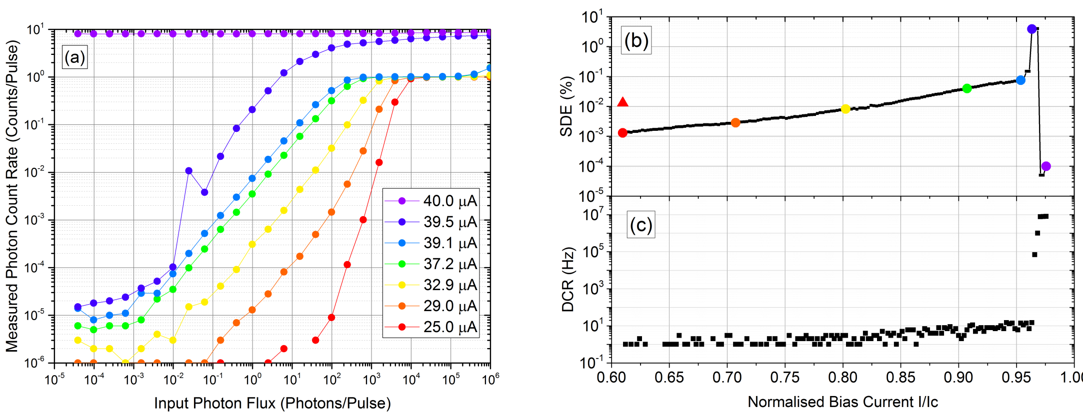

Figure 5.21: SDE measurement results for device S22258_Beta_West. (a) Measured photon count versus input photon flux. Only a select number of data points have been shown, which correspond to the points of SDE in graph (b). (b) SDE and (c) DCR vs bias current. The efficiency peaks at 4.0% under a bias $0.96I/I_C$ (39.5μA) and with a DCR of ∼10Hz (Navy circles). Multi-photon efficiency marked by red triangle.

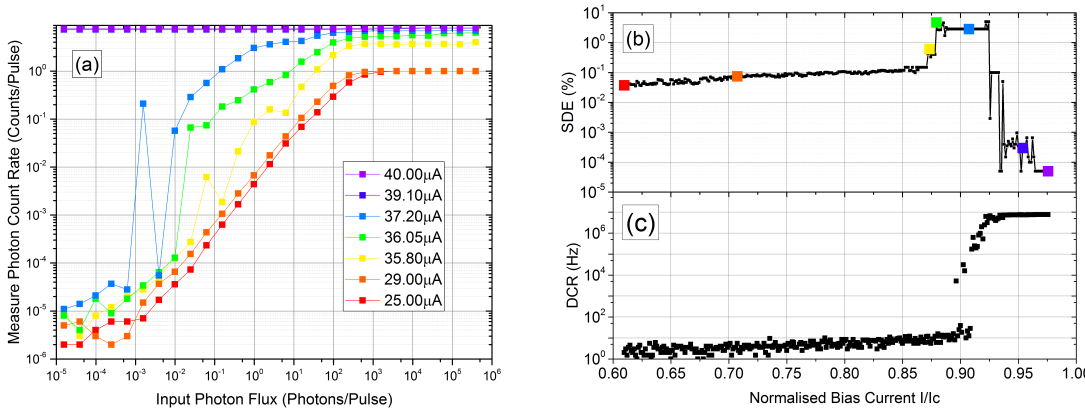

Figure 5.22: SDE measurement results for device S22258_Beat_West. (a) Measured photon count versus input photon flux. Only a select number of data points have been shown, which correspond to the points of SDE in graph (b). (b) SDE and (c) DCR vsersus bias current. The efficiency peaks at 4.77% under a bias 0.88I/I_C (36.05μA) and with a DCR of ∼10Hz (Green square).

DCR

In each of the results for bias against DCR, the DCR sits at 10Hz over a majority of the data. At a bias near the switching current, the DCR dramatically jumps to the saturation point of the counter at 10^7 Hz. It is likely this is caused by latching (§2.3.3. Latching); the current is high enough that it impairs the device's ability to return to its superconducting state. As discussed in §2.3.1. Dark Count Rate, there is a visible relationship between the DCR and I: $log(DCR) \propto I$. This occurs at a much lower bias before the effect of latching dominates. The scarcity of dark counts for most biases is an effect of the low temperature setup and 3K shielding of the Rankinator (§3.3. Rankinator Design) reducing the effect of external counts on the detector from BBR (§2.2.2. The Quantisation of Light). There is a rise in count rate at higher biases – 38.4μA for Figure 5.20, 0.90I/I_C for Figure 5.21(c) and 0.96I/I_C for Figure 5.22(c). It is likely the intrinsic effect of edge vortices.

5.4 Conclusion

The transport properties of in-house $Mo_{80}Si_{20}$ superconducting film, grown by Archan Banerjee, were characterised. This involved fabricating 4-pin test structures of varying nanowire widths and measuring critical current values from 3.5-6.2K. The data was fit to an equation for critical current dependence within the local London limit, allowing values of material energy gap to be extracted. The devices returned an energy gap $2\Delta(0) = (1.8156 \pm 0.0484)$meV, which was slightly out from values found in literature. This had a possible attribution to the thicker films used here compared with the literature.

Several photoresponse maps were taken of two of the 4-pin test structures (173nm and 364nm). Both showed signs of constrictions near the edges of the wire, indicating an increased dose. For the thicker nanowire, a high flux of photons returned a uniform response, which is as expected.

$Mo_{83}Si_{17}$ nanowire hairpins fabricated from films provided by Cambridge University were optically characterised in the Rankinator at 350mK using perpendicularly coupled 1550nm light. Its transport characteristics show a relatively high transition temperature of 6.7K. This suggests MoSi will perform well even in GM closed-cycle fridges at 2.2K. A perpendicular counts map of the device returned uniform responsiveness across the hairpin, implying excellent fabrication results and that this device would achieve almost unity absorption efficiencies if optically coupled in-plane. The device achieved an SDE of 5% through perpendicular coupling. Convolution calculations of the Gaussian spot perpendicular to the hairpin nanowires suggested a registering efficiency close to unity. This suggests MoSi is an excellent superconductor for nanowire SPDs.

The next step will be characterising in-plane light coupled waveguides. Currently, the Quantum Sensors group is focusing on improving the yield of MoSi devices and optimising the fabrication of grating coupled waveguides. A new repeatable sorption cryostat is also being designed which will be capable of angled coupling from a v-groove fibre array into on-chip grating couplers. Vertical device testing for edge cleaved waveguides will also be possible using the additional vertical sample mounts created by Dr. Jian Li.

Chapter 6

Conclusions

6.1 Summary of Thesis Work

The aim of this research was to study and characterise next generation SNSPDs for optical QIP applications. In support of this effort I fabricated simple MoSi test structures to assess the in-house capabilities of MoSi growth as well as construct a 0.35 K cryostat in order to characterise and map SNSPD meanders and waveguides.

By using a ^{3}He/^{4}He sorption cryostat attached to a two-stage pulse tube as a heat disperser, the Rankinator has achieved characterisation temperatures $<$0.4K. By using low heat capacity and superconducting wiring for high heat load elements, the cryostat can test multiple devices and perform reflection and photoresponse maps also $<$0.4K. Due to the high heat load of the components, the cycle time of the cryostat sits at just under 4 hours.

6.2 Characterisation of NbTiN Cavity Devices

One of the focus points of the UK Quantum Technologies hub is to establish an optical QKD network across the south of the UK. This requires fast SPDs that achieve high SDEs and low timing jitter. To achieve these, variations of SPD devices must be tested and characterised to achieve higher performance metrics. NbTiN is a material which offers relatively high temperature single photon detection and can achieve viable SDE percentages with the aid of a cavity structure. By characterising a series of NbTiN SNSPDs, the highest performing devices can be applied to optical QKD networks.

Two groups of NbTiN cavity SNSPDs were fibre-coupled and characterised at 2-3K. The double cavity achieved higher SDEs with a peak value of $\sim$45% at 0.35K. The results of this device were used to perform a simulation of the T12 QKD protocol over an increasing distance. With its low DCR and high SDE, the device could achieve a positive key generation rate at 1kbps over a distance of 200km, roughly the distance between Bristol and London. This suggests these devices could be used in establishing a QKD network across the south of the UK.

6.3 MoSi Test Structures

The focus of this work was to begin fabricating SNSPDs from in-house grown superconducting films, using the recently purchased MP 600S sputtering machine. MoSi was the focus material as the amorphous properties achieved high SDEs and clean edges during fabrication. In-house grown $Mo_{80}Si_{20}$ films were used to fabricate test structures to characterise their transport properties. The films achieved close to expected values of the BCS superconducting energy gap. The variation of this value from literature was attributed to the different thicknesses of the films.

6.4 MoSi Waveguide Integrated SNSPDs

In order to realise linear optical quantum computing, single photon sources, gates and detectors will need to function on a monolithic chip. Hairpin nanowire SNSPDs offer integration onto Si optical waveguide and have been shown to achieve almost unity absorption efficiencies at 10μn lengths. $Mo_{83}Si_{17}$ nanowire hairpins fabricated from films provided by Cambridge University were optically characterised in the Rankinator at 350mK using perpendicularly coupled 1550nm light. A perpendicular counts map of the device returned uniform responsiveness across the hairpin, implying excellent fabrication results and that this device would achieve almost unity absorption efficiencies if optically coupled in-plane. The device achieved an SDE of 5% through perpendicular coupling. Convolution calculations of the Gaussian spot perpendicular to the hairpin nanowires suggested a registering efficiency close to unity. This suggests MoSi is an excellent superconductor for nanowire SPDs.

Future work on integrated SNSPDs will require improvements in both yield and coupling methods. The difficulty in fabricating consistent nanowires arises from edge defects after etching. It is considered that more robust results could be achieved with a slower acting etching plasma, such as SF_6. Regarding coupling methods, the Glasgow Quantum Sensors group is currently designing and building a new cryostat with a repeating sorption pump that inputs light at an angle into the sample to test grating coupled waveguides. Fabrication work also focuses on multiple SNSPD coupling designs, including key-hole designs, spliced waveguides and grating couplers.

6.5 Efforts for a Monolithic Quantum Computer

The hairpin nanowire devices demonstrated in this thesis require further development to demonstrate high yields for scalability to large quantum photonic circuits. Follow up studies will include design and testing of grating couplers as a prelude to the full testing of waveguide integrated detectors. Looking ahead, the Bristol-led EPSRC Programme Grant 'Engineering Quantum Photonic Technologies' (2014-2019) (EP/L024020/1), in which the Quantum Sensors group at the University of Glasgow is a partner, will continue to focus on building a monolithic chip for quantum computing experiments. This will require scalable, on chip components for single photon generation, manipulation and detection. For this project the firm focus is on silicon photonic platforms, with photon pair generation around 1550 nm wavelength being implemented via four-wave mixing in silicon ring resonators[134]. On III-V platforms progress is also being made: quantum dots are currently the most promising source of single photons as they can be located and optically pumped to produce photons deterministically. Numerous proof-of-principle experiments have also been carried out on QDs emitting in the near infrared (900-950 nm wavelength) to show their compatibility with GaAs integrated quantum photonics and with the implementation of phase shifters[135]. In both silicon and III-V platforms considerable work is still required to implement all of the components of quantum logic gates on a single chip. Outstanding challenges include implementation of low power switches, highly efficient on-chip optical filtering and development of high speed cryogenic control electronics. Nevertheless, given the considerable interest and effort being invested by research groups worldwide, this goal may yet be achieved.

Appendix A

Publications

A.1 List of Peer-reviewed Journal Publications

- A. Banerjee, **L. J. Baker**, A. Doye, M. Nord, R. M. Heath, K. Erotokritou, D. Bosworth, Z. H. Barber, I. MacLaren, R. H. Hadfield. "Characterisation of amorphous molybdenum silicide (MoSi) superconducting thin films and nanowires." *Superconductor Science and Technology*, 30(8):084010, 2017.
- J. Li, R. A. Kirkwood, **L. J. Baker**, D. Bosworth, K. Erotokritou, A. Banerjee, R. M. Heath, C. M. Natarajan, Z. H. Barber, M. Sorel1, and R. H. Hadfield. "Nano-optical single-photon response mapping of waveguide integrated molybdenum silicide (MoSi) superconducting nanowires." *Optics Express*, 24(13):13931, 2016.

A.2 Conference Presentations

- L. J. Baker *et al*, "Nano-Optical Single-Photon Response Mapping of Waveguide Integrated Molybdenum Silicide Superconducting Nanowires", Applied Superconductivity Conference, Denver CO, USA, September 2016, Poster Presentation.
- L. J. Baker *et al*, "Characterisation of Superconducting Nanowire Single Photon Detectors", SUSSP71: Frontiers in Quantum Dynamics & Quantum Optics, University of Strathclyde, Glasgow, July 2015, Poster Presentation.
- L. J. Baker *et al*, "Characterisation of Waveguide Integrated MoSi SNSPDs", IOP: Winter Science Meeting, University College London, London, December 2015,

Poster Presentation.

Appendix B

List of Samples Tested

Table B.1 and Table B.2 details all of the samples discussed in §4. Cavity SNSPD Devices and §5. MoSi Devices, respectively.

Delft	NbTiN films on SiO substrate with Si/SiO_x interface for front side coupled testing.	B17	Well aligned device, but achieved low SDE at ∼3%.
		C10	7.5µm I-V, 16% SDE at 2.2K. High polarisation dependence.
NICT	NbTiN films on Si substrate in a double cavity for backside coupled testing.	BS-5	10% SDE achieved at 2.2K at a DCR of 1kHz.
		BS-6	Despite imperfect alignment, device achieved 43% SDE at 0.35K at a DCR of 1kHz. Simulation of T12 protocol achieved 1kbps key rate over 200km.
		BS-7	30% SDE achieved at 2.2K at a DCR of 1kHz.

Table B.1: Table of devices tested in §4. Cavity SNSPD Devices

S27383	10nm MoSi nanowire 4-pin test structures of 100nm to 2µm.	Spades_25	2003nm width, 70µA I-V, 0.95meV energy gap
		Spades_50	957nm, 30µA I-V, 0.75meV
		Spades_100	459nm, 14µA I-V, 1.5meV
		Spades_125	364nm, 11µA I-V, 0.95meV
		Spades_167	258nm, 7µA I-V, 1.1meV
		Spades_250	173nm, 4µA I-V, 0.55meV
		Hearts_100	459nm, Photoresponse maps taken at 0.35K show constrictions.
		Hearts_125	364nm, Photoresponse maps taken at 3.5K show constrictions at nanowire edge and uniform response at high flux.
S22278	10nm MoSi hairpin nanowire devices on Si waveguides for perpendicular response map testing.	Delta_West	40µA I-V at 0.35K, showed uniform responsiveness to perpendicular illumination, suggesting ideal conditions for in-plane coupling.

Table B.2: Table of devices tested in §5. MoSi Devices

Appendix C

Additional Programs

This supplementary section lists all Python programs written for device measurements and cryostat control.

C.1 Measurement Programs

SDE Measurement – Written by Dr. Chandra Mouli Natarajan, this program records the count rate of a detector over a changing attenuation and biases. Low biases return the DCR of the device, whilst the attenuation sweep can be used to extract the device's SDE.

WaSTe Measurement – Written by Dr. Robert M. Heath, this program measures the count rate of a detector while altering the flux wavelength, attenuation and polarisation for a fixed detector bias. This returns the SDE of the device at different wavelengths and for high and low polarisation alignments. The program does not find the maximum or minimum polarisation alignment, but traces out a fixed path on the Poincaré sphere, estimating these values.

C.2 Rankinator Specific Programs

Rankinator_Repeater.py – An automated program for reaching 0.35K with the sorption fridge. Records and monitors cryostat temperatures and device resistance. It is also capable of dealing with low and high heat load setups, which alter the process of the cooldown. A variation of this program allows the user to set a timer for when they need the cryostat to be below 0.4K.

Rankinator_Heater.py – Monitors the temperatures of the cryostat and resistances of four devices with temperature during PTs cooldown from 300K to 5K. It also switches on the pump heaters. Due to the severe thermal isolation of the 3He head, the pump heaters need to be kept in a desorbtive State to aid in cooling the $_3$He head down to 5K. A vanilla version of this program also exists that does not switch on the heaters: Rankinator_Temperature_Monitor.py

Rankinator_I-V.py – Performs a current sweep across the device while measuring its potential difference.

Rankinator_I-V_With_Temperature.py - Performs repeated I-V's as the ^{3}He head warms from 0.4K to 5K or higher. This gives a reading of the change in the device's critical current with temperature.

PyANC350\FocusMapAutomatic.py – Steps the Z-axis stepper motor across a chosen range, recording the intensity of reflected laser light across the chip. This program is used to find the Z-axis position with the highest focus intensity.

PyANC350\StepperMapping.py – Creates a reflection map of the chip using the stepper motors. The user can set a map range up to 4mm^2, with a minimum step size of 2µm. This version records the location of the steppers based on a resistive readout and is used to take detailed maps of the entire chip at 5K. Variations of this program use less accurate positioning methods to achieve quicker maps.

PyANC350\ScannerMapping.py – Creates a reflection map of the chip using the scanner motors. The user can set a map range up to $\sim$30µm, with a minimum step size of 2.2Å, though the visibility of the final image is limited by the laser's spot size.

PyANC350\ScannerMappingCounter.py – Creates a counts map of the chip using the scanner motors, sweeping through a range of different light intensities at each pixel. The user sets a map range, likely based on the reflection map taken using the program above. Alternate versions of this program come with the ability to change the polarisation of the input light and the scanning pattern direction across the chip.

Rankinator_QE.py - This program sweeps bias and laser flux, recording the pulses counted by the detector. This program is normally used after creating a counts map, allowing the user to position the laser over the region of the detector with the highest photon response.

Rankinator_Compressor_Monitor.py – Written by Dr. Robert Heath, this program exchanges hash values with the compressor to monitor its in/out He flow temperature and in/out oil flow temperature. This program is useful in debugging any malfunctions that occur with the cryostat.

Bibliography

[1] E. Knill, R. Laflamme, and G. J. Milburn, "A scheme for efficient quantum computation with linear optics.," *Nature*, vol. 409, no. 6816, pp. 46–52, 2001.

[2] M. G. Tanner, C. M. Natarajan, V. K. Pottapenjara, J. A. O'Connor, R. J. Warburton, R. H. Hadfield, B. Baek, S. Nam, S. N. Dorenbos, E. B. Ureña, T. Zijlstra, T. M. Klapwijk, and V. Zwiller, "Enhanced telecom wavelength single-photon detection with NbTiN superconducting nanowires on oxidized silicon," *Applied Physics Letters*, vol. 96, no. 22, p. 221109, 2010.

[3] F. Marsili, V. B. Verma, J. A. Stern, S. Harrington, A. E. Lita, T. Gerrits, I. Vayshenker, B. Baek, M. D. Shaw, R. P. Mirin, and S. W. Nam, "Detecting single infrared photons with 93% system efficiency," *Nature Photonics*, vol. 7, no. 3, pp. 210–214, 2013.

[4] S. Miki, T. Yamashita, H. Terai, and Z. Wang, "High Performance fibre-coupled NbTiN superconducting nanowire single photon detectors with Gifford-McMahon cryocooler," *Optical Society of America*, vol. 1, no. 8, pp. 4–5, 2013.

[5] V. B. Verma, B. Korzh, F. Bussières, R. D. Horansky, S. D. Dyer, A. E. Lita, I. Vayshenker, F. Marsili, M. D. Shaw, H. Zbinden, R. P. Mirin, and S. W. Nam, "High-efficiency superconducting nanowire single-photon detectors fabricated from MoSi thin-films," *Optics Express*, vol. 23, no. 26, p. 33792, 2015.

[6] B. Korzh, C. Wen, R. Houlmann, N. Gisin, M. J. Li, D. Nolan, B. Sanguinetti, R. Thew, and H. Zbinden, "Provably Secure and Practical Quantum Key Distribution over 307km of Optical Fibre," *Nature Photonics*, vol. 9, pp. 163–168, 2014.

[7] R. H. Hadfield, J. L. Habif, J. Schlafer, R. E. Schwall, and S. W. Nam, "Quantum key distribution at 1550nm with twin superconducting single-photon detectors," *Applied Physics Letters*, vol. 89, no. 24, p. 241129, 2006.

[8] H. Takesue, S. W. Nam, Q. Zhang, R. H. Hadfield, T. Honjo, K. Tamaki, and Y. Yamamoto, "Quantum key distribution over a 40-dB channel loss using superconducting single-photon detectors," *Nature Photonics*, vol. 1, no. 6, pp. 343–348, 2007.

[9] T. Honjo, S. W. Nam, H. Takesue, Q. Zhang, H. Kamada, Y. Nishida, O. Tadanaga, M. Asobe, B. Baek, R. Hadfield, S. Miki, M. Fujiwara, M. Sasaki, Z. Wang, K. Inoue, and Y. Yamamoto, "Long-distance entanglement-based quantum key distribution over optical fiber," *Optics Express*, vol. 16, no. 23, p. 19118, 2008.

[10] D. Stucki, N. Walenta, F. Vannel, R. T. Thew, N. Gisin, H. Zbinden, S. Gray, C. R. Towery, and S. Ten, "High rate, long-distance quantum key distribution over 250km of ultra low loss fibres," *New Journal of Physics*, vol. 11, no. 7, p. 075003, 2009.

[11] P. J. Clarke, R. J. Collins, P. A. Hiskett, M.-J. García-Martínez, N. J. Krichel, A. McCarthy, M. G. Tanner, J. A. O'Connor, C. M. Natarajan, S. Miki, M. Sasaki, Z. Wang, M. Fujiwara, I. Rech, M. Ghioni, A. Gulinatti, R. H. Hadfield, P. D. Townsend, and G. S. Buller, "Analysis of detector performance in a gigahertz clock rate quantum key distribution system," *New Journal of Physics*, vol. 13, no. 7, p. 75008, 2011.

[12] H. Shibata, T. Honjo, and K. Shimizu, "Quantum key distribution over a 72dB channel loss using ultralow dark count superconducting single-photon detectors," *Optics Letters*, vol. 39, no. 17, p. 5078, 2014.

[13] J. L. O. Brien, "Optical Quantum Computing," *Science*, vol. 318, no. 5856, pp. 1567–1571, 2007.

[14] P. Kok, K. Nemoto, T. C. Ralph, J. P. Dowling, and G. J. Milburn, "Linear optical quantum computing with photonic qubits," *Reviews of Modern Physics*, vol. 79, no. 1, pp. 135–174, 2007.

[15] C. R. Fitzpatrick, *Single-photon metrology with superconducting nanowire single-photon detectors.* PhD thesis, Heriot-Watt University, United Kingdom, 2013.

[16] A. McCarthy, N. J. Krichel, N. R. Gemmell, X. Ren, M. G. Tanner, S. N. Dorenbos, V. Zwiller, R. H. Hadfield, and G. S. Buller, "Kilometer-range, high resolution depth imaging via 1560 nm wavelength single-photon detection," *Optics Express*, vol. 21, no. 7, p. 8904, 2013.

[17] N. R. Gemmell, A. McCarthy, B. Liu, M. G. Tanner, S. D. Dorenbos, V. Zwiller, M. S. Patterson, G. S. Buller, B. C. Wilson, and R. H. Hadfield, "Singlet oxygen

luminescence detection with a fiber-coupled superconducting nanowire single-photon detector.," *Optics Express*, vol. 21, no. 4, pp. 5005–13, 2013.

[18] H. K. Onnes, "Further experiments with Liquid Helium: Sec. VI. On the sudden change on the rate at which the resistance of mercury dissapears," Tech. Rep. 14, KNAW, Amsterdam, 1911.

[19] W. Meissner and R. Ochsenfeld, "Ein neuer Effekt bei Eintritt der Supraleitfahigkeit," *Die Naturwissenschaften*, vol. 21, no. 44, pp. 787–788, 1933.

[20] C. Gorter and H. Casimir, "On supraconductivity I," *Physica*, vol. 1, no. 1-6, pp. 306–320, 1934.

[21] C. P. Poole, H. A. Farach, R. J. Creswick, and R. Prozorov, *Superconductivity.* Academic Press, second ed., 2007.

[22] F. London and H. London, "The Electromagnetic Equations of the Supraconductor," *Proceedings of the Royal Society A: Mathematical, Physical and Engineering Sciences*, vol. 149, no. 866, pp. 71–88, 1935.

[23] J. Pearl, "Current distribution in superconducting films carrying quantized fluxoids," *Applied Physics Letters*, vol. 5, no. 4, pp. 65–66, 1964.

[24] J. Bardeen, L. N. Cooper, and J. R. Schrieffer, "Theory of superconductivity," *Physical Review*, vol. 108, no. 5, pp. 1175–1204, 1957.

[25] G. N. Gol'tsman, O. Okunev, G. Chulkova, A. Lipatov, A. Semenov, and K. Smirnov, "Picosecond superconducting single-photon optical detector," *Applied Physics Letters*, vol. 79, no. 6, pp. 705–707, 2001.

[26] B. Mühlschlegel, "Die thermodynamischen Funktionen des Supraleiters," *Zeitschrift für Physik*, vol. 155, pp. 313–327, jun 1959.

[27] R. Khasanov, P. W. Klamut, A. Shengelaya, Z. Bukowski, I. M. Savić, C. Baines, and H. Keller, "Muon-spin rotation measurements of the penetration depth of the Mo_3Sb_7 superconductor," *Physical Review B - Condensed Matter and Materials Physics*, vol. 78, no. 1, pp. 1–5, 2008.

[28] A. Carrington and F. Manzano, "Magnetic penetration depth of MgB_2," *Physica C: Superconductivity*, vol. 385, no. 1-2, pp. 205–214, 2003.

[29] A. Engel, J. J. Renema, K. Il'in, and A. Semenov, "Detection mechanism of superconducting nanowire single-photon detectors," *Superconductor Science and Technology*, vol. 28, no. 11, p. 114003, 2015.

[30] D. Henrich, S. Dörner, M. Hofherr, K. Il'in, A. Semenov, E. Heintze, M. Scheffler, M. Dressel, and M. Siegel, "Broadening of hot-spot response spectrum of superconducting NbN nanowire single-photon detector with reduced nitrogen content," *Journal of Applied Physics*, vol. 112, no. 7, p. 074511, 2012.

[31] E. J. Nicol, *Pair-Breaking in Superconductivity.* PhD thesis, McMaster University, 1991.

[32] M. Fox, *Quantum Optics*, vol. 53. Sheffield: Oxford University Press, first ed., 2013.

[33] A. Saleh and M. C. Teich, *Fundamentals of Photonics*, vol. 5. Madison, Wisconsin: John Wiley and Sons, INC, 1st ed., 1991.

[34] C. K. Hong and L. Mandel, "Experimental realization of a localized one-photon state," *Physical Review Letters*, vol. 56, no. 1, pp. 58–60, 1986.

[35] K. G. Palmett, A. U. Ren, F. Kaneda, K. Garay-palmett, A. B. U. Ren, and P. G. Kwiat, "Heralded single-photon source utilizing highly nondegenerate, spectrally factorable spontaneous parametric downconversion," *Optics Express*, vol. 24, no. 10, p. 10733, 2016.

[36] A. Ling, A. Lamas-Linares, and C. Kurtsiefer, "Absolute emission rates of spontaneous parametric down-conversion into single transverse Gaussian modes," *Physical Review A*, vol. 77, no. 4, p. 043834, 2008.

[37] L. Zhang, L. You, D. Liu, W. Zhang, L. Zhang, X. Liu, J. Wu, Y. He, C. Lv, Z. Wang, and X. Xie, "Characterization of superconducting nanowire single-photon detector with artificial constrictions," *AIP Advances*, vol. 4, no. 6, pp. 1–10, 2014.

[38] M. Pelton, C. Santori, J. Vuckoviv, B. Zhang, G. S. Solomon, J. Plant, and Y. Yamamoto, "Efficient Source of Single Photons: A Single Quantum Dot in a Micropost Microcavity," *Physical Review Letters*, vol. 89, no. 23, p. 233602, 2002.

[39] R. H. Hadfield, "Single-photon detectors for optical quantum information applications," *Nature Photonics*, vol. 3, no. 12, pp. 696–705, 2009.

[40] C. P. Dietrich, A. Fiore, M. G. Thompson, M. Kamp, and S. Höfling, "GaAs integrated quantum photonics: Towards compact and multi-functional quantum photonic integrated circuits," vol. 10, no. 6, pp. 870–894, 2016.

[41] J. Claudon, J. Bleuse, N. S. Malik, M. Bazin, P. Jaffrennou, N. Gregersen, C. Sauvan, P. Lalanne, and J. Gérard, "A highly efficient single-photon source based on a

quantum dot in a photonic nanowire," *Nature Photonics*, vol. 4, no. 3, pp. 174–177, 2010.

[42] H. Li, "Evanescent wave of a single photon," *Optical Engineering*, vol. 52, no. 7, p. 74103, 2013.

[43] C. M. Natarajan, M. G. Tanner, and R. H. Hadfield, "Superconducting nanowire single-photon detectors: physics and applications," *Superconductor Science and Technology*, vol. 25, no. 6, p. 063001, 2012.

[44] L. You, X. Yang, Y. He, W. Zhang, D. Liu, W. Zhang, L. Zhang, L. Zhang, X. Liu, S. Chen, Z. Wang, and X. Xie, "Jitter analysis of a superconducting nanowire single photon detector," *AIP Advances*, vol. 3, no. 7, p. 072135, 2013.

[45] K. Smirnov, Y. Vachtomin, A. Divochiy, A. Antipov, and G. Goltsman, "Dependence of dark count rates in superconducting single photon detectors on the filtering effect of standard single mode optical fibers," *Applied Physics Express*, vol. 8, no. 2, p. 22501, 2015.

[46] A. Engel, A. Semenov, H. W. Hübers, K. Il'In, and M. Siegel, "Fluctuations and dark count rates in superconducting NbN single-photon detectors," *Physica Status Solidi C: Conferences*, vol. 2, no. 5, pp. 1668–1673, 2005.

[47] G. A. Morton, "Photomultipliers for scintillation counting," *RCA Rev.*, vol. 10, pp. 525–553, 1949.

[48] R. H. Hadfield and G. Johansson, *Superconducting Devices in Quantum Optics*. Quantum Science and Technology, Springer International Publishing, 1st ed., 2016.

[49] A. E. Lita, A. J. Miller, and S. W. Nam, "Counting near-infrared single-photons with 95% efficiency," *Optics Express*, vol. 16, no. 5, p. 3032, 2008.

[50] S. Cova, M. Ghioni, A. Lotito, I. Rech, and F. Zappa, "Evolution and prospects for single-photon avalanche diodes and quenching circuits," *Journal of Modern Optics*, vol. 51, no. 9-10, pp. 1267–1288, 2004.

[51] C. M. Natarajan, *Superconducting Nanowire Single-Photon Detectors for Advanced Photon-Counting Applications*. PhD thesis, Heriot-Watt University, UK, 2011.

[52] D. D. E. Martin and P. Verhoeve, "Superconducting tunnel junctions," *ISSI Scientific Reports Series*, vol. 9, pp. 441–457, 2010.

[53] B. Josephson, "Possible new effects in superconductive tunnelling," *Physics Letters*, vol. 1, no. 7, pp. 251–253, 1962.

[54] B. A. Mazin, *Microwave Kinetic Inductanc.* PhD thesis, California Institue of Technology, 2004.

[55] S. Doyle, P. Mauskopf, J. Naylon, a. Porch, and C. Duncombe, "Lumped element kinetic inductance detectors," *Journal of Low Temperature Physics*, vol. 151, no. 1, pp. 530–536, 2008.

[56] R. M. Heath, M. G. Tanner, A. Casaburi, M. G. Webster, L. San Emeterio Alvarez, W. Jiang, Z. H. Barber, R. J. Warburton, and R. H. Hadfield, "Nano-optical observation of cascade switching in a parallel superconducting nanowire single photon detector," *Applied Physics Letters*, vol. 104, no. 6, p. 063503, 2014.

[57] M. Tarkhov, J. Claudon, J. P. Poizat, A. Korneev, A. Divochiy, O. Minaeva, V. Seleznev, N. Kaurova, B. Voronov, A. V. Semenov, and G. Gol'Tsman, "Ultrafast reset time of superconducting single photon detectors," *Applied Physics Letters*, vol. 92, no. 24, pp. 1–4, 2008.

[58] W. J. Skocpol, M. R. Beasley, and M. Tinkham, "Self-Heating Hotspots in Superconducting Thin-Film Microbridges.," *Journal of Applied Physics*, vol. 45, 1974.

[59] A. M. Kadin and M. W. Johnson, "Nonequilibrium photon-induced hotspot: A new mechanism for photodetection in ultrathin metallic films," *Applied Physics Letters*, vol. 69, no. 25, p. 3938, 1996.

[60] J. K. W. Yang, A. J. Kerman, E. A. Dauler, V. Anant, K. M. Rosfjord, and K. K. Berggren, "Modeling the Electrical and Thermal Response of Superconducting Nanowire Single-Photon Detectors," *IEEE Trans. Appl. Supercond.*, vol. 17, no. 2, pp. 581–585, 2007.

[61] A. J. Kerman, E. A. Dauler, W. E. Keicher, J. K. W. Yang, K. K. Berggren, G. Gol'tsman, and B. Voronov, "Kinetic-inductance-limited reset time of superconducting nanowire photon counters," *Applied Physics Letters*, vol. 88, no. 11, pp. 3–6, 2006.

[62] A. Casaburi, R. M. Heath, M. G. Tanner, R. Cristiano, M. Ejrnaes, C. Nappi, and R. H. Hadfield, "Current distribution in a parallel configuration superconducting strip-line detector," *Applied Physics Letters*, vol. 103, no. 1, p. 013503, 2013.

[63] A. J. Kerman, E. A. Dauler, J. K. Yang, K. M. Rosfjord, V. Anant, K. K. Berggren, G. N. Gol'tsman, and B. M. Voronov, "Constriction-limited detection efficiency of superconducting nanowire single-photon detectors," *Applied Physics Letters*, vol. 90, no. 10, 2007.

[64] Y. P. Korneeva, M. Y. Mikhailov, Y. P. Pershin, N. N. Manova, A. V. Divochiy, Y. B. Vakhtomin, A. A. Korneev, K. V. Smirnov, A. G. Sivakov, A. Y. Devizenko, and G. N. Goltsman, "Superconducting single-photon detector made of MoSi film," *Superconductor Science and Technology*, vol. 27, no. 9, 2014.

[65] L. Zhao, Y.-R. Jin, J. Li, H. Deng, and D.-N. Zheng, "Fabrication and properties of the meander nanowires based on ultra-thin Nb films," *Chinese Physics B*, vol. 23, no. 8, p. 087402, 2014.

[66] A. Verevkin, J. Zhang, R. Sobolewski, A. Lipatov, O. Okunev, G. Chulkova, A. Korneev, K. Smirnov, G. N. Gol'tsman, and A. Semenov, "Detection efficiency of large-active-area NbN single-photon superconducting detectors in the ultraviolet to near-infrared range," *Applied Physics Letters*, vol. 80, no. 25, pp. 4687–4689, 2002.

[67] V. B. Verma, A. E. Lita, M. R. Vissers, F. Marsili, D. P. Pappas, R. P. Mirin, and S. W. Nam, "Superconducting nanowire single photon detectors fabricated from an amorphous $Mo_{0.75}Ge_{0.25}$ thin film," *Applied Physics Letters*, vol. 105, no. 2, p. 022602, 2014.

[68] H. Takesue, S. D. Dyer, M. J. Stevens, V. Verma, R. P. Mirin, and S. W. Nam, "Quantum teleportation over 100km of fiber using highly efficient superconducting nanowire single-photon detectors," *Optica*, vol. 2, no. 10, p. 832, 2015.

[69] G. F. Hardy and J. K. Hulm, "The Superconductivity of Some Transition Metal Compounds," *Phys. Rev.*, vol. 93, no. 1949, pp. 1004–1016, 1954.

[70] A. Banerjee, L. J. Baker, A. Doye, M. Nord, R. M. Heath, K. Erotokritou, D. Bosworth, Z. H. Barber, I. MacLaren, and R. H. Hadfield, "Characterisation of amorphous molybdenum silicide (MoSi) superconducting thin films and nanowires," *Superconductor Science and Technology*, vol. 30, no. 8, p. 084010, 2017.

[71] A. Semenov, B. Günther, U. Böttger, H.-W. Hübers, H. Bartolf, A. Engel, A. Schilling, K. Ilin, M. Siegel, R. Schneider, D. Gerthsen, and N. A. Gippius, "Optical and transport properties of ultrathin NbN films and nanostructures," *Physical Review B*, vol. 80, no. 5, p. 054510, 2009.

[72] M. Caloz, B. Korzh, N. Timoney, M. Weiss, S. Gariglio, R. J. Warburton, C. Schönenberger, J. Renema, H. Zbinden, and F. Bussières, "Optically probing the detection mechanism in a molybdenum silicide superconducting nanowire single-photon detector," *Applied Physics Letters*, vol. 110, no. 8, p. 083106, 2017.

[73] K. M. Rosfjord, J. K. W. Yang, E. A. Dauler, A. J. Kerman, V. Anant, B. M. Voronov, G. N. Gol'tsman, and K. K. Berggren, "Nanowire single-photon detector with an integrated optical cavity and anti-reflection coating," *Optics Express*, vol. 14, no. 2, p. 527, 2006.

[74] D. Taillaert, F. Van Laere, M. Ayre, W. Bogaerts, D. Van Thourhout, P. Bienstman, and R. Baets, "Grating Couplers for Coupling between Optical Fibers and Nanophotonic Waveguides," *Japanese Journal of Applied Physics*, vol. 45, no. 8A, pp. 6071–6077, 2006.

[75] A. J. Miller, A. E. Lita, B. Calkins, I. Vayshenker, S. M. Gruber, and S. W. Nam, "Compact cryogenic self-aligning fiber-to-detector coupling with losses below one percent.," *Optics express*, vol. 19, no. 10, pp. 9102–9110, 2011.

[76] J. R. Clem and K. K. Berggren, "Geometry-dependent critical currents in superconducting nanocircuits," *Physical Review B - Condensed Matter and Materials Physics*, vol. 84, no. 17, pp. 1–27, 2011.

[77] S. N. Dorenbos, E. M. Reiger, N. Akopian, U. Perinetti, V. Zwiller, T. Zijlstra, and T. M. Klapwijk, "Superconducting single photon detectors with minimized polarization dependence," *Applied Physics Letters*, vol. 93, no. 16, p. 161102, 2008.

[78] E. F. C. Driessen, F. R. Braakman, E. M. Reiger, S. N. Dorenbos, V. Zwiller, and M. J. A. de Dood, "Impedance model for the polarization-dependent optical absorption of superconducting single-photon detectors," *The European Physical Journal Applied Physics*, vol. 47, no. 1, p. 10701, 2009.

[79] V. Anant, A. J. Kerman, E. A. Dauler, K. W. Joel, K. M. Rosfjord, and K. K. Berggren, "Optical properties of superconducting nanowire single-photon detectors," *Optics Express*, vol. 16, no. 14, pp. 46–52, 2008.

[80] V. Burenkov, H. Xu, B. Qi, R. H. Hadfield, and H.-K. Lo, "Investigations of afterpulsing and detection efficiency recovery in superconducting nanowire single-photon detectors," *Journal of Applied Physics*, vol. 113, no. 21, p. 213102, 2013.

[81] A. J. Kerman, J. K. Yang, R. J. Molnar, E. A. Dauler, and K. K. Berggren, "Electrothermal feedback in superconducting nanowire single-photon detectors," *Physical Review B - Condensed Matter and Materials Physics*, vol. 79, no. 10, pp. 1–5, 2009.

[82] X. Hu, S. Member, C. W. Holzwarth, D. Masciarelli, E. A. Dauler, and K. K. Berggren, "Efficiently Coupling Light to Superconducting Nanowire Single-Photon Detectors," *IEEE Trans. Appl. Supercond.*, vol. 19, no. 3, pp. 336–340, 2009.

[83] W. Pernice, C. Schuck, O. Minaeva, M. Li, G. Goltsman, A. Sergienko, and H. Tang, "High-speed and high-efficiency travelling wave single-photon detectors embedded in nanophotonic circuits," *Nature Communications*, vol. 3, p. 1325, 2012.

[84] C. Schuck, W. H. P. Pernice, H. X. Tang, E. Engineering, and N. Haven, "NbTiN superconducting nanowire detectors for visible and telecom wavelengths single photon counting on Si_3N_4 photonic circuits Current address : Institute of Nanotechnology , Karlsruhe Institute of Technology , 76133," in *Applied Physics Letters*, vol. 1, pp. 1–5, 2013.

[85] E. Schelew, M. K. Akhlaghi, and J. F. Young, "Waveguide integrated superconducting single-photon detectors implemented as near-perfect absorbers of coherent radiation," *Nature Communications*, vol. 6, pp. 1–8, 2015.

[86] J. P. Sprengers, a. Gaggero, D. Sahin, S. Jahanmirinejad, G. Frucci, F. Mattioli, R. Leoni, J. Beetz, M. Lermer, M. Kamp, S. Hfling, R. Sanjines, and a. Fiore, "Waveguide superconducting single-photon detectors for integrated quantum photonic circuits," *Applied Physics Letters*, vol. 99, no. 18, pp. 2013–2016, 2011.

[87] F. Najafi, J. Mower, N. C. Harris, F. Bellei, A. Dane, C. Lee, X. Hu, P. Kharel, F. Marsili, S. Assefa, K. K. Berggren, and D. Englund, "On-chip detection of non-classical light by scalable integration of single-photon detectors," *Nature Communications*, vol. 6, no. 5873, p. 5873, 2015.

[88] P. Sarrafi, E. Y. Zhu, K. Dolgaleva, B. M. Holmes, D. C. Hutchings, J. S. Aitchison, and L. Qian, "Continuous-wave quasi-phase-matched waveguide correlated photon pair source on a III–V chip," *Applied Physics Letters*, vol. 103, no. 25, p. 251115, 2013.

[89] C. Schuck, W. H. P. Pernice, and H. X. Tang, "Waveguide integrated low noise NbTiN nanowire single-photon detectors with milli-Hz dark count rate," *Scientific Reports*, vol. 3, no. 1, p. 1893, 2013.

[90] P. W. Shor, "Polynomial-Time Algorithms for Prime Factorization and Discrete Logarithms on a Quantum Computer," *Society for Industrial and Applied Mathematics*, vol. 41, no. 2, pp. 124–134, 1996.

[91] L. K. Grover, "Quantum Mechanics helps in searching for a needle in a haystack," *Physical Review Letters*, vol. 79, p. 325, 1994.

[92] H. L. Hortensius, E. F. C. Driessen, T. M. Klapwijk, K. K. Berggren, and J. R. Clem, "Critical-current reduction in thin superconducting wires due to current crowding," *Applied Physics Letters*, vol. 100, no. 18, pp. 3–7, 2012.

[93] J. L. O'Brien, A. Furusawa, and J. Vučković, "Photonic quantum technologies," *Nature Photonics*, vol. 3, no. 12, pp. 687–695, 2010.

[94] N. Brunner, D. Cavalcanti, S. Pironio, V. Scarani, and S. Wehner, "Bell nonlocality," *Reviews of Modern Physics*, vol. 86, no. 2, pp. 419–478, 2014.

[95] L. M. Vandersypen, M. Steffen, G. Breyta, C. S. Yannoni, M. H. Sherwood, and I. L. Chuang, "Experimental realization of Shor's quantum factoring algorithm using nuclear magnetic resonance.," *Nature*, vol. 414, no. 6866, pp. 883–7, 2001.

[96] J. A. Jones, "Quantum computing with NMR," *Progress in Nuclear Magnetic Resonance Spectroscopy*, vol. 59, no. 2, pp. 91–120, 2011.

[97] J. C. F. Matthews, A. Politi, A. Stefanov, and J. L. O'Brien, "Manipulation of multiphoton entanglement in waveguide quantum circuits," *Nature Photonics*, vol. 3, no. 6, pp. 346–350, 2009.

[98] C. M. Natarajan, A. Peruzzo, S. Miki, M. Sasaki, Z. Wang, B. Baek, S. Nam, R. H. Hadfield, and J. L. O'Brien, "Operating quantum waveguide circuits with superconducting single-photon detectors," *Applied Physics Letters*, vol. 96, no. 21, p. 211101, 2010.

[99] A. Politi, M. J. Cryan, J. G. Rarity, S. Yu, and J. L. O'Brien, "Silica-on-Silicon Waveguide Quantum Circuits," *Science*, vol. 320, no. 5876, pp. 646–649, 2008.

[100] D. Bonneau, E. Engin, K. Ohira, N. Suzuki, H. Yoshida, N. Iizuka, M. Ezaki, C. M. Natarajan, M. G. Tanner, R. H. Hadfield, S. N. Dorenbos, V. Zwiller, J. L. O'Brien, and M. G. Thompson, "Quantum interference and manipulation of entanglement in silicon wire waveguide quantum circuits," *New Journal of Physics*, vol. 14, pp. 0–12, 2012.

[101] F. Bussières, C. Clausen, A. Tiranov, B. Korzh, V. B. Verma, S. W. Nam, F. Marsili, A. Ferrier, P. Goldner, H. Herrmann, C. Silberhorn, W. Sohler, M. Afzelius, and N. Gisin, "Quantum teleportation from a telecom-wavelength photon to a solid-state quantum memory," *Nature Photonics*, vol. 8, no. 10, pp. 775–778, 2014.

[102] R. Ursin, T. Jennewein, L. Cacciapuoti, T. Scheidl, A. Acin, J. Capmany, D. Giggenbach, R. H. Hadfield, N. Lutkenhaus, M. Peev, J. Rarity, E. Samain, W. Tittel, M. Toyoshima, V. Pruneri, I. Walmsley, and A. Zeilinger, "Space-QUEST: Experiments with quantum entanglement in space," *Europhysics News*, vol. 40, no. 3, p. 4, 2009.

[103] P. J. Shadbolt, M. R. Verde, a. Peruzzo, a. Politi, a. Laing, M. Lobino, J. C. F. Matthews, and J. L. O'Brien, "Generating, manipulating and measuring entanglement and mixture with a reconfigurable photonic circuit," *Nature Photonics*, vol. 6, no. 1, p. 6, 2011.

[104] D. Bonneau, M. Lobino, P. Jiang, C. M. Natarajan, M. G. Tanner, R. H. Hadfield, S. N. Dorenbos, V. Zwiller, M. G. Thompson, and J. L. O'Brien, "Fast path and polarization manipulation of telecom wavelength single photons in lithium niobate waveguide devices," *Physical Review Letters*, vol. 108, no. 5, pp. 1–5, 2012.

[105] K. De Greve, P. L. McMahon, L. Yu, J. S. Pelc, C. Jones, C. M. Natarajan, N. Y. Kim, E. Abe, S. Maier, C. Schneider, M. Kamp, S. Höfling, R. H. Hadfield, A. Forchel, M. M. Fejer, and Y. Yamamoto, "Complete tomography of a high-fidelity solid-state entangled spin–photon qubit pair," *Nature Communications*, vol. 4, p. 2228, 2013.

[106] C. Schuck, X. Guo, L. Fan, X. Ma, M. Poot, and H. X. Tang, "Quantum interference in heterogeneous superconducting-photonic circuits on a silicon chip," *Nature Communications*, vol. 7, p. 10352, 2016.

[107] R. L. Rivest, A. Shamir, and L. Adleman, "A method for obtaining digital signatures and public-key cryptosystems," *Communications of the ACM*, vol. 21, no. 2, pp. 120–126, 1978.

[108] D. Rosenberg, C. G. Peterson, J. W. Harrington, P. R. Rice, N. Dallmann, K. T. Tyagi, K. P. McCabe, S. Nam, B. Baek, R. H. Hadfield, R. J. Hughes, and J. E. Nordholt, "Practical long-distance quantum key distribution system using decoy levels," *New Journal of Physics*, vol. 11, pp. 1–10, 2009.

[109] C. H. Bennett and G. Brassard, "Quantum Cryprography: Public Key distribution and coin tossing," in *Internation Conference on Computers, Systems & Signal Processing*, 1984.

[110] M. G. Tanner, V. Makarov, and R. H. Hadfield, "Optimised quantum hacking of superconducting nanowire single-photon detectors," *Optics Express*, vol. 22, no. 6, p. 6734, 2014.

[111] T. Honjo, M. Fujiwara, K. Shimizu, K. Tamaki, S. Miki, T. Yamashita, H. Terai, Z. Wang, and M. Sasaki, "Countermeasure against tailored bright illumination attack for DPS-QKD," *Optics Express*, vol. 21, no. 3, p. 2667, 2013.

[112] W. Hwang, "Quantum Key Distribution with High Loss: Toward Global Secure Communication," *Physical Review Letters*, vol. 91, no. 5, p. 057901, 2003.

[113] H.-k. Lo, X. Ma, and K. Chen, "Decoy State Quantum Key Distribution," *Physical Review Letters*, vol. 94, no. 23, p. 230504, 2005.

[114] M. Lucamarini, K. a. Patel, J. F. Dynes, a. W. Sharpe, Z. L. Yuan, R. V. Penty, and A. J. Shields, "Efficient decoy-state quantum key distribution with quantified security," *Optics Express*, vol. 21, no. 21, pp. 24550–24565, 2013.

[115] K. Koshelev, M. Ali Mohammad, T. Fito, K. L. Westra, S. K. Dew, and M. Stepanova, "Comparison between ZEP and PMMA resists for nanoscale electron beam lithography experimentally and by numerical modeling," *Journal of Vacuum Science & Technology B, Nanotechnology and Microelectronics: Materials, Processing, Measurement, and Phenomena*, vol. 29, p. 06F306, nov 2011.

[116] T. P. Chow and A. J. Steckl, "Plasma etching characteristics of sputtered $MoSi_2$ films," *Applied Physics Letters*, vol. 37, no. 5, pp. 466–468, 1980.

[117] S. N. Dorenbos, E. M. Reiger, U. Perinetti, V. Zwiller, T. Zijlstra, and T. M. Klapwijk, "Low noise superconducting single photon detectors on silicon," *Applied Physics Letters*, vol. 93, no. 13, pp. 2–5, 2008.

[118] D. Rosenberg, A. J. Kerman, R. J. Molnar, and E. A. Dauler, "High-speed and high-efficiency superconducting nanowire single photon detector array," *Optics Express*, vol. 21, no. 2, pp. 1440–1447, 2013.

[119] D. Bosworth, S.-L. Sahonta, R. H. Hadfield, and Z. H. Barber, "Amorphous molybdenum silicon superconducting thin films," *AIP Advances*, vol. 5, no. 8, p. 087106, 2015.

[120] "Pulse Tube Cryocoolers versus Gifford-McMahon Cryocoolers: a comparison of vibration levels." https://www.janis.com/products/Cryocoolers/PulseTubeVsGifford-McMahonCryocoolers.aspx. Date accessed: 1 August 2017.

[121] V. K. Pecharsky and K. A. Gschneidner Jr, "Magnetocaloric effect and magnetic refrigeration," *Journal of Magnetism and Magnetic Materials*, vol. 200, no. 1-3, pp. 44–56, 1999.

[122] Preiffer, *Vacuum Technology*, vol. II. Pfeiffer Vacuum GmbH, 1st ed., 2013.

[123] R. Radebaugh, "Development of the Pulse Tube Refrigerator as an Efficient and Reliable Cryocooler," *Proceedings of Institute of Refrigeration*, vol. 96, 2000.

[124] R. Radebaugh, "Refrigeration for superconductors," *Proceedings of the IEEE*, vol. 92, no. 10, pp. 1719–1734, 2004.

[125] *Model PT405-RM Cryogenic Refrigerator Manual.* Syracuse, NY: Cryomech, 2013.

[126] C. Wang, G. Thummes, and C. Heiden, "A two-stage pulse tube cooler operating below 4 K," *Cryogenics*, vol. 37, no. 3, pp. 159–164, 1997.

[127] R. Bhatia, S. Chase, S. Edgington, J. Glenn, W. Jones, A. Lange, B. Maffei, A. Mainzer, P. Mauskopf, B. Philhour, and B. Rownd, "A three-stage helium sorption refrigerator for cooling of infrared detectors to 280mK," *Cryogenics*, vol. 40, no. 2000, pp. 685–691, 2000.

[128] S. Chase and L. Kenny, *Two-Stage Sub-Kelvin ^{3}He Cooler Manual.* Sheffield: Chase Cryogenics, 2012.

[129] Rayleigh, "XXXI. Investigations in optics, with special reference to the spectroscope," *Philosophical Magazine*, vol. 8, no. 49, pp. 261–274, 1879.

[130] J. A. O'Connor, *Nano-Optical Studies of Superconducting Nanowire Single- Photon Detectors.* PhD thesis, Heriot-Watt University, United Kingdom, 2011.

[131] C. M. Sparrow, "On Spectroscopic resolving power," *The Astrophysical Journel*, vol. 44, p. 76, 1916.

[132] M. B. Ward, O. Z. Karimov, D. C. Unitt, Z. L. Yuan, P. See, D. G. Gevaux, A. J. Shields, P. Atkinson, and D. A. Ritchie, "On-demand single-photon source for 1.3 micron telecom fiber," *Applied Physics Letters*, vol. 86, no. 20, pp. 1–3, 2005.

[133] A. Lita, V. Verma, R. D. Horansky, J. Shainline, R. Mirin, and S. Nam, "Materials Development for High Efficiency Superconducting Nanowire Single-Photon Detectors," *MRS Online Proceedings Library (OPL)*, vol. 1807, pp. 1–6, 2015.

[134] J. W. Silverstone, D. Bonneau, K. Ohira, N. Suzuki, H. Yoshida, N. Iizuka, M. Ezaki, C. M. Natarajan, M. G. Tanner, R. H. Hadfield, V. Zwiller, G. D. Marshall, J. G. Rarity, J. L. O. Brien, and M. G. Thompson, "On-chip quantum interference between silicon photon-pair sources," *Nature Photonics*, vol. 8, no. 2, pp. 104–108, 2013.

[135] L. Midolo, S. L. Hansen, W. Zhang, C. Papon, R. Schott, A. Ludwig, A. D. Wieck, P. Lodahl, and S. Stobbe, "Electro-optic routing of photons from single quantum dots in photonic integrated circuits," *ArXiv e-prints*, July 2017.